



# Contents

<b>1</b>	<b>Introduction to <math>\gamma</math>-Ray Astronomy .....</b>	<b>5</b>
1.1	Cosmic-ray physics .....	6
1.2	Acceleration mechanisms .....	8
1.2.1	Electric field acceleration .....	8
1.2.2	Stochastic acceleration .....	11
1.2.3	Diffusive Shock Acceleration .....	11
1.3	Production of $\gamma$ -rays .....	13
1.3.1	Bremsstrahlung .....	15
1.3.2	Inverse Compton scattering .....	15
1.3.3	Synchrotron emission .....	17
1.3.4	Curvature radiation .....	17
1.3.5	Matter-Antimatter annihilation .....	18
1.3.6	Hadronic collisions .....	18
1.4	$\gamma$ -ray Absorption mechanisms .....	19
1.4.1	Interaction with electrons: Compton effect .....	19
1.4.2	Pair production processes .....	20
1.4.3	The Extragalactic Background Light .....	20
1.5	Dark Matter and $\gamma$ -rays: WIMP annihilation .....	22
1.6	$\gamma$ -ray sources .....	26
1.6.1	Galactic sources .....	26
1.6.2	Extragalactic sources .....	34
1.6.3	Potential Dark Matter annihilation emission sources .....	39

<b>2</b>	<b>Detection of <math>\gamma</math>-rays .....</b>	<b>43</b>
<b>2.1</b>	<b>Space detectors .....</b>	<b>44</b>
2.1.1	Compton detectors .....	44
2.1.2	Pair production detectors .....	47
<b>2.2</b>	<b>Extensive Air Showers .....</b>	<b>48</b>
2.2.1	Electromagnetic Showers .....	50
2.2.2	Hadronic showers .....	52
2.2.3	Electronic showers .....	54
<b>2.3</b>	<b>Cherenkov radiation .....</b>	<b>54</b>
<b>2.4</b>	<b>Ground-based detectors .....</b>	<b>58</b>
2.4.1	Particle detectors .....	58
2.4.2	Atmospheric Cherenkov Telescopes .....	59
<b>3</b>	<b>The Cherenkov Telescope Array .....</b>	<b>67</b>
<b>3.1</b>	<b>Introduction .....</b>	<b>67</b>
<b>3.2</b>	<b>CTA Requirements and Performance .....</b>	<b>68</b>
<b>3.3</b>	<b>CTA Telescopes .....</b>	<b>73</b>
3.3.1	Large Size Telescope (LST) .....	75
3.3.2	Medium Size Telescope (MST) .....	77
3.3.3	Small Size Telescope (SST) .....	80
<b>3.4</b>	<b>Reconstruction and Analysis tools .....</b>	<b>83</b>
3.4.1	Monte Carlo simulations .....	83
3.4.2	Low level analysis: ctapipe .....	85
3.4.3	Science analysis: ctools .....	86
<b>4</b>	<b>Analysis chain of Single Telescope data and sensitivity calculation for the LST1 .....</b>	<b>89</b>
<b>4.1</b>	<b>Introduction .....</b>	<b>89</b>
<b>4.2</b>	<b>The LST1 analysis chain overview .....</b>	<b>89</b>
4.2.1	Calibration .....	90
4.2.2	Image cleaning and parameterization .....	92
4.2.3	Reconstruction of energy and source position .....	93
4.2.4	$\gamma$ -hadron separation .....	95
<b>4.3</b>	<b>Sensitivity of the LST1 .....</b>	<b>97</b>
4.3.1	Reweighting .....	98
4.3.2	Cut optimization .....	100
4.3.3	Expected LST1 Performance .....	100

<b>4.4</b>	<b>Expectation-Maximization method for Hillas Parameters...</b>	<b>105</b>
4.4.1	The Expectation-Maximization algorithm .....	107
4.4.2	Comparison of EM without cleaning and tailcuts cleaning .....	109
<b>4.5</b>	<b>Results on real data</b>	<b>111</b>
<b>4.6</b>	<b>Summary and conclusion</b>	<b>113</b>
<b>5</b>	<b>Characterization of the Large Magellanic Cloud at TeV energies and prospects on Dark Matter detection for CTA</b>	<b>115</b>
<b>5.1</b>	<b>Introduction</b>	<b>115</b>
<b>5.2</b>	<b>Emission Model</b>	<b>117</b>
5.2.1	Diffuse emission .....	118
5.2.2	Point Sources .....	119
5.2.3	PWNe population in the LMC .....	123
<b>5.3</b>	<b>Simulations and Analysis method</b>	<b>125</b>
5.3.1	Region of Interest and Observational strategy .....	125
5.3.2	Simulation parameters .....	126
5.3.3	Fitting method .....	127
<b>5.4</b>	<b>Results</b>	<b>130</b>
5.4.1	Point sources .....	130
5.4.2	Population of PWNe .....	130
5.4.3	Diffuse Emission .....	131
<b>5.5</b>	<b>Dark Matter annihilation in the LMC</b>	<b>131</b>
5.5.1	Dark Matter profile in the LMC .....	134
5.5.2	$\gamma$ -ray spectrum .....	137
5.5.3	Results on DM sensitivity curves .....	137
<b>5.6</b>	<b>Summary and conclusions</b>	<b>137</b>
<b>A</b>	<b>The L1 Trigger System of the LST1 .....</b>	<b>143</b>
<b>A.1</b>	<b>Introduction</b>	<b>143</b>
<b>A.2</b>	<b>Pixel Level: L0 trigger decision</b>	<b>144</b>
A.2.1	Majority trigger .....	145
A.2.2	Sum trigger .....	145
A.2.3	Camera Level: L1 trigger decision .....	145
A.2.4	Array Level trigger decision .....	146

<b>B</b>	<b>Characterization of analogue ASIC for L1 trigger decision</b>	149
B.1	Introduction	149
B.2	Quality control test	150
B.2.1	Test DAC .....	150
B.2.2	Voltage Test: Rate scan .....	150
B.2.3	Test Adder Channels .....	151
B.2.4	Analog Offset test .....	151
B.2.5	Digital Offset test .....	151
B.3	Characterization of the ASIC	151
B.3.1	Rate Scan Fit .....	151
B.3.2	Gain .....	152
B.3.3	Offset .....	152
B.3.4	Noise .....	154
B.4	Characterization: Summary and discussion	154
<b>C</b>	<b>Calibration method for the L1 analog trigger system of LST camera</b>	163
C.1	Introduction	163
C.2	L1 transfer function calibration	164
C.2.1	Calibration algorithm .....	164
C.2.2	Calibration result .....	165
<b>D</b>	<b>Time calibration for implementation of the trigger distribution in the backplane network of LST camera</b>	167
D.1	Introduction	167
D.2	Time calibration procedure	167
D.3	Time calibration setup and tests	169
<b>E</b>	<b>Random Forests</b>	171
E.1	Introduction	171
E.2	Gini Index	171



# 1. Introduction to $\gamma$ -Ray Astronomy



During many centuries humanity has looked towards the skies and wondered about the mysteries of the universe. At first, with the naked eye, our ancestors measured the movements of astronomical objects and used them as calendars and guidance. We can say that modern Astronomy was born with the invention of the optical telescope by Galileo in 1609 AD. However, we were looking only to a small part of the universe, being only able to study the stars through the visible light they were emitting. Like an incomplete symphony where we can only listen to the melody of one instrument, our knowledge of the physics of the cosmos was purely limited to the thermal emission of stars. It was not until the first half of the XX century that we could start talking about the *multiwavelength* astronomy with the first infrared, radio, ultraviolet and X-ray observations. The most energetic part of the electromagnetic spectrum,  $\gamma$ -rays, were first detected in the 1960s. Along with the multiwavelength astronomy, other messengers from the sky were discovered: In 1912 the Austrian physicist Victor Hess found that the puzzling source of high levels of ionizing radiation in the atmosphere were actually charged particles coming from space. These particles were later named Cosmic Rays (CRs) by Millikan, and as will be explained later, their origin was thought to be closely related to the origin of  $\gamma$ -rays. The emission of this high energy radiation (above 100 keV), and the origin of such energetic particles as CRs were, could not be explained by means of thermal processes, thus other physical phenomena came into play, mostly involving interactions of relativistic particles.

The Astroparticle physics field studies the relation between  $\gamma$ -rays and CRs, combining astrophysics and particle physics, and includes other cosmic messengers, as neutrinos, to face unresolved problems like the origin and acceleration mechanisms of CRs, towards the completion of the cosmic symphony that is the Universe.

This chapter will be an overview of the basic concepts of CR and  $\gamma$ -ray physics, their production, acceleration and absorption, and their known sources of emission in

the universe.

## 1.1 Cosmic-ray physics

CRs are relativistic charged particles arriving to the atmosphere from the outer space. Their origin and the mechanisms that accelerate them to reach such high energies are still being debated. However, there are arguments pointing towards that they are accelerated in very violent events in the universe, such as supernova explosions. Several measurements strongly support that galactic CRs are in fact accelerated in Supernova Remnants (SNRs) [1], [2], [3].

As they are charged particles, they suffer from the effects of the magnetic fields (both interstellar and Earth magnetic fields) which divert their trajectories and make very difficult to trace back their original direction. Nevertheless, they can interact with the medium close to their sources producing  $\gamma$ -rays through processes such as Inverse Compton (IC) scattering or neutral pion decay. Observing  $\gamma$ -rays, which travel in straight lines from their origin, can provide information on how and where do CRs are produced and interact with the medium.

The composition of CRs arriving to the Earth is mainly protons (86%), alpha particles (11%), electrons (2%) and other heavy nuclei (1%). We can distinguish between two types of cosmic-rays: Those reaching the Earth unaltered from their source, known as *primary CRs*; and those resulting from inelastic collisions of the primary CRs with the Interstellar Medium (ISM), called *secondary CRs*.

The spectrum of CRs is shown in figure 1.1. Mostly it can be described as a piecewise Power Law with a spectral index  $\gamma$  that changes along different regions of the spectrum [4]:

$$\frac{dN(E)}{dE} \propto E^{-\gamma} \quad (1.1)$$

Where N is the differential flux of CRs and E is the energy. The different parts that can be observed are:

- From few keV to less than 10 GeV: CRs are produced locally in solar flares and coronal mass ejections from the Sun [5], with a spectral index  $\sim 5$  [6].
- Up to the *knee* (below  $10^6$  GeV): CRs follow a simple power law with spectral index  $\gamma \sim 2.7$ . In this region CRs are considered to have a galactic origin, accelerated in SNRs.
- From the *knee* to the *second knee* (at  $10^8$  GeV) the spectral index becomes  $\sim 3.1$ .
- Between the *second knee* (at  $10^8$  GeV) and the *ankle* the spectral index is  $\sim 3.3$ .
- Energies above the *ankle* ( $\sim 10^9$  GeV): CRs coming from extragalactic sources are predominant, with a hardening in the spectrum back to an index  $\sim 2.7$ . At

such high energies, particles are no more confined by galactic magnetic fields so they travel with their trajectories almost unperturbed [7], allowing to estimate their direction. These kind of very energetic CRs can be produced in Active Galaxy Nuclei (AGN), Gamma Ray Bursts (GRBs), radio galaxy lobes and intra-cluster medium in galaxy clusters [8].

- At energies above  $\sim 4-5 \times 10^{10}$  GeV a strong suppression is observed, interpreted as the GZK cutoff, which sets a theoretical upper limit on the energy carried by CR from distant sources.

As already mentioned, it is possible to differentiate two CR origins: galactic CR and extragalactic CR. Below the *knee*, CRs are produced in galactic accelerators (SNRs) and their maximum energy can be considered a limit on the acceleration that is possible to gain from these kind of objects. CRs with energies above the *ankle* are thought to come from extragalactic sources and so, their higher acceleration must come from different phenomena, more violent and energetic (AGN, GRBs, etc.). The Larmor radius defines the curved trajectory of charged particles moving perpendicular to a magnetic field. The "Hillas condition" [10] sets a minimum requirement for the accelerators to reach certain energies, stating that a necessary condition to accelerate particles to ultrahigh energy is that of confinement, meaning that they can stay in the acceleration region as long as their Larmor radius is smaller than the size of the accelerator. For energies over the *ankle*, the Larmor radius starts to become larger than galactic scales, hence extragalactic CRs propagate almost linearly and unaffected by the galactic magnetic field, while galactic (less energetic) CRs propagate diffusively through the ISM. Figure 1.2 shows the Hillas diagram, where different source classes are presented as function of their characteristic size and magnetic field strength.

The transition in the spectrum between galactic and extragalactic accelerators, although still not well understood, can be explained by the effect of the galactic magnetic field in the trajectories of CRs, and the effect of galactic wind termination shocks as a re-acceleration process [4].

The chemical composition of galactic CRs is very similar to that of the Solar System (see figure 1.3), suggesting a similar origin (stellar interiors) but with some discrepancies in certain elements. The most noticeable difference regards Li, Be and B, and to a lesser extent sub iron elements Mn, Cr, V, Ti and Se. The abundances of these elements are small in stars because they are rapidly consumed by nuclear reactions, but they are present in secondary CRs due to *spallation* of carbon and oxygen nuclei [11] and other abundant heavy nuclei as Fe and Ni [12].

## 1.2 Acceleration mechanisms

Acceleration mechanisms take place in astrophysical plasmas which in general consists on thermal plasma components, a magnetic field and non-thermal distributions of fast particles. Within the plasma, turbulence and plasma waves take place, having an important role in particle acceleration. The mechanisms that accelerate CRs to the huge energies observed, that can reach up to  $10^{20}$  eV are still a topic of debate and

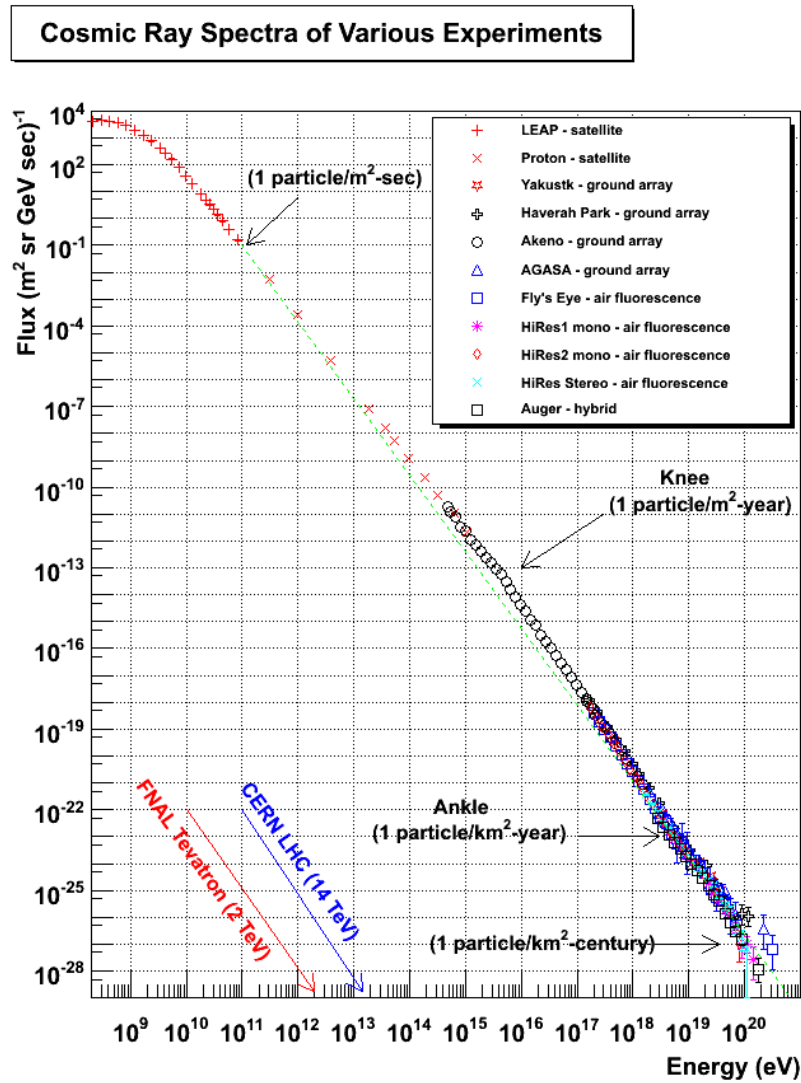


Figure 1.1: Cosmic ray spectrum from [9] built with data from several experiments. Red and blue lines represent the energy spectrum covered by Tevatron and LHC accelerators. Green line shows the fit to a power law with spectral index 2.7.

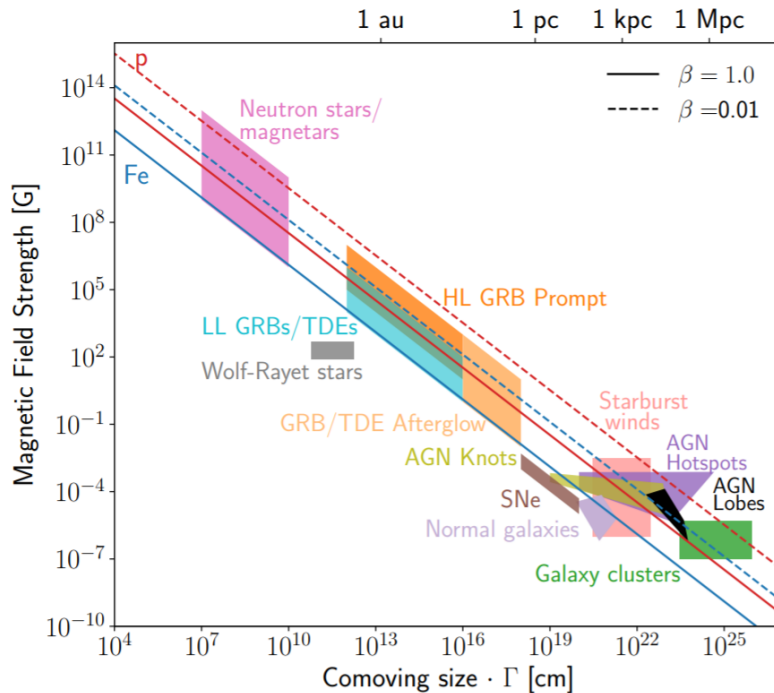


Figure 1.2: Hillas diagram, from [8]. Source classes as a function of their characteristic radius  $R$ , given as the comoving size of the source times the Lorentz factor  $\Gamma$ , and the magnetic field  $B$  in the comoving frame of the source. Solid (dashed) lines indicate the product of  $B \times R$  beyond which confinement of protons (red) and iron (blue) nuclei with energy  $10^{20}$  eV are possible for outflows with velocity  $\beta_{ish} = 1$  ( $\beta_{ish} = 0.01$ ).

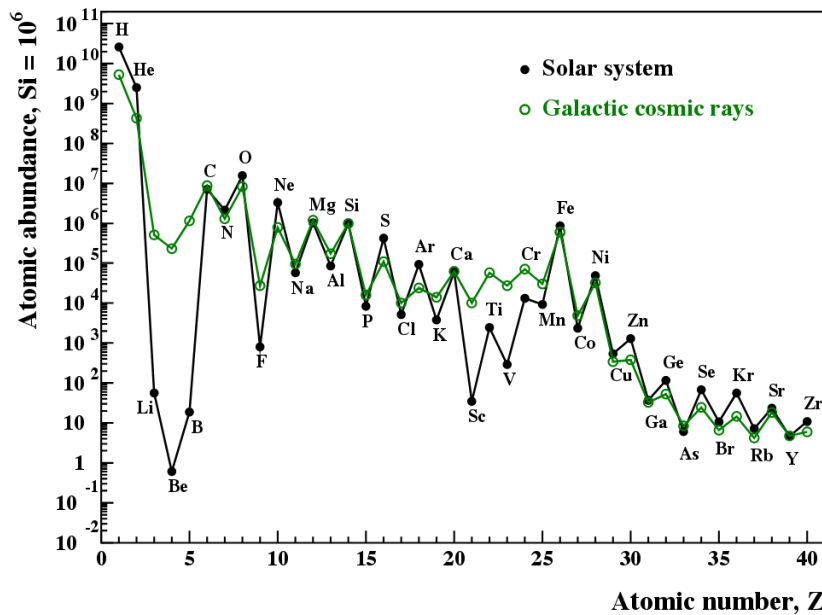


Figure 1.3: Abundances of elements of galactic CRs compared to the Solar System, from [12].

research in the high energy astrophysics field. Several particle acceleration mechanisms are proposed to explain the CR spectrum, which should be able to achieve the highest energies measured for CR and reproduce the spectral shape of a power law with an index  $\sim 2.7$ , and the abundances of elements measured [13], [14], [15].

### 1.2.1 Electric field acceleration

Electric fields parallel to magnetic fields can accelerate charged particles and can arise during magnetic field reconnection (the breaking and reconnecting of oppositely magnetic field lines in a plasma). Because ideal Magnetohydrodynamics (MHD) of plasmas require the paralell component of electric field to be null  $E_{\parallel} = 0$ , non-ideal MHD effects are needed to explain the development of  $E_{\parallel} = 0$ , such as resistivity or inertial effects on Alfvén waves (a type of MHD wave where ions oscillate in response to a restoring force provided by an effective tension on the magnetic field lines) [15]. This kind of acceleration is believed to take place in magnetic reconnection of the Earth's magnetotail, accelerating auroral electrons; Also, reconnection in pulsar gaps (see section 1.6.1) could produce this kind of acceleration which should involve large oscillations in  $E_{\parallel}$ .

### 1.2.2 Stochastic acceleration

Stochastic acceleration is also known as *Second Order Fermi acceleration* or simply *Fermi process*. This idea was developed by Enrico Fermi in 1949 [16] as a mechanism

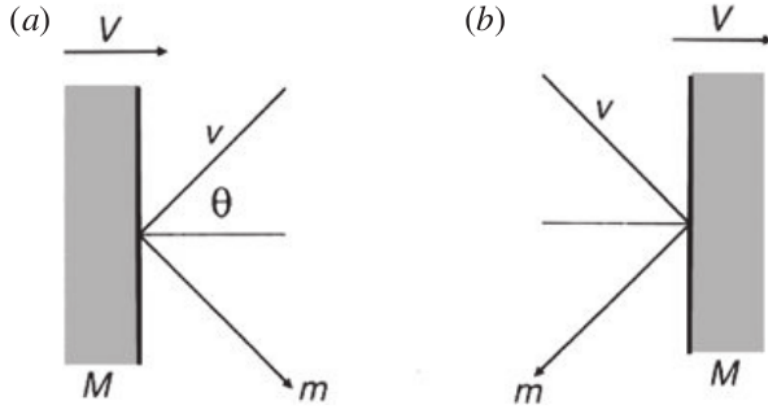


Figure 1.4: Collision of a particle of mass  $m$  with velocity  $v$  against a cloud of mass  $M$  and velocity  $V$ . a) head-on. b) head-tail. From [17].

to explain acceleration of galactic CRs. The basic concept is that particles can gain velocity after being reflected several times by randomly moving magnetized clouds in the ISM. Fermi showed that after a characteristic time  $\tau_{esc}$ , the spectrum of the accelerated particles would follow a power law. If the particle is moving with a pitch angle  $\theta$  (the angle between the particle velocity vector and the local magnetic field), the gain in energy after a collision with a cloud moving with velocity  $V$  will be [17]:

$$\Delta E = E \left[ \frac{2V \cos \theta}{c^2} + 2 \left( \frac{V^2}{c} \right) \right] \quad (1.2)$$

Where  $E$  is the energy of the particle before the collision. Between collisions the particle will be moving inside a plasma and will suffer scattering due to hydrodynamic waves, the total gain in energy has to be averaged over a set of random  $\theta$  angles. The probability of a collision is proportional to the relative velocities of the particle ( $v$ ) and the cloud ( $V$ ). If  $v \approx c$  the probability of a head-on collision  $P \propto 1 + (V/c)\cos\theta$  is slightly higher than the probability of head-tail collision  $P \propto 1 - (V/c)\cos\theta$  (see figure 1.4) hence the total, averaged in all  $\theta$  angles between 0 and  $\pi$ , gain in energy will be positive:

$$\left\langle \frac{\Delta E}{E} \right\rangle = \frac{8}{3} \left( \frac{V}{c} \right)^2 \quad (1.3)$$

Being the increase in energy *second order* proportional to  $V/c$ . However, this process cannot be the main source of particle acceleration: the velocities of interstellar clouds in the ISM is too low ( $V/c \simeq 10^{-4}$ ), the mean free path of CRs in the ISM is too high (the number of collisions would be  $\sim 1\text{yr}^{-1}$ ) and the particles should be

injected in the acceleration region with already high velocities (this is known as the *injection problem* and actually is present in every acceleration mechanism).

### 1.2.3 Diffusive Shock Acceleration

The most popular acceleration mechanism in astrophysical plasmas, which is believed to take place in SNRs (the best candidates for galactic CR production) is known as Diffusive Shock Acceleration (DSA) or *First Order Fermi acceleration*. This mechanism revisits the original idea formulated by Fermi of particles colliding with randomly moving "magnetic mirrors" in the ISM, but with all the collisions happening always head-on. For example, when two clouds are approaching each other and the particle bounces back and forth [15]. This process can happen in the presence of strong supersonic shock waves propagating through a diffuse medium, like the ones produced after a Supernova (SN) explosion (see figure 1.5). A flux of relativistic particles is assumed to exist in both sides of the shock, which are moving much faster than the latter. Each time a particle crosses to one side or the other, their velocity becomes isotropic in the frame of reference of the moving fluid. Since on every crossing the particle encounters gas moving towards it at a velocity proportional to the shock velocity ( $U$ ), which for a fully ionized plasma composed by monoatomic perfect gas is  $\sim 3/4U$  [17] it will receive a boost in energy of the order  $\sim U/c$ . That is why this process is called *first order* in counterpart to the classical second order Fermi acceleration where the energy gain in each collision is proportional to  $\sim (U/c)^2$ . DSA is able to predict a spectral index of  $\sim 2$ , very close to the observed for galactic CR. Also, is the only acceleration mechanism efficient enough to transfer the observed amount of energy in SNR to particles. On the other hand, it exists an upper limit on the maximum energy that a particle can gain through DSA which is set to  $\sim 10^{14}$  eV [18], so is still not enough to explain the full CR spectrum, which reaches up to  $\sim 10^{20}$  eV.

## 1.3 Production of $\gamma$ -rays

Although CRs have been known for many decades, it is difficult to make conclusions about their origin and acceleration mechanisms. As they are charged particles, their trajectories are deflected while travelling through the ISM, hence their incoming direction does not point towards the source of origin. Nevertheless, CRs can interact with the medium producing  $\gamma$ -rays through several mechanisms, which reach the Earth undeflected, offering a way to indirectly study CR origin, acceleration and diffusion in the ISM. When we talk about radiation production, we can distinguish between two main mechanisms which involve very different physical phenomena: thermal and non-thermal processes. A large fraction of the low energy radiation emitted by stars or interstellar dust is produced by thermal processes following a black body spectrum. To produce radiation as energetic as  $\gamma$ -rays a temperature of the order of  $10^{10}$  K would be needed, which is something that was only reachable in the Big Bang conditions. Therefore, to understand the production of  $\gamma$ -rays we must study

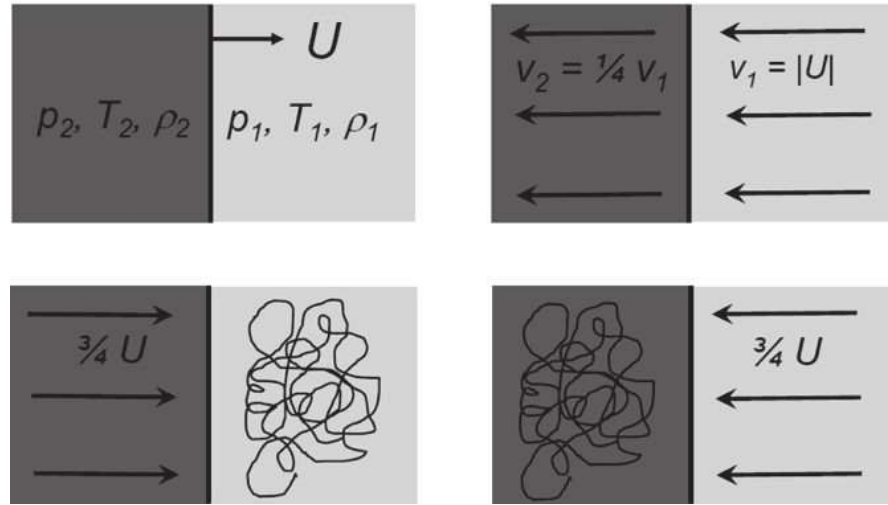


Figure 1.5: Scheme of the *Diffuse shock acceleration* from [17]. *Upper left*. Observer frame: A diffusive shock is propagating at velocity  $U$ . *Upper right*. Frame where the shock front is at rest. The velocities of the gas in both sides of the front, assuming is fully ionized, have a ratio of 4. *Lower left*. Frame of reference where the upstream gas is at rest, the distribution of velocities of the high energy particles is isotropic. *Lower right* Same case as previous, but in the reference frame of the downstream gas.

the so called *non-thermal universe*, where radiation is produced by interactions of relativistic particles moving in electromagnetic fields. In general,  $\gamma$ -rays are produced in two kinds of scenarios: leptonic emission (produced mainly by electrons) and hadronic emission (produced mainly by protons). Which one of those is dominant in astrophysical particle accelerators is still a subject of debate and will be commented in section 1.6 about  $\gamma$ -ray sources. In this section a brief summary on the different  $\gamma$ -ray production mechanisms (see figure 1.6) is given.

### 1.3.1 Bremsstrahlung

From the German "braking radiation", the bremsstrahlung process occurs when a charged particle is decelerated by the electric field produced by an atomic nucleus. While their trajectory is deflected, the particle emits electromagnetic radiation with amplitude proportional to the magnitude of the deceleration suffered. The differential cross section for a particle of charge  $e$ , mass  $m$ , carrying an energy  $E_e$  to radiate a photon between energies  $E_\gamma$  and  $E_\gamma + dE$  when interacting with the Coulomb field is:

$$\sigma(E_e, E_\gamma) dE_\gamma = 4\alpha Z^2 r_e^2 \frac{dE_\gamma}{E_\gamma} F(E_e, \nu) \quad (1.4)$$

Where:

$$F(E_e, \nu) = [1 + (1 - \nu)^2 - \frac{2}{3}(1 - \nu)] \left[ \ln \left( \frac{2E_e}{m_e c^2} \frac{1 - \nu}{\nu} \right) - \frac{1}{2} \right] \quad (1.5)$$

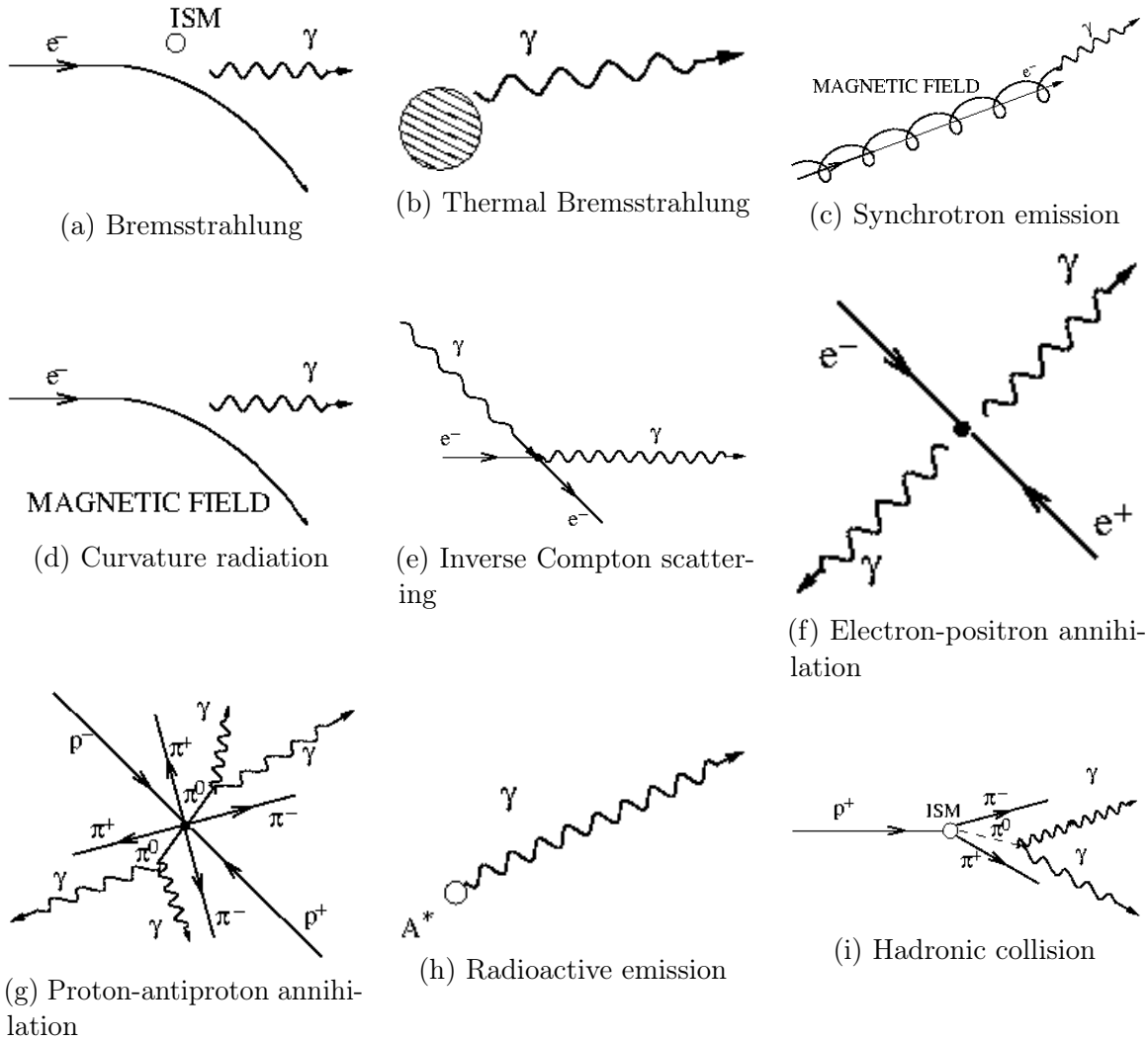


Figure 1.6: Diagrams of the different  $\gamma$ -ray production processes. Figures extracted from [22].

Being  $\alpha$  the fine structure constant and  $\nu = E_\gamma/E_e$  the fractional energy carried by the photon [19]. From equations 1.4 and 1.5 it can be seen that the acceleration suffered by the particle is  $\propto Ze^2/m$ , then while any charged particle can suffer bremsstrahlung, it is going to be much more efficient for electrons than for protons which have a higher mass. The photons emitted will have a continuum spectrum with energies of the same order of the particle, which for cosmic electrons in a gas is going to be a power law [20]. Bremsstrahlung is mainly efficient under high-density conditions. It takes place in gaseous nebulae that contain ionized gas, such as SNR, and in the intracluster medium of galaxy clusters [21].

### 1.3.2 Inverse Compton scattering

IC scattering is the inelastic interaction where a relativistic charged particle transfer a considerable amount of energy to a photon. In the frame of reference of the electron the photon will suffer an "energy boosting" [20]. The energy of the scattered particle is  $E = \Gamma mc^2$ , where  $\Gamma$  is the Lorentz factor, and we can define the parameter  $\alpha = h\nu/mc^2$ , where  $\epsilon = h\nu$  is the initial energy of the photon. We can differentiate between two regimes depending on the initial energy of the photon:

- *Thomson regime*: For low values of  $\alpha$ , particle recoil can be neglected and the energy of the photon after the scattering will be:

$$E_\gamma \simeq \frac{4}{3}\epsilon\gamma^2 \quad (1.6)$$

- *Klein-Nishina regime*: For large values of  $\alpha$ , particle recoil is significant and in this case the energy of the photon after the interaction is:

$$E_\gamma \simeq \frac{1}{2}E \quad (1.7)$$

Photons from the Cosmic Microwave Background (CMB) are typical targets for IC scattering, together with synchrotron photons or photons thermally emitted by astrophysical sources. This mechanism is predominant in Very High Energy (VHE)  $\gamma$ -ray emitters, like in the jets of AGN and TeV blazars. The spectrum of the photons boosted by this process will follow a power law related to that of the population of relativistic electrons in the medium ( $\propto E_e^{-\Gamma_e}$ ):

$$\frac{dN_\gamma}{dE} \propto E^{-\frac{(\Gamma_e+1)}{2}} \quad (1.8)$$

### 1.3.3 Synchrotron emission

Synchrotron emission is produced when a charged particle is moving in a magnetic field. The particle will follow an spiral path, with constant velocity along the field lines, while being accelerated towards the center of its orbit. The particle will suffer energy losses that for relativistic particles follow a continuum spectrum [20] with a critical frequency  $w_c$  at which the maximum power is emitted:

$$w_c = \frac{3eB}{2mc}\Gamma^2 \sin\phi \quad (1.9)$$

Where  $e$  and  $m$  are the charge and mass of the particle,  $B$  is the magnetic field,  $\Gamma$  is the Lorentz factor and  $\phi$  is the pitch angle bewteen the directions of the magnetic field and the particle. The total energy loss is given by

$$-\frac{1}{c} \left( \frac{dE}{dt} \right) = \frac{2e^4}{3m^2c^4}\Gamma^2 B^2 erg cm^{-1} \quad (1.10)$$

Following 1.10, the power emitted is inversely proportional to the mass of the particle so it will be comparatively much more efficient for electrons than for protons.

Synchrotron radiation of ultra-relativistic particles is the most important contribution to the non-thermal universe (radio, X-rays...). According to 1.9 the production of High Energy (HE)  $\gamma$ -rays will require too high values of B and  $E_e$ , but regions emitting synchrotron radiation contain relativistic electrons capable of IC scattering [23], which will acquire much higher energies.

### 1.3.4 Curvature radiation

In presence of very strong magnetic fields, of the order of  $10^{11}$ - $10^{13}$  G, electrons and positrons will be forced to follow a trajectory parallel to the magnetic field lines. Since the lines are curved, with a curvature radius  $\rho_c$ , the particle will emit *curvature radiation* in the direction of movement, with a characteristic photon energy [24]:

$$E_c = \frac{3}{2} \Gamma^3 \frac{\hbar c}{\rho_c} \quad (1.11)$$

Typical environment where curvature radiation takes place are the surroundings of pulsars, due to the extremely high magnetic fields close to their surfaces. An electron with an energy of 10 TeV moving along a field line with a curvature of  $10^8$  cm, which is typical for pulsars, emits photons of energy  $\approx 2.5$  GeV [19].

### 1.3.5 Matter-Antimatter annihilation

Matter-antimatter pair annihilation processes can produce  $\gamma$ -rays. The most common case is electron-positron annihilation ( $e^-e^+ \rightarrow 2\gamma$ ). If the two particles are at rest, they produce  $\gamma$ -rays with energy equal to their masses (0.511 MeV). If the particles are thermalized but with low energies, such as the electrons of the ambient gas/plasma, they form the unstable state called positronium which can annihilate into 3 photons forming a continuum [25]. For relativistic particles interacting in-flight, the annihilation cross section is:

$$\sigma_A = \frac{\pi r_e^2}{\Gamma} [\ln(2\Gamma) - 1] \quad (1.12)$$

Where  $\Gamma = E_e/m_e c^2$  is the Lorentz factor of the positrons and  $r_e = e^2/m_e c^2 = 2.82 \times 10^{-13}$  cm is the classical radius of the electron. The result of the interaction is the emission of two photons with a continuum of energies. At very high energies, the cross section of equation 1.12 is quite low, leading to very high mean free paths and long lifetimes for the positrons, which typically will be affected by other processes before annihilating. Positrons can lose energy gradually without escaping the galaxy until the cross section is high enough and they annihilate [19].

Proton-antiproton annihilation can also produce  $\gamma$ -rays indirectly by the production of neutral pions  $\pi^0$  which decay into  $\gamma$ -rays later on [26]. In theory, antiprotons can

be produced by interactions of protons with matter, but this process is much less efficient than the direct production of  $\pi_0$  mesons [20] so the production of  $\gamma$ -rays this way is considered marginal.

### 1.3.6 Hadronic collisions

While most of the processes described above were dominated by electron interactions (leptonic scenario), we now focus on the processes that constitute the hadronic contribution to the production of  $\gamma$ -rays, which are believed to be the dominant  $\gamma$ -ray production processes in SNRs and AGN.

Protons accelerated to relativistic energies in extreme environments, such as strong magnetic fields or jets, can collide with other hadrons producing mesons, kaons and hyperions. The most common interaction is the proton-proton collision to produce pions ( $\pi$  mesons):

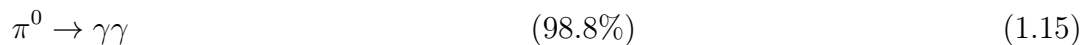


With a threshold energy of the proton, which is the minimum kinetic energy the pair of protons must have in the collision to produce the meson:

$$E_p = 2m_{\pi^0}c^2 \left( 1 + \frac{m_{\pi^0}}{4m_p} \right) \simeq 280 \text{ MeV} \quad (1.14)$$

Where  $m_{\pi^0} = 134.97$  MeV is the mass of the  $\pi_0$ -meson and  $m_p = 938.27$  MeV is the mass of the proton [25].

Neutral pions  $\pi^0$  decay into  $\gamma$ -rays within a short lifetime  $\tau = 8.6 \cdot 10^{-17}$ s through the channels:



Then the energy of the photons emitted by the  $\pi^0$  peaks at  $E_\gamma = m_{\pi^0}c^2/2 \simeq 67.5$  MeV, but in the laboratory frame of reference this energy depends on the energy of the  $\pi^0$  and the angle of the proton trajectory with respect to the  $\pi^0$  allowing the emitted  $\gamma$ -rays to reach very high energies.

The collision of protons can also produce charged mesons, which can decay into neutrinos  $\nu_{e,\mu}$  with a spectrum similar to that of the photons [25]. Finding a correlation between  $\gamma$ -ray emission and astrophysical neutrinos from a certain source would be an unequivocal way to differentiate between leptonic and hadronic emission. Their spectrum shape and the lack of correlation with X-rays could be other ways to distinguish hadronic and leptonic emission.

## 1.4 $\gamma$ -ray Absorption mechanisms

Because  $\gamma$ -rays are very energetic, they can travel long distances without being altered. However there are mechanisms that can produce losses of energy of astrophysical  $\gamma$ -rays or their total absorption, altering the spectrum that is measured from Earth. These mechanisms can be divided in  $\gamma$ -matter interactions and  $\gamma - \gamma$  processes.

### 1.4.1 Interaction with electrons: Compton effect

Compton effect is produced when a photon is scattered by an electron, shifting the wavelength of the photon to lower energies. The shift in the wavelength goes like:

$$\lambda' - \lambda = \frac{h}{m_e c} (1 - \cos\theta) \quad (1.17)$$

Where  $\lambda'$  is the wavelength of the scattered photon,  $\lambda$  the wavelength of the incident photon and  $\theta$  is the scattering angle. In the standard ISM density of 1 atom per  $\text{cm}^{-3}$ , for distances of  $\sim 10$  kpc, the mean free path for photons of 1 MeV would be of 2 Mpc, thus the Compton effect is negligible. In hot dense plasmas however, where densities are much higher, the effect can be quite important [19].

This effect is used in Compton  $\gamma$ -ray telescopes such as described in section 2.1.1.

### 1.4.2 Pair production processes

Pair production is the opposite process to pair annihilation, where two photons interact to produce a pair  $e^-e^+$ . This is the most common absorption mechanism for HE and VHE photons. A  $\gamma$ -ray with energy  $\epsilon_1$  which collides with a target photon with energy  $\epsilon_2$  will produce a pair of particles of mass  $m$  if  $\epsilon_1$  is greater than a threshold energy:

$$\epsilon_t = \frac{2m^2c^4}{\epsilon_2(1 - \cos\theta)} \quad (1.18)$$

where  $\theta$  is the angle between the trajectories of the photons. In astrophysics, this process occurs when energetic photons traveling through the Universe encounter a radiation field, such as the CMB ( $\epsilon_t \approx 4 \times 10^{14}\text{eV}$ ) or the light of stars ( $\epsilon_t \approx 4 \times 10^{11}$ ). Even though photon-photon collisions are not generally frequent, because the spatial density of the target photons is not very large ( $\approx 400 \text{ cm}^{-3}$  for the CMB radiation  $n$  and  $\approx 5 \times 10^{-3}\text{cm}^{-3}$  for extragalactic starlight) the attenuation effect can be appreciated, specially for VHE photons coming from high redshifts. This process also occurs when  $\gamma$ -rays penetrate the atmosphere and are absorbed, leading to the production of Extensive Air Showers (EAS), which are the key for ground based  $\gamma$ -ray detectors and will be explained in section 2.2.

### 1.4.3 The Extragalactic Background Light

The Extragalactic Background Light (EBL) is the accumulated radiation in the universe due to star formation processes and the emission from AGNs. It is a

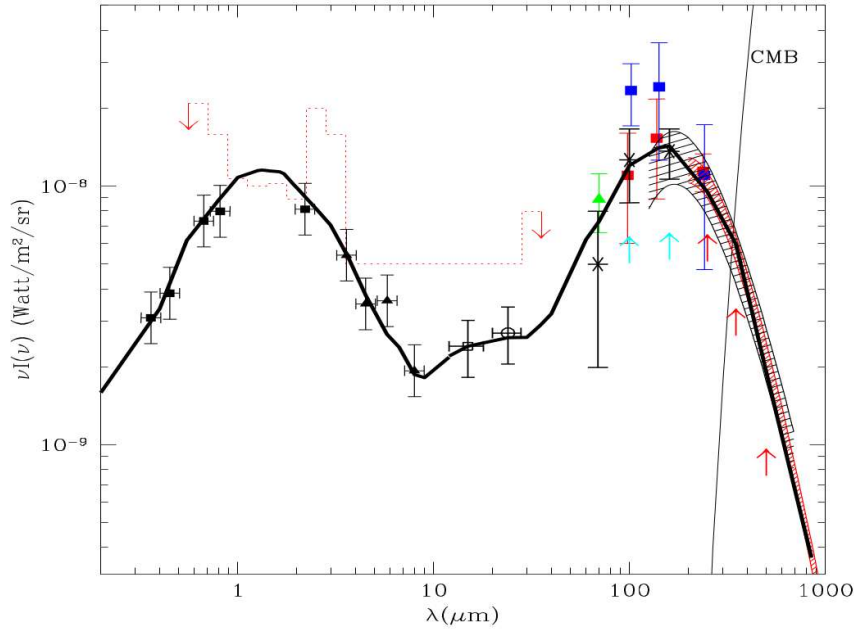


Figure 1.7: Best fit model prediction of the EBL energy density from [28] (thick black line).

fundamental constituent of the universe that permeates it uniformly. The direct measurement of the EBL is a very difficult task, mainly because of the foreground light from the Solar System. Phenomenological approaches try to predict an EBL model based on galaxy formation and evolution during the history of the universe and several direct measurements have been done from the far infrared to the optical, to set constraints on the density and spectrum of the EBL [27]. Besides the different proposed models, it is accepted that the energy density is characterized by two peaks, as seen in figure 1.7. The first peak, found at  $\sim 1\mu\text{m}$  is the stellar component and the second peak at  $\sim 100\mu\text{m}$  is the dust component, the light re-emitted by cosmic dust.

EBL photons are a typical target for  $\gamma$ -rays to produce pair production. The attenuation to the spectrum of a  $\gamma$ -ray source at the energy  $E$  follows the form:

$$F = F_0(E) e^{\tau(E,z)} \quad (1.19)$$

Where  $F$  is the observed flux and  $F_0$  the intrinsic spectrum of the  $\gamma$ -ray source,  $\tau$  is the optical depth which depends on the energy and the redshift  $z$  (as shown in figure 1.8). As a consequence of this dependence, for each energy there is a distance (redshift) at which the universe is optically thick to  $\gamma$ -rays, when the optical depth is equal to 1. The spectrum of the  $\gamma$ -ray source will suffer a cutoff at the energy that reaches the threshold optical depth, which decreases rapidly with redshift. Observations of this effect in distant sources in the VHE range is very useful to characterize the EBL in

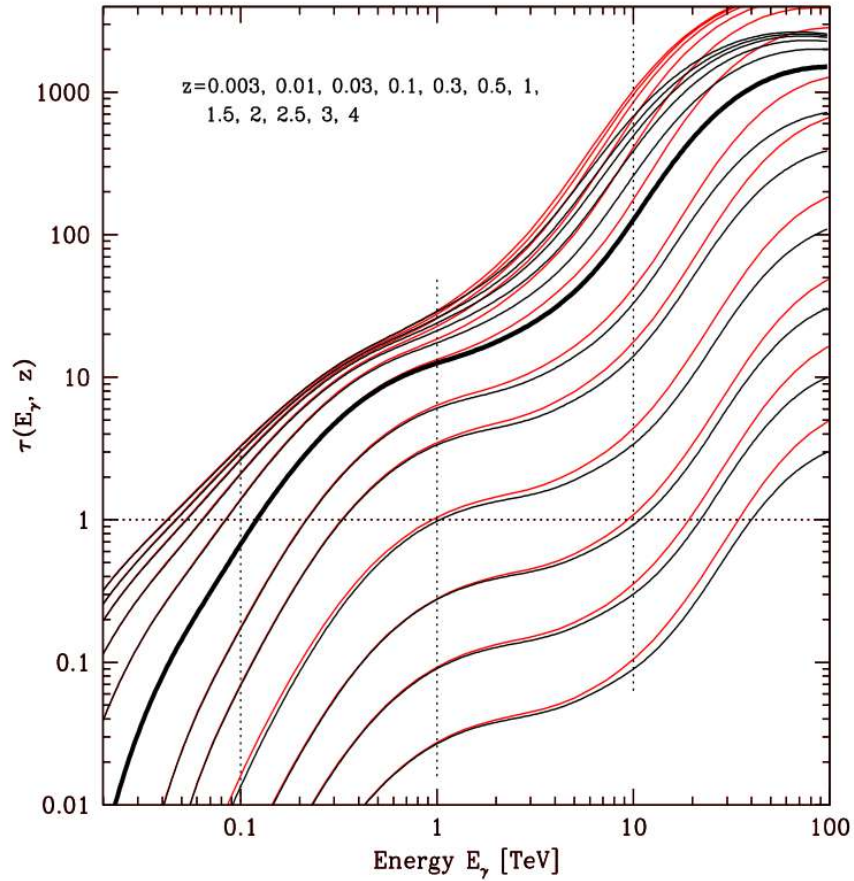


Figure 1.8: Optical depth due to photon-photon collision as a function of energy for different redshift values, from [28].

an indirect way, comparing the expected spectrum to the measured one [29].

## 1.5 Dark Matter and $\gamma$ -rays: WIMP annihilation

The nature of Dark Matter (DM) is one of the most important open questions in modern physics. There are many probes that suggest that the universe is composed of something more than the visible matter: From the Fritz Zwicky measurements on the velocity dispersion in the Coma galaxy cluster [30] and the rotation curves of high-luminosity spiral galaxies obtained by Vera Rubin [31], to the much more modern measurements of the CMB by Planck [32], all of them point towards the existence of a non-baryonic type of matter which only interacts gravitationally with Standard Model (SM) particles. Cosmological simulations and cosmological probes such as Wilkinson Microwave Anisotropy Probe (WMAP) point to a hierarchical structure formation of the universe, where small structures were formed first and then merged to the larger. To accomplish for that model, if DM is formed by particles, they should

be non-relativistic (Cold dark matter) which decoupled from the thermal equilibrium in the early universe. Hot dark matter models, where DM particles would be still largely relativistic (like neutrinos), would lead to large structures forming first and fragment out later [33].

With these assumptions, we can derive the number density evolution of DM particles today. In the early universe, DM and SM particles were in thermal equilibrium with the photon bath emitted in the Big Bang, and reactions of annihilation and formation of particles were taking place at the same rate. While the universe expanded, these reactions started to be slower than the rate of expansion, so these particles *decoupled* from the thermal bath. This is the moment of *freeze-out*. Before that, particles had an equilibrium number density  $Y_{eq}$ , which evolves with time while the universe keep expanding. For DM and using the Boltzmann equation, the number density evolution  $dY/dx$  follow the equation:

$$\frac{dY}{dx} = -\frac{xs\langle\sigma v\rangle}{H(m)}(Y^2 - Y_{eq}^2) \quad (1.20)$$

Where  $m$  is the mass of the DM particle,  $x$  is the scaled time variable  $x = m/T$  being  $T$  the temperature of the photon bath at the moment of freeze out,  $s$  is the total entropy density of the universe,  $Y$  is actually defined as the number density of DM rescaled to  $s$  ( $Y = n/s$ ) to account for the expansion of the universe,  $\langle\sigma v\rangle$  is the velocity averaged cross section for the reaction of DM particles annihilating into SM particles and  $H(m)$  is the Hubble rate (which defines the rate of expansion of the Universe) defined as  $H(x) = H(m)/x^2$ .

While the annihilation rate of the particles is higher than the expansion rate of the universe ( $\Gamma \gg H$ ), the number density  $Y$  remains close to  $Y_{eq}$ . After the moment of freeze-out  $x_f$  ( $\Gamma \ll H$ ), the number density will remain almost constant as shown in figure 1.9.

Following the approach of [34], after freeze-out, the evolution of DM abundance can be written as:

$$\frac{dY}{dx} \approx -\frac{\lambda}{x^{n+2}}, \text{ where } \lambda = \frac{\langle\sigma v\rangle_0 s_0}{H(m)} \quad (1.21)$$

To define  $\lambda$  the dependency of the cross section and entropy with  $x$  was pulled out through the change of variables:  $\langle\sigma v\rangle = \langle\sigma v\rangle_0 x^{-n}$  and  $s = s_0 x^{-3}$ , where  $n$  is an exponent which depends on details of the particle physics model. Taking  $n=0$ , the DM abundance today would be  $\simeq x_f/\lambda$ . There is no SM particle which can explain the cosmic density of DM measured today  $\Omega_\chi$ , but if we consider a weak interacting particle in the weak mass regime ( $m_\chi \sim 100$  GeV), the correct DM density measured by Planck and WMAP arises naturally:

$$\Omega_\chi = \frac{m_\chi s_{today} Y_{today}}{\rho_{cr}} \rightarrow \Omega_\chi h^2 \sim \frac{10^{-26} cm^3/s}{\langle\sigma v\rangle} \simeq 0.1 \left(\frac{0.01}{\alpha}\right)^2 \left(\frac{m_\chi}{100 GeV}\right) \quad (1.22)$$

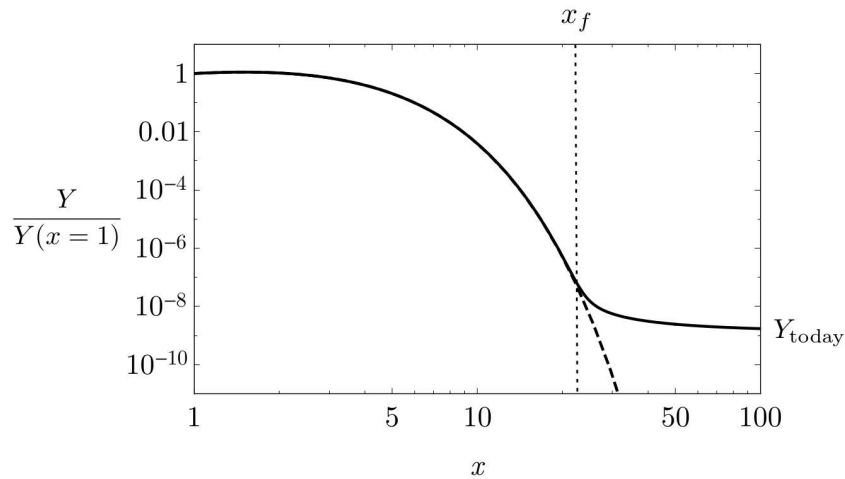


Figure 1.9: Evolution of Cold Dark Matter number density with time variable  $x$ ,  $x_f$  is the time of *freeze-out*, from [34].

where  $\rho_{cr}$  is the critical density in the universe required for it to be at balance. This is called the "WIMP miracle" for the theoretical Weak Interacting Massive Particles (WIMPs) which have some candidates within the Super Symmetry (SUSY) theory. Although the annihilation of these particles would be strongly suppressed after freeze-out, it can still occur in regions with high DM density. The products of this annihilation are pairs of SM particles that can be detected as an excess signal in particle detectors, giving an indirect evidence of the presence of DM.

This way,  $\gamma$ -ray astrophysics can contribute to the indirect detection of DM signatures: Two DM particles can annihilate directly into a pair of  $\gamma$ -rays with a characteristic line spectrum with  $E_\gamma = m_\chi$  or they can annihilate into pairs of other SM particles which afterwards decay giving out a continuum spectrum of  $\gamma$ -rays.

The differential flux of photons produced by DM annihilation is described as:

$$\frac{d\Phi}{dE} = \frac{1}{8\pi} \frac{\langle \sigma v \rangle}{m_\chi^2} \frac{dN_\gamma}{dE} \int_{\Delta\Omega} \int_{l.o.s} dl \rho^2(\vec{l}) \quad (1.23)$$

Where  $dN/dE$  is the spectrum of  $\gamma$ -rays from annihilation of a pair of dark matter particles,  $\langle \sigma v \rangle$  is the thermal velocity averaged annihilation cross section,  $m_\chi$  is the DM particle mass and  $\rho$  is the dark matter density profile. If DM particle is not its own antiparticle, equation 5.7 should be multiplied by a factor 1/2.

The first term of the equation comes from the already discussed particle physics, depends on the annihilation channel and the mass of the particle. The integral second term is known as the J-factor and is the integral over the line of sight and solid angle  $\Delta\Omega$  of the squared DM density profile ( $\rho$ ) and it dependent on the source. The most simple density profile for a dark matter halo that we can think of is a self-gravitating

isothermal gas sphere, where:

$$\rho(r) \propto 1/r^2 \quad (1.24)$$

However, to address the actual physics of galaxies evolution, we need to rely on structure formation simulations which follow the initial DM density perturbations until the formation of current halos. From these simulations and from actual observations [35] we know that the DM density profile can be well reproduced as a six-parameters function of distance  $r$  from the center of the profile [36][37][35]:

$$\rho(r) = \frac{\rho_0}{\left(\frac{r}{r_s}\right)^\gamma \left[1 + \left(\frac{r}{r_s}\right)^\alpha\right]^{\frac{\beta-\gamma}{\alpha}}} \Theta(r_{max} - r) \quad (1.25)$$

Where  $\Theta$  is the Heaviside step function,  $r_s$  is the scale radius and  $\rho_0$  is the characteristic density. These two last parameters depend on the specific DM halo. Setting  $(\alpha, \beta, \gamma) = (1, 3, 1)$  we retrieve the Navarro-Frenk-White profile [38]. Combinations of these parameters can be used to fit a possible DM signal to a specific profile. Other types of profiles have also been treated in the literature, such as the Einasto profile [39].

From 5.7, we can see that the best objects to search for a  $\gamma$ -ray signal will be those that are nearby and DM dense, so the J-factor would be sufficiently large relative to the background of  $\gamma$ -rays produced by ordinary matter interactions.

## 1.6 $\gamma$ -ray sources

In the previous section, the processes that produce  $\gamma$ -ray emission were introduced. In this section, the astrophysical objects where they take place are described. Two major classes of  $\gamma$ -ray emitters can be distinguished: galactic sources and extragalactic sources. At the end of the section, potential sources for DM annihilation signals will be also covered. Figure 1.10 show the current known population of VHE  $\gamma$ -ray sources based on the observations of the current generation of  $\gamma$ -ray detectors, either in space (*Fermi-LAT*) or ground based (the Major Atmospheric Gamma Imaging Cherenkov Telescopes (MAGIC), the High Energy Stereoscopic System (H.E.S.S.), the Very Energetic Radiation Imaging Telescope Array System (VERITAS) and the High-Altitude Water Cherenkov Observatory (HAWC)).

### 1.6.1 Galactic sources

As shown in figure 1.10, the richest region in  $\gamma$ -ray sources is the galactic plane, meaning that the majority of detected emitters belong to our galaxy. In this section, the different characteristics of these sources will be described.

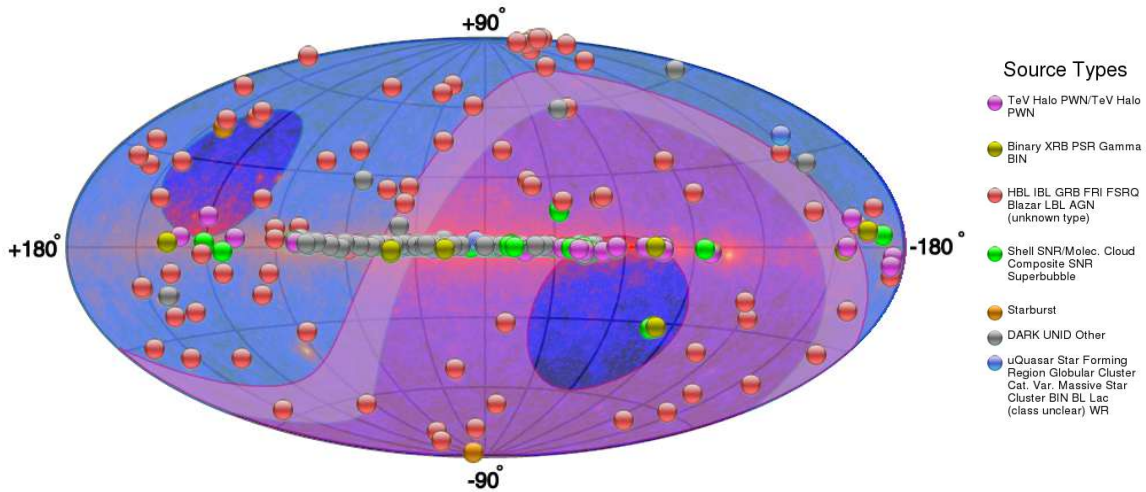


Figure 1.10: Full skymap from TeVCat[40] catalog as of July 2019, with all the detected TeV sources. In the background, the *Fermi*-LAT skymap is shown and the shadowed regions correspond to the MAGIC field of view (blue) and H.E.S.S. (pink).

### Pulsars

Pulsars are the most common type of  $\gamma$ -ray emitters known. When a massive star ( $< 8M_{\odot}$ ) suffers gravitational core collapse at the end of its life, the resulting object is a compact neutron star sustained by degeneracy pressure, where neutronization (the combination of protons and electrons) has taken place due to the extremely high pressures which lead to high densities ( $> 10^9 g/cm^3$ ). The neutron star comprises  $1 - 2 M_{\odot}$  in a radius of  $10 - 14$  km and as the angular momentum of the parent rotating star is conserved, the much more compact neutron star will spin at extremely high velocities with periods that can go from milliseconds to a few seconds. This fast spin produces strong magnetic fields in their surroundings where electrons and positrons are accelerated by the electric field aligned with the magnetic field. When the magnetic fields are aligned with the line of sight from the Earth, we can detect a pulsed emission (mainly synchrotron and curvature radiation) with the period of the rotation of the neutron star, and the object is called a pulsar. Pulsed emission from this kind of object has been detected a broad band in the electromagnetic spectrum, from radio to  $\gamma$ -rays.

It is generally accepted that the origin of the  $\gamma$ -ray emission from pulsars is due to curvature radiation, produced when relativistic electrons accelerated in gaps of the electromagnetic fields powered by the pulsar rotation, are trapped and propagate along the lines of the magnetic field [41]. However, the location of the gaps and the dominating acceleration mechanism are not well known and there are different models proposed (see figure 1.11).

Combined observations of the Crab pulsar from the Imaging Compton Telescope (COMPTEL), the Energetic Gamma Ray Experiment Telescope (EGRET)

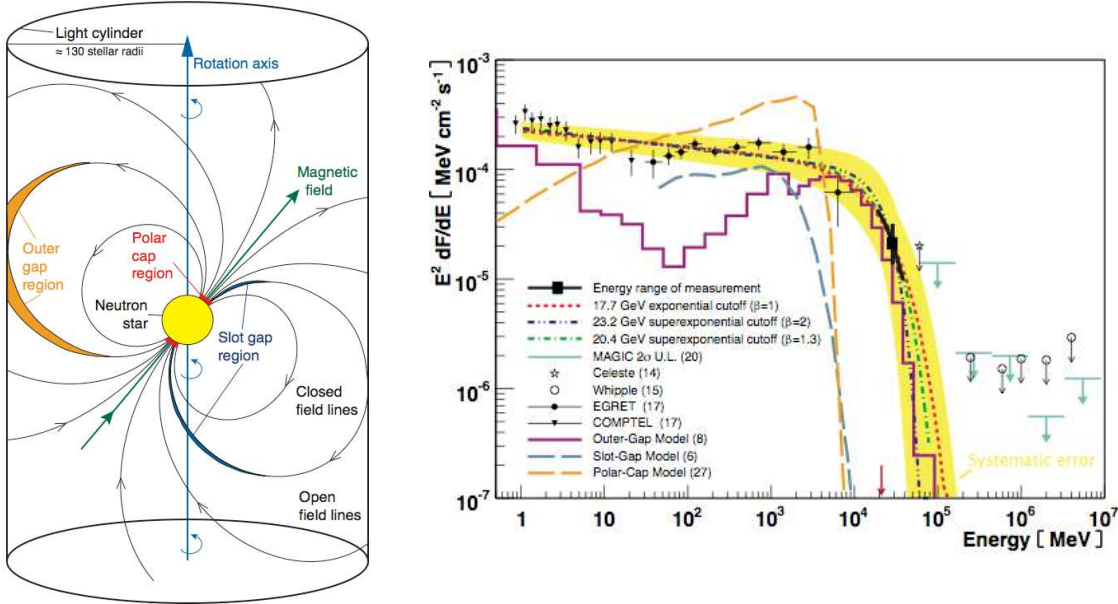


Figure 1.11: *Left:* Crab pulsar's magnetosphere where the location of the three models (Polar-Cap in red, Slot-Gap in blue and Outer-Gap in yellow) is shown. *Right:* Crab pulsar spectral cutoff. Figures from [41]

[42], MAGIC [41], VERITAS [43] and *Fermi*-LAT [44] have shown that their spectrum follows a power law with a cutoff at energies over a few GeV (see figure 1.11). The detection of the pulsar emission at energies over 25 GeV by MAGIC ruled out the possibility of acceleration happening too close to the pulsar (as the Polar-Cap model assets) because the magnetic pair-production attenuation would provide a super-exponential cutoff at much lower energies to those observed. Currently, the Outer-Gap model offers the best explanation of the observed Crab spectrum [45]. While pulsars are the most common  $\gamma$ -ray emitters, only two have been detected in the VHE range, up to TeV energies: the Crab and Vela pulsars [46].

### Supernova Remnants

Supernovae are the result of the evolution of a star, which suddenly becomes much brighter while shells of gas are expelled to the interstellar medium in an explosive event. They can be classified in different types by features in their spectrum which also imply a different origin of the explosion. Type II supernovae show hydrogen emission lines, meaning they come from very massive stars ( $M > 8M_\odot$ ) with hydrogen in their outer layers. After burning lighter elements (H, He, etc.) into heavy nuclei, fusion reactions become inefficient and the imbalance between gravitational forces and pressure radiation lead to the collapse of the central core into a neutron star or a black hole in a violent reaction, expelling shells of material at high velocities. Type I supernovae do not present hydrogen lines, meaning they come from a hydrogen-poor star. They usually are produced by white dwarfs in binary systems which accrete material until

reaching the Chandrasekhar limit [47] and suffer a thermonuclear explosion. Type I supernovae are classified in subtypes: Type Ia show Si lines in their spectra, whereas those without these lines are classified as Ib if they have He lines and Ic if not [48]. The structure of ejected material which is left in the surroundings of the parent star is the SNR. These structures can be classified in different types depending on their spectrum, but the most important feature to differentiate them is the presence (or not) of a shell. There are shell-type SNR, in which the material in the surroundings is heated by the power of the shockwave during the SN explosion. The so called *plerion* SNR or Pulsar Wind Nebula (PWN) do not present a shell. The result of the SN explosion is always a central pulsar and their emission is produced by the interaction between electrons ejected to the medium by the pulsar and its huge magnetic field. There is also a composite type of SNR where a plerion is surrounded by a shell and depending on the wavelength observed, they emit more like one type or the other [49]. Depending on the SNR type, the particle acceleration and  $\gamma$ -ray emission would have a different origin and features.

- **Shell-type remnants:** Shell-type remnants, the commonly referred simply as SNRs, are the most popular candidates for CR acceleration. CRs are deflected by magnetic fields in the ISM which makes it impossible to trace back the emission direction, but neutral particles, like neutrinos and  $\gamma$ -rays coming from SNRs can be used as tracers of CR acceleration. We know CRs can produce  $\gamma$ -rays via hadronic interactions with the gas and dust in the medium. For example, the production of pions and posterior pion decay would give rise to a spectrum with a characteristic peak at 67.5 MeV, if pions are at rest.

A simple energetic argument is used to pose shell type remnants as the main source of galactic CRs: As a rough estimation, if we assume that the typical total kinetic energy produced by a SN explosion is around  $E_{SN} \sim 10^{51}$  erg, with a SN rate in the galaxy of about one in 50-100 years, and a constant fraction  $\eta$  of the kinetic energy is transferred to hadrons, it can be shown that this fraction has to be of the order of the 10% to retrieve the approximated CR luminosity in the galaxy  $L_{CR} \sim 2 \times 10^{41}$  erg/s.

$$L_{CR} = \eta \cdot E_{SN} \cdot SN_{rate} = 0.1 \cdot 10^{51} \text{erg} \cdot 50 \text{yr}^{-1} \propto 10^{41} \text{erg/s} \quad (1.26)$$

A more detailed analysis using real data of galactic SNR was done by [50] arriving at the conclusion that future  $\gamma$ -ray data can be used to constrain the amount of CR energy coming from SNR. However, there are still problems on proving this hypothesis because many of the  $\gamma$ -ray signatures coming from SNR have a leptonic origin rather than hadronic. Also, for SNR to reproduce the full spectrum of CR, SNRs should be pevatrons (meaning they can accelerate CR to PeV energies) at some fraction of their lifetimes, to reach the region after the *knee*. Still, no SNR pevatron has been observed yet but high hopes are deposited in the next generation of  $\gamma$ -ray experiments [51].

- **Plerions or Pulsar Wind Nebulae.** As mentioned, PWN are powered by a central rotating pulsar which dissipates kinetic energy over time in the form of *spin down luminosity*. This energy is injected steadily into the surrounding nebula of ejected material that was formed during stellar evolution. To understand the features of the emission of Pulsar Wind Nebulae (PWNe), it is important to follow their evolution with time and how the period, spin down luminosity and magnetic field changes [52]. A pulsar is formed in a SN explosion and the final state of the pulsar and its PWN will depend on how it interacts with the SNR. If the SNR expands outward freely, the pulsar will remain in the center, but if a reverse shock happens, reverberations between the PWN and the shock can produce instabilities which in the end will displace the pulsar from its original position, even being able to cross away the SNR shell.

Strong magnetic fields in pulsars create currents of particles of the surrounding nebula, producing pulsar winds. Electrons accelerated this way produce synchrotron radiation from radio to X-ray wavelengths. The wind starts decelerating when reaching the nebula radius, due to the more slowly expanding material and thus a wind termination shock is formed. The TeV  $\gamma$ -ray emission from PWNe is explained as IC emission produced by the relativistic particles in the shocked wind interacting with the synchrotron photons. The Crab PWNe was the first source detected of this type, associated with a SN explosion observed in 1054 CE, and has become a sort of standard candle for  $\gamma$ -ray astrophysics.

- **Composite remnants.** A rare type of SNR is a combination of the previous two, where a PWN is surrounded by a shell-type SNR. Usually, PWN are considered young SNRs while shell-types are older systems. Composite SNRs could be an intermediate phase of evolution where the shell and the PWN evolve and interact together [53]. In these systems, the PWN formed in the interior of the SNR expands outwards and it can encounter the inward reverse shock of the SNR [54]. Some examples of this kind are SNRs W28, W44 and SNR G21.5-0.9, which is shown in figure 1.12.

### $\gamma$ -ray binaries

$\gamma$ -ray binaries are systems composed by two objects orbiting each other: One is a compact object, such as a pulsar and the other can be an ordinary massive star big enough to reach the Roche lobe of the pulsar and so stellar winds connect the two objects. Just a few objects (< 10) of this kind have been detected in HE and VHE  $\gamma$ -rays very recently [55], and yet the exact mechanisms of the origin of their emission are unknown. There are two main explanations to the HE and VHE emission in  $\gamma$ -ray binaries. It can be produced by accretion energy released in the form of relativistic jets, or on the other hand, by the energy emitted by the pulsar in the form of pulsar winds in a similar way as in PWNe. The first case is denominated the *microquasar* scenario due to its similarities with AGN (also known as quasars) but emitting jets in

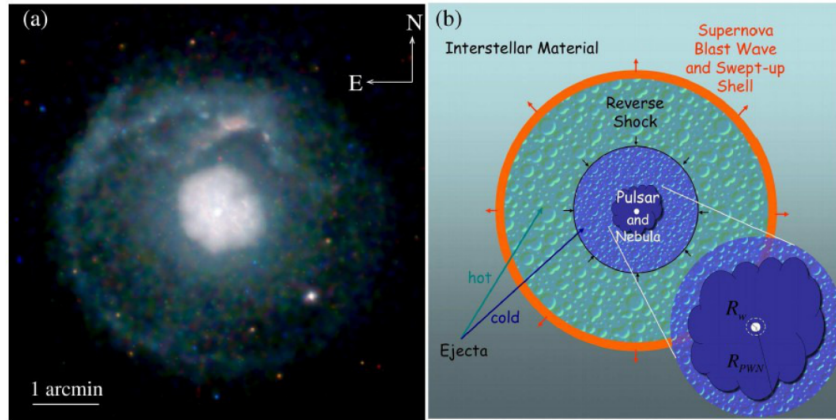


Figure 1.12: a): Chandra X-ray image of the composite SNR G21.5-0.9. b): Diagram of a PWN inside a SNR. Pictures from [54].

a smaller scale. However, a variety of indirect evidences seem to favour the pulsar wind interpretation mainly based in the spectral similarities of the known binaries with the power of a pulsar spindown. Also the presence of strong magnetic fields and morphological characteristics of radio emission are similar features to those found in PWNe [56].

### **Novae**

Binary star systems are rather common objects in the universe. One of the stars can be more massive than the other, evolving faster and becoming a white dwarf while the second star can still be in its main sequence phase. If this happens, the white dwarf can start accreting material from the companion, building an accretion disk. The hydrogen rich gas in the surface of the white dwarf starts heating the bottom layers which becomes electron-degenerated, leading to a chain of thermonuclear explosions [57]. This event is known as "classical nova". When the companion star is a red giant, which has highly increased its volume, the system is called a *symbiotic binary system*. In this case, the interaction between the stellar wind of the red giant and the white dwarf surface expansion give place to a favorable scenario for particle acceleration. Both classical novae and symbiotic systems have been detected in HE  $\gamma$ -rays by *Fermi*-LAT [58], [59] although these results do not allow to differentiate between the different emission scenarios.

### **The Galactic Center and the Fermi Bubbles**

The center of the Milky Way, known as the Galactic Center (GC), is a region of the sky situated at  $4^\circ$  longitude,  $2^\circ$  latitude, with a size of  $600 \times 300$  pc and at a distance of about 8 kpc. It is obscured by dust in the optical and ultraviolet range, but emission in infrared, radio, X-rays and  $\gamma$ -rays reveals a prolific region full of energetic sources.

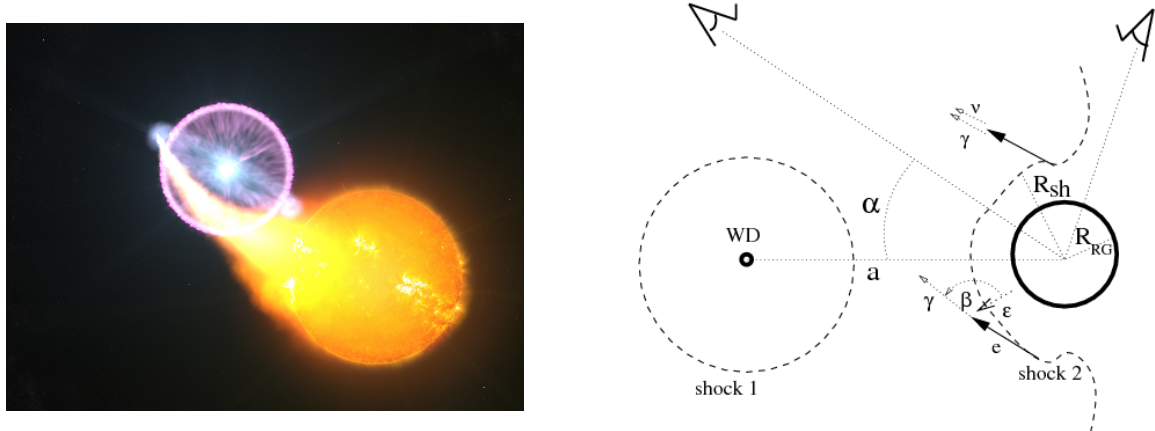


Figure 1.13: *Left:* Artist concept of a classical nova. Credits: NASA’s Goddard Space Flight Center/S. Wiessinger. *Right:* Diagram of the geometry of the symbiotic binary system V407 Cyg from [60]. The expanding shock (1) from the white dwarf partially overtakes the Red Giant (shock 2), producing particle acceleration through IC (leptonic scenario, with angle of interaction  $\beta$ ) and proton collisions with the red giant wind (hadronic scenario).

Among many SNRs, PWNe and stellar clusters in HII regions, there is also a Super Massive Black Hole (SMBH), Sagittarius A\*, whose detection has been one of the major motivations for GC surveys. Many  $\gamma$ -ray experiments have surveyed the GC region (*Fermi*-LAT , MAGIC [61], H.E.S.S. [62], VERITAS [63]) and emission from HE to VHE bands has been detected. The main problem with this highly populated region is the difficulty of tell apart individual sources, making it a big challenge to identify the actual emission from Sgr A\* [64]. The high energy emission from Sgr A\* has its origin in the strong winds produced by the presence of an accretion disk surrounding the black hole, where material is accelerated at very high energies [65].

Closely related to Sgr A\* might be the *Fermi bubbles*, two large  $\gamma$ -ray lobes that appear to be ejected from the center of the galaxy. They were discovered while searching for a  $\gamma$ -ray counterpart to the WMAP haze [66], which is a residual microwave emission that arises after subtracting all the other known emission components. They extend to  $55^\circ$  up and above the GC and are not symmetric, with an enhanced emission towards the south-east side of the bubbles. With well defined edges, an uniform power-law spectrum of index  $\sim 2$  and a cocoon-like shape, they resemble jet-like structures [67]. Their origin is still under debate: They could be jets, outflows or the result of accretion events from the black hole, winds from SN explosions or the remnant of AGN activity in the Milky Way in the past.

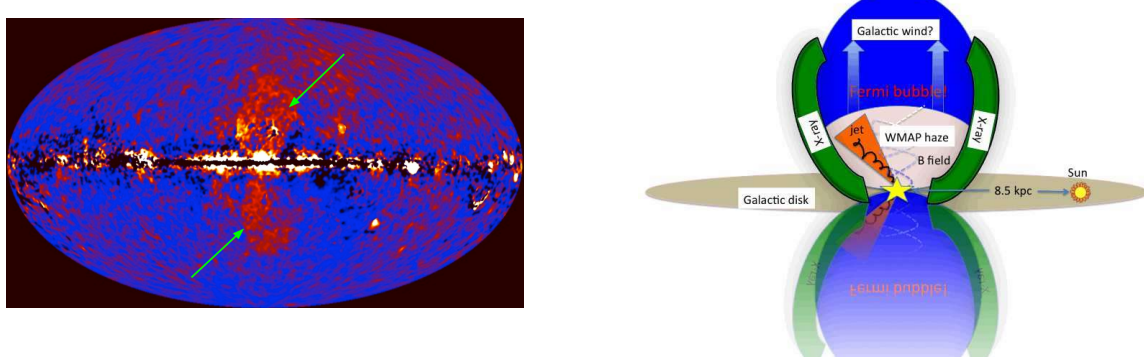


Figure 1.14: *Left:* The Fermi Bubbles as seen by *Fermi*-LAT after subtracting all the other known  $\gamma$ -ray components. Credits: NASA/DOE/Fermi LAR/D. Finkbeiner et al. *Right:* Schematic picture of Fermi Bubbles structure from [66].

### Globular Clusters

Globular clusters are compact gravitationally bounded stellar associations with spherical geometry which are distributed outside the galactic plane, conforming a spherical halo around the galaxy. They are old highly evolved systems with many compact objects like neutron stars, white dwarfs and pulsars even forming binary systems. Furthermore, the majority ( $\sim 80\%$ ) of Millisecond Pulsars (MSPs) (pulsars with a period of the order of milliseconds) detected up to date have been found in globular clusters.

Since all the mentioned objects are well known  $\gamma$ -ray emitters, globular clusters have been observed and detected in  $\gamma$ -rays by *Fermi*-LAT [68] and H.E.S.S. [69]. Even pulsed  $\gamma$ -ray emission have been observed from individual MSPs [70], [71]. Two types of models of  $\gamma$ -ray emission have been discussed to happen in globular clusters, both related to MSPs. One takes place in MSPs magnetospheres, where  $\gamma$ -ray emission would be produced by curvature radiation. The second type of models involve IC scattering of electrons accelerated close to the MSP with optical, infrared or CMB photons [72].

### 1.6.2 Extragalactic sources

While most of the  $\gamma$ -ray emission detected on Earth comes from the galactic plane, there is a big amount of individual sources outside our galaxy which produce HE radiation and allow the study of a new range of extragalactic phenomena. A big caveat for extragalactic sources is that the VHE range is suppressed by the EBL absorption, as described in section 1.4.

### Active Galactic Nuclei

AGN are the brightest steady sources of  $\gamma$ -ray in the universe and the most luminous known electromagnetic emitters. Known as *black-hole galaxies*, their strong emission is powered by infalling gas into a massive Black Hole (BH) located in the center. The

BH attracts gas and material from the galaxy forming an accretion disk, where matter loses angular momentum through viscous and turbulent processes, and emits a huge amount of energy from ultraviolet to soft X-ray bands [73]. AGN can be classified in two broad types, according to their radio emission: *Radio-quiet* and *radio-loud*. Further observational classification depends strongly on the orientation angle, which can make AGNs appear as spectroscopically completely different sources, depending on the region of the object that is showing. All AGN have a dusty tori, broad-line regions, narrow-line regions and strong blue/UV bump emissions from the accretion disk [74]. Depending on the angle, one or several of these regions will be observable and will show their particular features in the spectrum. Figure 1.15 show a scheme of AGNs taxonomy.

Radio-loud AGN, also known as *blazars*, are about three orders of magnitude brighter in radio band than their quiet counterparts. This radio emission is directly related with the presence of relativistic jets of plasma which carries a big part of the energy released during accretion and that afterwards is emitted as radiation from radio to  $\gamma$ -rays [75]. They are associated with elliptical galaxies that have undergone recent mergers. On the contrary, radio-quiet galaxies do not show jets and so do not account for high energy non-thermal emission. Also, they are typically spiral galaxies in lower density regions [76]. Blazars are rare among AGN, accounting only for 10% of the total, but a large number of them has been detected in  $\gamma$ -rays, with more than 1500 sources detected at GeV energies, and more than 60 at TeV energies [74].

### Gamma Ray Bursts

GRBs are short and intense flashes of  $\gamma$ -ray emission coming isotropically from random directions in the sky. With a range of luminosities from  $10^{51}$  ergs/cm<sup>2</sup> to  $10^{52}$  ergs/cm<sup>2</sup> they are the brightest transient objects in the sky [78]. They can be classified by their duration, having two distinct populations: short GRBs, which last just a few seconds; and long GRBs which can last for few minutes [79]. Long bursts are usually followed by afterglows in X-rays, optical and radio which can last for several years after the event. The so called *fireball* model is the generally accepted mechanism which drives GRB [80]. Since the observed emission of the bursts is not thermal, its origin must be the result of the conversion of an ultra-relativistic energy flow into radiation in an optically thin region. The energy flow could come from the kinetic energy of accelerated particles or electromagnetic Poynting flux. In this model, the process is ignited by an "inner engine" which is not possible to observe directly, but which activity can be characterized by the observed temporal structure of the bursts. The engine produces an explosive fireball of the size of the engine itself. There is an alternative model based in internal shocks, where the engine would produce a wind and a long energy flow. About the nature of the phenomena producing GRBs, there exist an apparent difference between the origin of short GRB and long GRB according on their hardness ratio (defined as the ratio of the flux in two separated bands) versus duration plot (see figure 1.16) [79].

These two populations in the hardness ratio vs. duration plot, together with rather

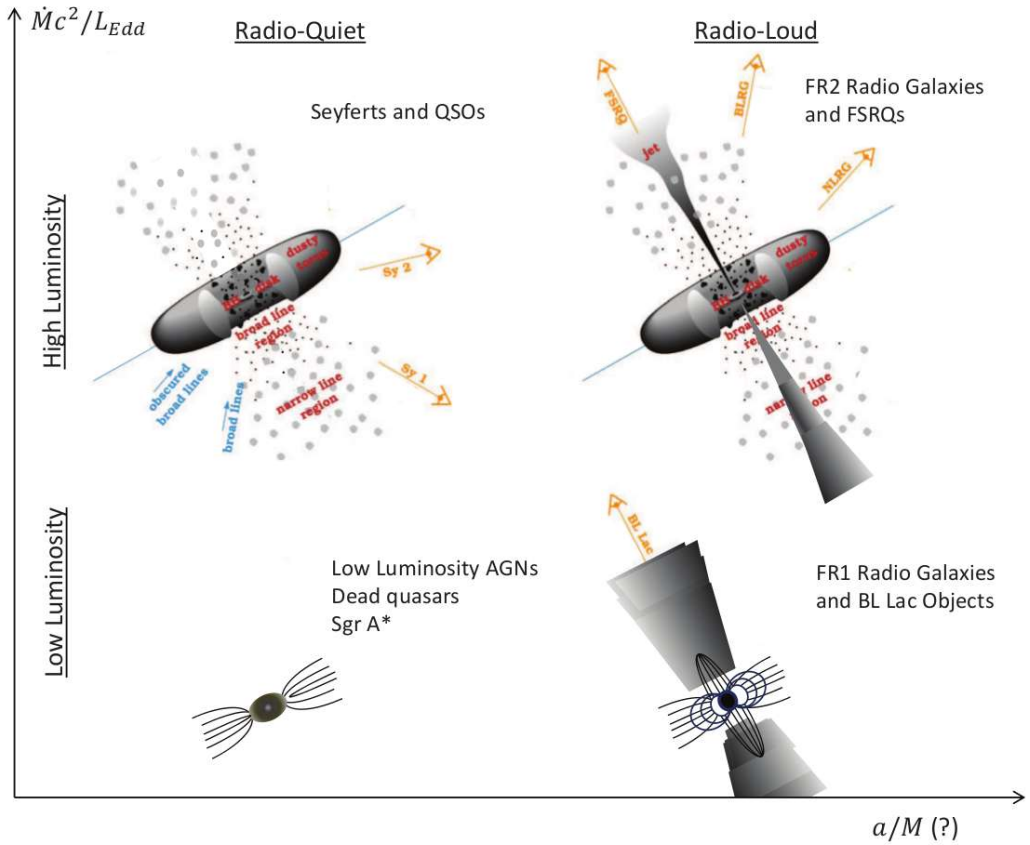


Figure 1.15: *Top:* AGN taxonomy as from [74]. In this scheme, the vertical axis represents the luminosity power in terms of the mass-accretion rate and horizontal axis represents the BH rotation. *Bottom:* Observational classification of active galaxies. QSO= quasi-stellar objects; Sy1(Sy2) = Seyfert 1(2); FR1(FR2)=Fanaroff-Riley 1(2). Pictures based on [77] from [74].

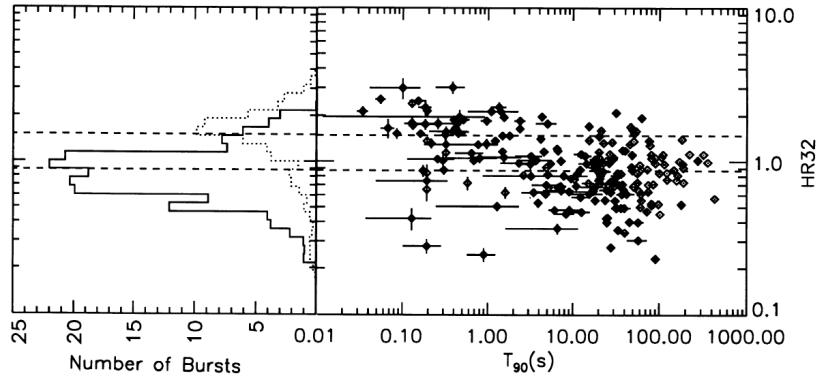


Figure 1.16: *Left:* Hardness ratios for the two duration classes of GRB. Solid lines corresponds to short GRBs, dashed line to long GRBs. *Right:* Hardness vs. duration plot, where duration  $T_{90}$  is defined as the time during which the cumulative counts > 25 keV increase from 5% to 95% above background. Dashed lines correspond to the mean hardness ratio of the two classes. Figure from [79].

significant spectral differences [81] and afterglow observations, suggest that long GRBs are closely related to star forming regions, compatible with SN explosions of massive stars. Short GRBs on the other hand, could be related to more evolved regions and be the result of neutron star mergers, such as the recently detected gravitational wave event GW170817 by LIGO/VIRGO [82] which was also detected as a GRB by the Fermi Gamma-Ray Burst Monitor and later observed by *Fermi*-LAT [83]. Also recently MAGIC, which were specifically designed to observe such objects, detected the first event in the VHE range [84].

### Starburst galaxies

Starburst galaxies are those with a greatly enhanced star formation, whose Star Formation Rate (SFR) is considered to be out of equilibrium, consuming gas for star formation at very short timescales ( $< 1$  Gyr). Since the SFR is highly correlated with the SN explosion rate, it is expected that  $\gamma$ -ray emission detected from starburst galaxies has its origin in SNRs.

The production and transport of CRs in the ISM significantly affects the star formation, because CRs penetrate deep into molecular cloud cores (molecular clouds are dense gas regions where star formation takes place) catalyzing complex chemical reactions which can affect the initial conditions of star formation and evolution [85]. The conditions of the ISM in starburst galaxies are very different from Milky Way [86]. The gas density is much higher and the high population of massive stars produce a huge amount of radiation, which is absorbed by dust and re-emitted in infrared. Magnetic fields are also affected by the presence of such population. Thereby particles accelerated in the region will suffer strong losses of energy and faster cooling. Detection of  $\gamma$ -rays from starburst galaxies is a key probe to understand the efficiency of CR acceleration in SNRs and CR transport in different ISMs.

The current generation of  $\gamma$ -ray telescopes have detected NGC253 and M82 starburst galaxies ([86], [87], [88]), which has been long predicted to emit  $\gamma$ -rays up to VHE range.

### **Galaxy clusters**

Galaxy clusters are the largest gravitationally bounded structures in the universe. They are mainly composed of DM (70-80% of the total mass) and their ordinary matter is composed by the galaxies and the filaments connecting them, plus a big amount of hot gas in the surroundings called the Intracluster Medium (ICM)[89]. In the standard paradigm of structure formation, clusters are formed by hierarchical mergers and accretion of smaller structures. Mergers are the most energetic phenomena to occur in the universe (they release  $10^{63}$ - $10^{64}$  ergs/Gyr) and they dissipate energy in the form of shocks which heat the gas, or through large-scale ICM motions [90]. Part of the energy dissipated during this process is fused into particle acceleration to ultra-relativistic energies, thus they are a source of CR production. Radio observations of galaxy clusters proves the existence of non thermal emission from synchrotron radiation processes in the ICM. Galaxy clusters can therefore be a source of HE photons which can be produced via leptonic scenario through IC scattering of CMB photons with ultra-relativistic electrons, or hadronic scenario by neutral pion decay.

Until recently,  $\gamma$ -ray experiments that tried to detect  $\gamma$ -ray signal from the closest galaxy clusters were only able to set upper limits [91], [92]. *Fermi*-LAT was able to report a detection of an extended  $\gamma$ -ray signal from the Coma cluster roughly correlated with the radio halo [93].

### **Neighbour galaxies**

The Local Group is the cluster of galaxies gravitationally bounded to the Milky Way. They are the closest galaxies to be observed and their characteristics are expected to be similar to those of our own galaxy. The second and third closest and spatially resolved galaxies (the first being the Canis Major dwarf galaxy) are the Large Magellanic Cloud (LMC) and the Small Magellanic Cloud (SMC). They are two irregular dwarf galaxies seen in the southern hemisphere, at a distance of 50 kpc [94]. They present a remarkable high star formation rate ( $\sim 0.2\text{yr}^{-1}$  for the LMC,  $0.3\text{yr}^{-1}$  for the SMC [95], compared to the  $0.68\text{yr}^{-1}$  to  $1.45\text{yr}^{-1}$  of the Milky Way [96] in a much smaller volume.). They can produce  $\gamma$ -ray emission due to the interaction of CR with ISM. The first detection of a  $\gamma$ -ray diffuse signal from the LMC was made by EGRET [97], being the first normal galaxy outside the Milky Way detected in  $\gamma$ -rays. The SMC was first detected in  $\gamma$ -rays by *Fermi*-LAT [98]. Further observations of the LMC from *Fermi*-LAT at HE [99], [100], [101] and H.E.S.S. [102], [103] at VHE revealed a complex structure of the diffuse emission and a population of very interesting individual sources comprising pulsars, SNRs, PWNe and  $\gamma$ -ray binaries. Since the LMC emission in  $\gamma$ -rays is one of the main topics of this thesis, it will be extensively

treated in chapter ??.

Apart from the before mentioned starburst galaxies M82 and NGC253, other close galaxies such as M31 and M33 have also been observed and detected in HE  $\gamma$ -rays by *Fermi*-LAT [104].

### 1.6.3 Potential Dark Matter annihilation emission sources

In section 5.5 the production of  $\gamma$ -rays through WIMP annihilation or decay was described. In the search for this kind of signal, one can analyze which would be the best sources in the universe for an indirect search of DM. First of all, they must have a high amount of DM, given by the astrophysical parameter J-factor (integral term in eq. 5.7). Also, a low background of other  $\gamma$ -ray sources would allow to unequivocally identify the DM signal. Following these premises, indirect DM searches have been performed by  $\gamma$ -ray experiments in the most promising sources, described in this section.

#### Milky Way Galactic Center

In the present evolutionary stage of the universe, galaxies are believed to be embedded in DM halos which extend much more than the visible matter, the center of the galaxies being the location of higher DM density [105]. The center of the Milky Way is therefore a promising target for DM searches. However, as explained in section 1.6.1, it is also a very populated region with many  $\gamma$ -ray sources which are even not fully resolved. This fact makes the GC a true challenge for disentangle a possible DM emission, needing a very good background modelling and control of the instrumental systematics [106]. Usually, DM searches in the GC tend to avoid the galactic plane region, observing a region with lower background at expenses of having a weaker DM signal due to the lower density.

The most constraining upper limits in the VHE energy range for the velocity averaged cross section  $< \sigma v >$  in the GC have been established by H.E.S.S. [107]. Both *Fermi*-LAT and H.E.S.S. have accounted for a  $\gamma$ -ray excess coming from the GC of unknown origin which has been tried to be fitted with the most conventional DM models, but the results were not sufficiently compatible [108], [109].

#### Dwarf Spheroidal Galaxies and Dark Clumps

Following the standard model of cosmology, N-body simulations of the evolution of CDM since the Big Bang predicts a hierarchical structure formation where DM clusters into subhalos which merge into higher structures. The final picture at galactic scales, are galaxies embedded in a big DM halo, surrounded by a population of subhalos with mass inversely proportional to their number [110]. Simulations like Via Lactea II predict that the Milky Way is surrounded by a large number of DM subhalos ( $\sim 50,000$ ). The heavier of these substructures are the so called Dwarf Spheroidal Galaxies (DSphe). They are very faint galaxies (in optical) orbiting the Milky Way.

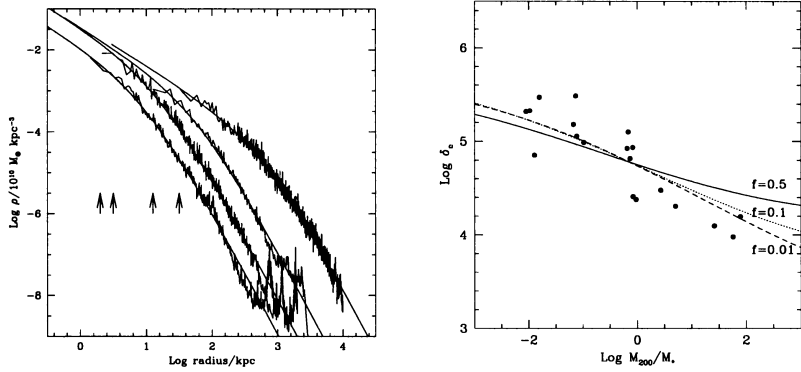


Figure 1.17: *Left:* Typical density profiles from Cold Dark Matter (CDM) halos obtained from N-body simulations. *Right:* Characteristic overdensity of halos as a function of mass. Masses are expressed in units of the current non linear mass corresponding to the standard biased CDM spectrum  $M_* = 3.3M_\odot$ . Figures from [105].

Many of the observed DSphe are strongly DM dominated, but have absent or very little star formation and no signal of ionized or neutral gas [111]. Smaller structures with no emission at all are known as Dark Clumps.

These kind of objects are a perfect target for DM searches because no  $\gamma$ -ray signal is expected from them due to ordinary astrophysical processes. Any  $\gamma$ -ray detection would be an unequivocal signal of DM annihilation.

The present generation of  $\gamma$ -ray experiments have widely studied these objects in the search for DM, not yet being successful at detection but setting very stringent upper limits on DM models using data from many DSphe ([112], [113], [114], [115], [116]).

### Galaxy Clusters

As has been mentioned before in section 1.6.2, galaxy clusters are mostly dominated by DM with a very high mass-to-light ratio. For this reason, they are good targets for indirect DM searches both for annihilation and decay. They are specially suitable for decaying DM, since at large volumes the signal of decaying DM which is proportional to the first power of the density overshines the signal of annihilation [117].

Strong constraints for a wide number of models for DM annihilation and decay have been set by *Fermi*-LAT [118], [119] and H.E.S.S. [120], and also constraints on the decaying lifetime of DM were set by MAGIC [121].

### The Large Magellanic Cloud

The LMC has been considered a well promising target for DM searches due to its proximity and rather high J-factor ( $10^{20}J/\text{GeV}^2\text{cm}^{-5}$ ). Kinematic studies of the LMC show that more than half of the LMC mass is forming a dark halo with a compact central bulge [122], [123].

*Fermi*-LAT has used five years of data to set constraints on the DM annihilation

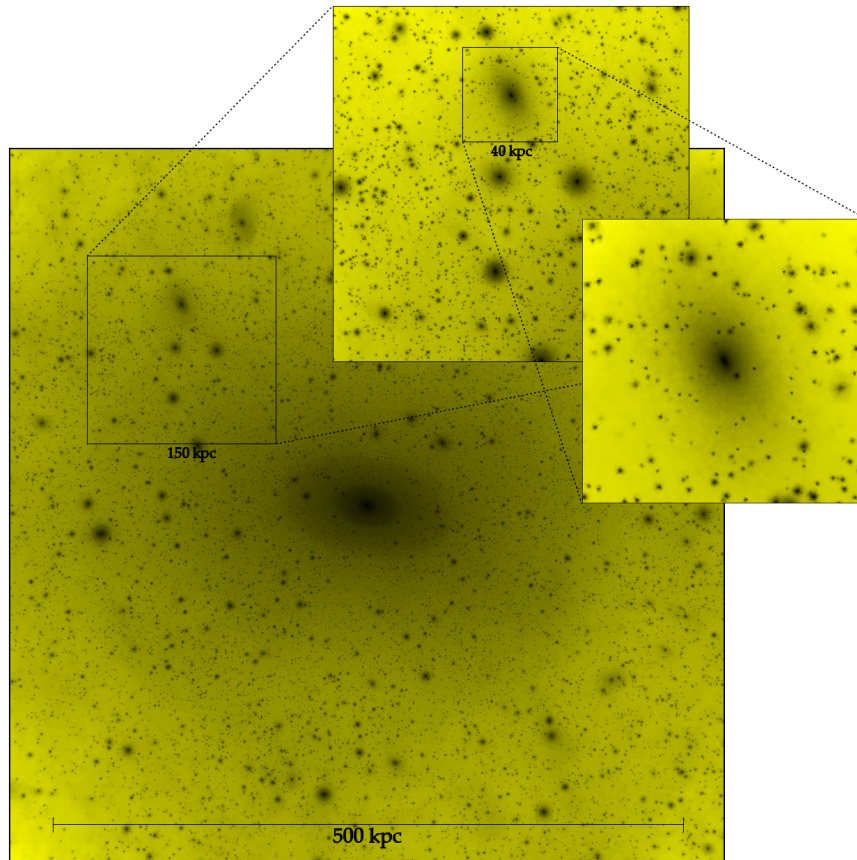


Figure 1.18: Results from *Via Lactea* N-body simulations of DM substructures. The picture show a projection of density squared in a  $566 \text{ kpc} \times 566 \text{ kpc} \times 566 \text{ kpc}$  region centered on the host halo at  $z = 0$ , from [110].

signal from the LMC in the HE regime [124]. No limits has yet been set in the VHE range though. As one of the main topics of this thesis, more on this subject will be extensively discussed in chapter ??.



## 2. Detection of $\gamma$ -rays



Discoveries in astronomy have always been directly related to technological advances of new instruments and observation techniques. The first astronomical telescope was developed by Galileo in the *XVII* century and it allowed him to observe for the first time the four brightest moons of Jupiter. Since then, and specially during the *XX* century, a broad new range of experiments, detectors and telescopes have been built either on the ground or in space. Thanks to them, astronomers have observed the universe in every wavelength from radio to  $\gamma$ -rays. Furthermore, the recent field of multimessenger astronomy has started a new era, combining electromagnetic radiation with other cosmic messengers such as neutrinos and gravitational waves.

This chapter is dedicated to the technologies used to detect  $\gamma$ -rays, from the history of first detectors, to the present generation and future of  $\gamma$ -ray observatories.

Contrary to the visible light that Galileo received with his first telescope,  $\gamma$ -rays cannot be directly observed from Earth. The atmosphere absorbs most of the radiation coming from space, limiting the range of the spectrum that can be detected with ground based detectors. As shown in figure 2.1, only visible and radio wavelengths reach the ground through the so called *atmospheric windows*, hence  $\gamma$ -rays can be observed only from outside the atmosphere, with detectors in balloons or satellites. A description of different types of such detectors and their used techniques is given in section 2.1.

Other possibility is to take advantage of the interactions of  $\gamma$ -rays with particles in the atmosphere when they are absorbed. When a  $\gamma$ -ray or any cosmic particle hits an atmospheric atom, a large number of secondary particles is produced which themselves suffer further interactions in a cascade reaction known as Extensive Air Showers (EAS). More on EAS and ground-based detectors can be found in sections

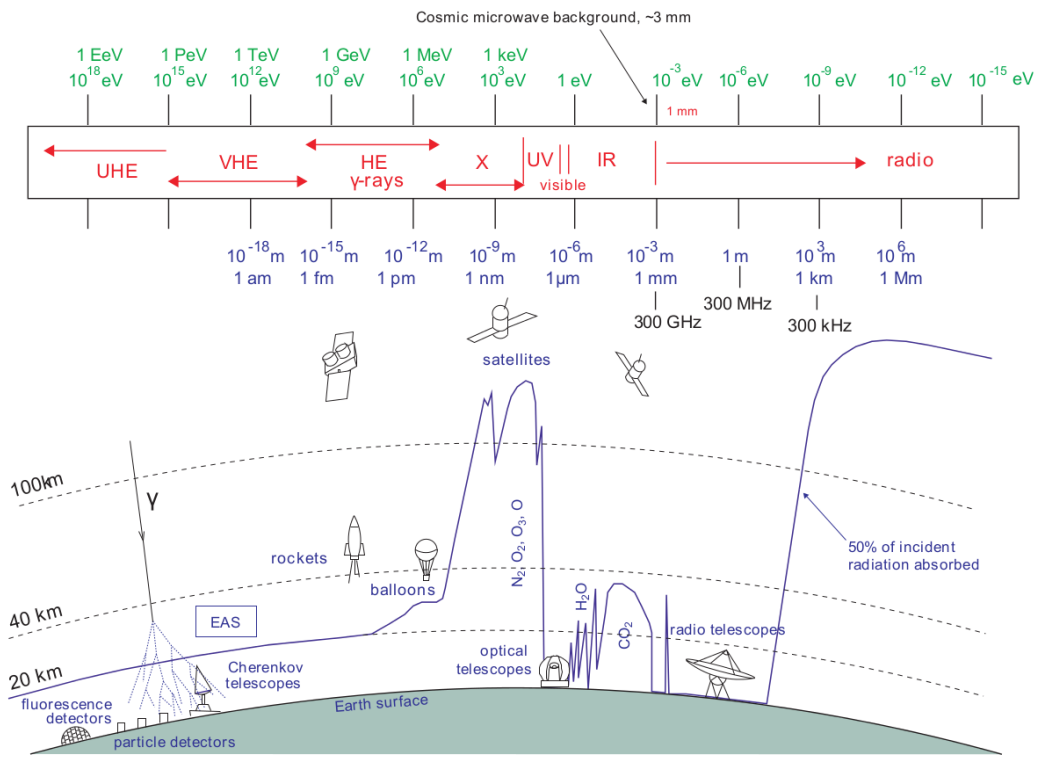


Figure 2.1: Atmospheric transparency for the whole electromagnetic spectrum, from [17]. The continuous line represents the height in the atmosphere where 50% of the light is absorbed.

2.2 and 2.4 respectively.

Space detectors and ground based detectors complement perfectly well, supplying the limitations of one another to cover the full  $\gamma$ -ray spectrum. Lower energy  $\gamma$ -rays are abundant, but so are hadronic backgrounds (Cosmic Rays (CRs)). Space detectors are perfectly suited to study these part of the spectrum, because beside their rather small collection areas ( $\sim 1\text{m}^2$ ), they have very good background rejection. At higher energies, the  $\gamma$ -ray flux decay strongly and much higher collection areas are needed. Ground based instruments detect the extended secondary products of  $\gamma$ -rays interacting in the atmosphere, they are designed to cover big areas, capturing even events from the highest energy  $\gamma$ -rays.

## 2.1 Space detectors

Direct detection of  $\gamma$ -rays can only be done outside the atmosphere, with particle detectors mounted in high altitude balloons or satellites. The main advantage of

these kind of detectors is the extremely efficient background rejection, being relatively easy to veto charged cosmic particles and distinguish them from neutral  $\gamma$  photons. However, they are limited in the energy of the  $\gamma$ -rays they can observe, not being able to go much further 100 GeV (High Energy (HE) regime) because of the technical difficulties to have a large collection area. The collection area corresponds to the size of the detector, which for space instruments is about  $1\ m^2$ , hindering the capture of Very High Energy (VHE) photons which flux decreases rapidly with energy.

In this section, different types of space detectors are described.

### 2.1.1 Compton detectors

Compton scattering occurs when a photon transfers part of its energy to an electron. At the low end of the  $\gamma$ -ray energy range (from 20 keV to 30 GeV) this is the process that dominates interactions between light and matter. Compton detectors are based on this interaction. Usually, they count on two parts: In the first level, the interaction between the  $\gamma$  photon and an electron occurs inside a scintillator. The trajectory deviation of the photon is measured, and then is possible to reconstruct its original direction. Afterwards, the photon travels to a second level where it is absorbed by a calorimeter and its energy is measured. The Imaging Compton Telescope (COMPTEL) instrument from the Compton Gamma Ray Observatory (CGRO) was operative between 1991 and 2000 and was able to do a survey of the galactic plane using this technique, detecting more than 60 sources (figure 2.2). Currently, the Imager on-Board the INTEGRAL Satellite (IBIS) [125] telescope [126] is the present representative of this kind of detectors.

### 2.1.2 Pair production detectors

A photon travelling with an energy over twice the rest mass of the electron (511 keV, usually photons over 20 GeV) passing close to a nucleus have a high probability to undergo through pair production process, giving rise to an electron-positron pair. Pair production detectors account for different layers of a heavy material where the interaction takes place, interleaved with a tracker material which measures the position of the resulting particles, being able to reconstruct the original direction of the  $\gamma$ -ray. A calorimeter measures the energy of the particles and an anti-coincidence detector acts as veto for the background of charged particles (CRs) which can enter the detector. A very prolific instrument of this kind, still on going, is the Large Area Telescope (LAT) instrument, on the Fermi Gamma-Ray Telescope which is formerly described in the next section.

#### The Fermi Gamma-ray Space Telescope

The Fermi Gamma-ray Space Telescope was launched in 2008 with the goal of performing a sky survey in the HE range. It follows a low Earth orbit, being able to observe the whole sky in 3 hours. It counts with two instruments: The LAT, which is the principal instrument for  $\gamma$ -ray detection, and the Gamma-Ray Burst Monitor

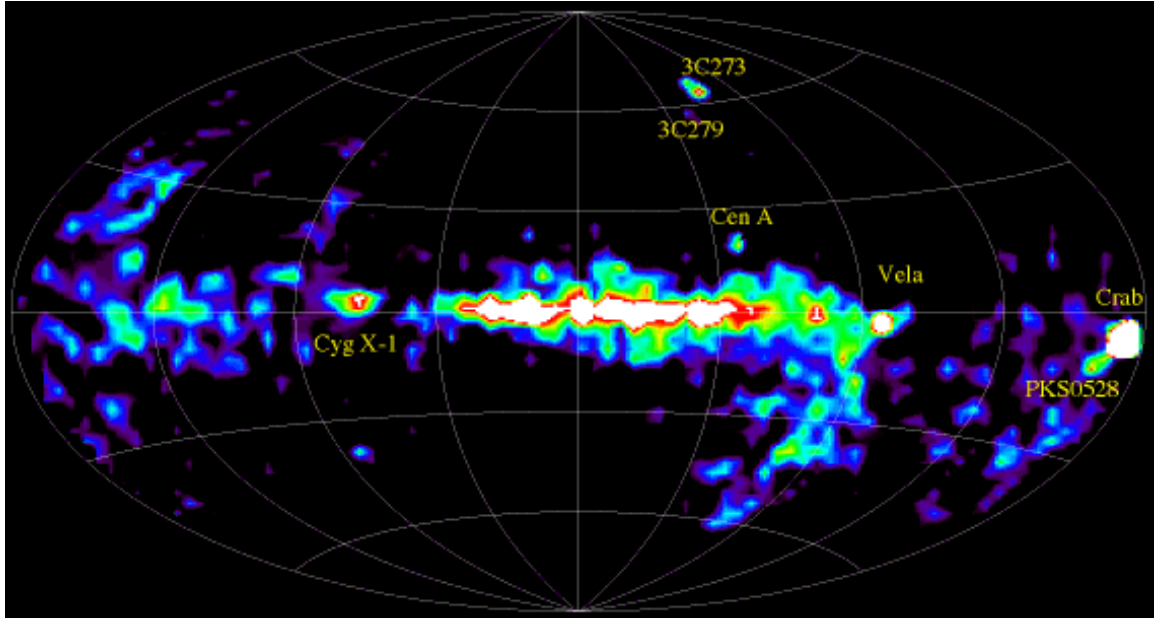


Figure 2.2: Skymap from COMPTEL source catalog. Credits to NASA.

(GBM), which is designed to detect Gamma Ray Bursts (GRBs).

- **The LAT:** This is the principal instrument of the Fermi telescope, a pair production  $\gamma$ -ray detector able to observe photons with energies from 20 MeV to more than 300 GeV [127]. It consists of 16 modular towers with 18 tungsten converter layers, where the pair production takes place, and 16 dual silicon tracker planes which measure the trajectory of the  $e^\pm$  pair. The 16 calorimeter modules have 96 long, narrow CsI scintillators which measure the deposited energy. When any particle enters the detector, it first passes through an anticoincidence plastic scintillator where, if it is a charged particle, it will produce a flash of light, making it possible to distinguish it from true  $\gamma$ -ray events.
- **The GBM:** Complementary to the LAT, the GBM is destined to detect GRBs and quickly alert the main instrument to reposition towards its direction. It is sensible to X-rays and  $\gamma$ -rays in the range between 8 keV to 40 MeV. The detector includes 12 Sodium Iodine (NaI) scintillation detectors which cover the lower part of the spectrum (up to 1 MeV) and provide the burst trigger, and 2 Bismuth Germanate (BGO) scintillation detectors with an energy range from  $\sim 150$  keV to  $\sim 30$  MeV, aimed to overlap the LAT energy range.

The principal scientific goals of Fermi are the study of unidentified sources detected by previous instruments like Energetic Gamma Ray Experiment Telescope (EGRET); understanding the mechanisms of particle acceleration in Supernova Remnants (SNRs) and GRBs; studying the behaviour of GRBs; performing indirect searches of Dark Matter and using  $\gamma$ -rays to probe the early universe and cosmic evolution of HE

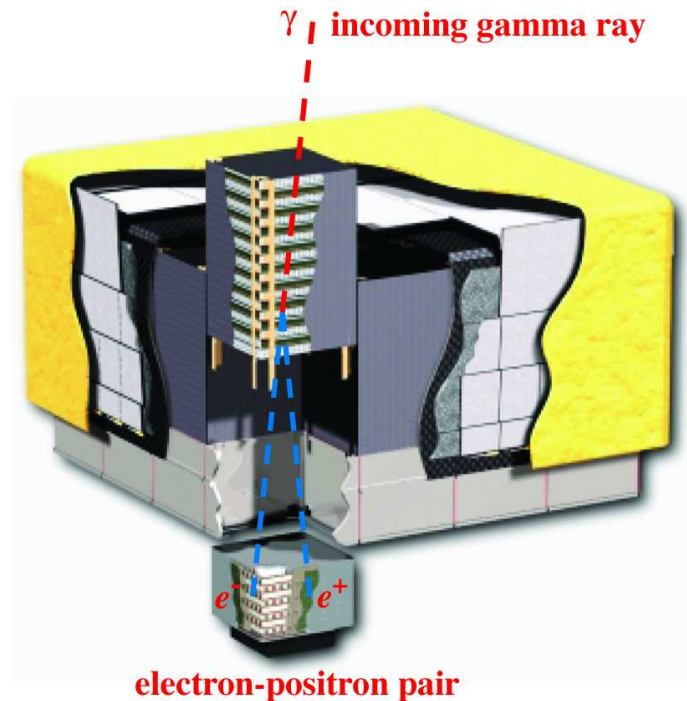


Figure 2.3: Schematic picture of the LAT from [127]. Dimensions are  $1.8 \text{ m} \times 1.8 \text{ m} \times 0.72 \text{ m}$ .

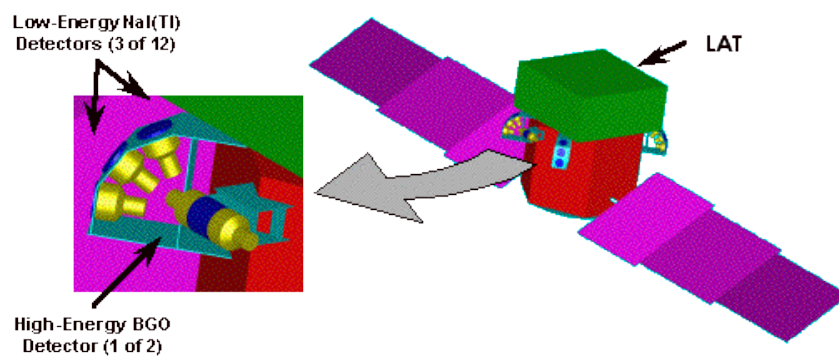


Figure 2.4: Schematic picture of the GBM integrated between the LAT and the shroud envelope of the Fermi's spacecraft.

sources.

During the more than 10 years of data taking up to date, the *Fermi*-LAT has been extremely prolific, launching several catalogs with thousands of sources. The 4FGL catalog is the last one released, based on the first 8 years of science data. It counts with 5065 detected sources above  $4\sigma$ , 1337 of which do not have a counterpart in other wavelengths.

Some of the scientific highlights during its lifetime are the discovery of the Fermi Bubbles (see section 1.6.1); the detection of hadronic signals in SNRs [128]; the detection of the most luminous GRB ever observed GRB130427A [129] and the detection with the GBM of the GRB after the LIGO event GW170817 [130], among many more.

## 2.2 Extensive Air Showers

As explained in the beginning of this chapter, the atmosphere absorbs the totality of the  $\gamma$  radiation coming from space. Any  $\gamma$ -ray entering the atmosphere will interact with an atomic nucleus triggering the production of a cascade of particles known as EAS. Furthermore, not only  $\gamma$ -rays can produce EAS, but CRs too, being in fact the responsible for the majority of EAS happening in the atmosphere ( $> 99\%$ ). The products of these cascades, whether being secondary particles or Cherenkov radiation (see section 2.3), are the targets for ground based  $\gamma$ -ray detectors. Depending on the type of detector, different techniques are required to reconstruct the energy and direction of the primary particle, in addition to distinguish between electromagnetic (produced by  $\gamma$ -rays) and hadronic (produced by CRs) showers. In this section, the characteristics and physical processes produced in the different types of EAS are described.

### 2.2.1 Electromagnetic Showers

When a primary  $\gamma$ -ray enters the atmosphere, it will produce a pair of  $e^\pm$  in the electric field of an atomic nucleus, typically after traversing one radiation length ( $\xi_0$  defined as the mean distance for a charged particle to reduce its energy by a factor  $e$  due to interactions with the medium), at about 20 km of altitude. This pair of particles, emitted in the forward direction will again interact with other atmospheric nuclei through bremsstrahlung, producing high energy photons. The result is a chain of pair production-bremsstrahlung processes, where a certain amount of energy is lost in each interaction, until the high energy photons reach a critical energy  $E_c \sim 83$  MeV. When this happens, ionization and Compton scattering of electrons and positrons become dominant over bremsstrahlung so the production of high energy photons is reduced until the shower slowly dies. Since the angle of emission in all the processes is proportional to  $\propto m_e c/E$  rad, the shower will not spread too much laterally, from an axis pointing towards the primary direction [20].

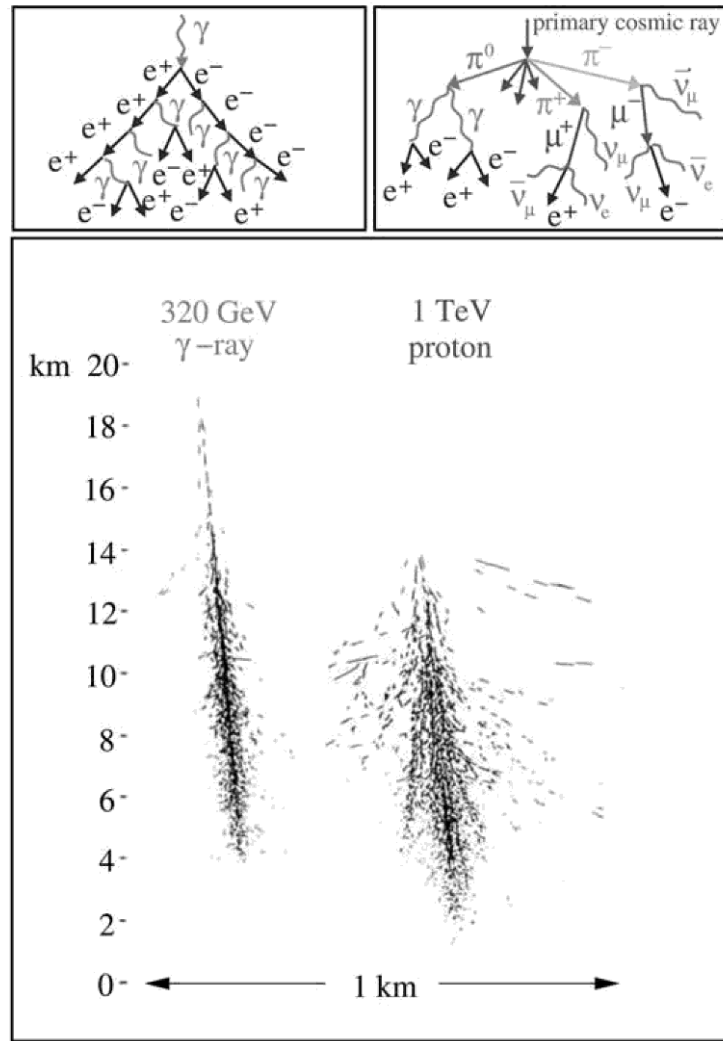


Figure 2.5: Montecarlo simulations of a 320 GeV  $\gamma$ -ray shower and a 1 TeV proton shower from [20]. The top panel show a schematic diagram of shower development with their secondary particles.

To understand in a simple way the evolution of the shower, It can be considered that it develops in discrete steps of one radiation length, just as in the model from [131]. The radiation length for the  $e^\pm$  pair is going to be close to the mean free path of photons of similar energy ( $\simeq 9/7\xi_0$ ) which for the air is  $36.7 \text{ g cm}^{-2}$ . Defining the atmospheric thickness as  $R=\xi_0 \ln 2$ , the probability of a photon, electron or positron of the shower to interact while traversing a longitude  $R$  will be  $\exp(-R/\xi_0) = 1/2$ . Since the distribution of energy in each step between the charged particles and the emitted high energy photon is considered symmetric, after traversing a thickness  $nR$ , the number of surviving  $e^\pm$  and photons will be  $2^n$ , and their mean energy  $E_\gamma/2^n$ , where  $E_\gamma$  is the energy of the primary  $\gamma$ -ray. When the energy reaches the critical energy  $E_c$ , the shower has reached the shower maximum, where the total number of particles is  $E_\gamma/E_c$ . The position of such maximum is:

$$X_{max} = \frac{R}{\ln 2} \ln \frac{E_\gamma}{E_c} = \xi_0 \ln \frac{E_\gamma}{E_c} \quad (2.1)$$

The shower maximum depends on the energy of the primary: higher energy photon showers penetrate more deeply in the atmosphere than lower energy showers, hence in order to lower the energy threshold of a ground based detector it must be located at high altitudes.

An analytical approach to shower development was carried out in [132]. The Greisen equation defines the number of electrons, positrons and photons in the shower before reaching the critical energy:

$$N_e(t) = 0.31 \left[ \log \frac{E_\gamma}{E_c} \right]^{-1/2} e^{T[1-(3/2)\log s]} \quad (2.2)$$

Where  $T$  is defined as the atmospheric depth expressed in radiation lengths, and  $s$  is the shower age parameter:

$$s = \frac{3T}{T + 2 \ln \left[ \frac{E_\gamma}{E_c} \right]} \quad (2.3)$$

The age parameter  $s$  indicates the degree of development of the shower, being equal to 0 at first interaction, 1 in the shower maximum and 2 in the dying point. While  $N_e$  describes the longitudinal distribution of the shower, the lateral distribution is given by the Nishimura-Kamata-Greisen function:

$$f(r) = \frac{\Gamma(4.5-s)}{\Gamma(s)\Gamma(4.5-s)} \frac{N_e}{2\pi r^2} \left[ \frac{r}{r_m} \right] \left( 1 + \frac{r}{r_m} \right)^{s-4.5} \quad (2.4)$$

Where  $r$  is the distance from the shower longitudinal axis and  $r_m$  is the Molière radius, characteristic from multiple scattering theory, and  $\Gamma$  is the gamma function.

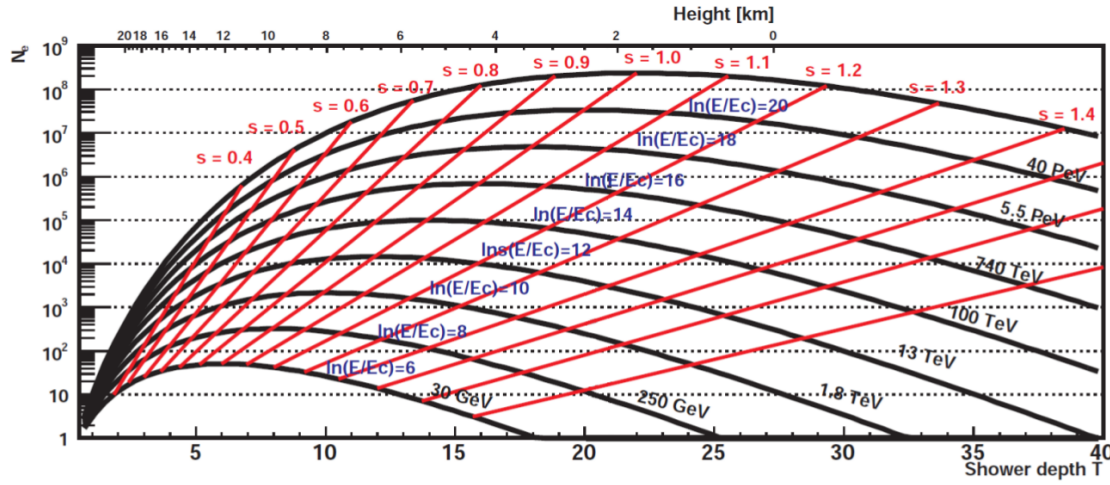


Figure 2.6: Longitudinal development of an electromagnetic shower in the Greisen approximation, from [133] and [134].

### 2.2.2 Hadronic showers

Hadronic showers are produced by CRs, mostly protons, colliding with atmospheric particles. Their development is substantially different from electromagnetic showers, since they produce a vast number of secondary particles of different nature (see figure 2.5) mainly fragments of atomic nucleus, pions and kaons, which end up decaying into muons and neutrinos. Hadronic showers have three components:

- **Hadronic core:** In the first interaction, a relativistic CR collides with a nucleus (O, N...) fragmenting it into smaller nucleons and transferring energy to them, which on their side keep colliding with other particles. They also produce charged mesons in each interaction ( $\pi$  and K mesons). Hadronic interactions will continue until the energy per nucleon becomes smaller than the pion production threshold around 1 GeV.
- **Electromagnetic component:** Around 90% of the particles generated in hadronic showers are pions, of which 1/3 are  $\pi^0$ . Neutral pions decay into two HE photons which generate pure electromagnetic showers. Charged K mesons can also decay into neutral pions through  $K^\pm \rightarrow \pi^\pm + \pi^0$ .
- **Muon and neutrino component:** Charged mesons can also decay into muons and neutrinos through  $\mu^\pm \rightarrow \nu_\mu(\bar{\nu}_\mu)$ . Muons traversing the atmosphere will only lose energy through ionization due to their long life and their small bremsstrahlung cross-section. They will decay into electrons/positrons and neutrinos through  $\mu^\pm \rightarrow e^\pm + \nu_e(\bar{\nu}_e)$  after a time of  $2.2 \cdot 10^{-8}$  s in their own reference frame, but due to their high Lorentz factor, time dilation can make

them reach ground level without decaying at all.

Despite their complexity, a model can be assumed to describe the evolution of hadronic showers, similar to the one for electromagnetic EAS. In the superposition model from [135] it is assumed that the shower induced by a nucleus of mass A and energy  $E_0$  is equivalent to A independent nuclei of energy  $E_0/A$ . The shower maximum in this case would be:

$$X_{max} \propto \xi_N \ln \left( \frac{E_0}{AE_c} \right) \quad (2.5)$$

Where  $E_c$  is the critical energy and  $\xi_N$  is defined as the mean path which reduces the number of relativistic charged particles by a factor  $1/e$  as they pass through matter, which for a proton of 1 TeV is  $83 \text{ gcm}^{-2}$ . Because  $\xi_N$  is larger than the radiation length for photons  $\xi_0$ , the altitude of first interaction of hadronic showers is higher than electromagnetic showers and they are able to penetrate deeper into the atmosphere. Furthermore, hadronic interactions are able to transfer considerable transverse momentum to the secondary products of the showers making them to disperse laterally. Also, hadronic showers are more irregular and present large fluctuations. These features are used in detectors to distinguish between electromagnetic and hadronic induced showers.

### 2.2.3 Electronic showers

There exist a third type of EAS produced by cosmic electrons and positrons entering the atmosphere. The type of cascade produced is very similar to electromagnetic showers, since the same processes take place: The electron/positron produces HE photons via bremsstrahlung while interacting in the electromagnetic field of atmospheric nuclei and those resulting photons produce  $e^\pm$  pairs. The main differences with electromagnetic showers have to do with the nature of the primary: Since it is a charged particle, interactions start just when it enters the atmosphere so the shower maximum is reached at higher altitudes. Also, it will be more affected by the deviations produced by the geomagnetic field of the Earth.

## 2.3 Cherenkov radiation

The Cherenkov radiation is a kind of electromagnetic radiation which is emitted when a charged particle travels through a dielectric medium at a velocity higher than the local speed of light. Many scientists during the XX observed that when a transparent material was placed in the neighbourhood of strong radioactive sources, they emitted a faint bluish light. From 1934 to 1938 Pavel Alekseyevich Cherenkov carried out a series of exhaustive experiments to try to explain the causes of this effect, named after him, and was awarded with the Nobel Prize in 1958 for his results.

Cherenkov radiation is a very important effect for ground-based  $\gamma$ -ray detectors

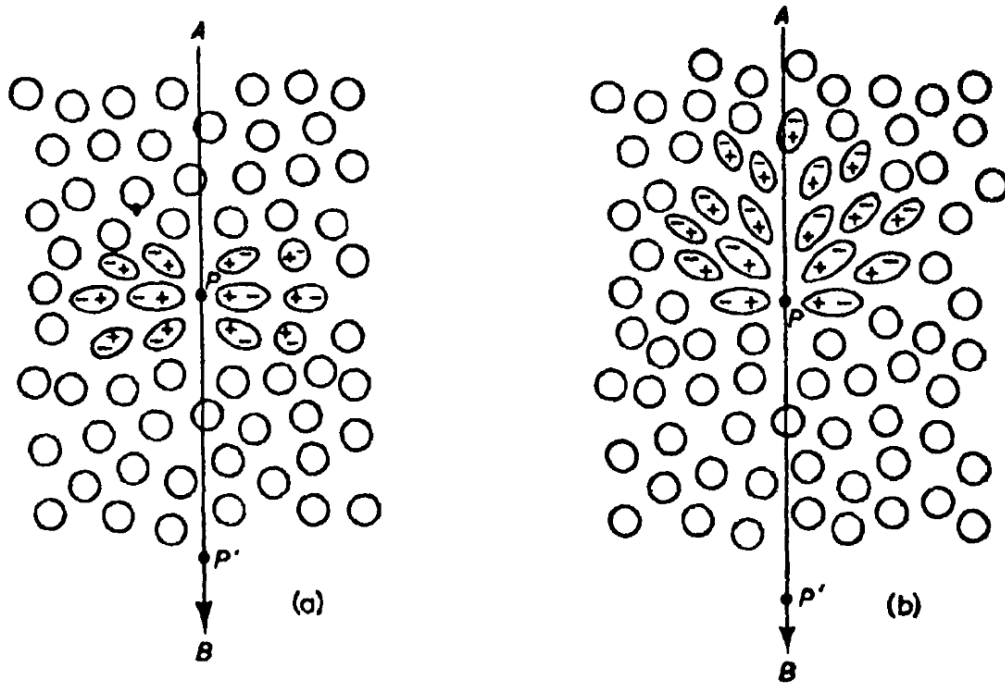


Figure 2.7: Polarization of a dielectric material at the passing of a charged particle by the point  $P$  at a) low velocity b) high velocity. Image from [136].

because EAS, which contain a large number of relativistic charged particles, are able to produce this kind of radiation in the atmosphere. Characterization of the Cherenkov signal from EAS allow to trace back the nature of the primaries.

This effect can be explained through the reaction of the atoms of a material when a charged particle is traveling through it. For example, in the case of an electron travelling through a glass, if the electron is travelling at a slow velocity, along its trajectory the electric field of the particle will distort the atoms, attracting the positively charged nucleus and repelling the negative electrons (see figure 2.7 a). The medium becomes polarized around the position of the particle, each atom behaving like a dipole and the region of the glass receiving a small electromagnetic pulse. Since the distribution of dipoles is symmetric, there will not be a resulting field thus no radiation will be emitted.

In the case the electron travels almost at the velocity of light in the medium the resulting field is not symmetric anymore along the direction axis of the particle (see 2.7 b). The dipole field will be noticeable even at long distances and the electron will produce the emission of wavelets of radiation at each point of its trajectory. In general, those wavelets will interfere destructively so that the resulting intensity of the field will be zero. If the velocity of the electron is higher than the speed of light in the medium, the wavelets can be in phase and produce a global field visible in the distance and thus, emit radiation. Figure 2.8 shows a diagram of a Huygens

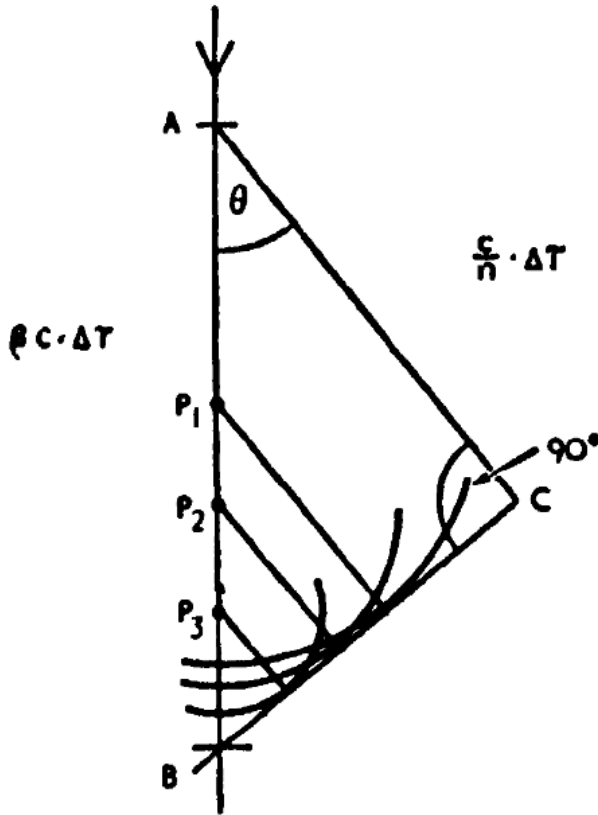


Figure 2.8: Diagram of Huygens construction showing coherence of waves emitted by a charged particle travelling faster than the speed of light in the medium, from [136].

construction of this effect. If a particle travels from A to B faster than the speed of light in the medium, it can travel that distance in the same amount of time that light will go from A to C, therefore when seen under an angle  $\theta$  all the waves emitted along the trajectory will be in phase and form a plane wave from B to C.

The angle  $\theta$  is named Cherenkov angle and can be expressed as:

$$\cos \theta = \frac{1}{n\beta} + \frac{\hbar k}{2p} \left( 1 - \frac{1}{n^2} \right) \quad (2.6)$$

Where  $\beta = v/c$ ,  $k$  is the emitted photon momentum,  $p$  is the charged particle momentum and  $n$  is the refractive index of the medium. Since  $p \gg k$ , the expression can be simplified to:

$$\cos \theta = \frac{1}{n\beta} \quad (2.7)$$

The Cherenkov light produced by EAS in the atmosphere will be emitted in the shape of a cone around the axis of the shower, leaving a ringlike signal when reaching

the ground. Because the refractive index of the atmosphere changes with altitude, the maximum angle will also vary and so the extension of the ring and the minimum energy required by a particle to produce Cherenkov radiation (when  $v = c/n$ ). The variation of the refractive index with altitude can be approximated by:

$$n(h) = 1 + n_0 e^{-\frac{h}{h_0}} \quad (2.8)$$

Where  $n_0$  is  $2.9 \times 10^{-4}$  and  $h_0 = 7.1$  km for an isothermal atmosphere, and the minimum energy:

$$E_{min} = \frac{m_e c^2}{\sqrt{1 - \beta_{min}^2}} = \frac{m_e c^2}{\sqrt{1 - (1/n)^2}} \quad (2.9)$$

Hence the minimum energy as a function of altitude:

$$E_{min} \approx \frac{m_0 c^2}{\sqrt{2n_0}} e^{\frac{h}{2h_0}} \quad (2.10)$$

and the maximum angle  $\theta$ :

$$\theta_{max} = \sqrt{(2n_0)} e^{-\frac{h}{h_0}} \quad (2.11)$$

This dependency means that at higher altitudes, the maximum angle is lower, so the Cherenkov signal in the ground will be less spreaded. Also, the minimum energy lowers with altitude, meaning that more developed EAS will more likely produce Cherenkov light.

About the spectrum of Cherenkov light in the atmosphere, while it could go from infrared to ultraviolet, photons below 290 nm are absorbed by ozone ( $O_3$ ), and over 800 nm by  $H_2O$  and  $CO_2$ . Also it suffers Rayleigh dispersion and aerosol dispersion. As a result, the peak of the spectrum at a detection altitude of about 2km is around 300 nm (blue light). The Cherenkov spectrum produced by a particle with charge  $z$  and velocity  $\beta$  is:

$$\frac{d^2N}{dxd\lambda} = \frac{2\pi\alpha z^2}{\lambda^2} \left( 1 - \frac{1}{\beta^2 n^2(\lambda)} \right) \quad (2.12)$$

## 2.4 Ground-based detectors

Ground-based detectors work capturing the products of EAS generated by primary  $\gamma$ -rays in the atmosphere. As explained in previous sections, EAS produce a cascade of particles which at the same time, emit Cherenkov light. There are two main types

of ground based detectors: Particle detectors, which capture the particles produced in the shower, and Cherenkov detectors, which measure the Cherenkov light. Because both  $\gamma$ -rays and CRs produce showers, the biggest challenge for ground based detectors is to differentiate the two kinds of events, being the background rejection less efficient than for space detectors. A proper knowledge of the differences in the development of electromagnetic and hadronic showers is crucial for this task. In general, ground based instruments take advantage of very precise Montecarlo simulations of EAS to find features in the signals which can help to do the  $\gamma$ /hadron separation.

#### 2.4.1 Particle detectors

Particle detectors measure the particles and secondary photons produced by EAS. Because the shower maximum depends on the energy of the primary, as seen in equation 2.1, only  $\gamma$  rays with extremely high energies can produce showers that reach the ground. In order to lower the energy threshold of detectors is necessary to place them at high altitudes (over 2000 m).

- **Particle counter matrices detectors** are classic particle detectors which record the arrival time of particles and direction to reconstruct the shower and eventually the primary characteristics. Examples of this kind of experiments are CASA-MIA [137], LHAASO-KM2 [138], Tibet-AS [139] and HEGRA [140].
- **Water Cherenkov detectors** are other kind of particle detector. They consist on a large number of big water tanks where particles from the shower produce Cherenkov light. ARGO-YBJ [141] and HAWC [142] are examples of this kind of detector.

The advantage of particle detectors is that they can be extended over hundreds of square meters, covering a very wide field of view. Also, they can work anytime, even under daylight. In general, they cover the higher energy range, being able to reach hundreds of TeV.

#### 2.4.2 Atmospheric Cherenkov Telescopes

Cherenkov photons produced by EAS in the atmosphere account for  $10^{-4}\%$  of the Night Sky Background (NSB) and they can be observed from the ground as flashes of around 10 ns. For that reason, unlike particle detectors, they require very clear and dark moonless nights, to differentiate Cherenkov photons from any background light. There are two types of atmospheric Cherenkov telescopes:

##### **Sampling detectors**

They consist on a grid of counters which measure the Cherenkov light from EAS at ground level with low-gain Photomultiplier Tubes (PMTs). The direction of the primary can be determined measuring the timing signals from the photons detected,

and the energy is reconstructed from the lateral distribution of the Cherenkov light. The energy threshold for these kind of detectors is high, being suitable for the study of VHE and Ultra High Energy (UHE)  $\gamma$ -rays. For example, the minimum energy threshold of the Air shower Observation By angle Integrating Cherenkov Counters (AIROBICC) was 20 TeV [143]. For sampling detectors, differentiating  $\gamma$ -ray showers from hadronic is truly problematic, and currently they have been outperformed by Imaging Atmospheric Cherenkov Telescopes (IACTs).

### **Imaging Atmospheric Cherenkov Telescopes (IACTs)**

IACTs are the most prolific type of ground based  $\gamma$ -ray detectors and their evolution is the key for the next generation of VHE  $\gamma$ -ray astrophysics.

They work similar to optical telescopes, with a large mirror which collects Cherenkov light into a camera, that records images of the showers. Because Cherenkov light flashes are very short, cameras need to be very fast to take snapshots of just a few nanoseconds. Also, as the number of photons of the NSB is very high compared to the small number of Cherenkov photons, is essential to have a very precise time correlation between camera pixels, given by state-of-the art electronics, to reject random signals from NSB and get the time evolution of the showers.

The reconstruction of the energy and incident direction of the primary photon as well as the separation of  $\gamma$  and hadron events can be achieved through a parameterization of the shower images, based on the work done by Michael Hillas [144]. With this method, the moments of the observed light distribution in the camera, which for  $\gamma$ -rays looks like an ellipse (named Hillas ellipse), are used as parameters to characterize the shower, which subsequently allow to distinguish between  $\gamma$  and hadronic showers. The intensity of Cherenkov light in the image is directly proportional to the energy of the primary and the orientation of the ellipse can be used to reconstruct their direction of arrival. Several techniques are used to reconstruct the primary information from Hillas parameterization, most of them based on modern Machine Learning algorithms. A quantity named *gammaness* (or *hadroness*) is used to designate how likely is an event to be a  $\gamma$ -ray (or hadron). The closer to 1, the more  $\gamma$ -like (hadron-like) the event is. Other important reconstructed quantity is the denominated  $\theta^2$  angle, which is the square of the angle between the reconstructed source position and the true source position.

Other techniques make use of the entire information of the camera image, comparing pixel by pixel with a template generated by a semi-analytical model of shower development. A detailed summary on reconstruction methods for Cherenkov Telescopes can be found in [145] and [146].

Either of the techniques improve substantially when using stereoscopy, taking shower images with several telescopes at the same time. This not only improves the reconstruction power, but also helps rejecting the hadronic background very efficiently. When pointing the telescopes to a  $\gamma$ -ray sources, in general, shower images from  $\gamma$  primaries will be oriented towards the position of the source in the cameras of all

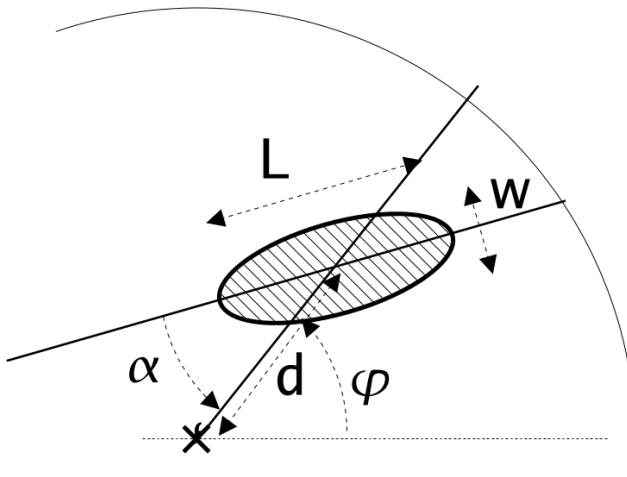


Figure 2.9: Geometrical definition of the Hillas parameters.  $L$  for Length ( $W$  for Width) is the RMS spread of light along the major(minor) axis of the image, it carries information of the longitudinal(lateral) development of the shower. Nominal distance  $d$  is the angular distance between the centre of the camera and the image centre of gravity. Angle  $\phi$  is the azimuthal angle of the image major axis and orientation angle  $\alpha$  is the angle between the major axis and the center of the camera. Figure from [145].

telescopes. Hadronic showers, which come from random directions in the sky, will point towards random directions in the camera, so they can be easily discarded.

The first telescope of this kind was the Whipple Observatory 10m reflector [147], with a camera of 37 pixels. It started operations in 1968 but it wasn't until 1988 that they detected the first  $\gamma$ -ray source, the Crab Nebula. The first stereoscopic system was the High Energy Gamma Ray Astronomy (HEGRA) complex, with a total of six IACTs which worked together with other types of  $\gamma$ -ray detectors (like the AIROBICC).

The current generation of IACTs is formed by Major Atmospheric Gamma Imaging Cherenkov Telescopes (MAGIC) [148], High Energy Stereoscopic System (H.E.S.S.) [149] and Very Energetic Radiation Imaging Telescope Array System (VERITAS) [150] telescopes:

- **MAGIC:** The MAGIC telescopes are a set of two IACTs of 17 m diameter, located in the Roque de Los Muchachos Observatory at the Canary Island of La Palma, Spain. They are at an altitude of 2200 m, separated by 85 m. The first telescope, MAGIC-I, started operations in mono mode in 2004, and in 2009 the second telescope, MAGIC-II was included, becoming an stereoscopic system. An upgrade was made during the years 2011-2012, to reduce differences between both telescopes and improving the stereo performance.

The energy threshold of MAGIC can reach 25 GeV when using the *sum trigger*

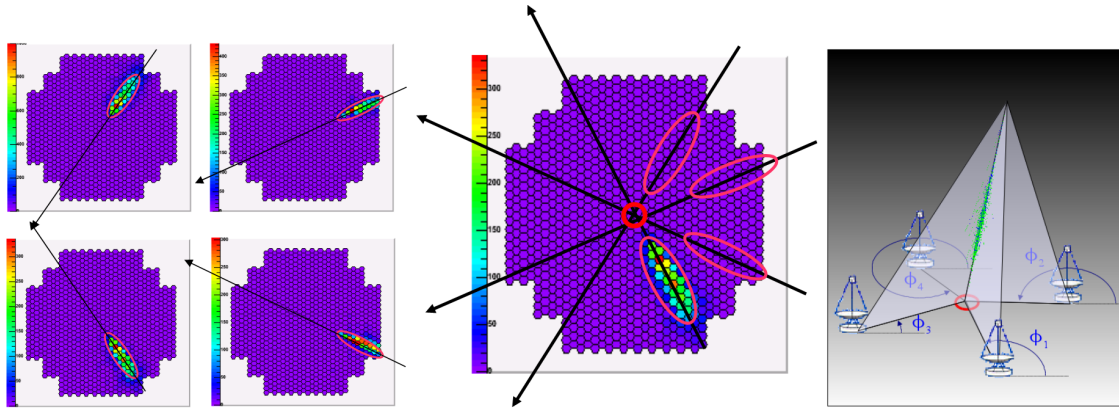


Figure 2.10: Geometric reconstruction of shower direction in stereo mode, from [146]. *Left and middle:* The shower image from 4 telescopes is combined to get the source position in the intersection of the main axis. *Right:* Intersection of the planes which contain the shower tracks and the telescopes give the shower Impact Parameter on the ground.

setup, becoming the most sensitive IACT system below 300 GeV in the northern hemisphere.

Due to their big size, the MAGIC telescopes are especially well suited to observe low energy events, which produce less Cherenkov photons and require bigger mirrors. This characteristic makes them especially ideal for observing high redshift Active Galaxy Nuclei (AGNs) and pulsars. Also, they were designed to be very light in order to be able to do a fast repositioning to follow up GRBs alerts. The MAGIC collaboration announced the first detection of a GRB in January 2019 [84].

During their fifteen years of operations the MAGIC telescopes have given prolific scientific results such as the detection in VHE of the Pulsar Wind Nebula (PWN) 3C 58, the one with the lowest luminosity and lowest flux ever detected in VHE  $\gamma$ -rays; the observation of  $\gamma$ -ray emission from a jet originated inside the event horizon of the central Black Hole (BH) of the galaxy IC 310; the detection of the galaxy PKS 1441+25, one of the two most distant galaxies detected at high energies; the detection of the Crab pulsar, located inside the well known Crab PWN; the detection of  $\gamma$ -rays from a gigantic explosion occurred in the galaxy QSO B0218+357 thanks to gravitational lensing; and the tracing of the source (the active blazar XS 0506+056) of a very rare cosmic neutrino event detected by IceCube experiment on September 2017 [151].

- **H.E.S.S.:** An array of 5 telescopes located in Namibia, close to the Gamsberg mountain, being the only IACT observatory in the southern hemisphere. The first four telescopes, operational since 2004, have 12 m diameter and are arranged in a square shape. The second phase of the experiment consisted in a

fifth telescope of 28m of diameter, sitting in the center of the square. It was inaugurated in 2012 and contributed to lower the energy threshold. An update in the cameras of the small telescopes was performed during the years 2015-2016 improving the performance of the whole array.

The energy range of H.E.S.S. goes from 30 GeV to 100 TeV, being the widest of IACT observatories.

Because it is located in the South, H.E.S.S. has been able to perform a galactic plane survey in VHE range, complementary to the HE survey done by *Fermi*-LAT (see picture 2.11). Some important scientific highlights of H.E.S.S. are the detection of the Vela pulsar and the colliding wind binary system Eta Carinae; the discovery of new SNRs in the galactic plane; the detection of VHE emission from the LMC P3 binary system discovered by *Fermi*-LAT, with a binary phase of  $\sim 0.3$ , being the most luminous binary system detected up to date; direct measures of the Extragalactic Background Light (EBL) spectral density thanks to the observations of a large number of AGN spectra; and observation of flares and variability in the AGNs Mrk 501 and 3C 279. A detailed summary on these topics among many more scientific highlights of H.E.S.S. can be found in [149].

- **VERITAS:** Is an array of four IACTs located in the Fred Lawrence Whipple Observatory in southern Arizona. They are 12 m diameter telescopes arranged in a diamond shape and their design is based on the original Whipple 10 m Telescope. The first light of the VERITAS prototype was in 2004 and the full array started operations in 2007. In 2012 the cameras PMTs were upgraded to high-quantum-efficiency PMTs. The total energy range goes from 85 GeV to 30 TeV. Among the most important scientific results from VERITAS are the detection of pulsed emission from the Crab pulsar; Regarding the observations of blazars (AGN), the detection of rapid variability in the blazar BL Lacertae, the detection of the high redshift blazar ( $z \sim 0.6$ ) PKS 1424+240 above 0.1 TeV, the discovery of the source VER J0521+211 and deep observations of the distant 1ES 0229+200 ( $z = 0.14$ ); and the survey of the Cygnus region which allowed to resolve new sources and contributed with new candidates of counterparts at TeV energies to *Fermi*-LAT sources in the region. A summary on the most recent VERITAS highlights can be found in [150].

The future of ground based  $\gamma$ -ray astronomy is in hands of the Cherenkov Telescope Array (CTA) currently in construction. CTA will be a  $\gamma$ -ray observatory without precedents, as the result of combined efforts of scientists from all over the astroparticle physics community. It will have two locations, one observatory in the northern hemisphere in the island of La Palma, Spain, and the other in the south, in the Atacama desert, Chile. This will allow to do full sky observations, with a sensitivity one order of magnitude better than the current generation of IACT observatories (see figure 3.6). An extended summary on CTA can be found in chapter 3.

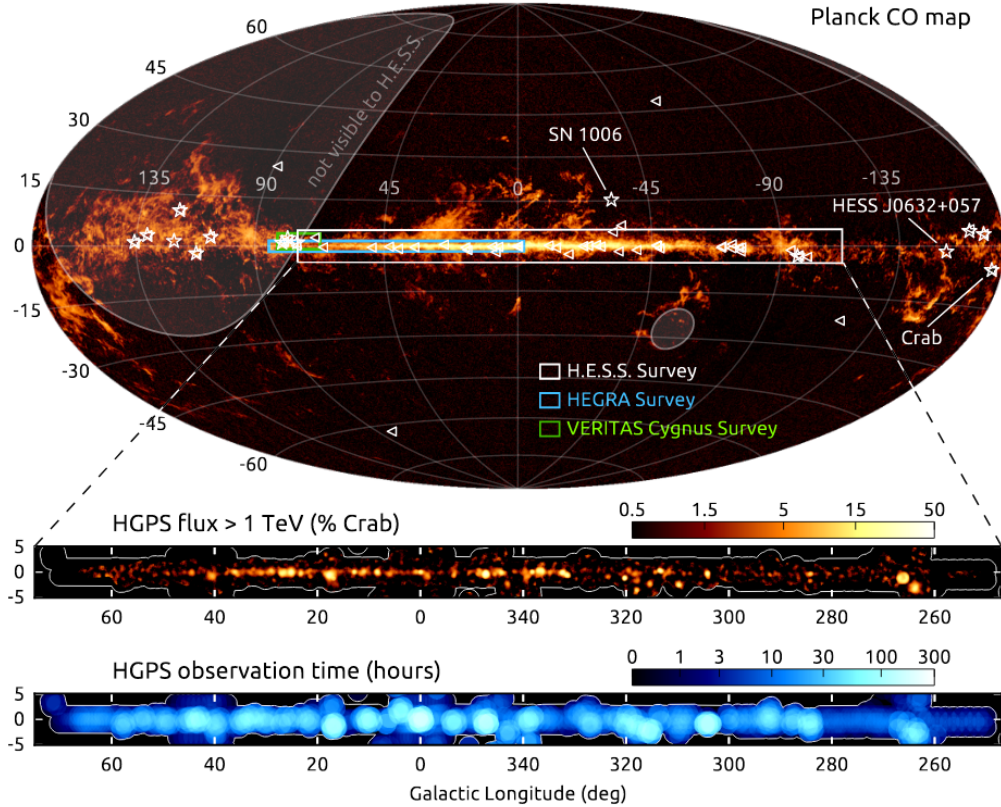


Figure 2.11: Illustration of the H.E.S.S. I galactic plane survey. The region surveyed is shown in the top panel as a white rectangle on top of the carbon monoxide gas sky map measured with the Planck satellite. Previous surveys from HEGRA and VERITAS are also represented. Triangles are sources detected at lower energies by *Fermi*-LAT and stars are galactic sources detected outside the survey region. Middle and lower panels show the observed flux and observation time. Picture from [149].

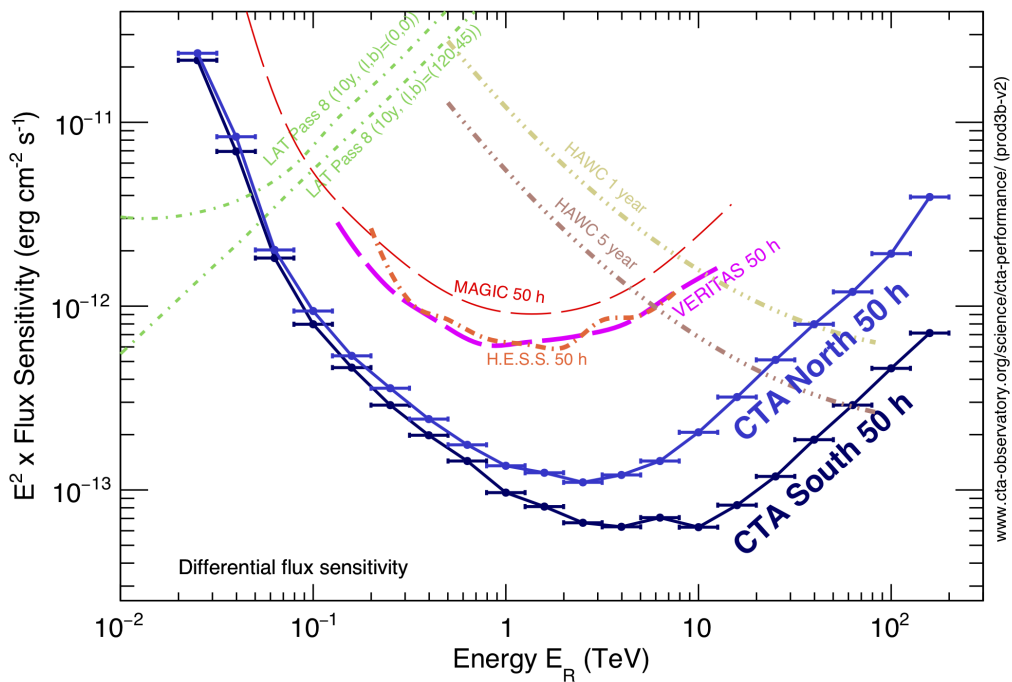


Figure 2.12: Differential sensitivity of CTA for 50 h observation compared to other  $\gamma$ -ray experiments, from [152].



## 3. The Cherenkov Telescope Array

### 3.1 Introduction

The Cherenkov Telescope Array (CTA) [153] is the next generation observatory for ground-based for  $\gamma$ -ray astronomy. It is the result of the combination of efforts from all the  $\gamma$ -ray community, to push the field of Very High Energy (VHE) astrophysics to new limits. It will consist on two arrays of Imaging Atmospheric Cherenkov Telescopes (IACTs) located in the Northern hemisphere, in the Roque de los Muchachos Observatory in the island of La Palma (Canary Islands, Spain) and in the Southern hemisphere in the Paranal desert (Chile). With this configuration, CTA will be the first ground-based observatory to be able to observe the full sky. CTA will have five to ten times more sensitivity than current instruments in the broader energy range ever reached by IACTs facilities, from 20 GeV to 300 TeV. Its angular resolution down to 2 arcseconds, with a field of view of  $\sim 10^\circ$  will allow the observation of fine structures in extended  $\gamma$ -ray sources. Its energy resolution, with an uncertainty less than 10%, will make CTA able to study features in the sources spectra, such as lines and cutoffs, in great detail.

To reach such improvements with respect to the current generation of IACTs observatories, CTA will count with more than 100 telescopes in three sizes, each optimized for observation in a specific spectral range. Large Size Telescopes (LSTs) have the bigger size, with a 32 m diameter mirror. They are optimal to observe the lowest part of the VHE spectrum covered by CTA ( $\sim$ 20 GeV to 3 TeV) where  $\gamma$ -rays are more abundant, so a small number of telescopes is enough, but the induced  $\gamma$ -ray showers emit a low number of Cherenkov photons, large mirrors are required to collect the maximum number of photons. Medium Size Telescopes (MSTs) have an intermediate size, with a diameter of  $\sim$  10m. They have the best performance at the range between  $\sim$  100 GeV and 50 TeV. Small Size Telescopes (SSTs) have much smaller mirrors ( $\sim$  4

m), and a large number of them will be installed to get big collection areas and be able to capture the highest energy photons (up to 300 TeV), which are very rare but produce huge amounts of Cherenkov light.

Thanks to the large number of telescopes, CTA will have great flexibility of operations, with different observation modes: with full array for best sensitivity; using subarrays to observe several sources at the same time; and divergent pointing mode where the field of view can be extended up to 20 deg.

In this chapter the main features of CTA are covered. A description of performance is given in section 3.2. In section 3.3 the three types of telescopes are described in detail. Section 3.4 is dedicated to CTA data analysis techniques and tools at different levels.

## **3.2 CTA Requirements and Performance**

The current generation of Cherenkov telescope observatories consist on arrays of 2 to 5 telescopes which reach sensitivities of about 1% of the Crab flux at the range of 0.1-1 TeV for 50h observation time. Their typical angular resolution is about 0.1°, but it can reach 0.02° for intense point sources of 20 to 30 arc seconds. The goal of CTA design is to advance the state of the art in  $\gamma$ -ray astronomy, improving sensitivity, energy range, angular and timing resolution and offering full sky coverage. The performance goals of CTA are shown in table 3.1. As a consequence of these goals, CTA will provide for two unique features: the ability to produce a deep survey of the VHE sky, potentially discovering hundreds of new sources; and the possibility to observe short time-scale phenomena, such as flares and jets from black holes in the center of active galaxies or periodic emission like such of pulsars. To achieve these improvements with respect to current IACT facilities, different types of telescopes are required and they should be spread over large areas to reach a collection area of several km<sup>2</sup> [154].

The final performance of CTA depends on the design of the telescopes, which will be discussed more deeply in next sections, and also on the arrangement of them in the two sites. To optimize the observatory configuration and estimate its performance, detailed Monte Carlo simulations were made [155], comprising simulations of shower development in the atmosphere, detector response and event reconstruction. A deep study of these simulations [156] for different configurations of telescopes and sites came up with the final array layout illustrated in picture 3.1.

The baseline design for Southern observatory foresees 4 LSTs, 25 MSTs and 70 SSTs. It will be dedicated to the study of galactic sources which emit the most energetic  $\gamma$ -rays that can reach the Earth. Because of their extremely low fluxes, it will cover very a large area ( $\sim 4$  km<sup>2</sup>), achieved thanks to the large number of SSTs, to capture as many events as possible.

The Northern observatory will mainly observe extragalactic sources and transient events from which only the less energetic photons reach the Earth due to absorption (see section 1.4). Its final configuration will consist on 4 LSTs and 15 MSTs.

The performance of CTA has been evaluated for the observation of a point source located at the centre of the field of view of telescopes cameras. A set of metrics are

Diff. sensitivity (erg cm <sup>2</sup> s <sup>-1</sup> )	at 50 GeV at 1 TeV at 50 TeV	$8 \times 10^{-12}$ $2 \times 10^{-13}$ $3 \times 10^{-13}$ (S) / $3 \times 10^{-12}$ (N)
Collection area (m <sup>2</sup> )	at 1 TeV at 10 TeV	$> 10^4$ $> 10^6$ (S) / $> 5 \times 10^5$ (N)
Angular resolution	at 0.1 TeV $> 1$ TeV	0.1° 0.05°
Energy resolution	at 50 GeV $> 1$ TeV	$\leq 25\%$ $\leq 10\%$
Field of view	at 0.1 TeV at 1 TeV $> 10$ TeV	5° 8° 10°
Sensitivity in FoV	at 1 TeV flat out to at 1 TeV	$> 2.5$ ° 5" per axis
Repointing time	<0.1 TeV 0.1-10 TeV	20s (goal), 50s(max) 60s (goal), 90s (max)

Table 3.1: Performance goals for CTA observatories, adapted from [154]. Sensitivity given in 5 bins per energy. (N)= Northern site, (S) = Southern site.

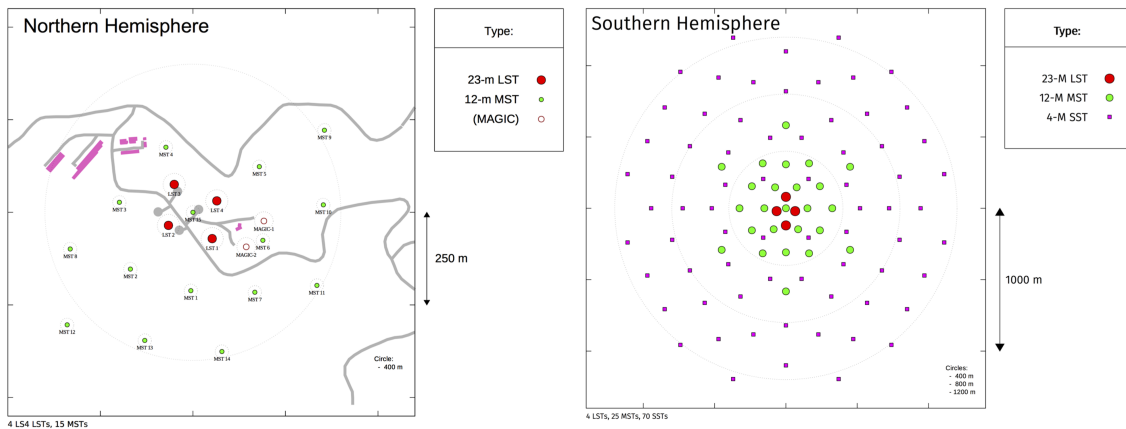


Figure 3.1: Array layout selected for CTA from [152]. Left is Northern site where also Major Atmospheric Gamma Imaging Cherenkov Telescopes (MAGIC) telescopes are located. Right is Southern location.

taken into account: Effective collection area, residual cosmic-ray background rate, angular resolution and differential sensitivity. Usually they are calculated after applying  $\gamma$ -hadron separation cuts, using the quantities *gammaness* and  $\theta^2$  (defined in section 2.4.2), optimized to maximize the sensitivity for a set of typical observation times. An overview of the mentioned metrics for performance evaluation is the following:

- **Effective collection area:** The effective collection area describes the area of the upper atmosphere where an incident  $\gamma$ -ray would be detected if CTA would have a detection efficiency, after cuts, of 100%. The effective collection areas for the assumed point sources are shown in figure 4.5.

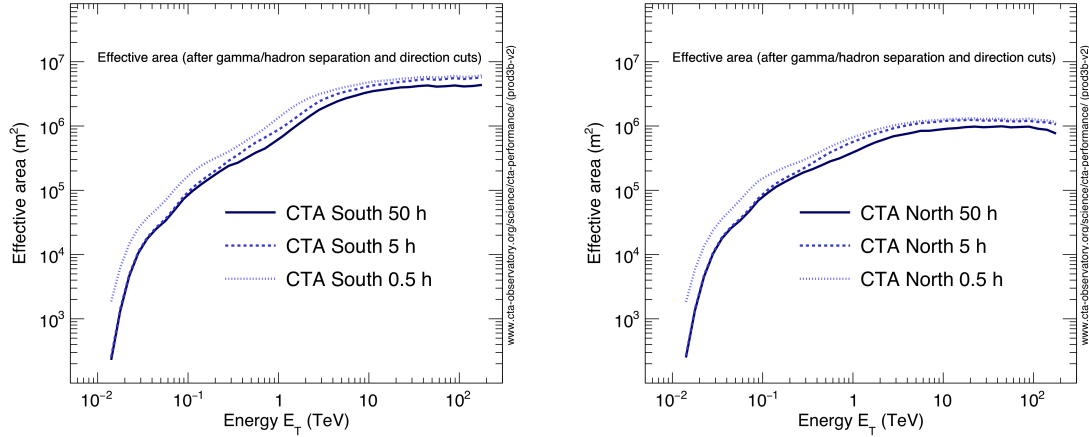


Figure 3.2: Effective collection area for point-like sources for CTA South(left) and CTA North (right) [152].

- **Residual cosmic-ray background rate:** The ability of CTA to reject background events due to showers produced by Cosmic Rays (CRs) instead of  $\gamma$ -rays is measured through the residual CR background rate. 99.9% of the showers reaching the telescopes are produced by CRs, so a good background rejection is mandatory for IACTs. In figure 3.3 the post-analysis resulting cosmic-ray background rate per square degree vs reconstructed  $\gamma$ -ray energy is shown. The rate is integrated in each bin, where five bins per decade has been taken. CTA background rejection capabilities allow to reject the majority of the background in the range 0.2-1.5 TeV, where the remaining background is due to cosmic-ray electrons and positrons [157] which produce showers very similar to those produced by  $\gamma$ -rays (see section 2.2.3), making them an irreducible background.
- **Angular resolution:** The angular resolution is defined as the angle within which 68% of reconstructed  $\gamma$ -rays fall, relative to their true direction. Figure 4.3 shows the angular resolution vs. reconstructed energy optimized for best

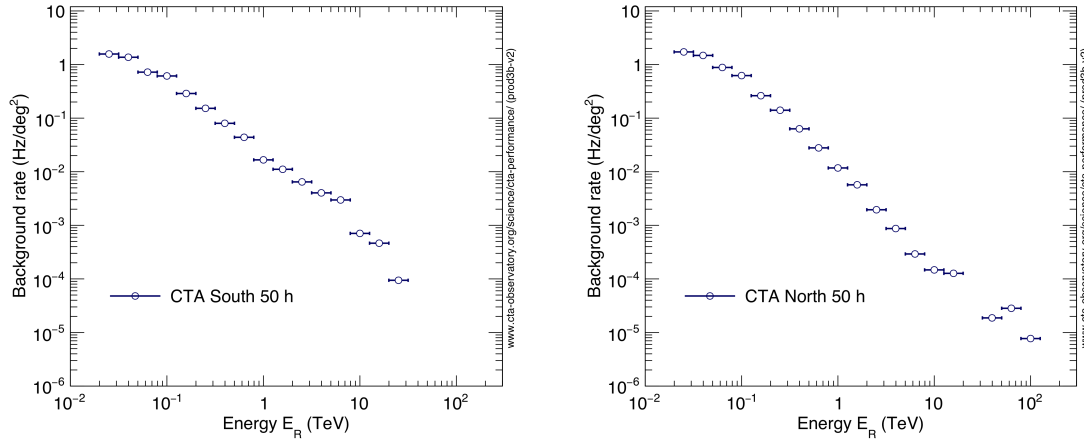


Figure 3.3: Residual cosmic-ray background rate vs reconstructed energy for CTA South(left) and CTA North (right) [152].

point-source sensitivity. It is possible to improve angular resolution at expenses of collection area for a better study of morphological features of bright sources.

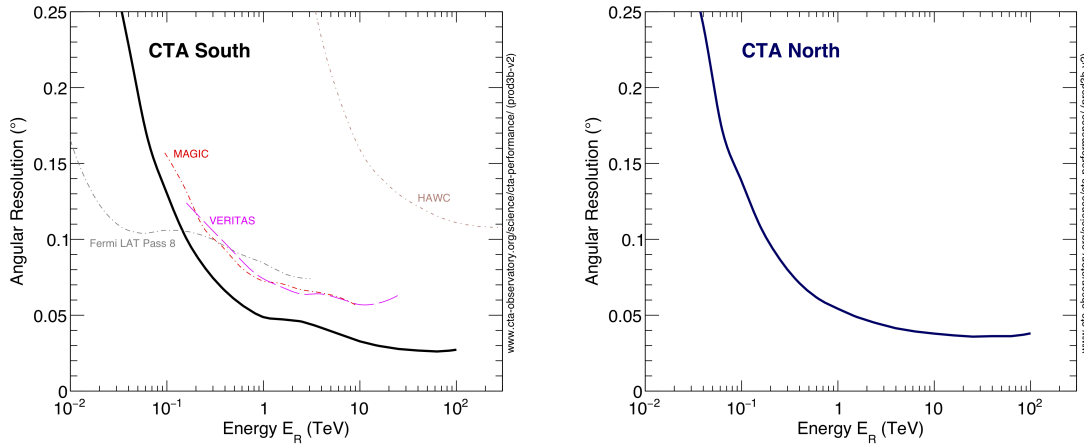


Figure 3.4: Angular resolution for CTA South compared to other experiments (left), and for CTA North (right) [152].

- **Energy resolution:** The energy resolution  $\Delta E/E$  is obtained from the distribution  $(E_{rec} - E_{true})/E_{true}$ , where  $E_{true}$  and  $E_{rec}$  are the true and reconstructed energies of  $\gamma$ -ray events. It is defined as the half-width of the interval around 0 which contains the 68% of the distribution. The energy resolution of CTA as a function of reconstructed energy is shown in figure 3.5. Note that for the range of 1-10 TeV the energy resolution is well below the required 10%.

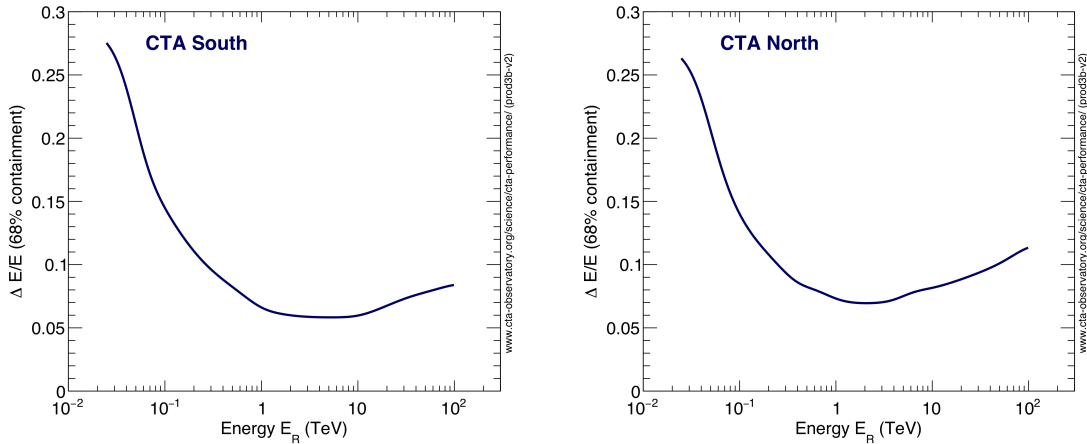


Figure 3.5: Energy resolution vs reconstructed energy for CTA South (left) and CTA North (right) [152].

- **Differential sensitivity:** The most important feature at evaluating the performance is the differential sensitivity, which indicates the minimum flux needed by CTA to detect a point-like source at  $5\sigma$  in 50 hours. The sensitivity is calculated in five energy bins per decade, where it is required that at least 10  $\gamma$ -rays are detected and the signal to background ratio is at least 1/20. The cuts in gammaness and source direction ( $\theta^2$ ) are optimized to improve this quantity. The differential sensitivity of CTA compared to that of other instruments for 50h observation time is shown in figure 3.6.

### 3.3 CTA Telescopes

While all telescopes share a basic design concept, they have particular features to accomplish the performance requirements for CTA. In general, subsystems of IACTs are divided in **structure**, **optics** and **camera**. In this section an overview of these subsystems and the particularities of each of the three types of CTA telescopes is given.

#### 3.3.1 Large Size Telescope (LST)

The LST has been designed to reach an effective energy threshold down to 20-30 GeV. This energy range has a particular interest because it covers the barely explored gap between the highest energies detected by satellite experiments, and the lowest by IACTs. The main science goals for LSTs are to observe high redshift Active Galaxy Nuclei (AGN), Gamma Ray Bursts (GRBs), pulsars and galactic transients. The first prototype for the LSTs (LST1) was installed in the CTA North site, in La Palma island, in 2018.

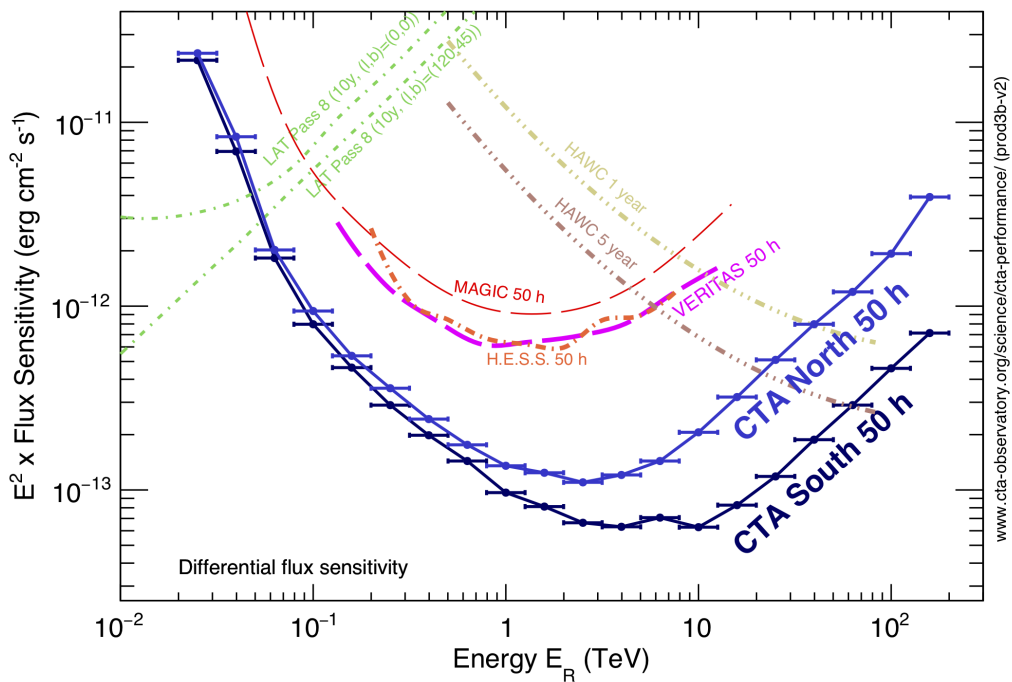


Figure 3.6: Differential sensitivity of CTA for 50 h observation compared to other  $\gamma$ -ray experiments, from [152].

A detailed description of LST subsystems can be found in [158], next sections offer a summary of each subsystem of the telescope, which consists of: the structure of the telescope, to support the optics, camera and driving system; the optics, composed by the 23 m diameter mirror which collects the Cherenkov light and focus it in the camera; and the camera, to record the photons coming from the showers.

### LST Structure

The structure of the telescope is divided in several parts: The azimuth system, the mirror support dish, the elevation system, the camera support structure and the drive system. All parts of the structure are specially designed to make the telescope lightweight ( $\sim 100$  tons), to ensure fast repositioning in the case of a transient alert (mainly GRBs), being able to re-position to any part of the sky within 20 seconds. The azimuth system allows the telescope to turn around its vertical axis. It consists in a circular rail of 24 m diameter where six wheeled bogies support the structure. The azimuth structure is a framed structure made of carbon fiber reinforced plastic (CFRP) and aluminum tubes. The mirror support dish is a double layer space frame made of CFRP tubes arranged in a tetrahedral structure, with a diameter of 23 m. The elevation system consists of a structure made in part of steel tubes, located in the backside of the dish, to help compensate the weight of the telescope and ensure the stiffness of the structure. The camera support structure, which holds the camera frame, consists on an arch with three curve sections on each arm, made of CFRP, and a total of 26 ropes to stiffen the structure. The drive system, designed to ensure a fast and precise repositioning, consist on 4 synchronous motors capable to supply a total mechanical power of 190 Kw to move the structure in azimuthal axis and elevation. The different parts of the structure are shown in figure 3.7.

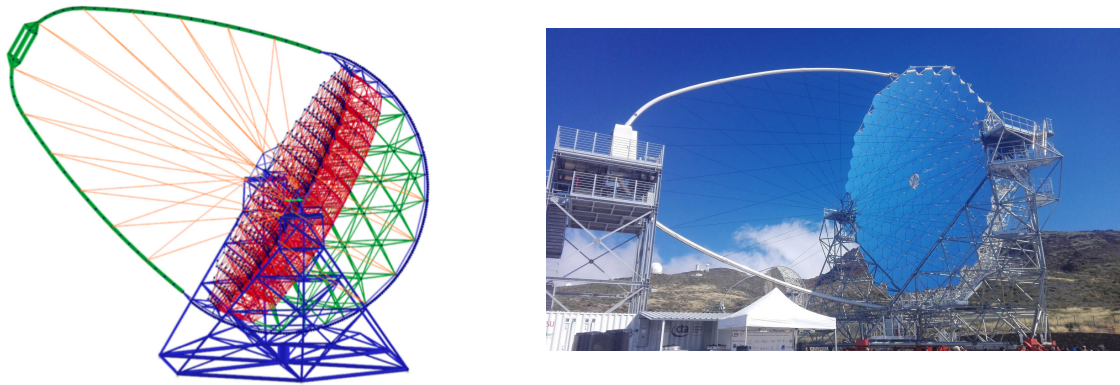


Figure 3.7: Left: Simplified diagram of the structures of LST without bogies, mirrors and camera. Azimuth substructure is blue color, the elevation system and the camera support structure are shown in green color and the mirror dish is red color, from [158]. Right: Photo of the first LST installed in CTA North site (Roque de los Muchachos Observatory, La Palma, Spain).

### LST Optics

The mirror of the telescope has a parabolic shape, to guarantee the isochronousity of the optics. It has 23 m diameter, 28 m focal length and it is segmented in 198 hexagonal facets. The mirrors are manufactured using the cold slump technique consisting in producing a sandwich of an aluminum honeycomb structure between two glass sheets [159]. Mirrors are fixed to the telescope structure by three knots, two of them mounted on actuators which allow to adjust each mirror panel in two directions. The *active mirror control* system controls these actuators in order to fine tune the focal distance and focusing, to account for the possible deformations and bending of the telescope structure. Each mirror segment is equipped with an infrared laser, and two more lasers are mounted in the center of the disk, which constantly point to the left and right of the camera. The directional offset of the mirror facets can be estimated by taking pictures of the reflected spots on a target in front of the camera with a high resolution IR CCD camera located in the center of the dish. The achievable positioning resolution can reach  $< 5\mu\text{m}$  [158].

### LST Camera

The camera focal plane instrumentation consists of 256 modules (sometimes also referred as clusters) with seven Photomultiplier Tubes (PMTs) each, making a total of 1855 pixels. The PMTs are mounted with a 50mm pitch, coupled to hexagonal light guides made of a reflective material (3M ESR), to collect all the light arriving to the camera. The PMT model is Hamamatsu R11920-100-20, specially developed to reach high quantum efficiency (42%) and low after pulse rates, which go below 0.02 % above 4 photoelectrons. Each module with seven photodetectors has one readout system based on the Domino Ring Sampler version 4 (DSR4). The signal from the PMTs is split in three branches: high and low gain ones, which are sampled at  $\mathcal{O}(\text{GS/s})$  in the DSR4 chips; and the trigger branch, which is feed into the Level 0 trigger asic [159]. A slow control board monitors the PMTs and controls the high voltage elevators. Analogue backplanes are dedicated to trigger distribution along modules and clock signal propagation. The mechanical structure of the camera consists of several parts, shown in figure 3.8. The modules are inserted in the load bearing structure from the front of the camera and connected to the backplane electronics on its rear part. The design of such modular structure guarantee an easy access to individual modules in case any repair is necessary, allowing to disconnect and extract one module without manipulating the rest of the camera. The load bearing structure is mounted inside the tubular structure which holds the camera external walls, doors and interfaces with the camera frame. In the front part of the camera there is the front window which can be totally covered by a shutter to avoid the entrance of sunlight during the day to maximize the life of the PMTs. In the back part of the camera lies all the cabling and auxiliary electronics. The total dimensions of the camera is  $2.9 \times 2.9 \times 1 \text{ m}^3$  and the weight is less than 2000 kg. Since all the electronics are stored inside the camera, the structure was required to accomplish a series of requirements related to the exposure to environmental conditions such as the protection to the entrance of

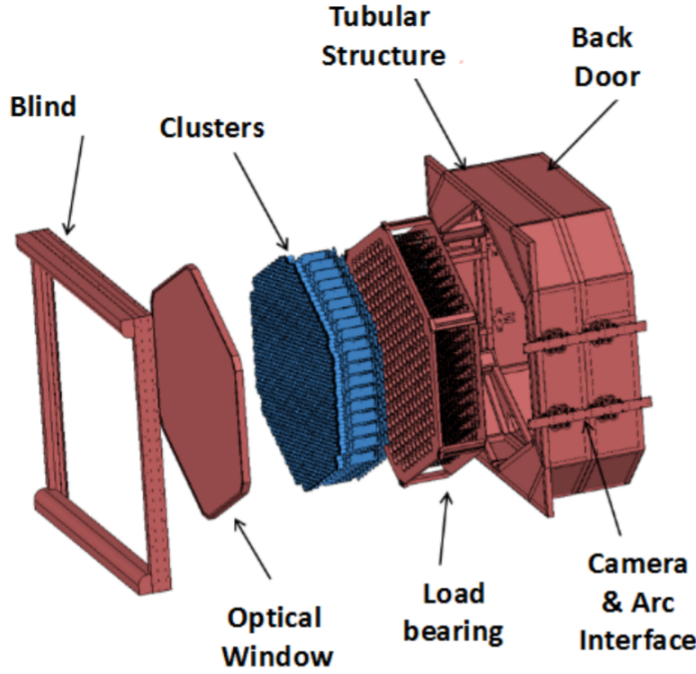


Figure 3.8: Different LST camera mechanical elements from [160].

dust, water and sunlight and guarantee a stable temperature between 20°C and 40°C [160]. Temperature regulation is possible thanks to the water cooling system, based on cold plates and a temperature controlled air flow cooling system.

An access tower allows to intervene in the camera during day-time operations when the telescope rests in park position, and also acts as an anchor in case of strong winds.

### 3.3.2 Medium Size Telescope (MST)

MSTs will cover the core energy range of CTA, from 100 GeV to  $\sim 10\text{TeV}$ . This is the usual range reached by current IACT generation so the improvements in sensitivity will come from the large area covered and the better image reconstruction due to the larger number of telescopes (15 in the north, 25 in the south). The MST 12 m diameter modified Davies-Cotton (DC) optical layout very similar to that of Very Energetic Radiation Imaging Telescope Array System (VERITAS) and High Energy Stereoscopic System (H.E.S.S.). The first prototype of this type, the Davies-Cotton MST (DC-MST) [161], was built in Adlershof, Germany. There are two different camera designs for DC-MST: *FlashCam* and *NectarCAM*, which characteristics will be discussed in this section. A detailed report of the status of the MSTs as of July 2019 can be found in [162]. A summary on the different parts of the telescopes is given in this section.

### MST Structure

The structure of the MST can be seen in figure 3.9. The main mechanical structure of the telescope is a cylindrical tower of 1.8 m diameter and 20 mm wall thickness. The tower is connected on top to the head of the telescope, that contains the azimuth bearing which allows the telescope to rotate in the horizontal axis, and the drive assemblies. It is possible to access to the tower through a door at the base. All electrical cabinets are stored and distributed over three floors of the tower. A combination of ventilation and air conditioning system is used to keep the temperature within the cabinets operation range. The drive assemblies are designed to reach any object above 30° in elevation in less than 90s. It is divided in the azimuth drive subassembly and two elevation drive subassemblies, mounted in the left and right of the telescope. To account for the possible sources of excitation, like wind gusts or structure flexibility, which can lead to oscillations of the structure, an active vibration damping control is used to reduce their effect on the pointing accuracy of the telescope. The dish structure is designed to host the mirrors and the camera support structure is attached to it [163].

### MST Optics

The optical system of the DC-MST consists on a mirror segmented in 86 hexagonal facets of 1.2m length, providing an effective mirror area  $> 88 \text{ m}^2$ . The focal length of the telescope is 16 m. Different mirror technologies are being tested, all based in cold slumping technique, with different layers of materials, coatings and structures. A system of actuators forms the Active Mirror Control (AMC) system of the MST allowing to adjust the mirror position for focusing. The structure is stiff enough to make unnecessary to readjust during observations to maintain the Point Spread Function (PSF). The AMC is used only for the initial mirror adjustment and for maintenance activities, or adjust the focal distance for specific observations.

### MST Cameras

Two camera prototypes have been designed and tested in the structure installed in Adlershof and showers have been detected, as shown in picture 3.10. The first design named FlashCam have 1764 PMT-based pixels divided in 147 modules of 12 pixels each. It implements a fully-digital trigger and readout system operating at 250 MS/s which allows to define flexible trigger patterns relying on the digitized PMT signals. The readout system is designed for a dead-time-free operation with trigger rates up to 30 kHz. FlashCam uses only one gain channel, reducing the required bandwidth for data transfer. The second camera design named NectarCAM counts with 1855 pixels, divided in 256 groups of 7 modules. The camera mechanics and many auxiliary systems have been designed to be equivalent to the LST camera. The signal digitizing of NectarCAM relies on a dedicated Nectar ASIC which digitizes the PMT signals at sampling speeds of around 1 GHz. It implements a digital trigger based on the binary outputs of individual pixels after comparing their analog signals with a threshold (Level 0 trigger).

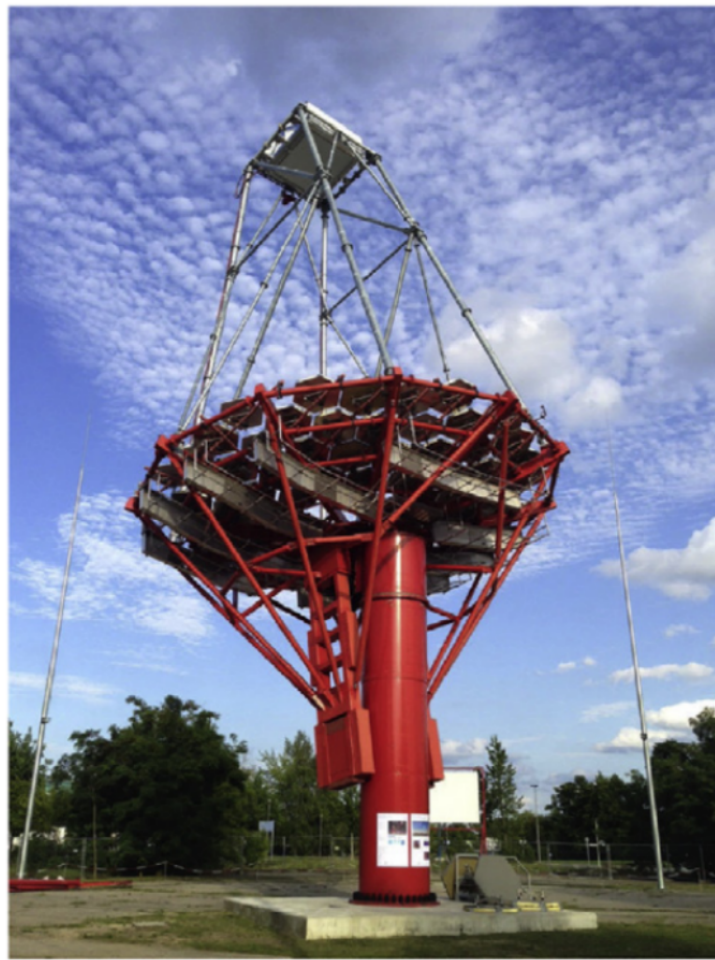


Figure 3.9: DC-MST prototype with FlashCam in Adlershof, from [164].

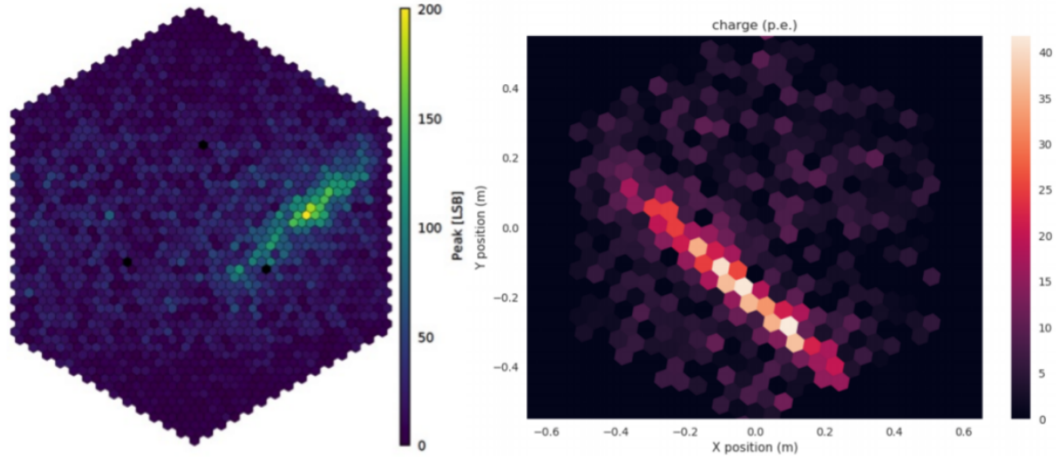


Figure 3.10: Left: DC-MST Showers obtained with FlashCam(*left*), Nectar-CAM(*middle*) and Schwarzschild-Couder MST (SC-MST) camera (*right*) prototypes, from [162].

### 3.3.3 Small Size Telescope (SST)

The smaller telescopes, SSTs, will be the more numerous in the CTA layout, with more than 70 telescopes in the southern site. These telescopes are dedicated to detect the highest energy  $\gamma$ -rays which in the majority of cases will come from the galactic plane. They need to be spread over a very large area, to catch as many  $\gamma$ -ray showers as possible, but they do not need large mirrors because VHE radiation produces a huge amount of Cherenkov light. They are designed to reach their peak sensitivity at energies greater than 10 TeV.

#### SST Structure

The optical design of SSTs is based on a Schwarzschild-Couder (SC) double mirror configuration. A column raises from the base of the telescope and interfaces at the top with the azimuth fork. The fork sustains the elevation assembly, which is composed by the mirror dish, the counterweight and the structure that sustains the two mirrors. The dish is designed to hold the segments of the primary mirrors, which can be individually controlled by actuators. A quadrupod is attached to the dish, which together with a central pole, are joint to the structure that supports the secondary mirror and also serves to counteract deformations due to gravity and wind. The structure for the monolithic secondary mirror accounts for three actuators and three lateral arms which support the transverse components of the mirror's weight. The drive of the azimuth is located at the base of the column. A scheme of the structure can be found in picture 3.11. A detailed description of the SST structure design can be found in [165].

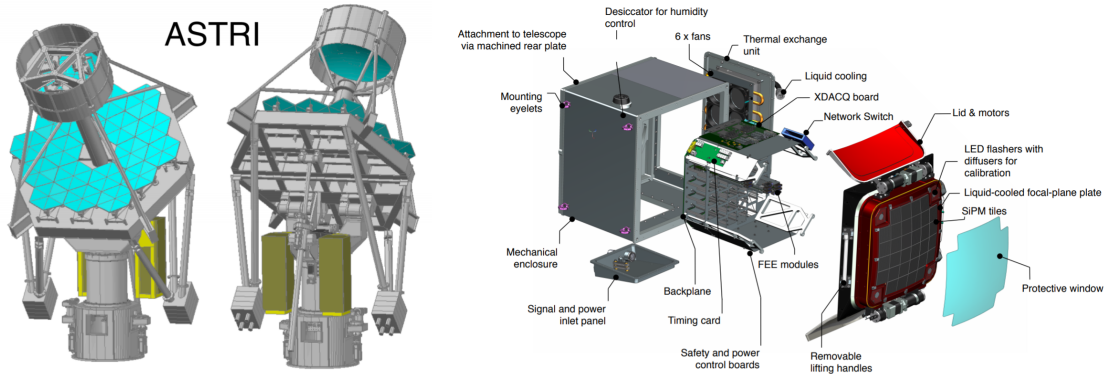


Figure 3.11: *Left:* General view of the SST structure and electromechanical subsystems, adapted from [165]. *Right:* CAD model of the Compact High-Energy Camera (CHEC) camera from [166]

### SST Optics

The SC design of the SSTs is composed by two mirrors, one primary of 4.3 m diameter segmented in hexagonal tiles, and a monolithic secondary mirror of 1.8 m. The primary mirror tiles have been manufactured using a cold slumping replication process. The secondary is made of a hemispherical thick glass shell thermally bent to 2.2 m radius of curvature. The focal length of the system is 2.15 m, f/0.5 and the field of view (FoV) reaches 10°.

The advantages of a double mirror configuration are a better PSF over a large FoV and better correction of aberrations [167] than for single mirrors.

### SST Camera

The camera is composed by 2048 pixels made of Silicon Photomultiplier (SiPM), instrumented in 32 modules which comprise 64 pixels of  $\sim 6 \times 6 \text{ mm}^2$ . The digitalization of the waveform is performed by Front-end electronics (FEE) based on TARGET ASICs [168] which also give the first trigger level, as the sum of four neighbouring pixels. A backplane provides the power, clock, trigger and data interface of the FEE. The trigger decision is formed in the backplane by combining trigger signals from all the FEE modules. In the camera structure, a lid protects the camera from the environment and a cooling system based on the circulation of chilled liquid through the camera focal plane plate and six internal fans, maintains a stable temperature. A diagram of the camera is shown in figure 3.11. A detailed description of the camera and results from its commissioning phase can be found in [166].

## 3.4 Reconstruction and Analysis tools

The best performance results from CTA with respect to the current generation IACTs will come not only from the telescopes designs, but it is also very important to have solid software tools, accessible and user friendly, which will allow to analyze the

forthcoming data. Also, especially during the initial phases of the development of the facility, to calculate the predicted sensitivity shown in section 3.2 it is necessary to produce precise and reliable simulations of the instrument response to the arrival of electromagnetic showers. In this section, the main software tools for the simulation and analysis of the different levels of CTA data are described.

### 3.4.1 Monte Carlo simulations

Monte Carlo (MC) simulations are of great importance for the IACT technique, where the detection of  $\gamma$ -rays is indirect and it is necessary to reconstruct the primary parameters from the signal received at the telescopes. Detailed simulations of the development of the Extensive Air Showers (EAS) in the atmosphere, combined with simulations of the instrument response to the Cherenkov light produced by those EAS are used for two main purposes: Separation of  $\gamma$  and hadron showers and reconstruction of the shower direction and energy of the primary. For the former, since hadrons produce the majority of Cherenkov light which reach IACTs, it is necessary to characterize the particular differences between photon and hadron induced showers thanks to the MC simulations. For the latter, comparing the shower parameters to those of the simulated showers, and applying different reconstruction methods, like Multi-variate analysis (MVA), Machine Learning (ML) or Deep Learning (DL) among others, the characteristics of the primary particles can be reconstructed.

MC simulations consist of two phases: The first is the simulation of the EAS development in the atmosphere, tracking the particles created, the products of their interaction and the amount of Cherenkov light produced. The second part consists on simulating the instruments, taking into account ray tracing, the optical features of the mirrors, the response of the electronics, etc.

For CTA, MC simulations have been performed using the programs **C**Osmic **R**ay **S**Imulations for **K**Ascade (CORSIKA), for the EAS simulation, and `sim_telarray`, for the telescopes response. These two software packages allow to configure a specific array of telescopes with their particular features and store only the information of the particles and light from the showers that fall in the surrounding of the telescopes. The current production of MC data, with the layout described in section 3.2, is the named *prod3b-v2* which used CORSIKA version 6.9. In the next subsections, a brief description of CORSIKA and `sim_telarray` is given.

#### CORSIKA

CORSIKA is a detailed MC program to study the development of EAS in the atmosphere [169], originally developed for the Kascade experiment [170]. The showers can be initiated by different kinds of primary particles, such as photons, protons or other heavier nuclei. The program treats every possible process taking place in the development of EAS to the present state of our knowledge. It takes into account the transport of particles through the atmosphere and their interactions with air molecules. The secondary particles produced are tracked along their trajectories and their parameters are stored when they reach an observation level, i.e. the stage of the

shower that can be detected by an instrument. The main problem of the simulation of EAS is the extrapolation of hadronic interactions at the higher energies which cannot be probed in collision experiments. The secondary particles emitted in the extreme forward direction, which are not accessible by colliders, are precisely the more important in EAS development because they are the one bringing the largest energy fraction to the atmosphere. The extrapolations must therefore rely on different theoretical models. To study the systematics of such models, in CORSIKA there are five different hadronic interaction models available. For CTA prod3b-v2 the model used was QGSJET-II [171]. An example of three different showers simulated with CORSIKA is shown in picture 3.12.

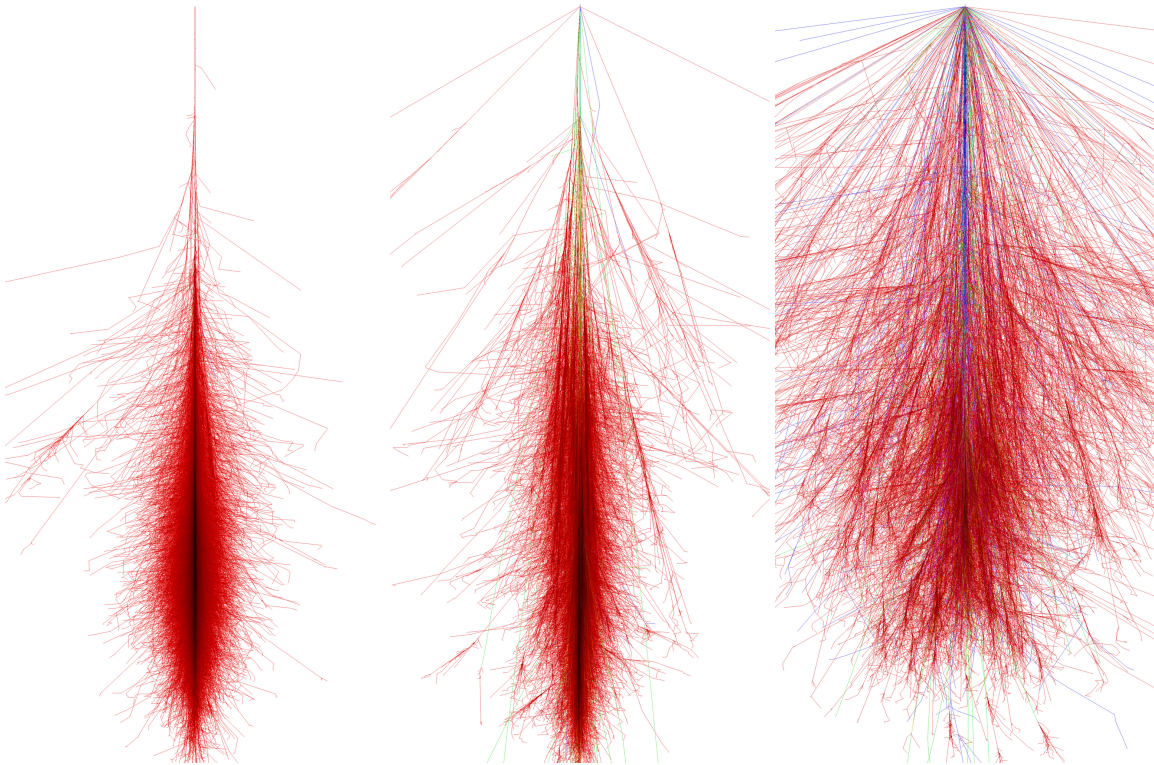


Figure 3.12: Photon (left), proton (center) and iron (right) produced showers for a primary energy of 1 TeV and 0° zenith angle, simulated with CORSIKA from [172].

### **sim\_telarray**

The second part of MC simulations is carried out by the program sim\_telarray [173], dedicated to the simulations of the detectors: Optical ray-tracing of photons, their registration by PMTs, the behaviour of discriminators or comparators for trigger at pixel and telescope levels, and the digitalization of resulting signals. It was originally created for the High Energy Gamma Ray Astronomy (HEGRA) IACT system, and has been improved and made fully configurable to be used with any kind of IACT layouts.

Data level	Description
R0	Raw data from camera, or MC data
R1	Calibrated data
DL0	Data Volume Reduced Data
DL1	Calibrated image with Hillas parameters
DL2	Reconstructed shower parameters (Energy, direction and $\gamma$ -hadron separation)
DL3	Reduced data, sets of gamma-like events with associated Instrument Response Function needed for science analysis
DL4	High level binned data products, like spectra, skymaps or light curves.
DL5	Legacy observatory data, like survey sky maps or source catalog.

Table 3.2: The different CTA data levels, based on [174] and [175]

The simulation of ray-tracing follows the trajectory of photons since they reach the mirrors of the telescopes and arrive to the camera pixels. The mirror optics are simulated taking into account the configured mirror morphologies, dish shapes and segmentation. The shadowing of the camera structure can be also included in the simulation. The final step of ray-tracing simulation is the angular acceptance of the pixels, which usually are equipped with Winston cones (lightguides) to avoid gaps between neighbouring pixels. From ray-tracing simulations, the PSF of the telescopes can be calculated and hence can be used to optimize their designs. In the simulation of the photon detection by the PMTs, the fluctuations in quantum efficiency in each pixel are taken into account. As pixels are permanently exposed to Night Sky Background (NSB), the number of photons arriving to each pixel is fully configurable assuming a specific NSB spectrum. In the final simulation, the amplitude of the NSB signal is subtracted from the signal baseline. The afterpulsing produced by ions is also taken into account, which is produced by ions hitting the photo-cathode, and can produce pulses of large amplitude which enter in the readout window of the front-end electronics of the cameras. The trigger system simulation takes into account the switching behaviour of discriminators or comparators, which can be configured to a specific logic (next-neighbour, pixel sectors...). The result from the pixel trigger system serves as input for the stereo level trigger, which usually requires that at least two telescopes trigger within a short time window. The final output of the sim\_telarray simulation is a data container in a format as closest as possible as the real data format from the actual instruments, based on the *eventio* machine-independent format.

### 3.4.2 Low level analysis: `ctapipe`

The analysis of CTA data, both real and simulated, goes through different steps before turning into a format with which real science can be done. A description of the different CTA data levels is given in table 3.2.

*Ctapipe* [174] is a framework for prototyping the low-level data processing algo-

rithms for CTA. It is written in Python and its currently in development, still suffering large and rapid changes to structure and functionality. While is not yet the final code for CTA analysis, and other alternatives are currently on development, *ctapipe* is the framework chosen for the low level data analysis carried on in this thesis and so it is the one that will be described in this section.

The goal of *ctapipe* is to reduce R0 data, that is raw data directly out of telescope cameras or MC simulated data out from `sim_telarray`, to DL2 data containing the reconstructed shower parameters.

Raw data can be read with *ctapipe* thanks to specific *EventSource* classes, which depend on the type of the input file (simulated data, real data from each specific telescope, etc.). It is possible to loop over the events of the source container to perform different operations on them. The first part of the data analysis is typically the calibration of the signal, requiring the treatment of the waveform signal in each pixel. *Ctapipe* allows to perform the integration of the signal from the registered waveform using different types of integrators (*LocalPeakWindowSum*, *FullWaveformSum...*) to calculate the total number of counts in the pixel and transform it to number of photoelectrons. The result is a camera image, where pixels contain the light from the shower and from background. Different cleaning methods, like to two-level tailcuts cleaning, can be applied to subtract the background light and get the shower image. Afterwards, the Hillas parameters can be calculated. Other function allows to compute a linear fit to the extracted charge arrival times projected along the longitudinal axis of the Hillas ellipse, to extract the timing parameters. All these shower parameters are stored in the DL1 format, with the possibility to lose pixel-wise information and reduce the size of data files. For the reconstruction of the primary parameters, that is the energy, direction and particle type, there are currently two different algorithms implemented: A moment-based stereo reconstruction, which combines the Hillas parameters of different triggered telescopes geometrically to estimate the shower direction; and a template-based stereo reconstruction, which uses a fit of the full camera image to an expected image model to find the best fit shower axis, energy and depth of maximum. Other methods using machine learning and deep learning techniques are also being explored but are not yet implemented in the main source code of *ctapipe*.

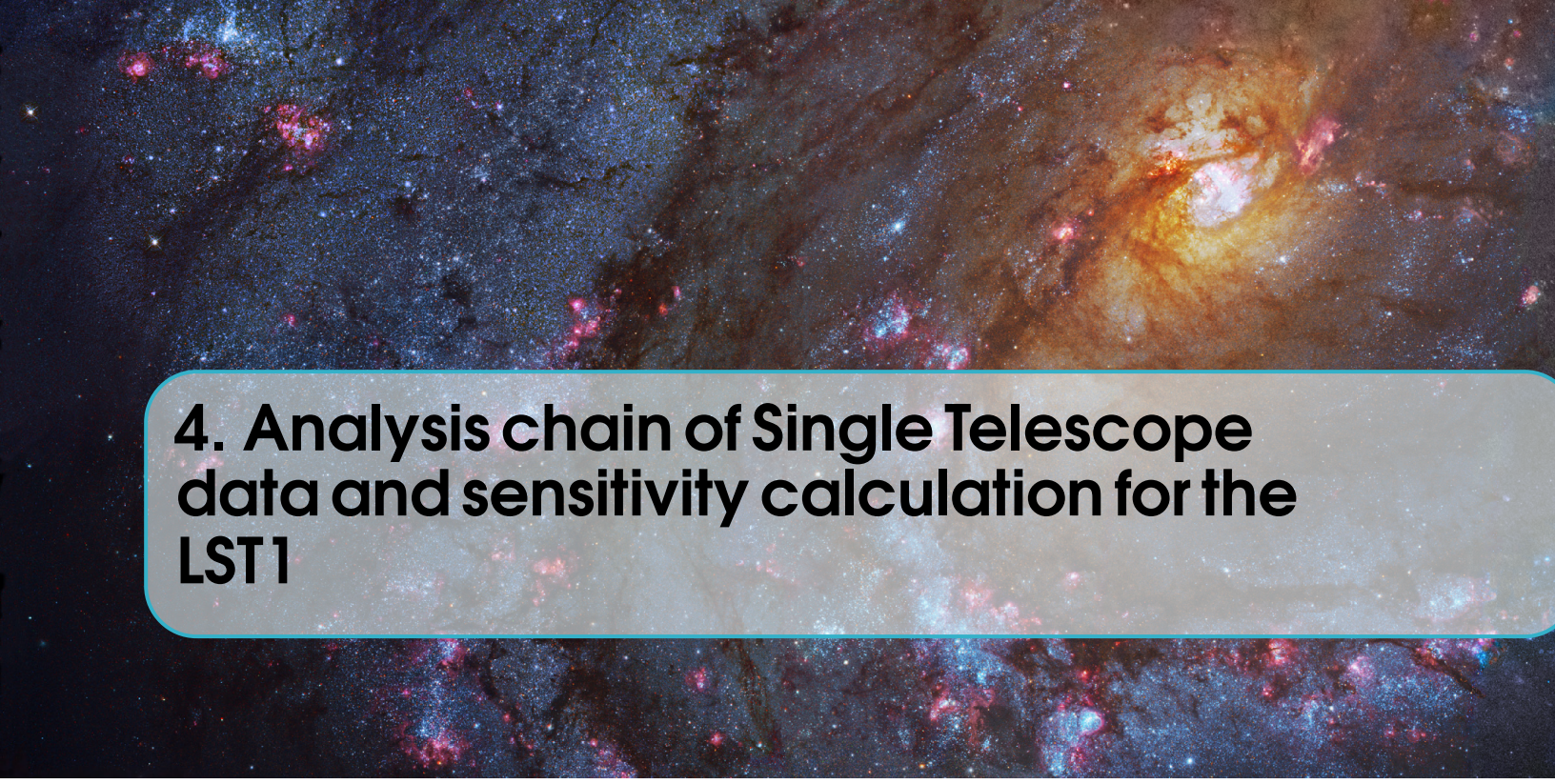
### **3.4.3 Science analysis: *ctools***

One of the proposed software packages for the scientific analysis of CTA data is *ctools*, based on *GammaLib* [176], a versatile toolbox for the scientific analysis of astronomical  $\gamma$ -ray data. It comprises a set of tools and python scripts with a command-line interface which allows interactive data analysis. It is possible also to create scripts and pipelines within Python using *ctools* functionalities. The data managed by *ctools* is at the level of DL3 and beyond, treating with observation events, skymaps, spectra and so on. For the analysis of observation events, *ctools* includes the possibility of doing a binned (separating the data in energy bins) or unbinned analysis, and also it can stack the data of several observations to be analyzed together. A likelihood fitting can be

performed to fit data to a given emission model, retrieving the best fit parameters of spectral, spatial and time components of the model of each emission source. Besides, *ctools* allow to perform simulations of observations, using a set of precomputed IRFs, to be used as *mock data* for the calculations of prospects of the future performance of CTA. Some of the most important tools of *ctools* that has been used in this thesis are:

- *ctobssim*: This tool produces simulations of event lists using the instrument characteristics specified by a given IRF and an input model. The model is composed of the individual models of each  $\gamma$ -ray source in the target FoV. Each model has a spatial component, given by the geometry of the source (point source, disk, gaussian, spatial map...), a spectral model describing the flux (it can be specific functions like power law or log parabola, or an user made spectrum where the flux per each energy is given in a file), and a time model, describing the variability of the source with time. The model also should include an instrumental background model to simulate background events, which are misclassified proton events. As input, *ctobssim* requires a pointing direction, radius of the simulation region, time interval, energy interval, an IRF and an input model. The result is an event list in fits format, which contains all the information of the observation in the header.
- *ctbin*: This tool creates a counts cube, with a certain number of energy bins, and fills it with events from an event list. It is possible to stack events from different observations in the same counts cube. The resulting cube can be used in further steps of the analysis, like the likelihood fitting.
- *ctlike*: Performs a maximum likelihood fitting of a model to binned or unbinned data. As input, it can take event lists or a count cube, and depending on the input it will perform a binned or unbinned likelihood fit. A joint likelihood fitting can be done for multiple observations, and the average response functions (exposure, PSF and background) can be precomputed using the tools *ctexpcube*, *ctpsfcube* and *ctbkgcube*. It is also possible to calculate the Test Statistics (TS) (which is a measure of the source significance) of a source. More details on the likelihood fitting with *ctools* will be given in chapter 5.
- *ctmodel*: This tool generates 3-D model cube which provides the number of predicted number of counts for an input model as a function of spatial coordinates and energy. As an input, it will require a counts cube, an event list or an observation definition file and it will need the definition parameters of the cube, such as sky coordinates, projection, energy binning, number of pixels and pixel scale.
- *ctulimit*: Computes the upper flux limit for a specific source model. Starting from the maximum likelihood parameters, the tool will look for the flux that produces a decrease in the likelihood which corresponds to a given confidence level. By default, it is set at 95% confidence level, but it can be configured. The result is the differential flux upper limit for a specified reference energy and the integrated flux in a certain energy range.





## 4. Analysis chain of Single Telescope data and sensitivity calculation for the LST1

### 4.1 Introduction

The first Large Size Telescope (LST) was inaugurated in October 2018 and is currently in commissioning phase. It is the first Cherenkov Telescope Array (CTA) telescope installed on site (in La Palma island), and it is expected to be operating on its own until LST 2-4 are built. This mean that LST1 needs its own analysis chain in monoscopic mode, which differs in several aspects from the stereoscopic analysis included in the benchmark analysis tools of CTA (see section 3.4.2). Although single telescope observations present a big challenge, especially regarding source position reconstruction and  $\gamma$ -hadron separation, it is expected that LST1 performance, thanks to its mirror size and camera design, will be competitive enough to offer scientific results in the time it will be operating alone.

This chapter will present a considerable amount of the work done during this thesis, which includes the development of the code for the single telescope analysis for LST1, the calculation of LST1 sensitivity based on Monte Carlo (MC) simulations, the development of a new technique for Hillas Parameters calculation without cleaning the shower images by using the Expectation-Maximization algorithm and the application of the analysis chain to real LST1 data.

### 4.2 The LST1 analysis chain overview

The software for the single telescope analysis of LST1, named *cta-lstchain*, has been developed due to the necessity of specific tools for single telescope analysis, which are not included in *ctapipe*. It has been written as a python package which relies heavily on *ctapipe*, and it is structured in several modules containing functions destined to the different parts of the analysis. The first version of *cta-lstchain* was written by the

author of this thesis and many contributors have joined the project over the last two years to improve and optimize the repository to its current version, which is able to perform every analysis step both for simulated MC data and real data. The analysis chain is divided in several steps, each of which can be executed through a python script which requires certain inputs and calls for the appropriate functions. All the configuration parameters of the different elements of the analysis are given through configuration files, which can be edited by the user. The input of the analysis chain are the raw data files of LST1 events, which for MC data are the output files from *sim\_telarray* (see section 3.4.1), and for real data are *zfits* files with a similar internal format. The files contain the full information available per pixel, known as *waveform* and which is the digitized signal amplitude vs. time for every triggered event, together with MC information in the case of a simulated file (such as the true energy, source position, number of simulated events, and so on), or recorded information from the different telescope subsystems in the case of real data (such as time, pointing, trigger type...). Throughout the analysis chain, the data including the images and image parameters, is stored in containers designed in *cta-lstchain* specifically for LST1, which can be dumped into *pandas* dataframes and saved in *hdf5* files.

The main steps of the analysis chain can be summarized as:

- **Calibration:** The waveforms of each pixel in the camera should be integrated after pedestal subtraction, and converted to number of photoelectrons. Also, the timing information of the signal is obtained.
- **Image cleaning and parameterization:** The images in the camera contain pixels with signal not related to the Cherenkov event, so a cleaning must be applied to remove them. Afterwards, the distribution of photons in the image is used to calculate the Hillas parameters.
- **Energy and direction reconstruction:** The energy and direction reconstruction of the triggered events are performed using a multidimensional regression technique based on Random Forests (RFs). A set of simulated diffuse  $\gamma$  events are used to train the RF.
- **$\gamma$ -hadron separation:** For the  $\gamma$ -hadron separation, a multidimensional RF classifier is used. Sets of simulated  $\gamma$  and proton events, which energies and directions have been reconstructed in the previous step, are used to train the classifier.

### 4.2.1 Calibration

In the calibration phase, the raw signal known as *waveform*, is integrated after background subtraction, to obtain a total number of counts per pixel, which afterwards is multiplied by a factor to be converted in number of photoelectrons. Depending on if MC data or real data is being analyzed the next steps vary and will be explained for each case.

### Signal extraction

For every triggered event, the signal in each pixel is recorded in a window of 40 samples from the 4096 samples of the Domino Ring Sampler version 4 (DSR4). This signal contains information not only from the Cherenkov light, but also from background light from Night Sky Background (NSB) and from the intrinsic noise induced by the readout chain. Before integrating the signal, it is necessary to subtract this baseline signal, known as *pedestal*. For simulated MC events the pedestal value for each pixel in the camera is already stored, but for real data it is necessary to take special runs, with randomly activated trigger, to obtain the values of the pedestal. In *cta-lstchain* a specific script is used to extract the pedestal values from pedestal runs and they are stored in a *hdf5* file to be used later in the calibration.

Once the pedestal is subtracted from the signal, the signal peak can be integrated. Typically, a smaller window of a few samples around the maximum is used for the integration, which can be performed with one of the several integrators implemented in *ctapipe*. By default, the integrator used in *cta-lstchain* is the *NeighborPeakWindowSum*, which sums the signal in a window around the peak defined by the waveform in neighbouring pixels. This avoids integrating noise around the peak. The default width of the integration window for this integrator is of 7 samples, but it can be configured by the user. These calibration steps are performed for the two gain channels of LST1 camera.

### Conversion to photoelectrons

Once the signal amplitude is extracted, it must be converted from Analog to Digital Converter (ADC) counts to photoelectrons through a calibration factor, which is different for each pixel and channel. For simulated MC data, these factors are stored in the simulated file and the conversion can be done simply by multiplying the image in ADC counts by the factor of each pixel. For real data, special calibration runs must be taken to calculate these factors. Calibration events are taken using Ultraviolet light pulses fired from the CaliBox [177], [178] located in the mirror dish. The calibration coefficients are obtained using the F-factor method [179], which assumes that the distribution of photoelectrons in a Photomultiplier Tube (PMT) follows a poissonian statistics with a mean  $N$  and a root mean square (RMS)  $\sqrt{N}$ . The signal distribution, however, will deviate from poissonian statistics due to an excess-noise factor  $F$ , which is different for each PMT and is measured in the laboratory. The relation between the relative widths of the two distributions can be written as:

$$F \cdot \frac{1}{\sqrt{N}} = \frac{\sigma_Q}{\langle Q \rangle} \quad (4.1)$$

Where  $\langle Q \rangle$  is the mean value of the pixel signal and  $\sigma_Q$  its RMS. The calibration coefficients will come from the relation between the number of photoelectrons  $N$  and the mean pixel signal  $\langle Q \rangle$ . From 4.1, and taking into account that the signal must be corrected from pedestal, the relation between number of photoelectrons  $N$  and the

pixel charge  $\langle Q \rangle$  is:

$$\frac{N}{\langle Q \rangle} = F^2 \frac{\langle Q \rangle - \langle ped \rangle}{\sigma_Q^2 - \sigma_{ped}^2} \quad (4.2)$$

The values of  $\langle Q \rangle$ ,  $\sigma_Q$ ,  $\langle ped \rangle$  and  $\sigma_{ped}$  are calculated from a sufficiently large number ( $\sim 1000$ ) of calibration and pedestal events, using a specific script from *cta-lstchain*, which stores the resulting calibration coefficients in an *hdf5* file to be used later in the calibration of data runs. For the LST1, the value of F factor used is the mean value for all PMT which is 1.2.

#### **4.2.2 Image cleaning and parameterization**

In order to extract information from the image of Cherenkov light recorded by the camera, it is necessary to get rid of the background light not belonging to the shower, which has arrived to all pixels. This background light is usually related to fluctuations in the NSB. A process named cleaning is used to eliminate all pixels which presumably do not contain light from the shower. The *clean* image is used later to perform the Hillas parameterization. Besides there exist several proposed cleaning algorithms in the literature [180], [181], [182], [183], for the time being in *cta-lstchain*, a classical two-level tailcuts cleaning is being applied (like the one used in [184]). This method requires only the information of the amount of light in pixels (already converted to number of photoelectrons) and compares it to two levels of thresholds in the following way:

- Pixels with a number of photoelectrons over the highest threshold level  $Th_{high}$  are selected.
- If pixels selected in the previous step have at least one neighbour also above the highest level threshold, those pixels are marked as core pixels from the shower.
- Neighbours of the core pixels with number of photoelectrons above the lower level threshold  $Th_{low}$  are selected as boundary pixels. The charge of not selected pixels is set to zero.

The standard values for the two levels used in *cta-lstchain* are  $Th_{high} = 6$  phe and  $Th_{low} = 3$  phe. Note that these values have not been yet fully optimized for the particular case of the LST1, and they can be changed easily in the configuration files. An optimization of the cleaning can lead to a better performance, especially for those small Cherenkov showers where information is lost because of the cleaning. Using other information apart from the number of photoelectrons, like the arrival times of the signals to pixels, can help to improve the image parameterization. Low energy showers of  $\gamma$ s and hadrons are much more difficult to differentiate, for that reason, an image parameterization which highly depends on the settings of the cleaning parameters can be problematic when trying to lower the energy threshold of the telescope. In section 4.4 a method for image parameterization not requiring previous cleaning is

proposed as an alternative.

The Hillas parameterization of the shower image after cleaning (see section 2.4.2 and figure 2.9), is performed by a specific function from *ctapipe*. The resulting parameters: intensity (total number of photoelectrons in the shower), width, length, coordinates of ellipse center of gravity, azimuthal angle  $\phi$ , the orientation angle  $\psi$ , and the third order moments: *skewness*, which is a measure of the asymmetry of the distribution; and *kurtosis*, which is a measure of whether the distribution is peaked or flat relative to a normal distribution. The calculation of the Hillas parameters with *ctapipe* only requires the image of the shower (i.e. the number of photoelectrons in each pixel) and the information of the camera geometry.

The time parameters, *time gradient* and *intercept* are also calculated as explained in section 3.4.2. These two parameters are especially important for single telescope analysis, because they reflect the direction of development of the shower, which give information of the side of the ellipse where the source position is located in the camera frame.

Other parameters are the *leakage2*, which indicates the percentage of the shower that falls in the two outer pixel rings of the camera. A large leakage indicates that the shower is highly truncated. The *number of islands* is also calculated, which accounts for the number of separated groups of pixels in the image. A typical  $\gamma$ -ray shower will only have one island with elliptical form, but hadronic and heavier nuclei showers tend to produce messy light distributions with several islands of irregular shapes.

The calibration and image parameterization is performed in *cta-lstchain* using the scripts *lstchain\_data\_r0\_to\_dl1.py*, *lstchain\_mc\_r0\_to\_dl1.py*, for real raw data or simulated one respectively. As is reflected in the script names, this steps reduces the data level from raw R0 data to DL1 (see table 3.2). In general, the image parameters describe the shower and therefore pixel wise information is not needed in further steps of the analysis. However, for testing and crosscheck purposes, *cta-lstchain* scripts offer the possibility to store DL1 data with the full images.

### 4.2.3 Reconstruction of energy and source position

After the calibration and image parameterization, the image parameters should be used to extract information of the primary particle type, whereas is a  $\gamma$ -ray or a background event (protons, electrons, heavier nuclei...). In *cta-lstchain* the first step is to reconstruct the energy and arrival direction of the event.

The direction reconstruction is problematic in single telescope mode, because even knowing that the Hillas ellipse should point towards the source position in the camera frame, we do not know in which side of the ellipse is located (this is known as head-tail degeneracy). In stereo mode, this is solved because the source position will be in the cross point between the line which follows the semi major axis of Hillas ellipses of all cameras, but for single telescope we must rely in other methods. In the case of *cta-lstchain* we make use of an observable known as *disp*. This is the vector going from the center of gravity of the ellipse to the source position.

Originally, the disp quantity could be parameterized in terms of the elongation of the image, that is the ratio between *width* and *length*. The first parameterization was proposed by the Whipple collaboration [185]:

$$Disp = \xi \cdot \left(1 - \frac{\text{width}}{\text{length}}\right) \quad (4.3)$$

Where  $\xi$  is a factor dependent on the amount of photoelectrons in the shower image (the *intensity* parameter). A more general parameterization was used for MAGIC-I [186]:

$$Disp = A(\text{intensity}) + B(\text{intensity}) \cdot \frac{\text{width}}{\text{length} + \rho(\text{intensity}) \cdot \text{leakage}} \quad (4.4)$$

Where A, B and  $\rho$  are second order polynomial function parameters of  $\log(\text{intensity})$ .

Instead of using a parameterization, in *cta-lstchain* the disp vector is directly reconstructed using the image parameters. The time parameters will be very important to reconstruct this quantity, because the Cherenkov light from the upper parts of the shower arrive before the light from later developed lower parts, giving rise to a the time gradient of the signal in the shower image. The time gradient will therefore give information on which side of the ellipse is pointing to the source position.

The method used in *cta-lstchain* for the reconstruction of these quantities, energy and disp vector, is based on a multidimensional regression technique relying on RFs. RF is a supervised learning algorithm which uses an ensemble of several decision trees ([187], or see appendix E). In the basic analysis of *cta-lstchain*, the one carried on in this thesis, a source independent approach is used, where it is not assumed what is the true position of the source. For that reason, the RFs for energy and disp reconstruction are trained using a set of MC simulated  $\gamma$  events triggering the LST1, with diffuse arrival directions distributed in a  $5^\circ$  radius field of view (FoV). The simulated data is divided in two sets, one for training and another for testing. The features used for the splitting of the tree nodes are  $\log_{10}(\text{intensity})$ , *width*, *length*, *x*, *y*, *psi*, *phi*, *width/length*, *skewness*, *kurtosis*, *r*, *time gradient*, *intercept*, *leakage* and *number of islands*, where *x*, *y* and *r* are the coordinates and module of the vector from center of gravity of the Hillas ellipse to the center of the camera. These quantities can be ordered based on their importance for the regression, as shown in figure 4.1, which is calculated based on the *Gini* index (see section ??). It can be seen for example that for direction reconstruction there are two features, time gradient and angle  $\psi$ , which are the best candidates to make a good splitting, while for  $\gamma$ -hadron separation all features supply with a similar amount of information. The trained RFs are used later to reconstruct the desired values (energy and disp) in the test data. For energy reconstruction, the reconstructed quantity is actually  $\log_{10}(E)$ . In the case of the disp

Parameter name	Value for regression	Value for classification	Description
n_estimators	150	100	Number of trees in the forest
criterion	mse	gini	Function to measure the quality of a split
max_depth	50	100	Maximum depth of the tree
min_samples_split	2	2	Minimum number of samples required to split an internal node
min_samples_leaf	2	2	Minimum number of samples to be at a leaf node
max_features	all	all	Number of features to consider when looking for the best split
random_state	42	42	Control the randomness of the bootstrapping and the sampling of features
n_jobs	4	4	Number of jobs to run in parallel

Table 4.1: Some parameters that can be configured for *RandomForestRegressor* and *RandomForestClassifier* classes, with the default values used in *cta-lstchain*.

vector, the two components of the vector (*disp\_dx*, *disp\_dy*) are reconstructed using the same RF.

For the implementation of the RFs, the Python package *scikit-learn* [188] is used, a machine learning package which offers a large amount of tools for predictive data analysis. The class *RandomForestRegressor* allow an easy training of the RFs, which can be saved to be used later to fit any set of test data with the same format as the training set. This class has a set of parameters that can be modified by the user to optimize the performance of the predictions. In *cta-lstchain* these parameters can be modified by a configuration file. The most relevant parameters and their default values in *cta-lstchain* are shown in table 4.1.

#### 4.2.4 $\gamma$ -hadron separation

The primary particle of the majority of Cherenkov showers produced in the atmosphere is actually not  $\gamma$ -ray but cosmic hadrons. These events trigger the telescopes  $\sim 10^4$  times more than  $\gamma$ -rays, therefore it is necessary a very efficient background rejection method to discard hadronic showers and analyze only  $\gamma$  events. The methods for  $\gamma$ -hadron separation in general rely on the morphological differences between the showers produced by the two kinds of particles, including temporal information. This task is much more efficient in stereo mode, because  $\gamma$ -ray showers which trigger different telescopes will produce images in the cameras with Hillas ellipses pointing towards the source position, while hadronic showers will produce much less correlated images. In mono mode we can only rely on the morphological features of the images, knowing that hadronic shower images will be much more extended, without a clear definite shape and with a higher number of islands than  $\gamma$  showers.

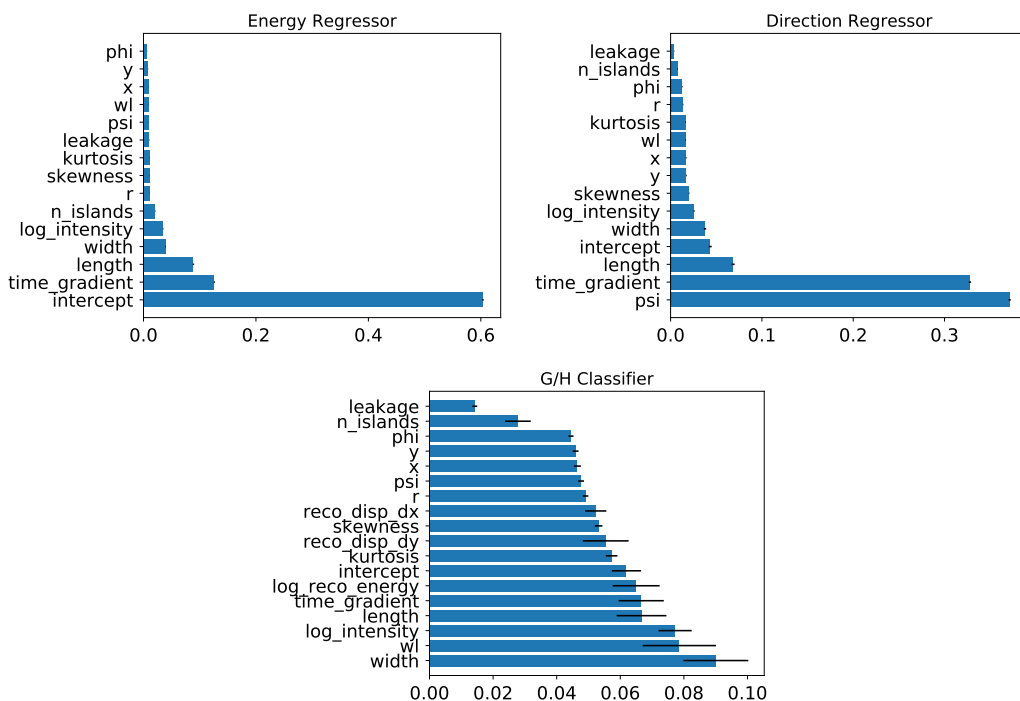


Figure 4.1: Parameters importance for the trained RF used in the analysis of MC simulated LST1 data. The higher the importance value, the more relevant is the feature for the regression/classification.

The task of  $\gamma$ -hadron separation is done in *cta-lstchain* with a RF classifier, which follows similar principles as the RF regressor explained in the previous section. Instead of calculating the value of a variable, it decides between a given number of classes to which each events belongs. In this case, it is only a two classes problem:  $\gamma$ s or hadrons. The best splitting criterion for classification is calculated in terms of the so-called gini index (see ??).

The training set for the  $\gamma$ -hadron classifier will consist on two sets of MC simulated events, one of diffuse  $\gamma$ s and one of protons, with arrival directions coming from a  $10^\circ$  radius FoV. Usually, the set of hadronic events used for training is taken from real background events recorded with the telescope when pointing to a direction in the sky without any  $\gamma$ -ray source, because of the uncertainties in the model used to simulate proton showers (see section 3.4.1). However, as by the time this thesis was written there were not enough real data from LST1 to build a big enough background data set, all the calculations have been done using MC simulations.

The features used for the splitting of the classifiers are the same from the ones used for the regressors of the previous section, but adding the reconstructed energies and disp vector. To do so, the original  $\gamma$  events set is splitted in a training set for the regressor, and a test set, to which the energy and disp vector are reconstructed. The regressors are also used to reconstruct the energy and disp vector of the set of proton events. Afterwards, this new set of  $\gamma$  and proton events, with reconstructed energy and disp is divided again in a training and test set to build the RF classifier. The classifier is implemented using the *RandomForestClassifier* class from *scikit-learn* which input parameters are listed in table 4.1

### 4.3 Sensitivity of the LST1

The sensitivity of a telescope is defined as the minimum flux of  $\gamma$ -rays over background that should be detected for a statistically significant detection. Using the simulated MC data and the analysis techniques explained in section 4.2 the differential sensitivity of LST1 in mono mode can be calculated.

The sensitivity is computed for the detection of a point source after 50 hours of observations. To do so, we are using the Li&Ma method, extensively described in [189], but here the basic concept is summarized.

The significance of detection of a source must be calculated, as a way to evaluate the statistical reliability of an observational result. A typical observation in  $\gamma$ -ray astronomy will consist on pointing to a region where it is supposed to exist a source, recording  $N_{on}$  counts in a time  $t_{on}$ . Then, to evaluate the background, a region without any source is observed, recording  $N_{off}$  counts in a time  $t_{off}$ . If the ratio between the observation time of the on and off regions is  $\alpha = t_{on}/t_{off}$  then the number of background photons in the on region is estimated by  $\hat{N}_B = \alpha N_{off}$  and the probable number of photons contributed by the source is  $N_S = N_{on} - \alpha N_{off}$ . The significance can be estimated in terms of the likelihood ratio method, where we test the *null hypothesis*, being the hypothesis where no source exist at all and all the excess counts

detected in the on region are due to fluctuations in the background. In this case,  $N_{on}$  will follow a Poisson distribution with variance equal to that of the background  $\langle N_B \rangle$ . The likelihood ratio can be written as:

$$\lambda = \frac{L(X|E_0, \hat{T}_c)}{L(X|\hat{E}, \hat{T})} \quad (4.5)$$

Where X are the observed data and  $(\hat{E}, \hat{T})$  are the maximum likelihood estimation of the unknown parameters. In the null hypotheses,  $E = E_0$  and  $T = \hat{T}_c$  are the parameters for the conditional maximum likelihood estimation. In our case, the unknown parameters will be  $N_S$ ,  $N_B$  where in the null hypothesis  $N_S = 0$ . The maximum likelihood ratio has the form:

$$\lambda = \left[ \frac{\alpha}{1 + \alpha} \left( \frac{N_{on} + N_{off}}{N_{on}} \right) \right]^{N_{on}} \left[ \frac{1}{1 + \alpha} \left( \frac{N_{on} + N_{off}}{N_{off}} \right) \right]^{N_{off}} \quad (4.6)$$

If the null hypothesis is true, and  $N_{on}, N_{off} \gtrsim 10$ , by the theorem exposed in [189], the quantity  $-2\ln\lambda$  will asymptotically follow a  $\chi^2$  distribution with one degree of freedom. Therefore,  $\sqrt{(-2\ln\lambda)}$  will be equivalent to the absolute value of a standard normal variable, so we can take it as the significance:

$$S = \sqrt{(-2\ln\lambda)} \quad (4.7)$$

Typically, a detection is claimed when the significance  $S$  is equal to or higher than 5 ( $5\sigma$  detection). To calculate the sensitivity of LST1 we need to know the number of excess counts with respect to the background from a hypothetical source  $N_S$  that will lead to  $S = 5$  for  $\alpha = 1/5$ .

To perform this calculation, we need to estimate the number of background (proton) events ( $N_B = \alpha N_{off}$ ) that will remain after analyzing the data and doing the  $\gamma$ -hadron separation. The steps followed to do so are described in the next sections.

### 4.3.1 Reweighting

The MC simulations of Extensive Air Showers (EAS) used for this work follow a power law spectrum:

$$\frac{dN}{dE} = KE^a \quad (4.8)$$

with a spectral index  $a = -2$ . However, we want to give the sensitivity with respect to the true spectrum of protons, and typically, the spectrum of the Crab nebula is used for the  $\gamma$ -rays. We need to transform the distribution of simulated events from number of events per energy to a rate of events (events per unit time)

per energy which follow the desired spectral shape. To this end, we will calculate a spectral weight  $w(E)$  for each event, which will depend on its true energy.

Suppose that  $N$  MC events have been generated in the energy range  $(E_1, E_2)$ , following the power law from 4.8, with isotropically distributed directions in a solid angle  $\Omega$  and impact parameters uniformly distributed in a circular area  $A$ , orthogonal to the incident direction of the particles. The quantity  $K$  will be:

$$K = \frac{N(a+1)}{E_2^{a+1} - E_1^{a+1}} \quad (4.9)$$

We want to change the shape of this spectrum, and get a new differential spectrum of the shape:

$$\frac{dF}{dE(E)} = \frac{dF}{dE(E_0)} \cdot f(E/E_0) \quad (4.10)$$

Where  $\frac{dF}{dE(E_0)}$  is a normalization factor referring to an arbitrary energy  $E_0$ , which should be between  $E_1$  and  $E_2$ , with units  $s^{-1}sr^{-1}m^{-2}TeV^{-1}$  and  $f$  is a function that satisfies  $f(E = E_0) = 1$ . In our case,  $f$  will simply be the new power law. To correct the  $dN/dE$  simulated spectrum to the desired power law, we should multiply it by  $(E/E_0)^{-a}$ , so it will become flat, and then by  $f(E/E_0)$  to get the correct form. Weighting by these two factors, the corrected number of MC events  $N'$  will be the integral:

$$N' = \int_{E_1}^{E_2} \left( \frac{E}{E_0} \right)^{-a} f(E/E_0) dE = \int_{E_1}^{E_2} K E_0^a f(E/E_0) dE \quad (4.11)$$

We need to transform the number of events to a rate (in Hz), in order to calculate the sensitivity, for a certain observation time. The total rate calculated in the energy range  $E_1, E_2$  will be:

$$R = \int_{E_2}^{E_1} \frac{dF}{dE} dEd\Omega dA \quad (4.12)$$

Therefore, the final weight  $w(E)$  for which the spectrum of each event should be multiplied is:

$$w(E) = \left( \frac{E}{E_0} \right)^{-a} \cdot f(E/E_0) \cdot \frac{N'}{R} \quad (4.13)$$

Where  $a = -2$  is the spectral index of the simulated events,  $E_0$  is taken as 1 TeV and  $f(E/E_0)$  would depend on the spectral shape to be reproduced. For  $\gamma$  events we take the spectrum of the Crab nebula measure by HEGRA [190]:

$$\left(\frac{dF}{dE}\right)_{Crab} = 2.83 \cdot 10^{-14} \left(\frac{E}{1TeV}\right)^{-2.62} GeV^{-1}cm^{-2}s^{-1} \quad (4.14)$$

And for protons, we use the results from the BESS spectrometer [191]:

$$\left(\frac{dF}{dE}\right)_{Crab} = 9.6 \cdot 10^{-9} \left(\frac{E}{1TeV}\right)^{-2.7} GeV^{-1}cm^{-2}s^{-1} \quad (4.15)$$

The values of the differential sensitivity will be given for a certain number of energy bins, therefore, we must calculate the number of weighted events in each energy bin and multiply them by the observation time. This will give us the quantities  $N_S$  and  $N_B$ . To calculate the sensitivity we only need  $N_B$ , which will be the number of weighted proton events divided by the factor  $\alpha = 1/5$ .

### 4.3.2 Cut optimization

To obtain the best possible sensitivity, instead of using all the weighted proton events, we can use the two parameters *gammaness* and  $\theta^2$  to perform cuts that will reject the majority of the background.

*Gammaness* is a number between 0 and 1 assigned by the RF classifier to make the decision on the  $\gamma$ -hadron separation. Events close to 1 will be more  $\gamma$ -like, and events close to 0 will be more proton-like.  $\theta^2$  is the angle between the reconstructed direction of the event and the true assumed direction of the source. Events with a high  $\theta^2$  are most likely to be proton events, while  $\gamma$ s will have a  $\theta^2$  close to 0. For protons, To optimize the cuts in these parameters, we define several bins in *gammaness* and  $\theta^2$ , calculate the number of weighted proton events left after the cuts in each bin and then use this quantity as  $N_B$  for the sensitivity calculation. For each energy bin, we will select the combination of cuts which provides the best sensitivity. We require that after the cuts, at least 10 events of  $\gamma$ s and protons remain in the energy bin.

### 4.3.3 Expected LST1 Performance

The analysis methods described before were used to compute the expected performance of the LST1 in mono mode for the observation of a point source, using a source independent analysis (meaning no assumption on the source position is made). In this section, the results on energy and angular resolution,  $\gamma$ -hadron separation and sensitivity are discussed.

#### Data

The data used for the analysis is a set of MC simulations produced specifically for the LST1 in the northern CTA site. The primaries produced were  $\gamma$ s as a point source

	$\gamma$ (PS) offset = $0.4^\circ$	$\gamma$ diffuse	electron	proton
Energy Range	5 GeV - 50 TeV	5 GeV - 50 TeV	5 GeV - 5 TeV	10 GeV - 100 TeV
Viewcone	$0^\circ$	$10^\circ$	$10^\circ$	$15^\circ$
Core Range	1000 m	1000	1000 m	2500
Input Events	South: $3 \cdot 10^7$ North: $3 \cdot 10^7$	South: $5 \cdot 10^8$ North: $5 \cdot 10^8$	South: $6 \cdot 10^8$ North: $6 \cdot 10^8$	South: $5 \cdot 10^9$ North: $5 \cdot 10^9$
Triggered Events	South: $1.08 \cdot 10^6$ South: $9.60 \cdot 10^5$	South: $1.22 \cdot 10^6$ South: $1.11 \cdot 10^6$	South: $1.18 \cdot 10^6$ South: $1.04 \cdot 10^6$	South: $8.25 \cdot 10^5$ South: $8.10 \cdot 10^5$

Table 4.2: Summary of the MC production dedicated to the LST1

with an offset of  $0.4^\circ$  from the center of the camera, diffuse  $\gamma$ s, protons and electrons, but for the results given in this thesis, electrons were not included. The injection of particles was split in the North and South direction, but only the South production has been used here. The zenith angle was  $20^\circ$ , the spectral index of the particle spectra was -2. A summary of the main characteristics of the production is given in table 4.2.

After calibrating and parameterizing the data, using three sets of cleaning parameters to study the effect on cleaning in the analysis, the diffuse  $\gamma$  events were used to train the RF regressors. Then, a subset of diffuse  $\gamma$ s and the hadron events to which the energy and direction was reconstructed, were used to train the RF classifier for  $\gamma$ -hadron separation. The point source  $\gamma$ s, together with a subset of hadron events as background, have been used to produce the performance results. A filter in intensity  $> 300$  phe, leakage  $< 0.2$  and gammaness  $> 0.5$  was applied to the reconstructed events.

### Energy resolution

The energy resolution gives information on the error committed in the reconstruction of the energy of the event. It is defined as the 68th percentile of the relative error  $\Delta E/E = (E_{reco} - E_{true})/E_{true}$ . If the relative error follows a normal distribution, the 68th percentile is equivalent to one  $\sigma$ . The results on energy resolution are shown in figure 4.2. The features used for the energy regression ordered by their importance can be seen in figure 4.1.

### Angular resolution

The angular resolution is calculated similarly to the energy resolution, but in this case the relative error shown in figure 4.3 refers to the angular difference between the true direction of the source and the reconstructed direction. The features used for the disp vector regression ordered by their importance can be seen in figure 4.1.

### $\gamma$ -hadron separation

The performance in  $\gamma$ -hadron separation can be studied in terms of the receiver operating characteristic (ROC) curve of the RF classifier. The ROC curve illustrates the diagnostic ability of a binary classifier as its discrimination threshold is varied. It

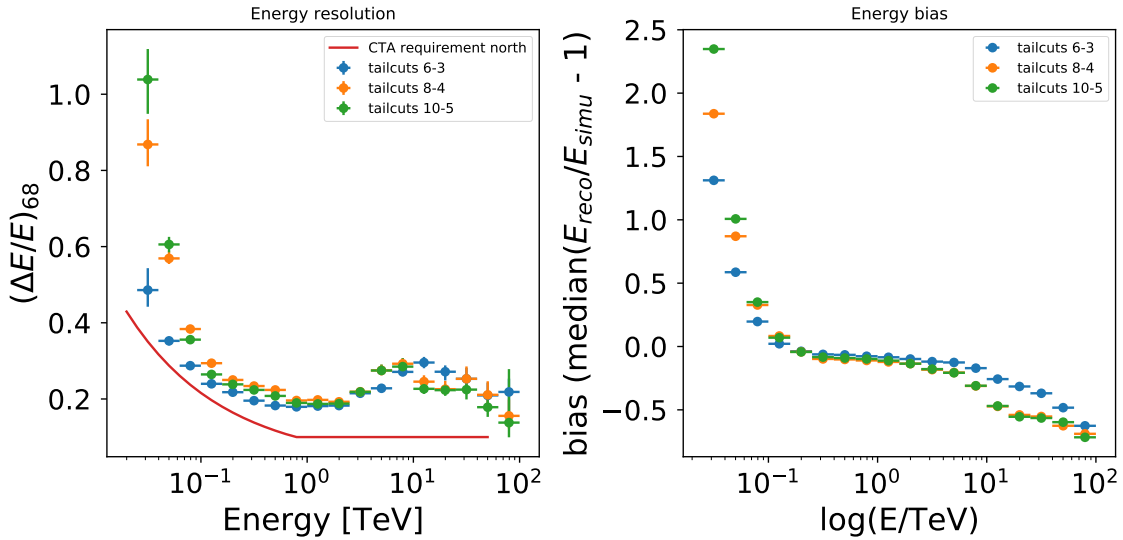


Figure 4.2: Energy resolution for the LST1 analysis applied to a MC production of point-like  $\gamma$  events, for three different sets of cleaning parameters (low level-high level threshold in number of photoelectrons). As a reference, the energy resolution requirement for CTA-north is also shown. The energy resolution plot of the *left* has been bias corrected.

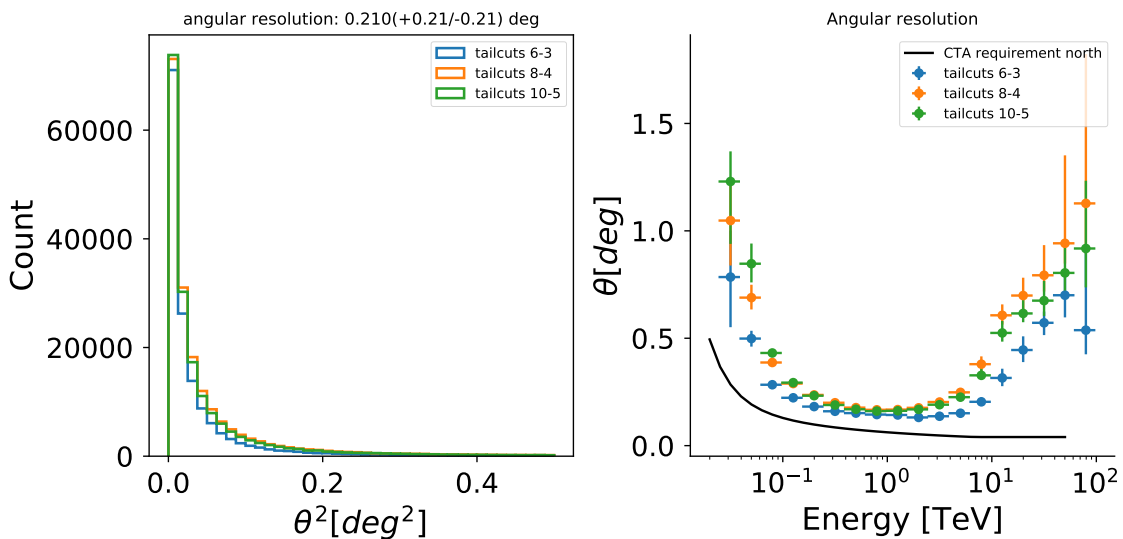


Figure 4.3: *Left:*  $\theta^2$  plot for the MC simulated  $\gamma$  point-like events, using three sets of cleaning parameters. *Right:* Angular resolution as a function of reconstructed energy.

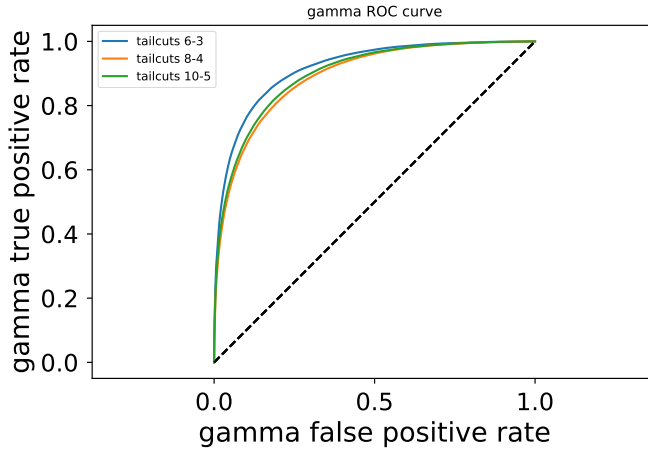


Figure 4.4: ROC curve of the RF classifier applied to point-like gamma and diffuse proton events, for three different sets of cleaning parameters.

is produced plotting the true positive rate (the rate of  $\gamma$ s correctly classified) versus the false positive rate (the rate of protons incorrectly classified as  $\gamma$ s) at several thresholds in gammaness. A value of 1 in true positive rate, while 0 in the false positive rate would mean a perfect classification. The closest of the ROC curve to a diagonal, the more similar to an uniformly random distribution is the classification. For this result, a subset of protons was used to test the RF classifier together with the point-like  $\gamma$ s, resulting in the plots shown in figure 4.4. The features used for the  $\gamma$ /hadron classification ordered by their importance can be seen in figure 4.1.

### **Effective Area**

The effective area calculated for the detection of showers from a point source with the LST1 is shown in figure 4.5.

### **Sensitivity**

For the calculation of the sensitivity, a subset of proton events was used as background (off) events. The point-like  $\gamma$  events were used together with the protons to calculate the cuts in gammaness and  $\theta^2$  which provided the best sensitivity in each of the 20 energy bins taken. To do so, the sensitivity was calculated for 10 cuts in gammaness and in  $\theta^2$  for each energy. The combination of cuts giving the lower value in sensitivity, keeping a minimum of 10  $\gamma$  and proton events in the bin (both before and after re-weighting), was selected. The resulting sensitivity curve is shown in picture 4.6.

## **4.4 Expectation-Maximization method for Hillas Parameters calculation without cleaning**

As explained in section 4.2.2, cleaning methods often require the adjust of some parameters, which have to be done empirically, trying to find a balance between

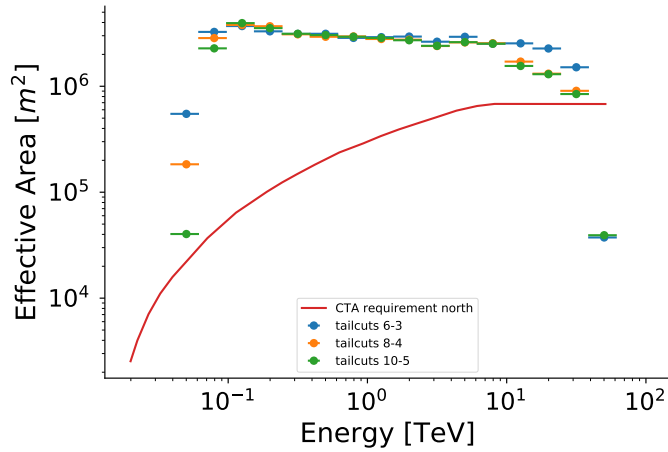


Figure 4.5: Effective area per energy bin for the MC simulated  $\gamma$  point-like events, using three sets of cleaning parameters.

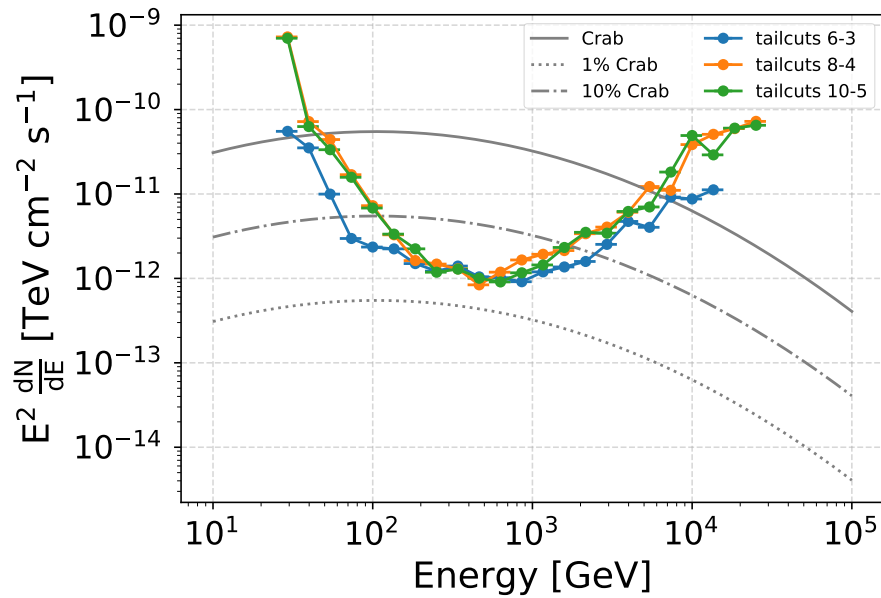


Figure 4.6: Sensitivity plot for 50h of observation of a point-like  $\gamma$ -ray source with a Crab-like spectrum, obtained by selecting the cuts in gammaness and  $\theta_2$  which provided the best differential sensitivity per energy bin. As a reference, the spectra of Crab, 10% of Crab and 1 % of Crab emission are shown.

a good enough background suppression without losing too much information from the shower. The cleaning parameters affect particularly the analysis of low energy showers. In the tailcuts method, too strong cleaning thresholds tend to eliminate too many pixels of the already small low energy showers, making the task of  $\gamma$ -hadron separation much more difficult. Also, losing the ellipse shape of  $\gamma$  showers lead to wrong calculation of Hillas parameters and consequently of the disp vector.

For all these reasons, with the aim to research for new analysis methods which could improve the performance of LST, a method for image parameterization which do not require a previous cleaning has been developed. It is based in the Expectation-Maximization (EM) algorithm, where recursively the light content in each pixel is assigned to be part of the shower or the background. In the next sections, the basic concepts of the EM method and how it can be applied to images of showers will be summarized. Then some results comparing the EM with the classic cleaning method will be shown.

#### 4.4.1 The Expectation-Maximization algorithm

The EM algorithm [192] is an iterative method for calculating maximum likelihood estimates of model parameters, where the model depends on unobserved data or latent variables. These latent variables would be those that cannot be observed in the data set, but still can influence other random variables. The algorithm will iterate until finding the model parameters and hidden variables that converge to a maximum likelihood estimation.

Given a statistical model which has generated a set of  $X$  observed data points, which depends on a set of latent variables  $Z$  and unknown parameters  $\theta$ , the basic iteration of the EM consist on two steps:

- **Expectation:** Creates an expectation function  $Q(\theta|\theta^{(t)})$ , which is the evaluation of the log-likelihood with the current estimate of the model parameters  $\theta^{(t)}$ , meaning it calculates the latent variables  $Z$ .

$$Q(\theta|\theta^{(t)}) = E_{Z|X,\theta^{(t)}} \quad (4.16)$$

- **Maximization:** Maximizes the log-likelihood function found in the previous step to find a new set of estimated parameters.

$$\theta^{(t+1)} = \operatorname{argmax} Q(\theta|\theta^{(t)}) \quad (4.17)$$

A common problem that has been successfully solved by the EM algorithm is the mixture models problem, where there is a set of data which has been produced by several density distribution functions, but is impossible to know which distribution has produced each data point. This distinction between distributions would be the latent variable. This is the particular case we face with shower images. We have a distribution of light in the pixels of the camera, and we know that some photoelectrons come from Cherenkov light, and others belong to background light from the night sky. We want to know the fraction of light in each pixel which belongs to each of the

distributions.

We assume that the Cherenkov light will follow a bi-dimensional Gaussian distribution, which will therefore produce the typical elliptical shape in the image, and the background is simply a two dimensional constant distribution. The parameters of the model will be the usual Gaussian parameters (mean and standard deviation in two dimensions)  $\{x_0, y_0, \sigma_{xx}, \sigma_{yy}, \sigma_{xy}\}$  and the latent variables will be the fraction of photoelectrons from the Cherenkov shower  $n_{Ch}/n$  and from the background  $n_{bkg}/n$  in each pixel with n total photoelectrons.

The number of photoelectrons belonging to each distribution will be:

$$N_i = \sum_{pixels} P(pixel/i) \cdot N \quad (4.18)$$

Where  $N_i$  is the number of photoelectrons produced by the distribution  $i$  (Cherenkov or background), N is the total number of photoelectrons in the image and  $P(pixel/i)$  is the probability of a photoelectron in the pixel to have been produced by the distribution  $i$ .

Using the Bayes theorem:

$$P(pixel/i) = \frac{P_i(pixel) \cdot P_i}{P(pixel)} \quad (4.19)$$

Where  $P_i(pixel)$  is the probability of a photoelectron produced by the distribution  $i$  to fall in the pixel,  $P_i$  is the probability of a photoelectron to be produced by the distribution  $i$  and  $P(pixel)$  is the probability of a photoelectron to fall in the pixel. This last probability will actually be:

$$P(pixel) = \sum_i P_i \cdot P_i(pixel) \quad (4.20)$$

Where probabilities  $P_i = (P_{Ch}, P_{Bkg})$  are equal to the fraction of photoelectrons in the image belonging to the shower(background) with respect to the total number of photoelectrons. The probabilities  $P_i(pixel)$  can be written as:

$$\begin{aligned} P_{Ch}(pixel) &= BiGaus(x_0, y_0, \sigma_{xx}, \sigma_{yy}, \sigma_{xy}) \cdot A_{pixel} \\ P_{bkg}(pixel) &= A_{pixel}/A_{total} \end{aligned} \quad (4.21)$$

Where  $A_{pixel}$  is the area of the pixel and  $A_{total}$  the sum of the areas of all pixels.

The loop in the EM to solve this problem will go as follows:

1. An initial assumption of the Gaussian parameters is made. Because the bi-dimensional Gaussian corresponds to the Hillas ellipse, the means of the distribution will coincide with the center of gravity of the ellipse, which will be close to the pixel with higher charge. To avoid committing a mistake choosing the initial value due to an outlier pixel, we take the initial means of the Gaussian

$(x_0, y_0)$  as the coordinates of the baricenter of the three more luminous pixels. The initial values of the standard deviations are set to arbitrary high values  $\sigma_{xx} = 20000$ ,  $\sigma_{yy} = 20000$ ,  $\sigma_{xy} = 0$ . Also we assume an initial estimation of the fraction of the light belonging to the shower and background as 50% of the total number of photoelectrons for each.

2. Expectation: Using the previous estimation of Gaussian parameters and fractions of photoelectrons, equation 4.19 is solved and the distributions of the shower and the background are obtained. For each pixel the number of photoelectrons belonging to the shower and to the background is calculated.
3. Maximization: Using the distributions from previous steps, the parameters of the bi-dimensional Gaussian corresponding to the Cherenkov light distribution are calculated, and also the fraction of the total photoelectrons produced by each distribution (which is simply the sum of all shower and background pixels content respectively). The new Gaussian parameters will be:

$$\begin{aligned}
 mean_x &= \frac{1}{N} \sum_{pixels} n_{Ch} x_{pix} \\
 mean_y &= \frac{1}{N} \sum_{pixels} n_{Ch} y_{pix} \\
 \sigma_{xx} &= \frac{1}{N} \sum_{pixels} n_{Ch} x_{pix}^2 - mean_x^2 \\
 \sigma_{yy} &= \frac{1}{N} \sum_{pixels} n_{Ch} y_{pix}^2 - mean_y^2 \\
 \sigma_{xy} &= \frac{1}{N} \sum_{pixels} n_{Ch} x_{pix}^2 y_{pix}^2 - mean_x mean_y
 \end{aligned} \tag{4.22}$$

4. Steps 2 and 3 are repeated until convergence.

The EM method was used to calculate the Hillas parameters of a small subset of the MC production described in section 4.3.3 ( $\sim 20k$  events of diffuse  $\gamma$ s and protons for training the RFs, and  $\sim 200k$  events of point-like gammas for testing the results). These parameters were used to do the energy and direction reconstruction and the  $\gamma$ -hadron classification. The results, compared to the ones obtained using the tailcuts cleaning and parameterization method are shown in the next section.

#### 4.4.2 Comparison of EM without cleaning and tailcuts cleaning

In this section, results on energy resolution, angular resolution and  $\gamma$ -hadron separation using the EM method for Hillas parameters calculation without previous cleaning are presented, compared to the results obtained applying the classic method of tailcuts cleaning for three sets of cleaning parameters.

The time parameters are not included in the features for RF training because the EM code developed for this work is not compatible with the function for the calculation of time parameters in *ctapipe*.

From figure 4.7 it can be appreciated that the results for the EM method are compatible with the tailcuts cleaning method, reassuring that this is a valid method of Hillas parameterization which allows to go through the step of cleaning which clearly can affect the performance results, as shown in section 4.3.3. The principal current caveat of the method is that it is much more time consuming than the simple tailcuts methods. Taking into account that no time optimization work has been done in the code, great improvements can be expected from the method, to become a potential useful tool for the analysis of low energy events.

## 4.5 Results on real data

Since the beginning of the commissioning of the telescope, three Crab datataking campaigns have been carried on, where the Crab nebula has been observed with the LST1 during several nights, in order to study the performance of the whole instrument and the analysis tools.

In this section the data taken during the second Crab campaign, from January 17 to February 02 202, has been analyzed following the methods described in previous sections, deriving the final detection significance of the Crab over the full campaign. Telescope data is taken in several runs of a certain duration, where events are recorded and stored in fits files. Each night, four kinds of runs are taken: DSR4 calibration runs (for pedestal subtraction), camera calibration runs (see section 4.2.1) and data runs of two types: ON and OFF runs. Data ON runs are taken pointing with the telescope to the  $\gamma$ -ray source, in this case the Crab nebula. OFF runs are taken pointing to a region without a  $\gamma$ -ray sources, where the Cosmic Ray (CR) background is similar to that of the ON region, allowing to estimate the background in the region of interest to extract the signal events as an excess over the background.

The data runs have been calibrated and parameterized using *cta-lstchain* following the steps described in section 4.2. The signal extractor used has been the *GlobalPeak-WindowSum* and the cleaning method applied is a two level tailcuts with  $Th_{high} = 6$  phe and  $T_{low} = 3$  phe. The RF models for energy and direction reconstruction, and  $\gamma$ /hadron separation has been trained with MC data, as described in sections 4.2.3 and 4.2.4, and applied to the ON and OFF data for reconstruction to DL2 data level. A set of cuts, summarized in table 4.3, has been applied to the data to allow a good background rejection and avoid showers with few photoelectrons (high cut in intensity) or which are truncated in the edges of the camera (cut in leakage).

In the ON region, close to the source position, an excess of events should be observed compared to the background. At further distances, the number of events should be comparable to that of the OFF region, where there are only background events. The number of background events  $N_{bkg}$  in the ON region can be estimated as  $N_{off}$  multiplied by a normalization factor,  $n = N_{on}/N_{off}$  calculated at a large

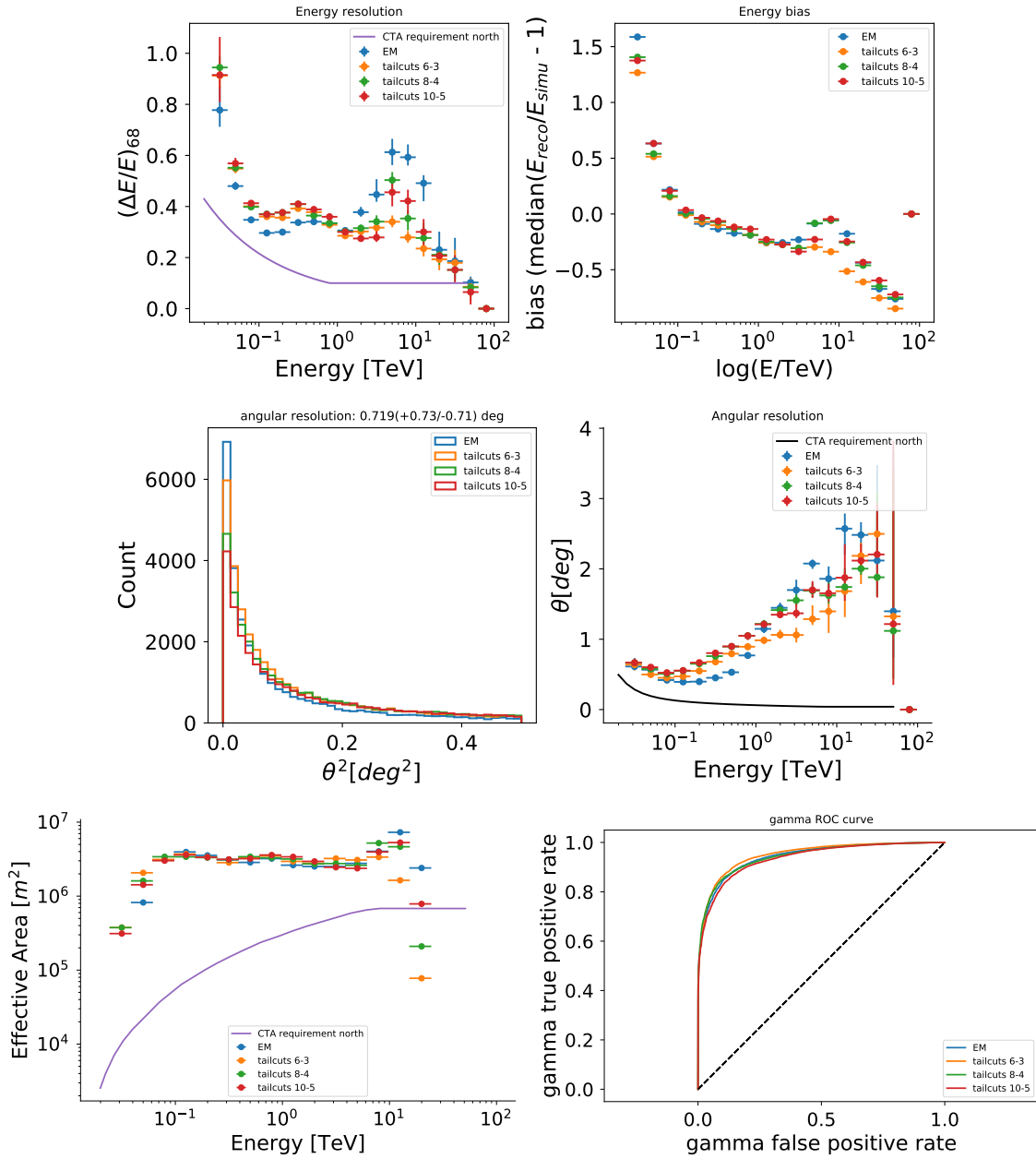


Figure 4.7: Energy resolution (*top*), angular resolution (*middle*), effective area (*bottom-left*) and ROC curve (*bottom-right*) plots for a small subset of events analyzed using the EM method for Hillas parameterization without cleaning, compared to three different subsets of tailcuts cleaning parameters.

Intensity min	500
Intensity max	80000
Leakage	< 0.2
Width/Length	> 0.1
Gammaness	> 0.6

Table 4.3: Set of cuts applied in the parameters of the reconstructed real data from the second Crab campaign.

distance from the assumed source position (the center of the camera), which accounts for the difference in observation time of the two regions. The significance of the excess in the ON region is defined as:

$$S = N_{ex} / \sqrt{N_{off}} \quad (4.23)$$

Where  $N_{ex}$  is defined as the number of excess counts in the ON region, calculated as  $N_{ex} = N_{on} - N_{off} * n$ .

The analysis can be performed following two different definitions for the distance from the source position. The first approach is the  $\theta^2$  analysis, where the  $\theta^2$  angle is defined as:

$$\theta^2 = X_S^2 + Y_S^2 \quad (4.24)$$

$X_S$  and  $Y_S$  represent the reconstructed position of the source in camera coordinates. If the telescope is pointing to the source position, the closer of  $\theta^2$  to 0 (the center of the camera), the closer to the true source position has been reconstructed the event direction. We can assume that background events have reconstructed source positions distributed uniformly over the FoV, but the events from the  $\gamma$ -ray source will have reconstructed positions with smaller  $\theta^2$ . The normalization factor  $n$  between the number of background events in the ON and OFF regions is calculated using events with  $\theta^2 > 0.5^\circ$ . To calculate the number of excess counts and the significance, a cut in  $\theta^2 < 0.25^\circ$  is applied. In picture 4.8, the value of  $\theta^2$  is plotted for the ON and OFF regions, observing clearly an excess around  $\theta^2 = 0$ . The rate of  $\gamma$  events (number of events per minute) can be calculated dividing the number of excess events  $N_{ex}$  by the total observation time.

The second analysis approach is made with respect to the  $\alpha$  angle, which is defined as:

$$\alpha = \arccos \left( \frac{X_{c.o.g.} \cos(\psi) + Y_{c.o.g.} \sin(\psi)}{X_{c.o.g.}^2 + Y_{c.o.g.}^2} \right) \quad (4.25)$$

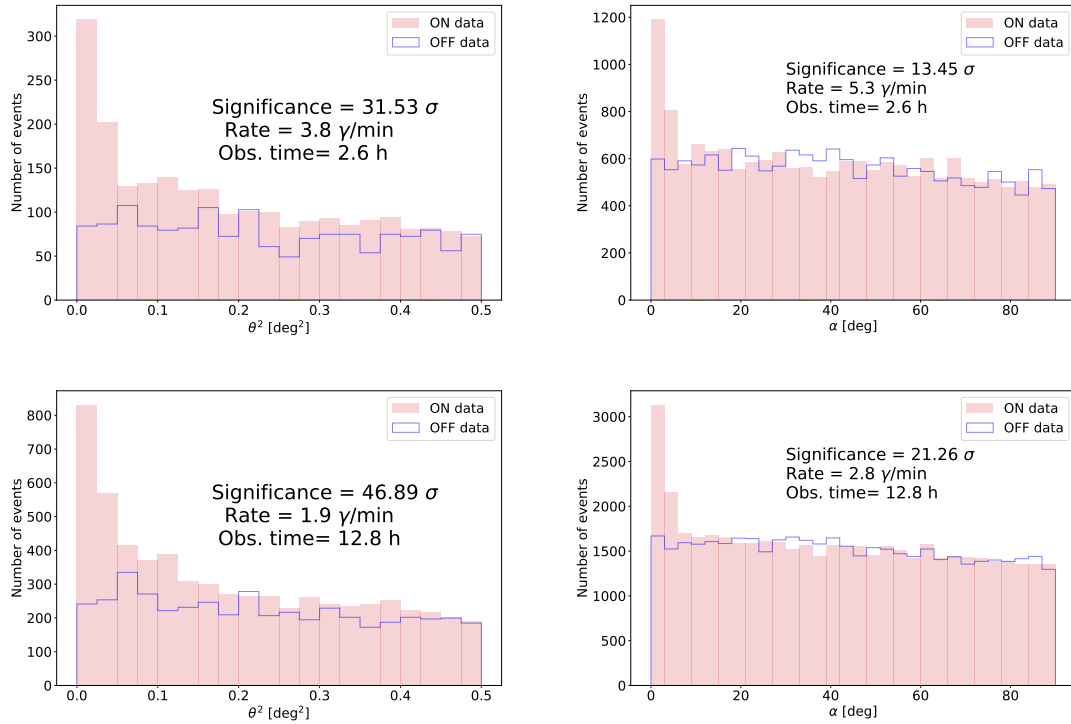


Figure 4.8: *Top:*  $\theta^2$  (*left*) and  $\alpha$  (*right*) plots for the Crab data taken during the night of the 18/01/2020. *Bottom:*  $\theta^2$  (*left*) and  $\alpha$  (*right*) plots for the data taken during full second Crab campaign, from 15/01/2020 to 02/02/2020. Results are calculated after applying the cuts from table 4.3.

Where  $X_{c.o.g.}$  and  $Y_{c.o.g.}$  are the coordinates of the center of gravity of the Hillas ellipse of the shower image, and angle  $\psi$  is the angle between the semi-major axis of the ellipse and the line between the center of the camera and the centroid of the ellipse. The  $\alpha$  angle is a measure of how deviated is the Hillas ellipse from pointing towards the center of the camera. Events with high alpha angle are more likely to be background events, whereas  $\gamma$  events will point towards the same position, close to the center, having small  $\alpha$  angles. To estimate the background normalization factor  $n$ , events with  $\alpha$  angle between  $20^\circ$  and  $80^\circ$  are used. To calculate the excess signal and sensitivity a cut in  $\alpha < 8^\circ$  is applied.

The  $\theta^2$  and  $\alpha$  plots are shown in picture 4.8 for the full campaign and for just one day of observation. The data was taken between January 15th and February 2nd, summing a total of 12.8 hours of observation, which combined lead to a final detection significance of  $46.9\sigma$  for the  $\theta^2$  analysis, and  $21.26\sigma$  for the  $\alpha$  analysis, after applying the cuts listed in table 4.3.

## **4.6 Summary and conclusion**

Along this chapter, the chain for the single telescope data analysis of LST1 has been described, and successfully used to derive the performance of the LST1, and to analyze the first real data taken with the instrument.

About the performance estimated using MC simulations, it has been shown that the energy resolution reaches an error as low as 20% in the range from  $\sim 100$  GeV to a few TeV and the angular resolution in the same energy range is  $\sim 0.2^\circ$ . From the three sets for tailcuts parameters, the one giving best results has been the 6-3 tailcuts. The best sensitivity of LST1 for 50 hours of observation is reached in the range between 100 GeV and 1 TeV, going below the 10% of the Crab flux.

The EM method for Hillas parameterization without cleaning has been presented as a potential alternative, with similar performance to the classic tailcuts cleaning (without time parameters), to avoid the necessity to adjust the tailcuts parameters which clearly affect the performance results. This method is useful for low energy events, with very few photoelectrons, where tailcuts cleaning can suppose the loss of information from the shower.



## 5. Characterization of the Large Magellanic Cloud and prospects on Dark Matter detection for CTA

### 5.1 Introduction

The Large Magellanic Cloud (LMC) is one of the closest satellite galaxies of the Milky Way (MW) located at a distance of  $\sim 50$  kpc [193]. Thanks to its proximity, large volume and orientation angle ( $\sim 30^\circ$  [194]), it is observed as an extended object of about  $10^\circ$  diameter in the sky, which has allowed the study of its structure and individual components in great detail. Observations of the LMC in the whole electromagnetic spectrum have revealed the presence of a big number of extreme objects such as pulsars [195] [196], Supernova Remnants (SNRs) [197] [198] [199], Pulsar Wind Nebulae (PWNe) [200] [196] [201] [202] and  $\gamma$ -ray binaries [203]. Many of these objects are known to be cosmic-ray accelerators and therefore potential  $\gamma$ -ray emitters.  $\gamma$ -ray emission up to TeV energies from several sources within the LMC has already been detected by the current generation gamma-ray experiments *Fermi*-LAT and High Energy Stereoscopic System (H.E.S.S.) and it is expected that many more objects will be discovered by the future Cherenkov Telescope Array (CTA). The LMC Survey is one of the Key Science Projects (KSP) of CTA [204], with more than 300h of dedicated observations and many scientific objectives: population studies of SNRs and PWNe, transport of Cosmic Rays (CRs) and searches of Dark Matter (DM). Thanks to its high star formation activity, which implies a high supernova rate and thus a large population of  $\gamma$ -ray sources, the LMC offers a unique opportunity to study the relation between star formation and cosmic-ray production and propagation, as an alternative to the MW.

CRs are an important component of the Interstellar Medium (ISM) in galaxies, with energy densities comparable to that of magnetic fields. As discussed in previous chapters, the origin and propagation of CRs is still a field of study as well as their role in galaxy evolution. It is believed that they have a significant effect in star formation,

acting as an extrinsic feedback source. Even the energy injection rate of CRs is negligible compared to other by-products of star formation, such as photons, winds and supernova shocks, they interact with the ISM and exchange a significant amount of momentum. Studies on starburst galaxies luminosities [205] have established that it is possible that cosmic-ray winds are produced in high star formation rate regions, perturbing the hydrostatic balance and truncating star formation. On the other hand, infrared observations of Ultraluminous Infrared Galaxies (ULRIGs) suggest that CRs are able to heat gas in molecular clouds and are their main agent of temperature regulation and ionization, fundamentally altering the initial conditions for star formation [206].

While LMC evolution must be closely related to the MW and the rest of the local group, observations of very young globular clusters in the LMC suggests that its Stellar Formation History (SFH) is fundamentally different to that of the MW. In fact, the LMC is currently in an enhanced star formation epoch with a rate of  $\sim 0.2 M_{\odot}/yr$  which was reignited 4-5 Gyrs ago after a dramatic event affecting the Magellanic System (MS) (composed by the LMC and the Small Magellanic Cloud (SMC)) [207].

The LMC is classified as an irregular galaxy, the most common type in the universe. In general, irregular galaxies are simpler, less dusty and with lower metallicity than spiral galaxies (like the MW). Because they are less evolved, they present higher gas content and lower abundance of heavy elements [208]. All these differences with respect to the MW affecting the characteristics of the ISM, are fundamental for the study of the production and propagation of CRs in star forming regions, and allow to use the LMC as an alternative probe to the MW. Characterizing the CRs origin and propagation throughout the ISM is not an easy task, as charged particles are deflected by magnetic fields, making it impossible to reconstruct their trajectories and thus, pointing back to their origin from Earth. The best way to study cosmic-ray physics in the galaxies is through the diffuse emission from radio to  $\gamma$ -rays that they produce when interacting with other particles in the ISM and the radiation of magnetic fields. The leptonic component of this emission, produced by cosmic-ray electrons, can be studied by radio, X-ray and  $\gamma$ -ray observations. The radio diffuse emission comes from synchrotron emission of cosmic-ray electrons injected by supernova remnants. They can also suffer Inverse Compton (IC) scattering with photons of the interstellar radiation field or the Cosmic Microwave Background (CMB), producing emission from X-ray to  $\gamma$ -rays [209]. The hadronic component of diffuse cosmic-ray emission is produced (mainly) by cosmic-ray protons inelastic collisions with the ISM particles, which produce pions resulting in a continuum  $\gamma$ -ray emission from pion decay [210]. As hadrons make up the 90% of the CRs composition,  $\gamma$ -rays are a fundamental probe for cosmic-ray production and propagation. A galaxy like the LMC, externally viewed and nearly face on offers a unique opportunity for studying the diffuse distribution of CRs in a galaxy, in comparison with the MW which has the problem of line-of-sight confusion of sources. *Fermi*-LAT observations of the LMC revealed a diffuse  $\gamma$ -ray emission little correlated with the large scale distribution of the gas column density

of the galaxy [211]. This correlation would be observed if cosmic-rays could freely diffuse in the ISM as it is observed in the MW. Instead, it appears to be much more correlated with tracers of massive star forming regions such as the 30 Doradus region [212].

Beyond the extraordinary opportunities for cosmic-ray physics, the LMC offers also the possibility to help solving the fundamental problem of DM. The LMC has a mass of the order of  $10^9 M_\odot$  enclosed in 8.9 kpc and more than a half is due to a dark halo [213]. Study of the rotational curves of the LMC revealed that also it must contain a dark compact bulge with an anomalously high mass-to-luminosity ratio as large as  $\sim 20 - 50 M/L$  [214] compared of that of the calculated for the MW  $\sim 7 M/L$  [215]. With these characteristics, LMC would be the most DM massive object after the Galactic Center (GC) offering an alternative source for indirect searches of DM signal. Among all the theories trying to explain the nature of DM, the Weak Interacting Massive Particle (WIMP) theory is one of the most popular, considering DM to be composed by thermal relic particles which can suffer annihilation or decay into Standard Model (SM) particles. Different channels of annihilation would produce a certain spectrum of gamma-rays [216] which could be detected as an excess over the  $\gamma$ -ray flux produced by baryonic backgrounds. Following this scheme, *Fermi*-LAT used five years of data to search for a DM annihilation signal in  $\gamma$ -rays and placed competitive bounds on the annihilation cross section as a function of the dark matter particle mass and annihilation channel [211].

In this chapter, which is the core of this thesis, a characterization of the LMC in the energy range of CTA is performed, in order to cast predictions on the possible results of the LMC survey. The methodology followed has been building an emission model of the LMC, using a dedicated CTA software to perform simulations of the survey data products. A maximum likelihood approach is used to calculate the detection significance of the different sources of  $\gamma$ -rays in the LMC, and to set constraints on the diffuse cosmic-ray emission. In the same way, sensitivity curves for the detection of a possible DM annihilation signal are calculated. Section 5.2 is dedicated to the description of the  $\gamma$ -ray emission model of the LMC. In section 5.3 the analysis and simulation methods are explained. Results on the detectability of ordinary sources in the LMC (not DM) are presented in section 5.4. The case, analysis and results on the possible detection of annihilation DM signal is covered in section 5.5.

## 5.2 Emission Model

The LMC has been observed by *Fermi*-LAT and H.E.S.S. in the High Energy (HE) and Very High Energy (VHE) ranges. To perform predictions on how the LMC will look like in the range of CTA, up to hundreds of TeV, we must rely on the previous observations and make assumptions on how the emission extrapolate to higher energies. The  $\gamma$ -ray emission in the LMC can be divided in two types: emission from point-like sources and diffuse emission from CRs. The idea is to build a complete emission model of the LMC which afterwards will be convolved with CTA Instrument Response

Functions (IRFs) to simulate the data which will be obtained from the LMC survey. The simulations will be computed using the software *ctools*, described in chapter 3. These simulations are used to cast predictions on the detectability of the sources included in the emission model, which includes the point sources detected by previous models, an artificial population of PWNe and cosmic-ray diffuse emission from leptonic and hadronic origin.

The emission model computed is also used as background for the potential detection of a DM annihilation signal. The results on this topic are given in the shape of sensitivity curves for the detection of an array of DM models, characterized by a certain density profile, annihilation spectrum and DM particle mass. In this section, the emission model developed for the global  $\gamma$ -ray emission of the LMC is described. The baseline model consist on four already-known VHE point-like sources, galaxy-scale interstellar emission of both hadronic and leptonic origin, and a population of PWNe.

### **5.2.1 Diffuse emission**

Interstellar diffuse emission of  $\gamma$ -rays in the LMC is produced by the interaction of CR with the ISM. Two kinds of interactions were considered to compute the diffuse emission model: IC processes from CR electrons and pion-decay from proton interactions. The distribution of CRs in the LMC has been computed under the assumptions of steady CR injection from an ensemble of point sources, followed by diffusive transport in the ISM and interaction with simplified distributions of interstellar components (gas, photon and magnetic fields). The resulting interstellar emission model is obtained by convolving the distribution of injection sources with average emission kernels for pion-decay and IC scattering, plus a correction by the actual gas distribution for the pion-decay.

As has been discussed in chapter 1, CRs are accelerated by the power provided by winds and outflows around massive stars, supernova explosions and compact objects, which are traced by Star forming regions (HII regions). The HII regions catalog from [217] was used as template for the distribution of CR sources, taking only regions with  $H\alpha$  luminosity above  $10^{37}$  erg s $^{-1}$ , where the assumption of steady CR injection is valid. The most luminous HII region in the LMC is 30 Doradus, with a luminosity of  $10^{39.66}$  erg s $^{-1}$ . It is not included in the injection model because its mostly populated by very young OB stars ( $< 4$  Myrs) [218] and is unlikely that many Supernovae (SNe) have exploded recently in the region. The CR injection power is assumed to be proportional to the ionizing luminosity of the HII regions and constant in time, corresponding to the release of  $E_{SN} = 10^{51}$  erg per Supernova (SN) explosion, at an estimated rate of  $r_{SN} = 0.002$  SN yr $^{-1}$  [219], where the fraction of mechanical energy trapped by CR acceleration is  $\eta_p = 10^{-1}$  for protons and  $\eta_e = 10^{-3}$  for electrons. This total power is distributed among all the different star forming regions in proportion to their ionizing luminosity. The injection spectra is assumed to follow a power-law distribution in momentum, with an spectral index for protons(electrons) of 2.45(2.65), starting at 1 GeV/s, with an exponential cut off at 1 PeV/s.

The diffusion of CRs away from their sources is assumed to occur due to spatial

diffusion and energy losses. Energy loss processes include hadronic interactions for CR protons and synchrotron, IC scattering and Bremsstrahlung radiation for CR electrons interacting with the homogeneous gas, photons and magnetic fields of the ISM model adopted. The spatial distribution of protons and electrons around a stationary source is computed by integrating the solution of the diffusion loss equation, as of [220], over an injection duration of  $T_{inj} = 100$  Myr. This accounts for the SFH of the LMC which was not steady over recent times and exhibits a drop in star formation 100 Myr ago [207]. Surface brightness angular profiles are computed by integrating the particle spatial distributions along the line of sight over a thickness  $2H$ , where  $H$  is the half-thickness representative of the target distribution: a 180 pc gas disk scale height for CR protons and a 1 kpc magnetic and radiation field halo for CR electrons. The result of these calculations are the emission kernels for IC and pion-decay, which was convolved with the CR source distribution. Furthermore, for the pion-decay component a nuclear enhancement factor of 1.753 is introduced to account for the contribution of helium and heavier nuclei in CRs and the ISM. Also, the resulting emission cube is re-scaled by the gas column density map of the LMC, to recover the actual gas distribution structure of the galaxy.

About the ISM medium in the LMC, an average ISM model has been computed, which includes a description of the interstellar conditions in terms of gas mass and structure, stellar population feeding the radiation fields and magnetic field configuration. The CRs transport and subsequent  $\gamma$ -ray emission will be strongly affected by the characteristics of this ISM. For the interstellar gas, a disk having a radius of 3.5 kpc and a scale height of  $h=0.18$  kpc has been used, where the mass of atomic, molecular and ionized hydrogen has been computed. The interstellar radiation field model has been developed following the work of [221], where the broadband infrared dust emission in the LMC is computed for typical HII regions. About the magnetic field, the total magnetic field strength in the LMC is calculated to be  $4.3 \mu\text{G}$  [222].

The final mapcubes computed for the pion-decay component and the IC component are shown in picture 5.1 in the 1 TeV energy bin.

### 5.2.2 Point Sources

Observations in gamma-rays of the LMC have provided a very interesting catalog of point-like sources of different nature, which have revealed very interesting features. For this work, we use the LMC data collected by *Fermi*-LAT [211] [196] and H.E.S.S. [223] [200] [203] to build the emission models of the sources we have decided to include in this study. A description of the different point sources and their emission models is given in the next subsections.

#### Pulsar Wind Nebula N157B

A signal of  $\gamma$ -ray emission from the direction of the Pulsar Wind Nebula (PWN) N 157B associated to the pulsar PSR J053-6910 has been measured both by *Fermi*-LAT in the HE range ( $\sim 10\sigma$ ) and by H.E.S.S. in the VHE range ( $33\sigma$ ). This is the first

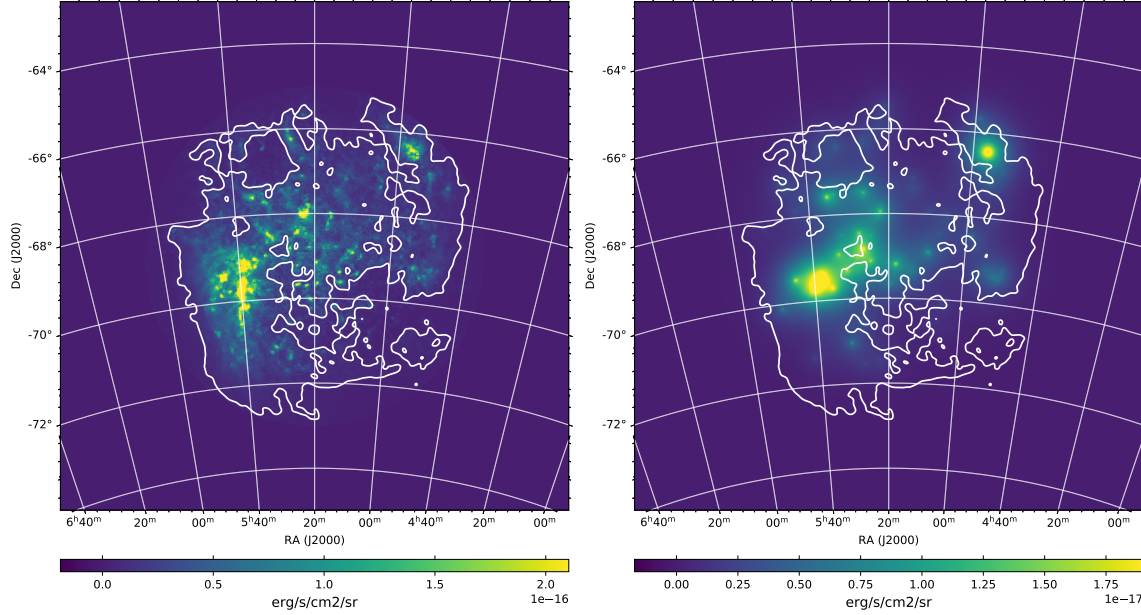


Figure 5.1: Mapcubes of the diffuse components of the LMC model at 1 TeV, generated as described in section 5.2.1. *Left:* Pion-decay diffuse emission. *Right:* IC diffuse emission.

and only PWN ever detected outside the MW in  $\gamma$ -rays [224]. PWNe are the result of a supernova explosion, where a fast-rotating, highly-magnetized central pulsar powers a nebula of ultra-relativistic particles with its spin-down energy, i.e. the loss rate of rotational energy. The well known Crab PWN is an object of this kind, which seems to present large similarities with N157B. The central pulsar of this system, PSR J053-6910 was first discovered in X-ray energies and seems to be the most powerful pulsar known, with a spin-down power of  $\Delta E = 4.9 \cdot 10^{34}$  erg s $^{-1}$  [225]. The TeV  $\gamma$ -ray emission of this kind of objects is directly connected to their spin-down power and has its origin in the IC scattering of lower energy photons by relativistic electrons (and positrons). Besides its extremely high power, the emission from N157B can be detected despite its large distance ( $\sim 48\text{kpc}$  [226]) because it is embedded in the strong infrared photon-fields from nearby sources of the superbubble formed by the stellar association LH99, which serve as additional targets for IC scattering. To model this source, we follow the results from [200], where the multiwavelength data (X-rays from Chandra [227] and  $\gamma$ -rays from *Fermi*-LAT and H.E.S.S.) can only be explained with a leptonic IC model where the highest possible magnetic field should be  $45\mu\text{G}$ . The spectral model adopted for this source is shown in figure 5.2.

### Supernova Remnant N132D

Both *Fermi*-LAT and H.E.S.S. have detected *gamma*-ray emission with strong evidences to belong to the SNR N132D, a very bright thermal X-ray remnant. It is the brightest remnant of the LMC and belongs to a rare type of oxygen-rich remnants

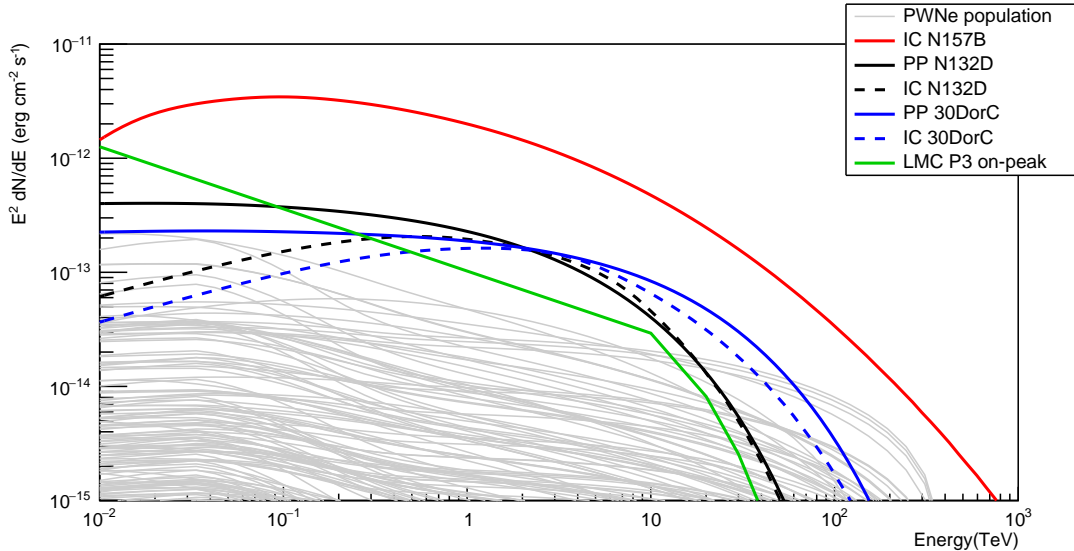


Figure 5.2: Spectral energy distribution of the point sources in the LMC. Spectra from N157B, N132D and 30DorC are extracted from [200]. Spectrum of LMC P3 is a power-law with the spectral parameters of the on-peak orbital region from [203], with an exponential cut-off at 10 TeV. Spectra from the PWNe population are derived following the baseline model described in section 5.2.3

which show optical emission from pure heavy-element ejecta, similar to the MW SNR Cas A [228]. The origin of this SNR, deduced by its chemical composition, is the core-collapse supernova of a massive progenitor star of mass  $> 35M_{\odot}$  [228]. The origin of the  $\gamma$ -ray emission yields on the interaction of the supernova shock with the cloud of dense material ejected by the progenitor star during its lifetime. The flux detected by H.E.S.S. [200], with a  $\gamma$ -ray luminosity in the 1-10 TeV band of  $0.9 \pm 0.2 \times 10^{35}(d/50kpc)^2$  erg/s, allow to contemplate the possibility of two origins of the radiation: In the hadronic scenario the flux of  $\gamma$ -rays is produced by the decay of neutral-pions, which would imply a remarkably high fraction of energy injected to cosmic rays by the supernova explosion, or a gas density higher than the one expected from X-ray observations. Either possibility is plausible given the observations in the optical and infrared bands, which reveals a structure produced by the interaction of the remnant with shocked interstellar gas [229]. In the leptonic scenario,  $\gamma$ rays are produced by IC scattering of low energy-photons. This model could be supported by the high synchrotron radio emission in radio and X-rays, however, it would require a lower magnetic field than the one inferred from radio observations ( $20\mu G$  vs.  $40\mu G$ ). The fluxes and spectral index measured by *Fermi*-LAT in [196] seem to rule out this model.

For this work, we assume the hadronic (PP) model shown in figure 5.2 based on H.E.S.S. measurements.

### **Superbubble 30 Dor C**

The Superbubble 30DorC, detected by H.E.S.S. in the VHE range, is a radiation emitting shell which stands out in X-rays, being the largest X-ray synchrotron shell known (with a radius of 47pc) [230], and also emits radio and optical radiation [231]. Its origin seems to be related to the stellar winds and supernovae of the stellar association LH 90 [232]. Both leptonic and hadronic scenario could explain the  $\gamma$ -ray flux detected by H.E.S.S. from this source as discussed in [200]. The two models are shown in figure 5.2. For this work we tested both models, existing the possibility that CTA observations from 100 GeV will be able to set which is the most probable model, thanks to the slope differences up to 1 TeV.

### **Binary system LMC P3**

This object was first detected by *Fermi*-LAT at HE energies in [196], but was classified as an unidentified source in the environment of the HII regions NGC 2029/NGC2032. They measured a very soft power-law spectrum (index  $\sim 2.8$ ) but did not notice any variability down to a monthly basis. Later, emission from this object in the VHE range was detected by H.E.S.S. [203]. They discovered a variability of 10.3 days period, classifying the object as the first extragalactic  $\gamma$ -ray binary system. The position of LMC P3 is consistent with a soft X-ray source, which variability of X-ray flux and radial velocity of Balmer absorption lines confirmed that it is very likely a binary system [233], [234]. From optical radial velocity measurements, it is derived that the system must be composed by a neutron star with an O5III star companion [235].  $\Gamma$ -ray binaries are believed to be a brief phase of the evolution of high-mass X-ray binaries, in which the  $\gamma$ -ray emission dominates the electromagnetic output [236].

The spectrum of LMC P3 (HESS J0536-675) was fitted by H.E.S.S. to a simple power law of the form  $\frac{dN}{dE} = \Phi_{1TeV} \left(\frac{E}{1TeV}\right)^{-\Gamma}$  with an on-peak spectral index  $\Gamma$  of 2.1, and an off-peak index of 2.4, where on-peak represents the orbit region where most of the  $\gamma$ -ray radiation is emitted. The detection of the source only achieved enough statistical significance during the on-peak period.

For simplicity in this work, we will assume the on-peak spectral parameters of the source without any temporal modulation ( $\Gamma = 2.1$ ,  $\Phi_{1TeV} = 5 \cdot 10^{-13} cm^{-2}s^{-1}TeV^{-1}$ ). The justification is that the on-peak orbital phase lasts for  $\sim 50h$ , which is way below the total observation time assigned to the LMC survey. A test on the possibility of detecting the off-peak emission with CTA, in the shape of an upper limit, was also carried on and results are given in section 5.4.

#### **5.2.3 PWNe population in the LMC**

PWNe are the predominant class of TeV emitters in our Galaxy, with more than 30 sources detected up to date [237]. If we assume that the same is true for the LMC, we can model a typical PWNe population reproducing the so called *baseline* spectral model, first introduced by [238] and revised by [239]. The model is a one-zone, time-dependent model which allows to trace the evolution of VHE lepton population and hence, radiative output of a PWN. In the model, the number of leptons with

Parameter description			Parameter values
Braking index	n		3.0
Initial spin-down power	$\dot{E}_0$	( $10^{39}$ erg s $^{-1}$ )	2.0
Initial spin-down timescale	$\tau_0$	(kyr)	0.5
Initial magnetic field strength	$B_0$	( $\mu$ G)	200
Reverse shock interaction timescale	$\tau_{rs}$	(kyr)	4.0
PWN radius at t=3kyr	$R_3$	(pc)	6.0
Adopted const. ISM magn. field strength	$B_{ISM}$	( $\mu$ G)	3.0
Lepton conversion efficiency	$\eta$		1.0
Index of magnetic field evolution	$\alpha$		0.6
Index of lepton injection spectrum	$\beta$		1.75, 2.0, 2.25
Lower bound of lepton energy distribution	$E_{min}$	(TeV)	0.03
Upper bound of lepton energy distribution	$E_{max}$	(TeV)	300

Table 5.1: Parameters used for the modelling of the PWNe population, based on table A.1 from [239].

energy  $E$  residing in the nebula at time  $t + \delta t$  will be determined by the balance between the injected leptons and those cooled out in the respective energy interval:

$$\frac{dN}{dE}(E, t + \delta t) = \frac{dN_{cooled}}{dE}(E, t + \delta t) + \frac{dN_{inj}}{dE}(E, t + \delta t) \quad (5.1)$$

Where for the number of injected leptons  $dN_{inj}/dE$  a power-law spectral shape is assumed:

$$\frac{dN_{inj}}{dE}(E, t) = \Phi_0(t) \left( \frac{e}{1TeV} \right)^{-\beta} \quad (5.2)$$

with a power-law index  $\beta$ , also known as injection index. The normalization  $\Phi_0(t)$  will depend on the amount of spin-down energy converted into relativistic electrons and positrons in a time step  $t + \delta t$ . The cooling mechanisms comprise synchrotron escape and adiabatic losses, and the number of cooled leptons can be approximated by:

$$\frac{dN_{cooled}}{dE}(E, t) = \frac{dN}{dE}(E, t - \delta t) \cdot \exp \left( -\frac{\delta t}{\tau_{eff}(E, t)} \right) \quad (5.3)$$

Where  $\tau_{eff}$  is the effective cooling timescale, which will depend on the time evolution of the PWN radius and magnetic field strength.

The baseline model requires a series of parameters which are listed in table 5.1:

Three equally probable values of the injection index  $\beta$  have been considered, and the interstellar magnetic and radiation fields have been adapted to the average

conditions in the LMC.

The population of PWN has been generated considering that pulsars are born at a rate of  $r_{CC} = 0.0011SNyr^{-1}$ , in agreement with the assumed rate of SNe explosion and ratio of core-collapse to thermonuclear SNe, assuming that all core-collapse SNe lead to the formation of a spinning neutron star. The lifetime for each PWN is approximated as of  $\tau_{PWN} = 200kyr$ , which yields to an average number of  $r_{CC} \times \tau_{PWN} = 220$  PWNe in the LMC if the pulsar creation is in steady state during the time  $\tau_{PWN}$ . The following steps have been carried on to generate the synthetic population of PWNe:

- (i) Draw a random number of objects from a Poisson distribution with mean  $r_{CC} \times \tau_{PWN}$ .
- (ii) Draw random ages from a uniform distribution over 0 to  $\tau_{PWN}$ .
- (iii) Random select an injection index among the three values considered, listed in table 5.1.
- (iv) From the baseline spectral model, compute the spectra of all objects given their ages and injection indices.
- (v) Distribute them spatially among the different massive star forming regions, in proportion to their ionizing luminosity.
- (vi) Add some luminosity scatter to reflect the properties of the observed PWNe population in the MW.
- (vii) Apply two cuts in the synthetic population: First, remove objects younger than 2kyr, because we already know at least two objects of that age (SN 1987A and N158A); second, remove all objects with  $> 1\text{TeV}$  luminosity above  $2.2 \times 10^{34}$  erg s $^{-1}$ , because they would have been detected by H.E.S.S. already, as shown in the upper limits calculated for SN1987A in [223].

The total number of 189 PWNe have been included in the simulated model, and their spectral energy distributions are shown in figure 5.2. A mapcube of the emission of the PWNe population at 1 TeV is shown in picture 5.3.

## 5.3 Simulations and Analysis method

### 5.3.1 Region of Interest and Observational strategy

As before mentioned, the Region of Interest (ROI) of the LMC extends about 10° in the sky. In order to reach this large field of view (FoV), CTA will adopt a novel survey mode, which is an observational technique never applied before by Imaging Atmospheric Cherenkov Telescopes (IACTs). It will consist on covering the full region by a series of slightly overlapping pointings with a FoV of ∼ 3° each. The total amount of hours assigned to the LMC survey is 340h plus 150h more in case the SNR 1987A is detected. For this work, different pointing patterns have been tested in order to adopt the observational strategy which will maximize the significance of detection both for point sources and extended sources, for a total observation time of 340h. The final scheme consist on 7 pointings of ∼ 1.75 × 10<sup>5</sup>s each, arranged in 3 rows with a 2-3-2 configuration centered in the coordinates RA=80.0°, dec=-69.0° with a separation of 2° between pointings, as shown in figure 5.4. In this observation

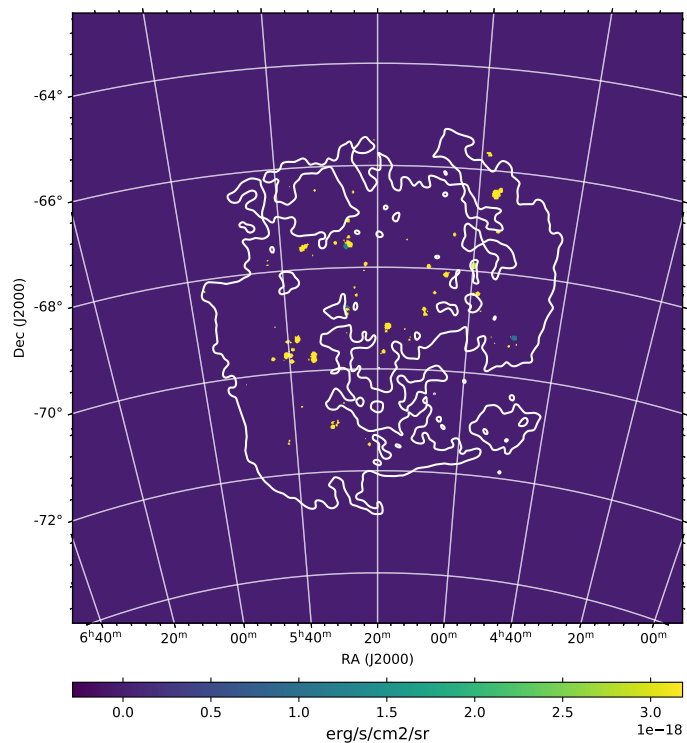


Figure 5.3: Mapcube of the PWNe synthetic population generated as described in section 5.2.3 at 1 TeV.

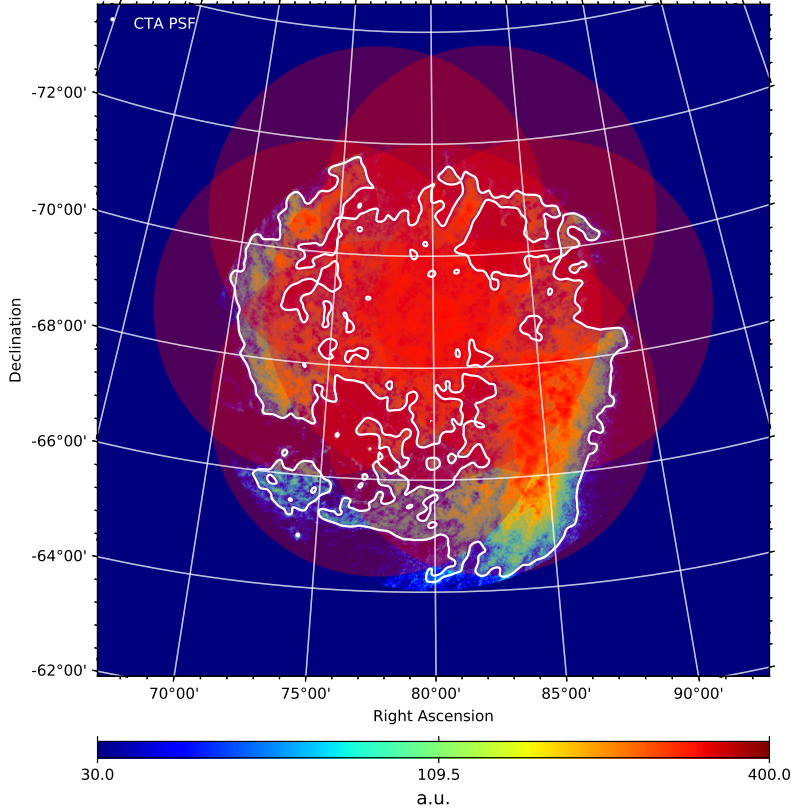


Figure 5.4: Skymap of the region of interest of the LMC. The pointing pattern is overlapped in the shape of red circles.

mode, all telescope types of CTA South are involved.

### 5.3.2 Simulation parameters

To calculate the predicted number of counts from a certain emission model, the CTA collaboration provides a set of IRFs [152] with information about the effective area and angular resolution of the instrument for several zenith angles. For this work we have used the IRF *South\_z40\_50h* from the production *prod3b-v2*. This IRF only accounts for the southern observatory and is optimized for zenith angles around 40° (LMC will be seen at  $\sim 46^\circ$  from the southern site) and 50h observations.

To perform the simulations of the predicted number of counts using the mentioned pointing pattern and IRF we use *ctools* and *gammalib* [240], a software framework for the analysis of astronomical  $\gamma$ -ray data, specifically designed for CTA. The tool *ctobssim* uses a Monte Carlo (MC) generator to recreate event lists for observations. As input, it requires a full model of the ROI, including each individual source with a spatial and spectral component, and a model of the instrumental background accounting for cosmic-ray events misidentified as  $\gamma$ s. Also, *ctobssim* requires the IRF for the observation and the desired energy range must be specified. Each running of

*ctobssim* results in a realization of the model where the event list is generated with a random number generator. We have performed realizations of the full emission model of the LMC with the pointing pattern described before, in the energy range from 0.05 TeV to 150 TeV. *Ctobssim* is able to combine the different observations of the overlapping pointings, averaging the IRFs of each region. The resulting event lists are written into FITS files, one for each pointing, which can be combined afterwards for the analysis.

The tool *ctmodel* uses the resulting event lists from *ctobssim* and the emission model to calculate an averaged expected number of events. Instead of one realization of the model, it represents the expected number of counts that will be obtained by an infinitely large number of realizations. The result is a counts map, where the averaged number of counts is given for each spatial pixel and for each energy bin.

### 5.3.3 Fitting method

A binned likelihood analysis has been performed in this work, to fit the emission model to the simulated data. The event lists for the 7 pointings have been combined and then the data has been binned into  $\sim 110$  energy bins. The boundaries of the energy bins have been generated using the *ctools* function *csbins*, which inspects the variation in the effective area and background template of the IRF for the specific simulations, according to a threshold settled by the user. To ensure a sufficiently large number of energy bins (it is recommended to have at least 30 bins per decade), the threshold for the fractional change in effective area has been settled to 0.06, and to 0.16 for background rate.

The energy range chosen for the analysis is from 100 GeV to 100 TeV. The higher lower limit, compared to the full range of CTA (which can go down to 30 GeV) comes from the limitations of performance at high zenith angles, given that LMC will be always observed at  $z > 40^\circ$ . For the combination of data the procedure for stacked analysis of *ctools* has been followed, where the binned counts map of the data is produced using the function *ctbin* and then the combined background model, the exposure cube and the point spread function cube are precomputed using the functions *ctbkgcube*, *ctexpcube* and *ctpsfcube* respectively. The results are a series of mapcubes which will be used to calculate the maximum likelihood function.

A so-called *Asimov* data set has been computed to produce the results presented in this chapter. The *Asimov* data set [241] is a representative data set which, when fitted, will retrieve the true values of the model parameters. It can be computed with *ctools* using the function *ctmodel*, and allow to give mean results for significance and upper limits without needing a large number of realizations of the simulated data.

The mapcube of the Asimov dataset produced for this analysis is shown in picture 5.5 for the 0.975-1.04 TeV energy bin.

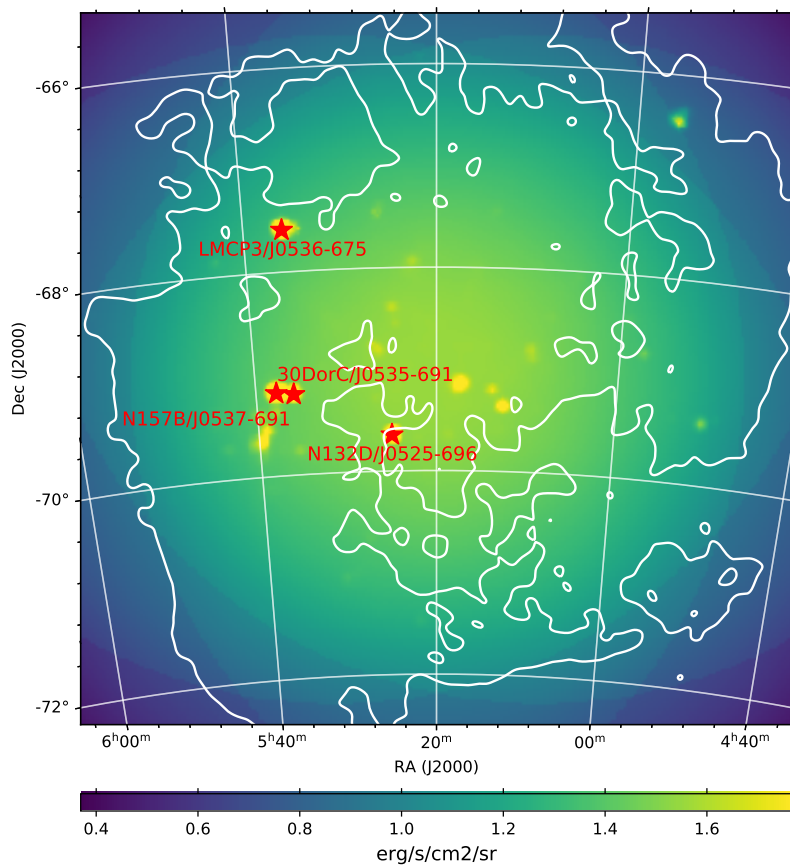


Figure 5.5: Asimov mapcube at the energy bin 0.975-1.04 TeV produced with the full emission model of the LMC described in section 5.2. The four point sources are marked with red stars.

### 3D Likelihood Analysis for $\gamma$ -ray sources

The likelihood analysis is based in the typical Poisson likelihood function:

$$\mathcal{L}(\mu|n) = \prod_{i,j} \frac{\mu_{ij}^{n_{ij}}}{n_{ij}!} e^{-\mu_{ij}} \quad (5.4)$$

Where  $n_{ij}$  represents the simulated counts and  $\mu_{ij}$  the model prediction for each bin in energy(i) and space (j). The model  $\mu_{ij}$  is the result of the combination of the models for each of the  $\gamma$ -ray sources described in section 5.2. Each source accounts for a spectral model and a spatial model. For extended sources, both components are combined in one mapcube. In the likelihood fitting the only free parameter for each of these models is the normalization  $A^X$ , which determine the relative weight of component  $X$ . The only exception is the point source LMC P3, which spectral model is a power-law where the free parameters are the normalization and the spectral index. The shape of  $\mu$  is:

$$\mu_{ij}(A^X) = \sum_X A^X \mu_{ij}^X + A^{LMCP3}(E)^{-\Gamma} \quad (5.5)$$

The maximum likelihood is calculated finding the normalization parameters  $A^X$  which maximize equation 5.4.

The detection significance of a source is calculated in terms of the Test Statistics:

$$TS = 2\log \frac{\mathcal{L}(\mu(A^X)|n)}{\mathcal{L}_{null}} \quad (5.6)$$

Where  $\mathcal{L}(\mu(A^X)|n)$  is the maximum likelihood function and  $\mathcal{L}_{null}$  is the value of the likelihood function of the null hypothesis for the specific source (meaning  $A^X = 0$ ). With this definition, typically a source is considered to be detected when  $TS > 25$ , equivalent to  $5\sigma$ .

The maximum likelihood analysis has been performed using the function *ctlike* from *ctools*. The inputs are the data mapcubes from the stacked analysis and the description of the emission model. For the likelihood fit the same emission model used for the simulations is given as input, meaning that the fitting results will represent the most optimistic case, where the model is perfectly describing the data. *ctlike* calculates the best fit parameters ( $A^X, \Gamma$ ) and the TS values for the requested sources (setting the variable *tscalc*=”1”).

### Upper limits calculation

For sources which have a flux too low to be detected ( $TS < 25$ ) we calculate upper limits on the minimum flux needed for the source to be detected with CTA. We calculate this upper limits as the flux that leads to a decrease in the likelihood that corresponds to a certain Confidence Level (CL). Using the definition of TS from

5.6, according to Wilks' theorem [242], the TS function asymptotically approaches a  $\chi^2$ -distribution with one degree of freedom under the null hypothesis, therefore to get the flux that yields to the 95% CL upper limit, we must find the normalization parameter  $A_{max}^X > A^X$  which corresponds to  $TS = 2.71$ .

This calculation is performed using the function *ctulimit* from *ctools*, which requires as input the mapcube of the simulated data and a model with all the sources, including the source for which the upper limit will be calculated. In this case, we use the model resulting from the maximum likelihood fit. The only free parameters must be the normalizations. The results from *ctulimit* are the upper limit in the differential flux for a reference energy, the integrated upper flux limit for a specific energy range and the integrated upper energy flux limit for the same range.

We have used this method to set constraints on the DM annihilation cross section  $<\sigma v>$  as described in section 5.5.

## 5.4 Results

### 5.4.1 Point sources

The results for the fitting of the four point sources tested in this work are given in table 5.2. The significance of detection of the sources is given in terms of the Test Statistics described in the previous section. For LMC P3 three cases have been tested: The case of a spectrum following a power-law with the on-peak parameters from [203]; the same power-law but with an exponential cut-off at 10 TeV; and a last case where no source has been simulated, but an upper limit on the flux for a source with the off-peak spectral index has been computed in the energy range 0.1-100 TeV. Also, energy flux upper limits for three energy ranges are shown in figure 5.7.

The point sources have been fitted in the full energy range to the same models used for simulation, where the only free parameter is the spectral normalization. The results show that CTA will be able to detect with high significance all the known point sources in the LMC, including the binary system LMC during the on-peak orbital region, and will be able to test the flux of the off-peak region.

### 5.4.2 Population of PWNe

For the fitting of the PWNe population, a mapcube including all the artificially computed candidates has been used for simulation. Then, each PWN spectrum has been fitted individually, keeping all the rest of the PWNe and other model components fixed. The results show that 15 from the total of 189 simulated PWNe would be detected with  $TS > 25$ , giving an estimation of the number of new PWNe that could be discovered by CTA. Also, 12 more PWNe were fitted giving a  $TS > 9$  ( $3\sigma$  significance). It must be taken into account that this is a very optimistic result, giving that the true spectrum and position of each PWNe is being used for fitting. In reality, a totally blind search will be performed, scanning the full region in the search for excesses, and assuming a generic spectral shape. The results on the PWNe are shown

Source name	RA( $^{\circ}$ )	Dec( $^{\circ}$ )	Normalization ( $0.1 - 100 TeV$ )	TS	Significance( $\sigma$ )
Point Sources					
N157B/HESS J0537-691	84.44	-69.18	$1 \pm 0.005$	130951.51	$361.9$
N132D/HESS J0525-696	81.26	-69.64	$1 \pm 0.019$	5370.19	$73.3$
30DorC/HESS J0535-691 (PP)	83.96	-69.2	$0.999 \pm 0.022$	4762.83	$69.0$
30DorC/HESS J0535-691 (IC)	83.96	-69.2	$0.999 \pm 0.022$	3919.0	$62.6$
LMCP3/HESS J0536-675 (on-peak, cut-off 10 TeV)	84.0	-67.59	Prefactor: $4.99 \pm 0.05 \cdot 10^{-19}$ ( $cm^{-2}s^{-1}MeV^{-1}$ ) Index: $2.1 \pm 0.01$	27353.83	$165.4$
LMCP3/HESS J0536-675 (on-peak)	84.0	-67.59	Prefactor: $4.99 \pm 0.05 \cdot 10^{-19}$ ( $cm^{-2}s^{-1}MeV^{-1}$ ) Index: $2.1 \pm 0.006$	48021.95	$219.14$
LMCP3/HESS J0536-675 (off-peak)	84.0	-67.59	Int. flux ulimit (99 % CL): $1.23 \cdot 10^{-13}$ ( $cm^{-2}s^{-1}$ )	-	-
Diffuse emission components					
LMC Pion-decay	-	-	$1 \pm 0.185$	29.06	$5.39$
LMC IC	-	-	Int. flux ulimit(99% CL): $7.33 \cdot 10^{-12}$ ( $cm^{-2}s^{-1}$ )	-	-

Table 5.2: Results of the fit for the point sources and diffuse components included in the emission model. For the first three sources, the normalization of the spectrum is the only free parameter to fit. For LMCP3, a power-law spectrum with exponential cut-off at 10 TeV has been fitted, accordingly with the results of [203]. For the off-peak region, the upper limit at 99% CL for the integrated flux has been calculated. From the diffuse components, only the hadronic emission could be detected at  $TS > 25$  therefore an upper limit has been computed for the leptonic IC component.

in figure 5.6, showing the fitted flux compared to the true flux, and the TS value vs. the true flux.

### 5.4.3 Diffuse Emission

The diffuse emission models for pion-decay and IC scattering have been fitted as mapcubes where the only free parameter left is the normalization. The fit in the full energy range has resulted in a positive detection for the pion-decay component, with a mean TS value of 29.06 ( $5.39\sigma$  significance). For the IC component, the TS obtained is 0.282, resulting in a non-detection. Upper limits for this model have been calculated instead, giving an upper limit at 99% confidence level in the integral flux limit of  $7.33 \cdot 10^{-12} \text{ ph cm}^{-2}\text{s}^{-1}$  in the range 100 GeV-100TeV. In figure 5.7, energy flux upper limits for three energy ranges (0.1-1 TeV, 1-10 TeV, 10-100 TeV) are shown.

## 5.5 Dark Matter annihilation in the LMC

In this section, forecasts on the detection of an additional component of the diffuse  $\gamma$ -ray emission in the LMC, due to the annihilation of DM are developed. The assumption on the DM model is that it is composed by stable particles which can annihilate and produce a shower of SM particles, which in turn would lead to either direct or secondary production of  $\gamma$ -rays, as explained in section . The range of energies for this process can go from a few GeV to several TeV, making it potentially observed by CTA.

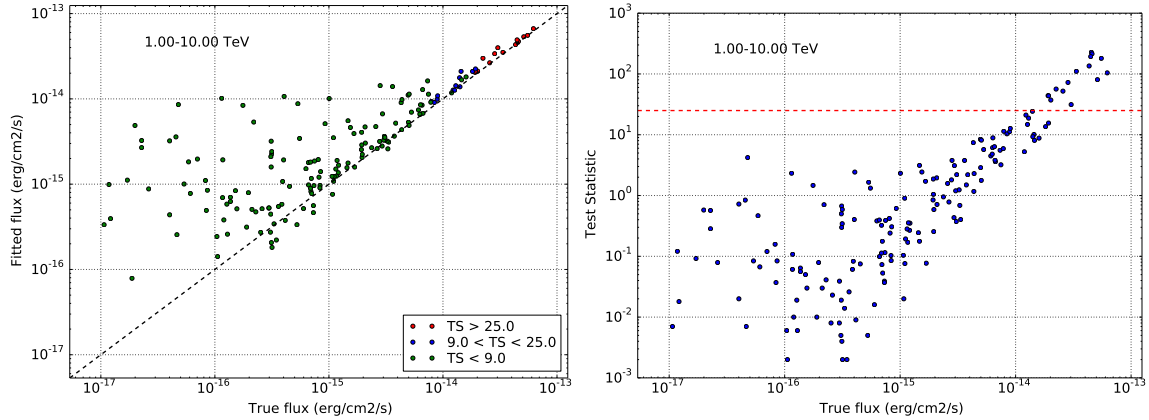


Figure 5.6: *Left:* True flux vs. fitted flux for the synthetic population of PWNe. Each PWN has been fitted individually, keeping the rest of the model components fixed. *Right:* TS value vs. true flux of the PWNe population. Red line corresponds to TS=15 (5 $\sigma$  detection significance).

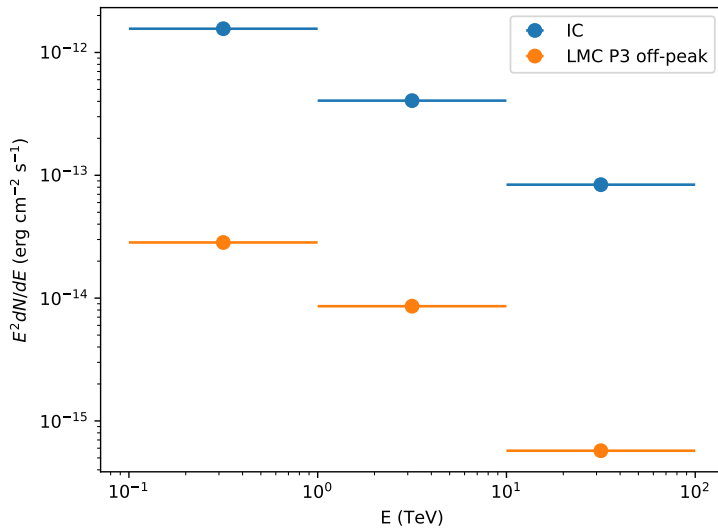


Figure 5.7: Energy flux upper limits computed for the IC diffuse component and LMC P3 off-peak model in three energy ranges.

It must be taken into account that there exists plenty of DM candidates in the literature [243], [244], [245], but in this work the model of WIMPs is the one considered.

The goal is to explore whether CTA will be able to observe the annihilation of WIMPs in the LMC, or in the negative case, what constraints on DM candidates will it set. The flux of  $\gamma$ -rays produced by DM annihilation was presented in equation 5.7, shown again here for convenience:

$$\frac{d\Phi}{dE} = \frac{1}{8\pi} \frac{\langle \sigma v \rangle}{m_\chi^2} \frac{dN_\gamma}{dE} \int_{\Delta\Omega} \int_{l.o.s} dl \rho^2(\vec{l}) \quad (5.7)$$

Where  $dN/dE$  is the spectrum of  $\gamma$ -rays from annihilation of a pair of dark matter particles,  $\langle \sigma v \rangle$  is the thermal velocity averaged annihilation cross section,  $m_\chi$  is the DM particle mass and  $\rho$  is the dark matter density profile. If DM particle is not its own antiparticle, equation 5.7 should be multiplied by a factor 1/2.

Along the full analysis, the mass of the DM particle and the annihilation cross section will be treated as free parameters. A single annihilation spectra will be assumed where the branching ratio of the reaction is one, meaning that the entire annihilation happens in a specific channel. The results will be presented in the shape of sensitivity curves where the minimum annihilation cross section needed for detection is plotted against the mass of the DM particle for a specific annihilation channel and DM profile.

### 5.5.1 Dark Matter profile in the LMC

The DM distribution of the LMC can be inferred by the gravitational structure of its disk, following the rotation curve method. Assuming circular orbits, the mass of a galaxy enclosed in a certain radius can be calculated thanks to the rotation velocity,  $v_{rot} = GM(<r)/r$ . Measurements of the rotation velocities of stars and gas in the LMC allow to calculate the total mass [246], and subtracting the contribution to the rotation curve of the luminous matter, the remaining DM can be estimated. The dark matter profiles used in this section rely on the works of [247], where the gas mass component of HI+He as a function of the radius is taken from [248]; and the stellar mass is extracted from [122]. The rotation curve of the LMC can be seen in picture 5.8.

A generalized six-parameter Hernquist-Zhao DM profile has been adopted for this work [249], [37], following equation 5.5.1 already shown in section 5.5, repeated here for convenience:

$$\rho(r) = \frac{2^{\frac{\beta-\gamma}{\alpha}} \times \rho_0}{\left(\frac{r}{r_s}\right)^\gamma \left[1 + \left(\frac{r}{r_s}\right)^\alpha\right]^{\frac{\beta-\gamma}{\alpha}}} \Theta(r_{max} - r) \quad (5.8)$$

Where  $\Theta$  is the Heaviside step function,  $r_s$  is the scale radius and  $\rho_0$  is the characteristic density. These two last parameters depend on the specific DM halo.

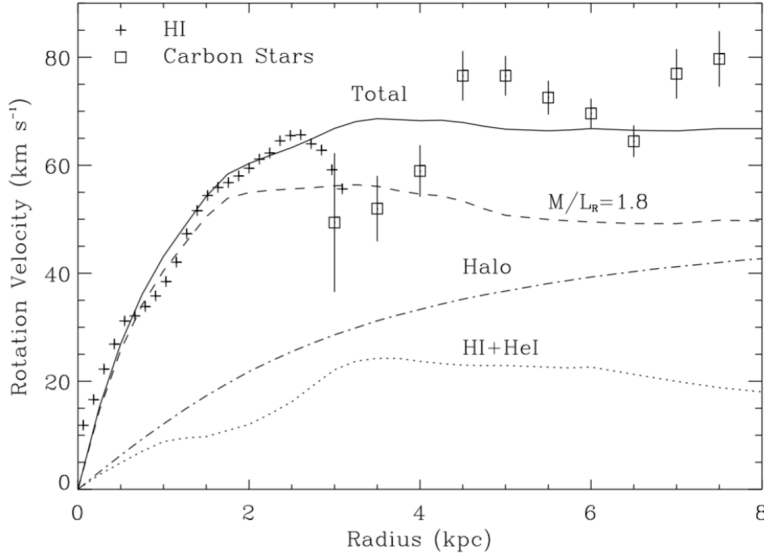


Figure 5.8: Rotation curve of the LMC, from [246]. The solid black line is the total predicted rotation curve constructed from the following components: (a) HI mass distribution from [248], and a 30% He contribution (*dotted line*). (b) R stellar light distribution based on the data from [250] and  $M/L_R = 1.8$  (*dashed line*). (c) Pseudoisothermal dark halo with core radius 2.5 kpc and central density  $0.009 M_\odot \text{pc}^{-3}$ .

Setting  $(\alpha, \beta, \gamma) = (1, 3, 1)$  we retrieve the Navarro-Frenk-White (NFW) profile [38]. An isothermal profile is obtained setting  $(\alpha, \beta, \gamma) = (2, 2, 0)$ . Variations of these two profiles have been tested, with their parameters shown in table 5.3 and plotted in figure 5.9. For the NFW profile, a more cuspy profile with  $\gamma = 1.5$  and a more cored profile, with  $\gamma = 0.5$  are tested. In the case of the isothermal profile, the scale radius is varied from the iso-mean profile with  $r_S = 2.4$  (kpc) to iso-max with  $r_S = 3$  (kpc) and iso-min with  $r_S = 1$  (kpc).

The DM profiles were simulated using the software *clumpy*, a code for  $\gamma$ -ray and neutrino signals from DM structures [251]. It allows to compute simulations of DM halos characterized by a series of parameters depending on the DM profile. *Clumpy* was used in this work to simulate maps of the J-factor in the region of the LMC in order to create the spatial distribution of the different DM models, which afterwards were combined with the spectra of several annihilation channels to reproduce the  $\gamma$ -ray flux in the LMC. The 2D J-factor of the different profiles used in this work, computed with *clumpy* can be seen in figure 5.10.

### 5.5.2 $\gamma$ -ray spectrum

For the spectral part of the DM emission model ( $dN_\gamma/dE$  in equation 5.7), the recipes from [216] were used, where the energy spectra of  $\gamma$ -rays produced by different DM annihilation channels are provided. For this thesis, the studied channels were  $b\bar{b}$ ,  $W^+W^-$ ,  $\tau^+\tau^-$ ,  $\mu^+\mu^-$  including electro-weak corrections as computed in [252], and

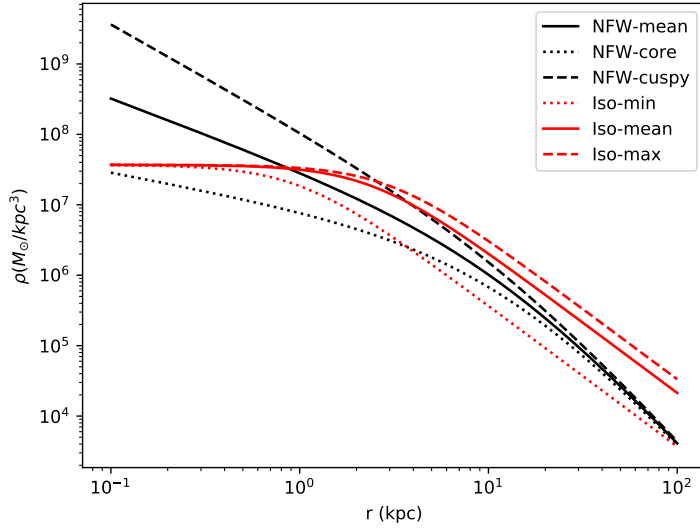


Figure 5.9: DM profiles plotted against the radius  $r$  from the LMC center, with the parameters listed in table 5.3.

Profile	$\alpha$	$\beta$	$\gamma$	$r_S(kpc)$	$\rho_0(M_\odot/kpc^3)$	$J(10^\circ)(GeV^2/cm^5)$
NFW-mean	1	3	1	12.6	$2.6 \times 10^6$	$1.36 \times 10^{21}$
NFW-core	1	3	0.5	12.6	$2.6 \times 10^6$	$5.13 \times 10^{20}$
NFW-cuspy	1	3	1.5	12.6	$2.6 \times 10^6$	$4.22 \times 10^{22}$
Iso-min	2	2	0	1	$3.7 \times 10^7$	$8.51 \times 10^{19}$
Iso-mean	2	2	0	2.4	$3.7 \times 10^7$	$9.71 \times 10^{20}$
Iso-max	2	2	0	3	$3.7 \times 10^7$	$1.74 \times 10^{21}$

Table 5.3: Parameters of the DM profiles used in this work. Values of NFW-mean and Iso-mean profiles are the same as of [247]. The  $J$ -factors are integrated over  $10^\circ$  from the halo center.

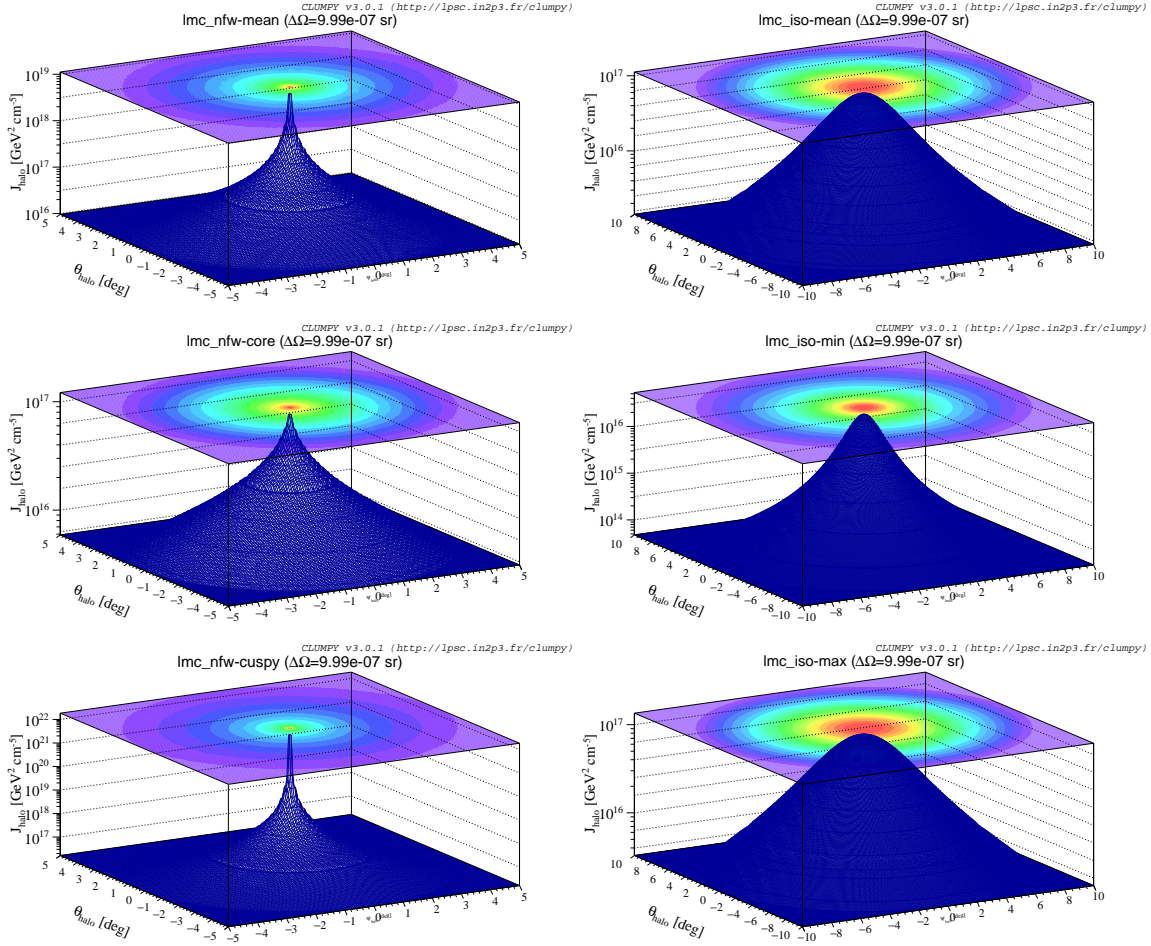


Figure 5.10: 2-D J-Factors of the LMC DM profiles probed in this work. The NFW and Isothermal profiles were computed using the same parameters as in [247].

their spectra can be seen in figure 5.11, computed for a set of DM particle masses.

### 5.5.3 Results on DM sensitivity curves

Using the DM profiles and spectra described in previous section, a likelihood analysis was performed to obtain the minimum flux needed for the LMC DM component to be detectable by CTA. The Asimov data set with the astrophysical  $\gamma$ -ray sources described in section 5.2 is used for this task as a background on top of which the flux needed to be emitted by each DM model in order to be detected is calculated. To do so, the procedure for upper limits calculation described in section 5.3.3 is applied. Each DM model is included in the fitted model as a new source, for which the differential upper flux limit for a reference energy, the integrated upper flux limit over the energy range 0.1 GeV-DM particle mass, and the integrated energy limit are calculated.

From the resulting flux  $\frac{d\Phi_{ulim}}{dE}$ , using equation 5.7, the velocity averaged annihilation cross section  $\langle \sigma v \rangle$  can be extracted. The sensitivity curves where  $\langle \sigma v \rangle$  plotted versus DM particle masses are shown in figure 5.12. Each curve corresponds to a specific DM profile and annihilation channel. The space above the curves represent the parameter space of  $\langle \sigma v \rangle$  and DM mass that could be detected by CTA.

## 5.6 Summary and conclusions

The deep survey of the LMC will be an ambitious task which will account for many challenges, but that will potentially provide many scientific results and new discoveries. Besides a lot of work can be done in the subjects until CTA is fully available, in this work the first hints on the possible results of the survey have been studied.

Regarding the known point sources observed by other  $\gamma$ -ray experiments, a remarkable high significance has been obtained for all of them, meaning they will be easily detected within the survey with a binned likelihood analysis, which will allow to characterize the sources spectra in the CTA range, at least over 100 GeV. Given the duration of the survey ( $>300$  h), it will also be possible to study the variability of LMC-P3, for which an upper flux limit for the off-peak emission has been derived. From the artificial population of PWNe introduced in the emission model, a big number of them have been fitted with a significance sufficiently large to be detected, providing an estimation of the number of new sources that CTA will be able to detect. The computed distribution of PWNe will serve as a trace for the blind search when dealing with real data from the survey.

One of the most interesting features of the LMC is the fact that, as an extended source, it is possible to study the structure of its  $\gamma$ -ray emission, allowing to probe models of CR injection and propagation. In this work, two models of diffuse emission of CR due to leptonic IC scattering and hadronic interactions leading to pion decay have been tested. The possibility to take into account the structure and distribution of CR sources in the LMC leads to the positive result on the detection of pion-decay emission following the model described in section 5.2.1. This is however a best-case

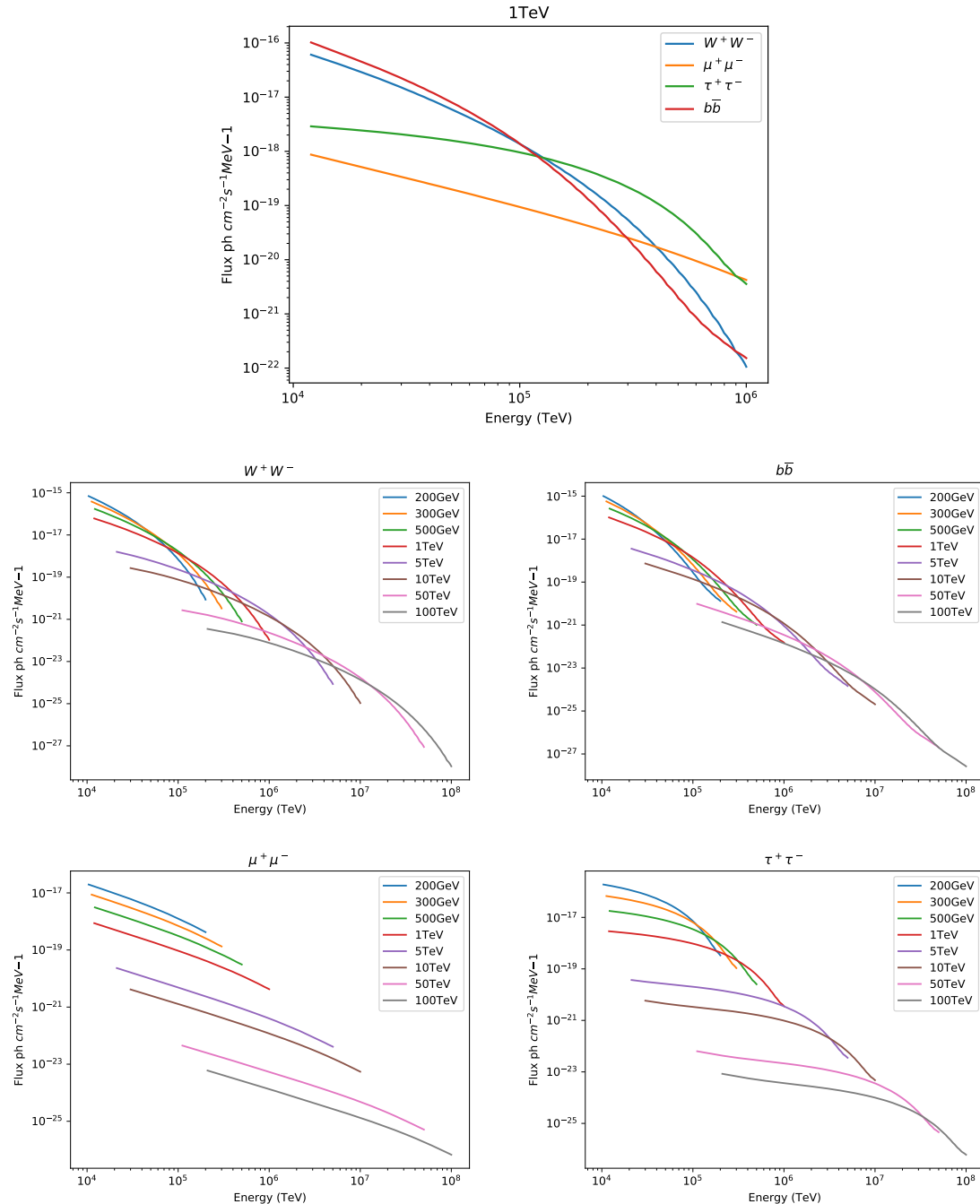


Figure 5.11:  $\gamma$ -ray spectra of DM pair annihilation, for different annihilation channels and masses of DM particle.

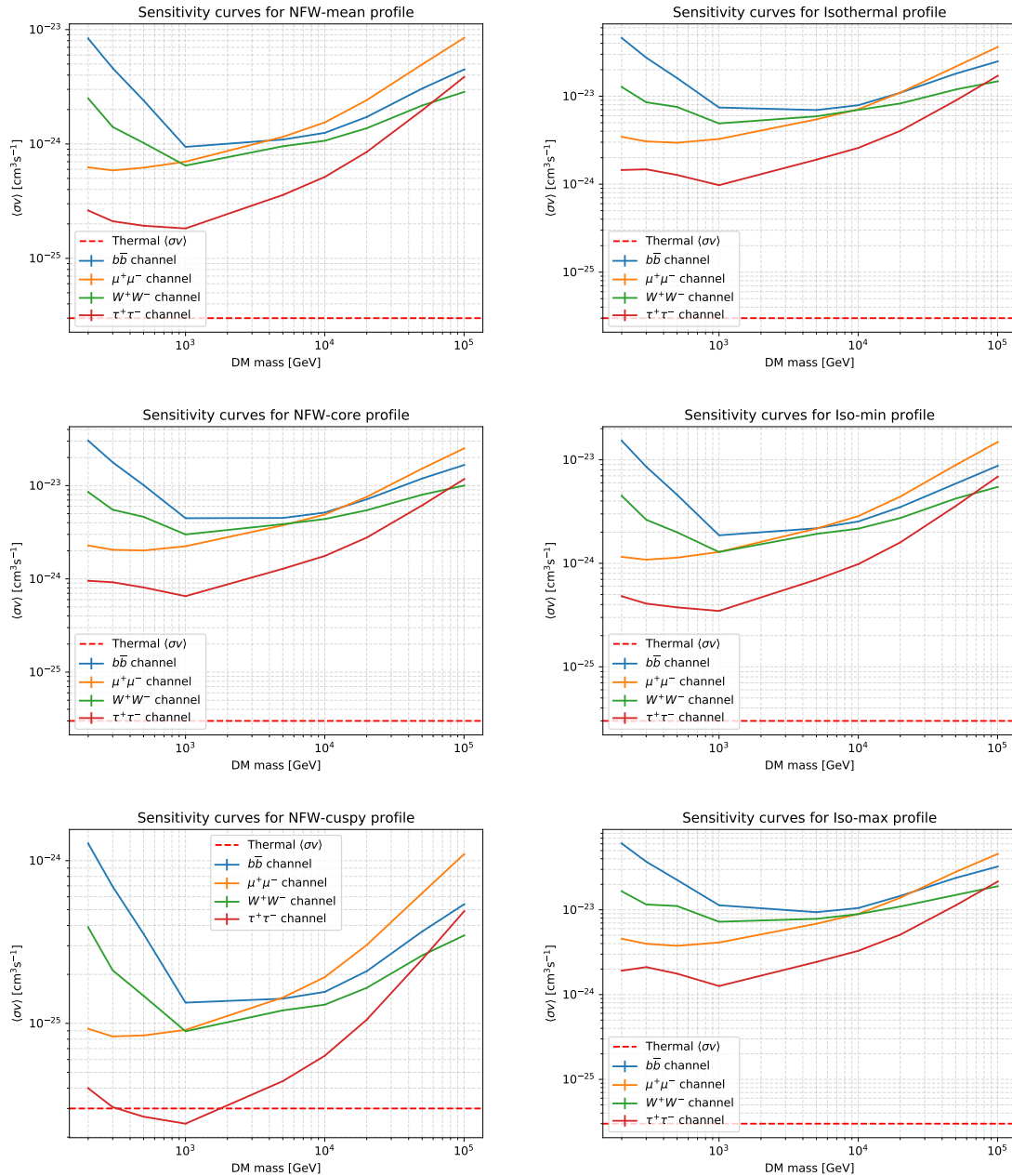


Figure 5.12: Sensitivity curves of  $\langle \sigma v \rangle$  vs. DM particle mass, resulting for the profiles listed in table 5.3, and for four annihilation channels:  $b\bar{b}$ ,  $W^+W^-$ ,  $\mu^+\mu^-$ ,  $\tau^+\tau^-$ .

scenario, where uncertainties in the model are not taken into account. However, it is an encouraging result to make efforts on the refinement of the analysis and model computation of the diffuse emission in the LMC for the future real data. The IC component, on the other hand, has resulted in a too low significance, meaning it would be not possible to disentangle this emission component from the rest of the background. An upper flux limit has been derived instead for this model.

Finally, prospects on the detection of a possible  $\gamma$ -ray signal from DM annihilation have been calculated. The results have established the parameter space of DM models which will be possible to study with CTA. The main reasons to point towards the LMC were its extended nature, which allow to rely on DM spatial structure for its differentiation from the background and its relatively high J-factor, comparable to other popular DM candidates such as Dwarf Spheroidal Galaxies (DSphe). However, the big population of other  $\gamma$ -ray emitters difficult the task of extracting a  $\gamma$ -ray signal coming from DM annihilation. In the results presented in this thesis, several DM profiles, annihilation channels and DM particle masses has been tested on top of the emission model of the LMC to compute the velocity averaged annihilation cross section needed for the model to be detected. It can be seen from picture 5.12, that the majority of the models lie several orders of magnitude over the canonical thermal cross section, which is the self-annihilation cross section of WIMP DM in the case of being a thermal relic. This result predicts that CTA will unlikely be able to exclude the canonical cross section for the typical WIMP DM models, except for the most cuspy ones(yet not very realistic) at DM masses  $\sim 1\text{TeV}$  (case of nfw-cuspy profile and  $\tau^+\tau^-$  channel).

The work performed within the scope of this thesis will serve as a starting point for the future work that can be done regarding the LMC KSP. The emission model developed to perform the predictions presented will serve as a benchmark for future studies and for the analysis of real data from the LMC survey. Other topics which have been left out of the scope of this thesis, but which still will benefit from its results could be: A more detailed and realistic study on the possible new discovered sources, performing a totally blind search over the PWNe population, setting a more realistic analysis approach. The PWNe model can also be used to study the possibilities of detecting TeV halos in the LMC, following a similar approach as [253]. Other known sources, not yet detected in the VHE range in the LMC, such as SNR 1987A can be studied on top of the emission model to predict its detectability within the LMC survey.



# A. The L1 Trigger System of the LST

## A.1 Introduction

Imaging Atmospheric Cherenkov Telescopes (IACTs) work detecting the Cherenkov light produced by the interaction of  $\gamma$ -rays and other particles in the atmosphere. This Cherenkov photons must be distinguished from those of the Night Sky Background (NSB) that fill the atmosphere, and constantly reach the telescopes. An efficient trigger system is necessary to decide whether the light reaching the camera must be stored as a Cherenkov event, or discarded as background.

Typically this task is accomplished by recognizing a concentration of signal from several pixels both in space and time, because showers are produced in a time window of a few nanoseconds, reaching a group of near pixels, while NSB light is randomly distributed over the entire camera.

Two possible approaches for the detection of coincident light are used in IACTs, known as *majority trigger* or *sum trigger*. In majority trigger the light of each pixel is compared to a certain threshold. If the signal of several (the majority of) pixels in a certain region exceeds the threshold in a short time, the trigger is fired. This approach presents a disadvantage when detecting low energy photon showers, as happens in Large Size Telescope (LST). The problem is that as the pixels must overcome the threshold individually, if the signal is too low, it is possible that some of them do not exceed the threshold and therefore the event would be mislead as NSB.

On the other hand, the sum trigger approach takes into account the total signal coming to a group of several pixels. The light arriving to each pixel of the group is added and this sum is compared to a threshold to fire the trigger. If several close groups of pixels surpass the threshold at a given time window, then the event is recorded as a shower event.

In the LST, a multilevel trigger system is implemented, that guarantees the rejection

of the majority of the NSB.

The pixels in the LST camera are distributed in 265 hexagonal modules of 7 pixels, that are connected to each of its 6 neighbours. The first trigger level (L0) sums the signal of the pixels in each module, and if it is higher than the configured threshold, it sends the L0 signal to the neighbouring modules. In the second trigger level (L1), each module takes the trigger signal coming from its neighbours and compares it to another threshold to decide if the camera trigger is fired. Finally, the third level compares the camera trigger of several telescopes and if two or more telescopes have triggered in a certain time window, the event is recorded. A scheme of the trigger system of LST is shown in picture A.1. In the next sections, a detailed description of the three trigger levels is given.

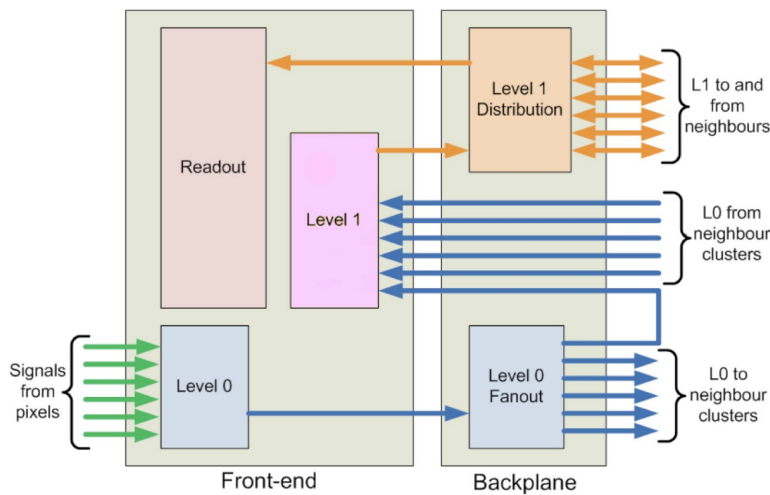


Figure A.1: Architecture of the analog trigger system of the LST.

## A.2 Pixel Level: L0 trigger decision

The pixel level trigger, known as L0, takes into account the signals from the pixels in one module or cluster. If the trigger is fired, the signal is replicated and distributed by the L0 fan out to the local L1 and to the neighbouring modules. Both, the majority and sum trigger approaches have been implemented in LST.

### A.2.1 Majority trigger

The majority approach counts the number of pixels in a module that have a signal over a certain threshold voltage, generating a digital signal. The signal from all the pixels is added, with a resulting amplitude proportional to the number of activated pixels, that goes to the local L1 trigger system, and to the neighbouring modules. This approach do not account for the number of photoelectrons that activated each

pixel, only for the number of pixels that have surpassed the threshold. This means that even if a large number of pixels in a region receive a flash of light, if in each pixel the amount of photoelectrons is not over the threshold, the event will not be recorded, possibly losing very low energy events.

### A.2.2 Sum trigger

The sum trigger adds the signal received in each pixel of the module and the resulting signal is compared with a threshold voltage. If the threshold is surpassed, the signal is sent to local L1 and neighbouring modules. This way makes it possible to take into account the photoelectron contribution of all pixels of the module, raising the sensitivity to low energy events while still rejecting NSB events. After adding the signals of all pixels, a clipping is applied to overcome afterpulse effects in the photomultipliers. Afterpulses are sometimes produced after a real pulse in the photosensors, due to the ionization of residual gases, and can contribute with a very high amplitude to the sum.

### A.2.3 Camera Level: L1 trigger decision

Camera level trigger decision system, known as L1, analogically adds the resulting signals of L0 trigger from neighbouring modules and compares the result with a threshold voltage. If the analog sum is over the configured threshold, a signal is sent to through the L1 distribution system to trigger the whole camera. Each module can combine the L0 fan-out signals from six neighbours, plus the local L1. To ensure that all modules are participating in the trigger and addings are made in an efficient way, it is possible to configure by slow control different modes where smart configurations of neighbouring signals are added. In figure A.2 the three possible modes are shown. These configurations make it possible, through combinations of two, three or four modules, to evaluate any trigger region.

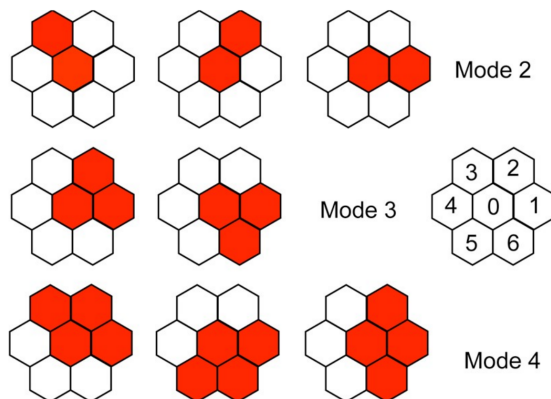


Figure A.2: Illustration of the three possible modes for adding signals of neighbouring modules. Each hexagon represents a group of seven photomultipliers.

The threshold voltages for each module should be calibrated, in order to find the threshold level which produce a trigger signal in a rate of the 50%. The calibration algorithm developed for LST camera, is described in appendix C.

### L1 Trigger Distribution

The L1 trigger distribution system allows the L1 signal to reach the data adquisition systems of all the modules and start the digitalizing process. Every module can propagate the L1 signal to each of its six neighbours, being aware of its position in the camera. This way, when a module receives a L1 signal, it can be delayed depending on the position in the camera, and be sent to the appropriate neighbours following the preconfigured paths (See figure A.3). The distribution paths are firmware configurable and they can automatically be reconfigured to go through the full camera, even if one module is malfunctioning or deactivated. The algorithm developed for the time delay calibration of the L1 signal, depending on the camera position of the modules, is described in appendix D.

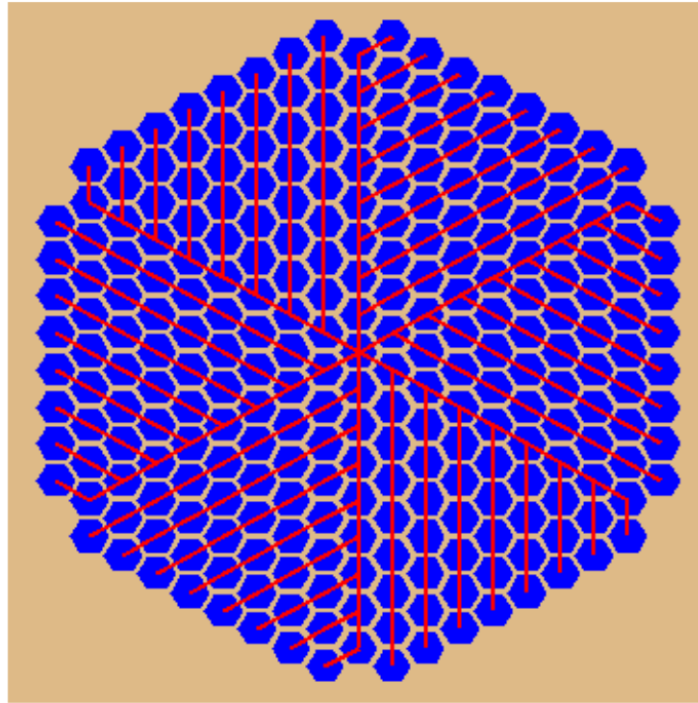


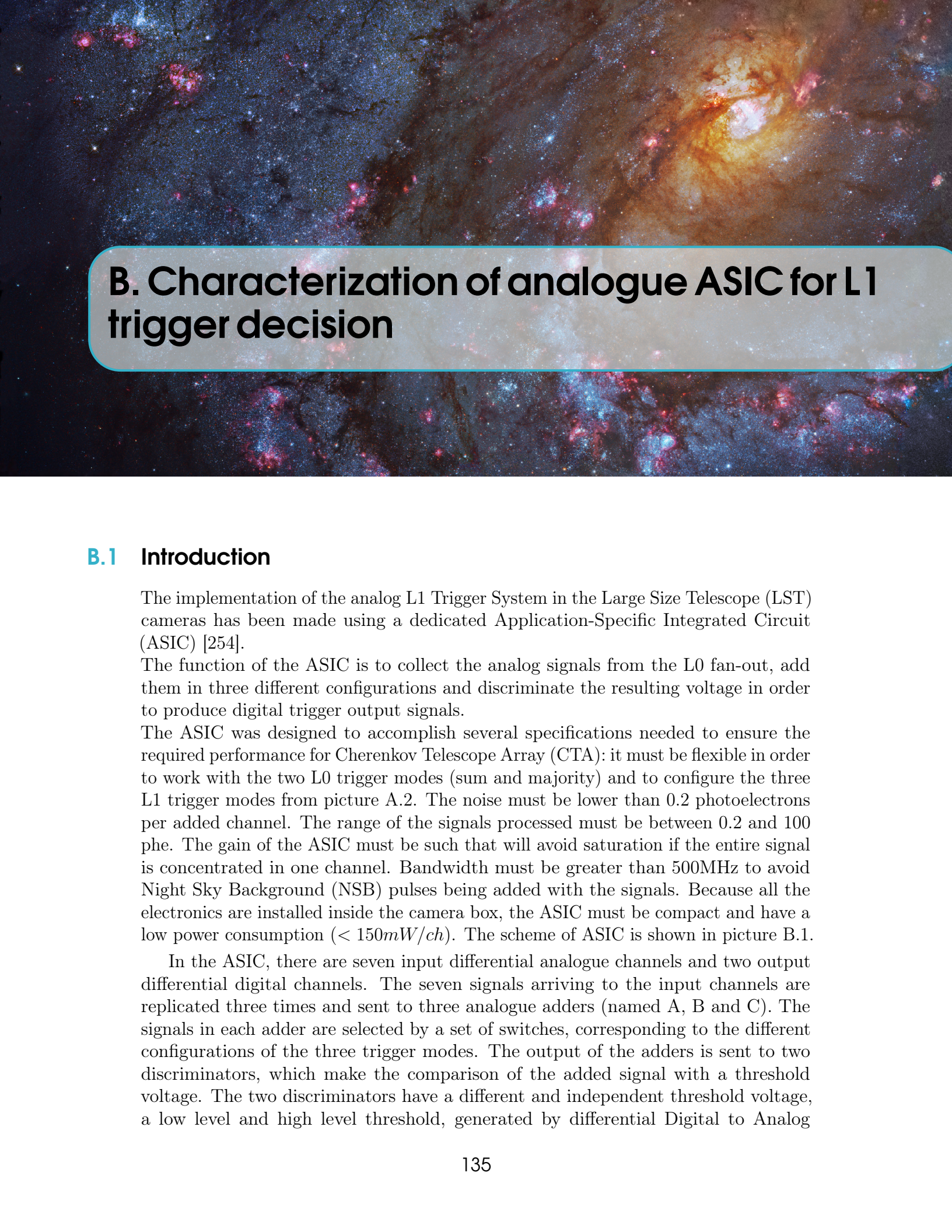
Figure A.3: Paths for trigger distribution over the entire camera.

#### A.2.4 Array Level trigger decision

Array level trigger looks for coincidences in events recorded by several telescopes. If more than one telescope produces a camera trigger in a certain time window, it is likely that the light is produced by a Cherenkov shower, so the event will be stored.

This level allows to reject the majority of NSB events that have overcomed the lower level triggers.





## B. Characterization of analogue ASIC for L1 trigger decision

### B.1 Introduction

The implementation of the analog L1 Trigger System in the Large Size Telescope (LST) cameras has been made using a dedicated Application-Specific Integrated Circuit (ASIC) [254].

The function of the ASIC is to collect the analog signals from the L0 fan-out, add them in three different configurations and discriminate the resulting voltage in order to produce digital trigger output signals.

The ASIC was designed to accomplish several specifications needed to ensure the required performance for Cherenkov Telescope Array (CTA): it must be flexible in order to work with the two L0 trigger modes (sum and majority) and to configure the three L1 trigger modes from picture A.2. The noise must be lower than 0.2 photoelectrons per added channel. The range of the signals processed must be between 0.2 and 100 phe. The gain of the ASIC must be such that will avoid saturation if the entire signal is concentrated in one channel. Bandwidth must be greater than 500MHz to avoid Night Sky Background (NSB) pulses being added with the signals. Because all the electronics are installed inside the camera box, the ASIC must be compact and have a low power consumption ( $< 150\text{mW}/\text{ch}$ ). The scheme of ASIC is shown in picture B.1.

In the ASIC, there are seven input differential analogue channels and two output differential digital channels. The seven signals arriving to the input channels are replicated three times and sent to three analogue adders (named A, B and C). The signals in each adder are selected by a set of switches, corresponding to the different configurations of the three trigger modes. The output of the adders is sent to two discriminators, which make the comparison of the added signal with a threshold voltage. The two discriminators have a different and independent threshold voltage, a low level and high level threshold, generated by differential Digital to Analog

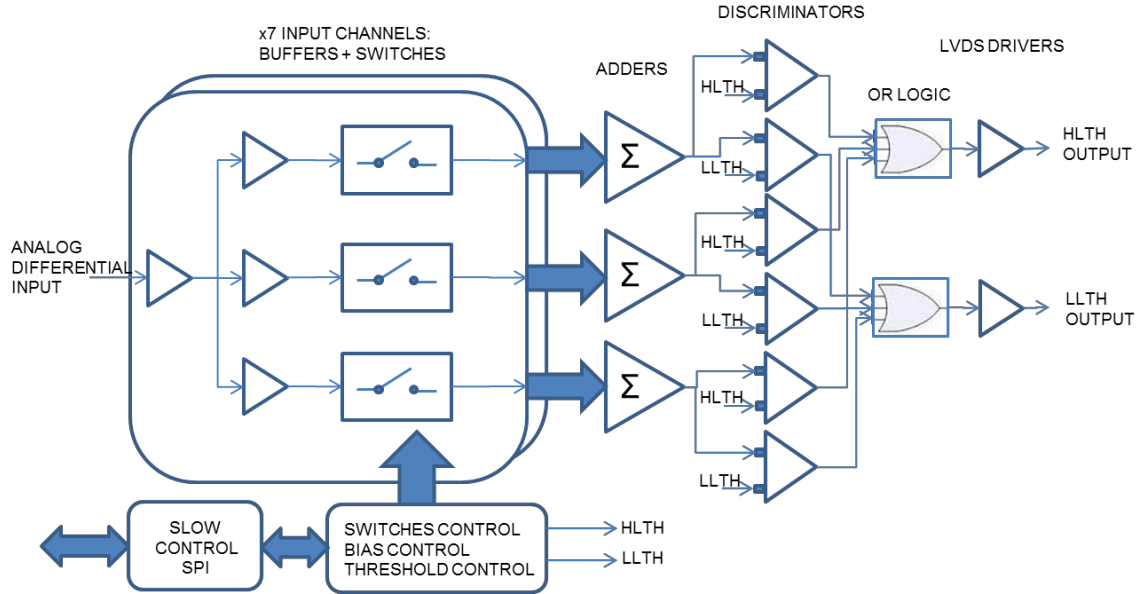


Figure B.1: L1 ASIC Block diagram

Converters (DACs). The discriminator outputs are connected to two OR gates which are in turn connected to Low-Voltage Differential Signalling (LVDS) transmitters that provide the trigger signal.

About 400 asics were produced at CIEMAT, passing a quality control to validate their performance. The quality control tests probed several characteristics of the ASICs, such as gain, noise and offset, for all the channels, adders and discriminators. From all the ASICs tested, 389 surpassed the quality control test and the results were analyzed to characterize the general behaviour of the ASIC. Averaging to all the ASIC analyzed, the result is an overall view of the features that a default ASIC would have, shown in table B.2. In this appendix, the results of the characterization of the L1 ASICs produced at CIEMAT are summarized, using the data from the quality control tests.

## B.2 Quality control test

The quality control test consisted of several steps to qualify the behaviour of the ASIC in its different parts (seven input channels, three adders and two LVDS outputs).

The quality control provided a datasheet for each individual ASIC with the results of the tests which were analyzed to characterize the manufactured ASICs. Each combination of channel (7), adder (3) and discriminator(2) is accounted separately, having a proper gain, offset and noise. This procedure allows the detection of outliers that could imply the existence of a defect in a part of the ASIC. The quality control tests provided direct measures of offset and noise, but gain must be calculated from the rate scan results in the test voltage. This procedure also offers other way of

measuring the offset. The computation of gain and offset from the rate scan, described in section B.2.2, was performed considering a linear behaviour of the input voltage vs. threshold voltage for the 50% trigger rate. From a linear fit, the gain and offset are obtained. In the next sections, the different steps of the quality control test are described.

### B.2.1 Test DAC

Measurement of the maximum and minimum voltage of the DAC was taken directly from the output pin of the ASIC by a multimeter. Each DAC set is composed by 2 DACs of 9 bits to get a final resolution of 10 bits (positive and negative parts). The measurement is made setting the code in the register with the maximum and minimum values for both positive and negative parts.

### B.2.2 Voltage Test: Rate scan

The Voltage test measured the gain of all seven input single channels and the two outputs for 10 different voltages (from 100mV to 1000mV) using a rate scan methodology, consisting on the comparison of the input trigger rate from a generator on the evaluation setup and the ASIC trigger output rate. This computation is performed with scalers implemented in the FPGA board.

### B.2.3 Test Adder Channels

The gain of different sum combinations was obtained by the same rate scan methodology. There are 3 different methods combining different channels of different adders.

### B.2.4 Analog Offset test

The Analog offset test consisted in the measurement of the offset in the Analog Adder Output test, which is the output of a multiplexor that selects among the available analog output adder, plus a buffer for the output pins. The measurement is made directly from the differential output pin of the ASIC by a Multimeter.

### B.2.5 Digital Offset test

The Digital offset test procedure measures the offset in the LVDS digital outputs, by the evaluation of the output status as a function of the threshold. The methodology consists in increasing the threshold from 0 Volts using the DAC values until finding the minimum value where the output goes from 1 to 0, and the maximum for which it goes from 0 to 1. The voltage difference between these two points is the noise of the digital output, and the mean point is the offset. Setting the Threshold to 0, three possible behaviours are observed:

- If the status of the digital output is a logic '1' (tagged as type 'Pos') it is possible to measure the minimum and the maximum points and therefore it is possible to calculate the offset and the noise.

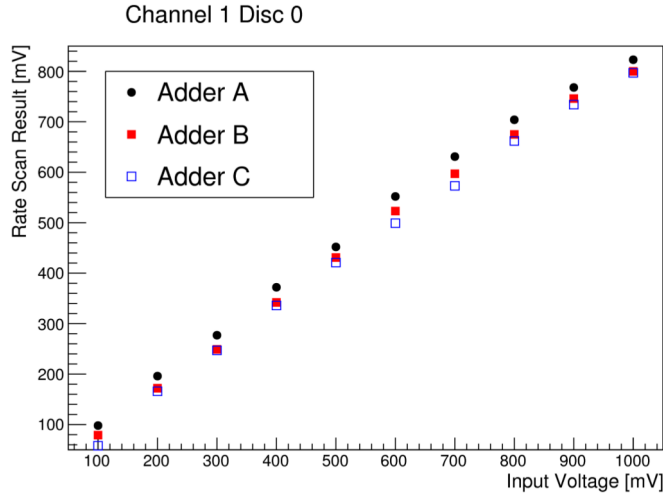


Figure B.2: Rate scan result from one of the voltage tests for ASIC #61. It can be observed a linear tendency which deteriorates at high voltages. Similar plots where obtained from the rest of channel-adder-discriminator combinations.

- If the status of the digital output is a logic '0' (tagged as type 'Neg'), it is not possible to measure neither the minimum nor the maximum point, and then a value of zero is assigned by the program both to the noise and the offset.
- If the status of the digital output is switching (tagged as type 'Com'), it is only possible to measure the maximum value, and the other is assigned to 0. In this case the noise is underestimated and the threshold is overestimated.

## B.3 Characterization of the ASIC

In this section, the results from the quality control tests for all ASICs are analyzed and discussed.

### B.3.1 Rate Scan Fit

For the calculation of the gain, the output of the Voltage test is used to perform a linear fit. If we assume a linear model, the relation between the input voltage and the rate scan result should be:

$$V_{rs} = Gain * V_{input} + Offset \quad (B.1)$$

In figure B.2 the rate scan result versus ten input voltages for a certain path (channel, adder, discriminator) of one ASIC is shown. The linearity can be easily appreciated, specially for low input voltages (under 500 mV).

Where  $V_{rs}$  represents the threshold voltage that gives a rate of 50% trigger, and  $V_{input}$  is the input voltage. The use of this method has the advantage of obtaining

Channel	Mean Gain	RMS
1	0.871	0.035
2	0.839	0.036
3	0.880	0.036
4	0.873	0.036
5	0.876	0.036
6	0.873	0.036
7	0.878	0.036

Table B.1: Mean gains for the seven channels, averaged to the sample of all asics, without the outliers.

not only the gain but also the offset of the ASIC without having to measure it with a multimeter. Since linearity seems to depend on the input voltage, it is necessary to consider a range for the fitting where the linearity is better. To do so, several ranges were fitted and the offset obtained was compared to the offset measured with the multimeter in the analog offset test. The range where the difference between the two offsets was lower was selected as the best range to fit the linear model. The resulting range was from 0 V to 300 V and so this range was used to calculate the gain and offset for every path of each ASIC.

### B.3.2 Gain

The gain was calculated with the model fitting described in the previous section. Figure B.3 shows the distribution of gain values over the paths of the 389 asics. A clear gaussian profile is observed, centered in the characteristic gain of 0.87, the expected result according to the design specifications. Some outliers were identified having gain values that are too low for the requisites of the ASIC, which could mean a malfunctioning in the ASIC. Fitting the distribution to a gaussian, it is possible to see that the probability of an ASIC to have a gain lower than 0.7 in any of its paths is lower than 0.025%. There are some outliers with higher gain values, but the probability of any entry to have a gain over 1.05 is lower than 0.007%. The outliers are identified in image B.3 by their ASIC number.

Cleaning the outliers from the sample, the characteristic gain is  $0.87 \pm 0.038$ , obtained from the gaussian fit. This is an average to all the possible paths of channel, adder and discriminator in the ASICs analyzed. A single path characterization is given in table B.2, each entry averaged to all ASICs. When observing the average gain for each channel separately in table B.1, and in image B.4 it can be observed that the second channel has a slightly lower gain than the others, and the third one a slightly higher gain. This effect comes out from the configuration used during the quality control tests. The third channel was connected directly to the pulse generator, while the second channel had to be fed with a cable of different length than the others.

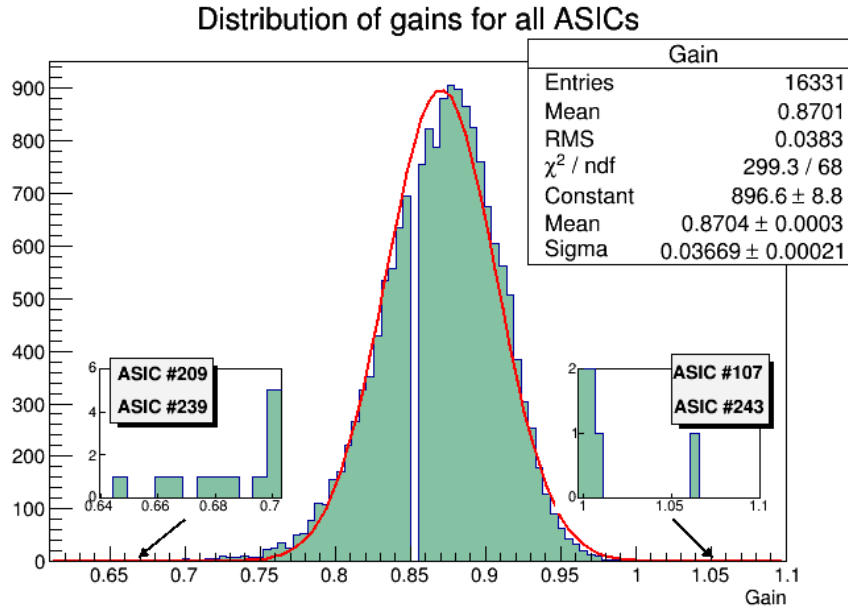


Figure B.3: Distribution of gains for all ASICs. Each entry represents the gain of one possible path (combination of channel-adder-discriminator). The red line represents a gaussian fit with mean 0,8704 and sigma 0,3669. The zoom-ins show several outliers with gains very deviated from the average.

To find if any part of the ASIC is dominating the fluctuations of the gain, correlation plots between channels, adders and discriminators were studied. A remarkable correlation is not observed in any of the elements of the ASIC, so we can conclude that all parts contribute to the final value of the gain in a similar way.

### B.3.3 Offset

The offset has been measured in three different ways. In the tests, the analog offset was directly measured with a multimeter, the digital offset was measured using the procedure described in section B.2.5, and finally, from equation B.1 an offset value that will be called fit offset was calculated.

In figure B.5 the distribution of the analog and digital offsets are shown. It must be noted that it was not possible to measure the digital offset for all the configurations, only the ones with an output status tagged as “Pos”, so it’s not possible to measure negative values of digital offset. Some outliers were detected, with digital offset values very deviated from the mean, which has been removed from the sample at the final characterizaton. Those outiers correspond to ASICs 110, 209,248 and 437.

The averaged value of the analog offset is  $-6.138$  mV with RMS of  $13.01$  mV while for the digital offset the mean is  $8.41$  mV with RMS of  $6.17$  mV. Plotting the correlation between the two measured offsets( B.6 it can be seen that there is a correlation between the two ways of measuring the offset. Regarding the fit offset, the

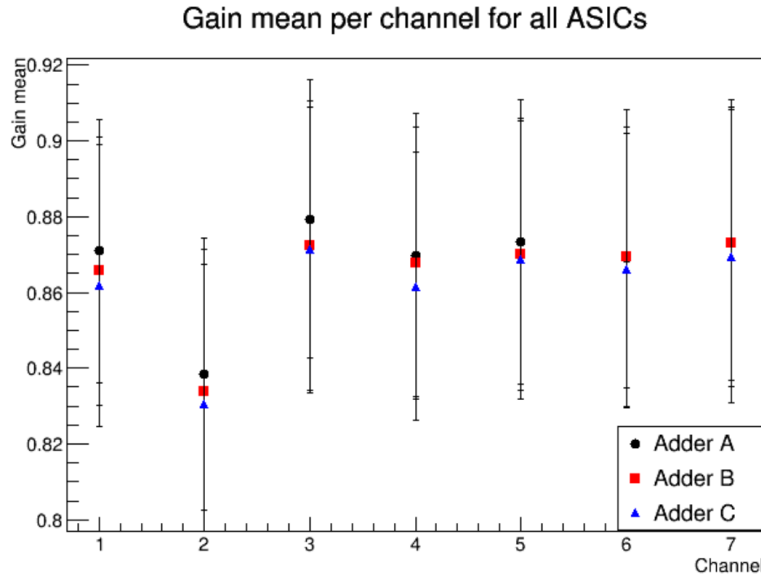


Figure B.4: Distribution of gains for all ASICs. Each entry represents the gain of one possible path (combination of channel-adder-discriminator). The red line represents a gaussian fit with mean 0,8704 and sigma 0,3669. The zoom-ins show several outliers with gains very deviated from the average.

distribution of the obtained values is shown in figure B.7. To check the validity of this method of obtaining the offset value, the difference between the fit offset and the analog offset has been studied. The averaged value of the fit offset is 0.1334 mV with RMS 13.75 mV. The mean difference between the analog offset and the fit offset is of 5.55 mV with RMS 8.06 mV. Checking the correlation between the two offset values (fig B.6) it can be observed that even there is a clear correlation between them, the fit offset is underestimating the analog offset measured. In figure B.8 the averaged offsets to all ASICs, separated by channels and adders are plotted. In general the offset takes similar values for all the channels and adders, without any remarkable outlier. In table B.2 the average offsets to all ASICs in every single path are shown.

To find out which part of the ASIC is responsible of the offset, correlation plots between channels, adders and discriminators were studied. Channels and discriminators show a clear correlation between pairs of them, but for adders, a real correlation is not observed. This implies that the offset do not depend on the channels or discriminators, but it is introduced by the adders. This result was expected from the original specifications of the ASIC.

#### B.3.4 Noise

The noise in the ASIC was measured during the Digital Offset test described in section B.2.5. The noise again can only be measured when the output status is tagged

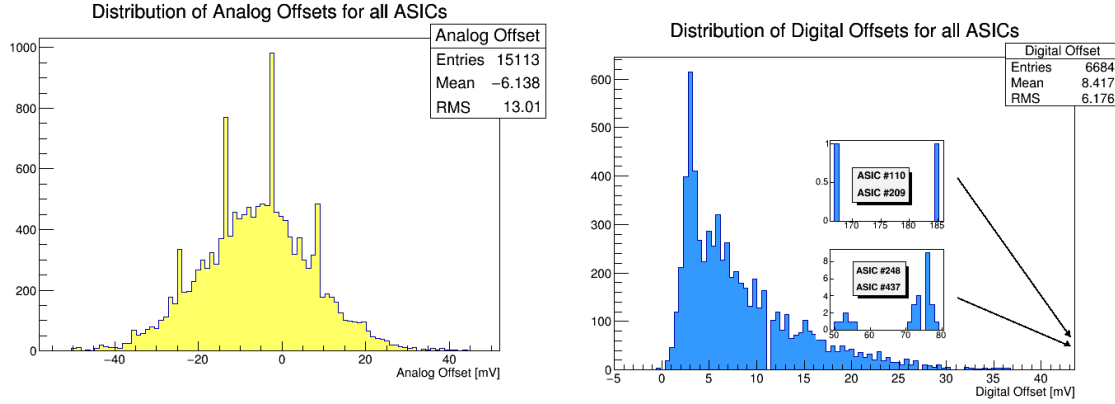


Figure B.5: Distribution of offsets for all ASICs. Each entry represents the offset of one possible path (combination of channel-adder-discriminator). *Top:* Analog offset. *Bottom:* Digital offset. The zoom-ins represent outliers in the digital offset.

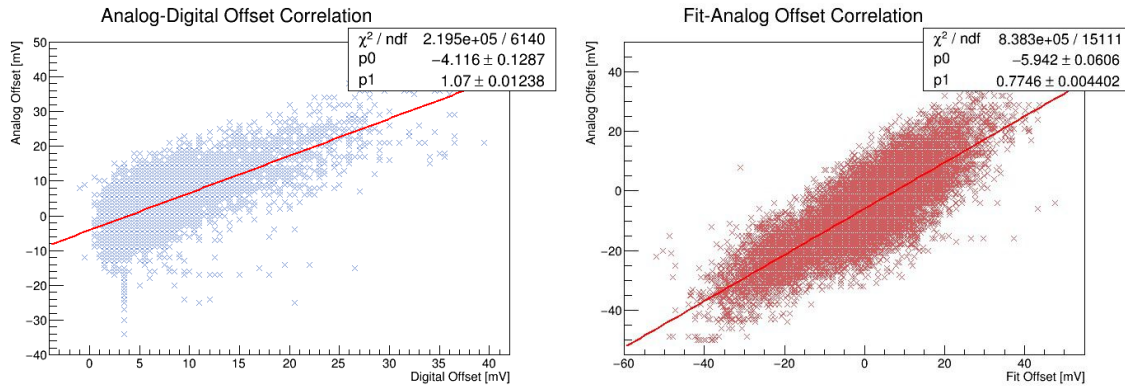


Figure B.6: *Left:* Correlation between analog offset and digital offset. *Right:* Correlation between analog offset and fit offset.

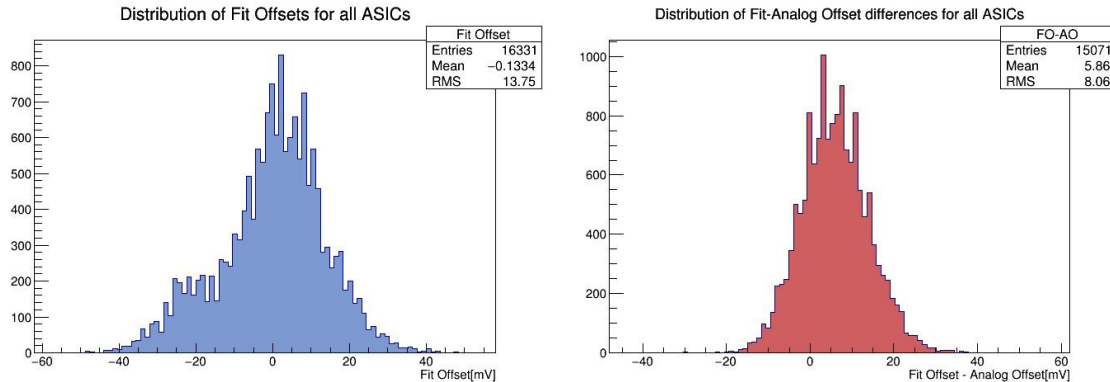


Figure B.7: *Left:* Distribution of offset calculated from the rate scan fitting. *Right:* Distribution of the difference between the analog offset and the fit offset.

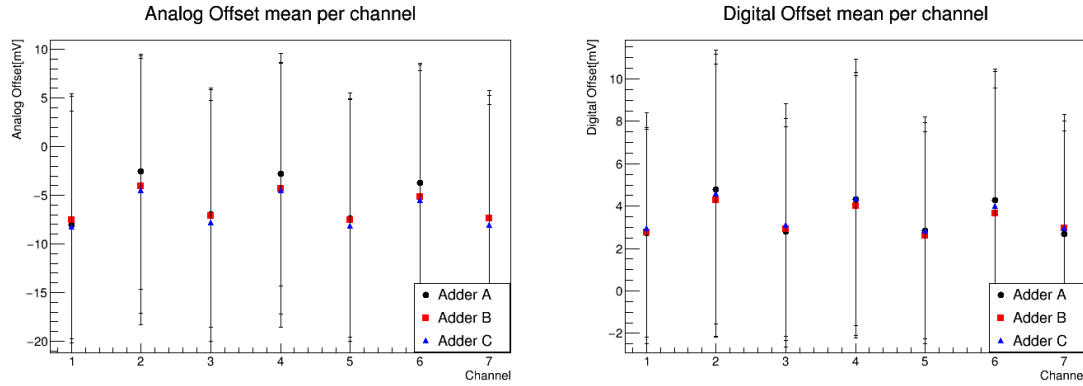


Figure B.8: *Left:* Analog offset averaged to all ASICs separated by channel and adder. *Right:* Digital offset averaged to all ASICs separated by channel and adder.

as “Pos”. In figure B.9 the total distribution of noise values is shown, having an average noise of 5.186 mV with RMS of 2.878 mV. Several outliers were spotted and are marked in the plot, with noises very deviated from the mean. If we fit a gaussian profile to the distribution, the probability of having an outlier with noise over 40 mV is 0% and over 10 mV is less than 1%. These outliers have been excluded from the general characterization.

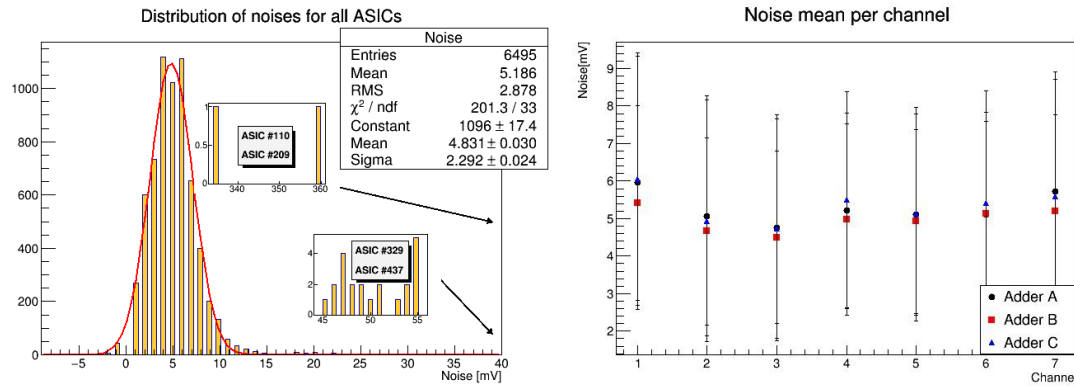


Figure B.9: *Left:* Distribution of noises measured for all ASICs. Each entry represent the noise in a certain path (channel-adder-discriminator combination). The zoom-ins show the outliers. *Right:* Noise averaged to all ASICs separated by channel and adder.

No correlation of the noise between pairs of channels, adders or discriminators have been observed, so the noise is being introduced in each part of the ASIC in a similar way.

In figure B.9 the average noise value separated by channels and adders show that its value is mostly uniform.

## B.4 Characterization: Summary and discussion

The gain measured in the ASIC has a typical value of about  $0,87 \pm 0,038$ , having two channels that slightly differ from the rest. In the case of the channels ( 2 and 3), that for all ASICs seem to have a deviation from the general mean, this effect is explainable by the setup configuration of the rate scan test. There are two ASICs where gain has a very low value, under 0,7, in several of their channels. Relative to the correlation study, there is not a strong correlation for the gain in any part of the ASICs, having all of them a correlation coefficient below 0,5.

The analog offsets measured in the test have a negative mean value, while the digital offset, as the rate scan only can provide positive offsets, gives a positive mean value. In the correlation plots for the analog offset, it can be observed a positive correlation between channels, with correlation coefficients  $\sim 0,8$ . For the adders however, no significant correlation is observed, concluding that in the adders, the offset measured is independent from each other, so they are the part of the ASIC where the offset is introduced. In the case of the digital offset, no correlation is observed at all, with coefficients very close to 0. It is needed to take into account that the data of digital offset is biased by the rate scan conditions. From the correlation plot of digital and analog offset, we can say that both offsets have a correspondence and we are measuring the same feature, having a linear correlation with slope  $\sim 1$ . In summary, the offset expected from a typical ASIC would be of  $-6 \pm 13$  mV.

A method to calculate the offset of the ASIC in an indirect way was applied assuming a model where the input signal and the rate scan result have a linear relation. The offset calculated by this method have in average, a difference with the analog offset of  $5,86 \pm 8$  mV. The correlation between the fit offset and the analog offset showed that they have a linear correlation by a factor of 0,774. The study of the fit offset in the different parts of the ASICs supported the idea that the adders are responsible for introducing the offset in the ASIC.

Finally, in table B.2 are presented the values of gain, offset and noise, averaged to all the ASICs studied. This values represent the typical values that should be expected from a correctly functional ASIC. If deviations from this numbers are observed, it might point to a defect in the ASIC, meaning a bad performance that will not fit the specifications.

Disc.	Ch.	Add.	Gain	RMS	Analog Offset[mV]	RMS[mV]	Digital Offset[mV]	RMS[mV]	Fit Offset[mV]	RMS[mV]	Noise[mV]	RMS[mV]
0	1	0	0.870941	0.0347202	-8.04178	11.7013	7.6831	5.41629	0.237361	12.2547	5.86861	3.00563
0	1	1	0.865733	0.0354431	-2.56825	12.0754	9.26942	6.00255	5.42159	13.151	4.73869	2.65657
0	1	2	0.861889	0.0372319	-6.90529	11.6572	7.38961	5.61574	0.459297	13.2761	4.40559	2.48136
0	2	0	0.838466	0.035875	-2.82682	11.5199	8.88718	5.92886	4.81186	12.0241	5.08421	2.35825
0	2	1	0.833886	0.0374605	-7.35196	12.2333	7.90845	5.88134	0.506872	13.5916	5	2.55973
0	2	2	0.830387	0.0369065	-3.70752	12.1045	8.92932	6.18108	3.99229	12.8837	4.79679	2.44105
0	3	0	0.879369	0.0367518	-7.35933	11.7325	7.87132	5.64872	0.784061	13.1786	5.64662	3.484
0	3	1	0.872314	0.0381587	-7.52089	12.7001	7.58562	5.68263	-0.450728	13.1254	5.22917	2.54056
0	3	2	0.871234	0.0377928	-4.04735	13.1041	9.25946	6.80006	3.55013	14.3746	4.32	2.18838
0	4	0	0.869755	0.0373787	-7.07521	12.9157	8.36331	6.00024	0.205656	13.5603	4.19231	2.25012
0	4	1	0.867655	0.0359559	-4.30168	12.8884	8.9435	6.38963	2.65292	13.278	4.65497	2.18266
0	4	2	0.861649	0.0354134	-7.55153	12.4649	7.70956	5.78174	0.0951152	13.1499	4.81395	2.60223
0	5	0	0.873273	0.0374989	-5.17827	12.9837	8.79697	6.41468	1.78835	13.7437	4.80921	2.19069
0	5	1	0.870116	0.0359688	-7.37604	12.6522	8.36525	5.49044	-0.487576	13.7508	5.05839	2.46957
0	5	2	0.868586	0.0368392	-8.2312	13.7086	8.84926	6.51816	-0.999143	14.8268	5.9771	3.5693
0	6	0	0.86892	0.0393618	-4.48189	13.8268	9.7963	7.14917	3.15424	15.5242	4.8895	3.11456
0	6	1	0.869291	0.0343526	-7.76602	13.8442	8.83929	6.63897	-0.61611	14.7812	4.48462	2.61721
0	6	2	0.866015	0.0360581	-4.48324	14.1144	9.44624	6.93439	3.11168	14.9143	5.3587	2.9565
0	7	0	0.873033	0.0379731	-8.15042	13.6576	8.28777	6.33279	-0.973436	14.9387	4.92537	2.75526
0	7	1	0.872879	0.0360707	-5.50418	14.0574	9.41124	7.01801	1.49357	14.6893	5.28402	3.06379
0	7	2	0.869562	0.0386874	-8.07242	13.8974	8.32168	6.35307	-0.732647	14.9372	5.6383	2.63978
1	1	0	0.881697	0.0341451	-8.04178	11.7013	7.4927	5.56054	-3.03256	12.605	6.04444	3.70158
1	1	1	0.876093	0.0328864	-2.56825	12.0754	9	6.24797	2.56555	12.6045	5.40816	3.62626
1	1	2	0.872108	0.0318161	-6.90529	11.6572	7.15753	5.46745	-2.59383	12.1416	5.12057	3.43424
1	2	0	0.847899	0.0314701	-2.82682	11.5199	8.46073	5.71851	1.5189	11.4802	5.34737	2.79574
1	2	1	0.845232	0.0323591	-7.34819	12.2164	7.43103	5.58897	-3.17824	13.3383	5.1958	2.79425
1	2	2	0.838856	0.0329706	-3.70752	12.1045	8.5582	5.93878	0.9006	12.3124	5.41711	2.95009
1	3	0	0.890874	0.0358411	-7.35933	11.7325	7.37132	5.31715	-3.06684	12.7281	5.78195	2.88199
1	3	1	0.884409	0.0339822	-7.52089	12.7001	7.07483	5.47237	-3.13453	13.5406	5.6069	2.64522
1	3	2	0.883612	0.0325719	-4.04735	13.1041	8.89503	6.50563	0.259641	13.9549	5.01156	2.73066
1	4	0	0.882881	0.034909	-7.07521	12.9157	7.51034	5.7519	-2.88689	13.3739	4.77698	2.30121
1	4	1	0.878196	0.0336269	-4.30168	12.8884	8.66384	6.19265	-0.0876289	13.5648	5.28977	2.82262
1	4	2	0.875941	0.0309881	-7.55153	12.4649	7.20438	5.55088	-3.23393	13.001	5.03759	2.28893
1	5	0	0.887686	0.034171	-5.17827	12.9837	8.5122	6.00304	-0.83976	12.6118	5.41718	2.66956
1	5	1	0.881864	0.0329572	-7.37604	12.6522	7.61986	5.27637	-3.32048	12.9181	5.34028	2.65666
1	5	2	0.877262	0.0327925	-8.2312	13.7086	7.81071	5.98285	-3.39332	14.0924	6.13971	3.1557
1	6	0	0.880771	0.0354957	-4.48189	13.8268	9.3288	6.61699	0.871464	14.3059	4.99444	3.31913
1	6	1	0.878608	0.0332089	-7.76602	13.8442	8.63603	6.52525	-3.29734	13.35	4.96296	3.16791
1	6	2	0.87653	0.031666	-4.48324	14.1144	9.18362	6.59579	-0.118557	13.5596	5.63793	2.83065
1	7	0	0.887339	0.0345601	-8.15042	13.6576	7.87037	6.10918	-3.0437	13.7544	5.31579	2.9389
1	7	1	0.88383	0.033284	-5.50418	14.0574	8.97059	6.77424	-0.674379	13.6534	5.5503	2.8985
1	7	2	0.881967	0.0317656	-8.07242	13.8974	7.93478	5.91143	-3.7892	14.0832	5.56115	3.54846

Table B.2: Values of the gain, offset (measured by three different methods) and noise for the different parts of the typical ASIC, obtained averaging to all the ASICs tested.





## C. Calibration method for the L1 analog trigger system of LST camera

### C.1 Introduction

During the year 2016, a connectivity test took place at CIEMAT involving 35 modules of the Large Size Telescope (LST)<sup>1</sup> camera, to evaluate the integration of the electronics and mechanical structure. As explained in chapter 3, the modules of the LST are designed to be manipulated individually, allowing an easy removal and substitution in case of malfunctioning modules. The goals of the C35 test were to evaluate the interface between cluster mechanics and cluster holder, check the possible interference of modules during assembly, establish an assembly procedure, find potential problems during assembly and test assembly time. Also, it was dedicated to check the interfaces between the different parts of the electronics such as the Dragon boards and mezzanines, and the connection between the clusters and the backplanes. During this test, 35 modules were assembled in the camera plate in different configurations, and several connectivity tests were performed, such as tests on the clock, PPS, camera trigger and busy signals, power supply, trigger distribution along the camera and time delays configuration.

Within the scope of the C35 test, it was necessary to design a calibration method for the L1 transfer function, to find the threshold voltage which produces a trigger rate of 50%, depending on the input signal.

In the next sections the calibration algorithm developed for this task is described and results on the calibration are commented. Note that this is the calibration method currently implemented in the telescope.

## C.2 L1 transfer function calibration

A method for the calibration of the L1 analog trigger system was developed and tested, based in a rate scan methodology. The goal of the calibration is to find the threshold voltage needed in each module to obtain a trigger rate of 50%. The calibration need to be performed for each one of the three adders and two discriminators of the L1 Application-Specific Integrated Circuit (ASIC). The 50% trigger rate threshold is obtained for several input signals in order to plot a curve that allows retrieving the gain and offset of the circuit, and compare them with the characterization of the ASICs.

The setup for the calibration consists on one module where a pulse with fixed amplitude and frequency can be injected in each of its seven pixels by the Slow Control Board (SCB). Increasing signal voltages are generated by adding the pulses injected in each of the seven channels of the module, meaning that in total it is possible to obtain up to 6 points for the calibration curve.

An algorithm based in a bisection method is applied to each input signal to calculate the 50% trigger rate threshold.

### C.2.1 Calibration algorithm

The algorithm for this calibration has been implemented using a scripting language specially designed for the C35 test. It proceeds by configuring a fixed gain and frequency pulse in the SCB, in a fixed number of pixel lines. This way, the amplitude of the input pulse can be modified by adding more pixels. Once the initial pulse is configured, a bisection method is used to find the 50% trigger rate threshold. The threshold voltage in the ASIC is configured through a Digital to Analog Converter (DAC) with 8 bits, that can provide up to 255 different voltages from 0 to 1.2 V in steps of 4.8 mV. The algorithm initiates setting the threshold at the maximum voltage (setting the 8 bits to 1) and runs bit by bit, from the most significant bit, changing 1 to 0. If the new threshold voltage provide a trigger rate that is less than the target rate (in this case the target is 50%) then that threshold voltage is stored and the algorithm goes to the next bit. This way, only 8 steps are necessary to find the required threshold voltage. A diagram describing the algorithm is shown in figure C.1.

Once the loop is finished, the 50% trigger rate threshold is calculated following the formula:

$$50TH = \frac{(TargetRate - Baseline)}{(Baseline - Rate[CurrentThreshold - 1])} + CurrentThreshold \quad (C.1)$$

Being baseline the rate at current threshold, say the last threshold that was stored in the loop.

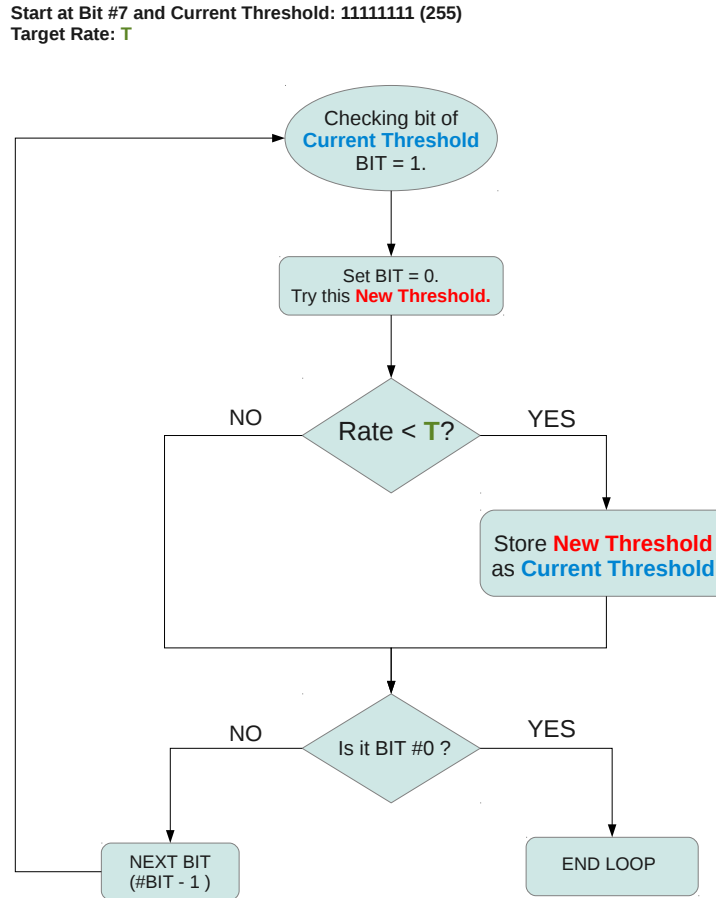


Figure C.1: Flux diagram of the calibration algorithm.

### C.2.2 Calibration result

When the full algorithm ends and runs over the 6 possible input signals, the obtained 50% threshold can be plotted against the number of pixels added to see the calibration curve (see figure C.2).

If the initial pulse injected by the SCB is known and assuming that the adding is correct, the amplitude of each pulse is simply the multiplication of the initial pulse by the number of pixels added, being possible to obtain the gain and offset of the ASIC.

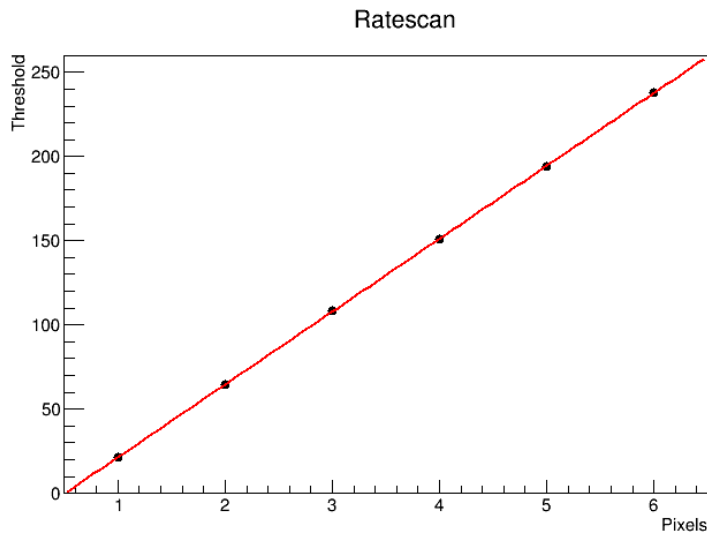
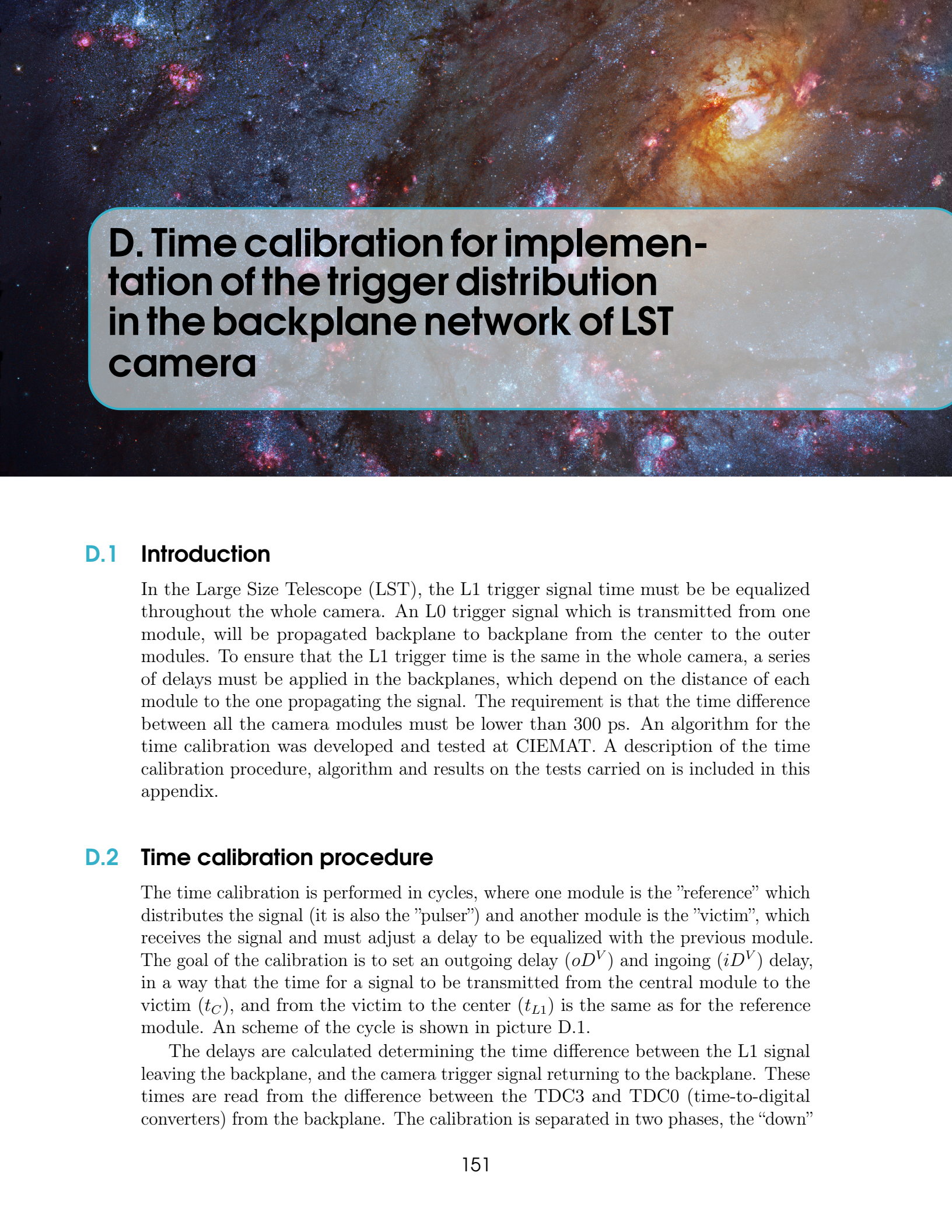


Figure C.2: Result of the rate scan for Adder A of one module.



## D. Time calibration for implementation of the trigger distribution in the backplane network of LST camera

### D.1 Introduction

In the Large Size Telescope (LST), the L1 trigger signal time must be equalized throughout the whole camera. An L0 trigger signal which is transmitted from one module, will be propagated backplane to backplane from the center to the outer modules. To ensure that the L1 trigger time is the same in the whole camera, a series of delays must be applied in the backplanes, which depend on the distance of each module to the one propagating the signal. The requirement is that the time difference between all the camera modules must be lower than 300 ps. An algorithm for the time calibration was developed and tested at CIEMAT. A description of the time calibration procedure, algorithm and results on the tests carried on is included in this appendix.

### D.2 Time calibration procedure

The time calibration is performed in cycles, where one module is the "reference" which distributes the signal (it is also the "pulser") and another module is the "victim", which receives the signal and must adjust a delay to be equalized with the previous module. The goal of the calibration is to set an outgoing delay ( $oD^V$ ) and ingoing ( $iD^V$ ) delay, in a way that the time for a signal to be transmitted from the central module to the victim ( $t_C$ ), and from the victim to the center ( $t_{L1}$ ) is the same as for the reference module. A scheme of the cycle is shown in picture D.1.

The delays are calculated determining the time difference between the L1 signal leaving the backplane, and the camera trigger signal returning to the backplane. These times are read from the difference between the TDC3 and TDC0 (time-to-digital converters) from the backplane. The calibration is separated in two phases, the "down"

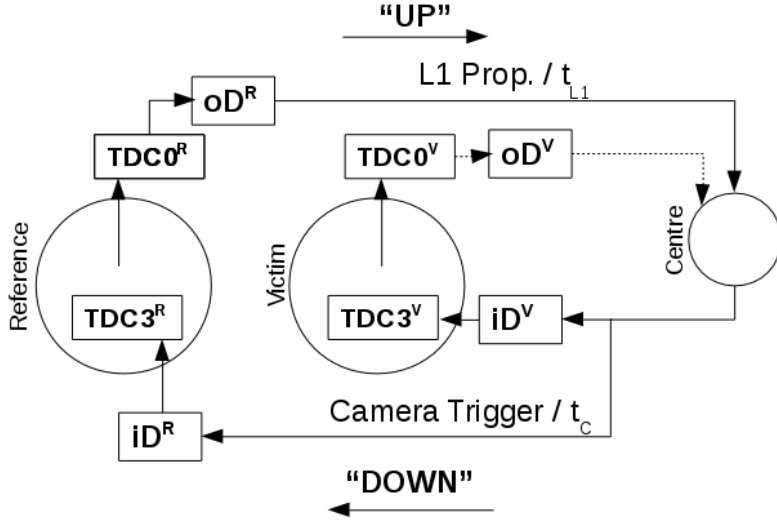


Figure D.1: Flux diagram of the calibration algorithm.

calibration and the “up” calibration, as shown in picture D.1.

- For the down calibration, the L1 signal distribution of the victim is deactivated, so the camera trigger signal is only triggered by the L1 of the reference. Because reference and victim are triggered by the same L0, the time at TDC0 for both modules will be the same. The difference  $TDC3 - TDC0 = \Delta$  can be measured both in the reference and victim modules, therefore the incoming delay is simply:

$$iD_V = (TDC3 - TDC0)^r - (TDC3 - TDC0)^V = \Delta^R - \Delta^V \quad (\text{D.1})$$

Once the required delay value is calculated, it is set in two steps: a coarse delay in steps of 10ns and a fine delay in steps of 36 ps.

- For the up calibration, the L1 signal distribution of the victim is activated, and the one of the reference is deactivated. The goal of the up calibration is to set the outgoing delay in a way that the difference  $(TDC3 - TDC0)^V$ , which is the total time the signal needs to go from the victim module to the center and back to the victim. The delay therefore is:

$$oD^V = L - (TDC3 - TDC0)^V = L - \Delta^V \quad (\text{D.2})$$

Where L is the latency, and corresponds to the  $\Delta^R$  measured in the down calibration. At the end of the cycle, the times  $t_C$  and  $t_{L1}$  will be the same both for reference and victim. At the start of the new cycle, the victim will be the new reference and other module is chosen as victim.

The calibration algorithm was implemented in a scripting language specifically designed for the communication with the different backplane registers.

### D.3 Time calibration setup and tests

Two calibration setups were configured at CIEMAT, to implement the time calibration procedure. At first, four modules were set as shown in picture D.2, allowing to run three time calibration cycles as described in the previous section. The test consisted in setting initial default values in the delays, given by the position of the modules, and running the calibration several times for different initial values to ensure the reliability of the procedure. After the success of the first implementation, a second setup was prepared involving eight modules. The calibration procedure was performed several times, to check the stability of the final TDC values and that the deviations with every backplane were in the allowed range of 300 ps.

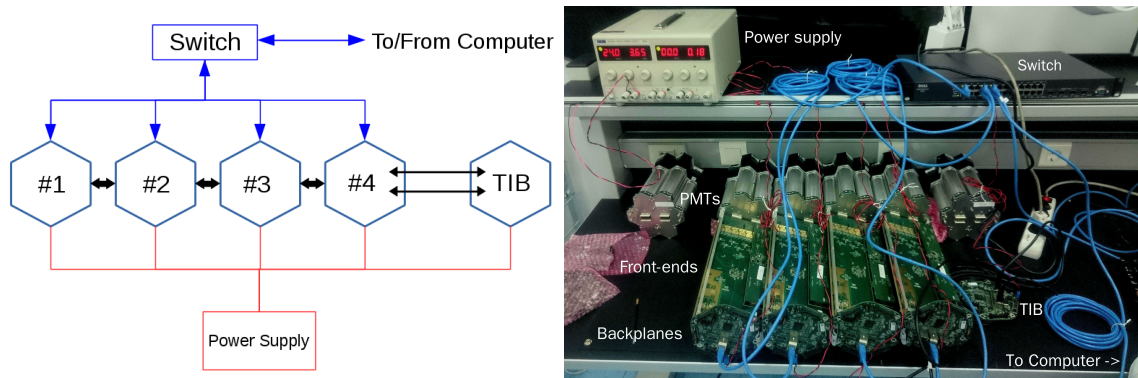


Figure D.2: *Left:* Diagram of the four modules setup. *Right:* Picture of the actual setup at CIEMAT clean room.

Thanks to these two setups, the time calibration procedure was successfully verified. The algorithm was then adapted to perform the calibration of the full camera, following the predefined paths of signal distribution as shown in picture A.3. This time calibration procedure must be run at least once every night of operation of the telescope.



# E. Random Forests

## E.1 Introduction

Random Forest (RF) is a supervised learning algorithm which uses an ensemble of several decision trees [187]. Decision trees are flow-chart-like structures where each internal node denotes a test on a selected feature. The result is a split in the dataset depending on the value of that feature. The best splitting criterion for regression is typically calculated using the mean squared error (MSE). For each node, the MSE of the two subsets is calculated for each feature and for each possible cut on that feature, until a minimum is reached. This step is repeated at each node until a condition is reached, typically that the MSE of the remaining data sample is below a threshold, or it has too few events to keep splitting. The termination nodes are also known as *leaves*. In the RF, a number of decision trees are trained using a randomly selected subset of the train data ('bootstrapping') and the prediction of all the trees is averaged to reach the final result. Also, the features are always randomly permuted at each split. These two sources of randomness in the RF prevent the typical problem of over-fitting from too complicated decision trees.

## E.2 Gini Index

??

The gini index or gini impurity is a measure of how often a randomly chosen event would be incorrectly classified if it was classified randomly following the distribution of classes. The formula for the Gini index  $I_G$  calculated for a set of events with J

classes is:

$$I_G(p) = 1 - \sum_{i=1}^J p_i^2 \quad (\text{E.1})$$

Where  $p_i$  is the probability of an event belonging to the class  $i$  to be correctly classified. The Gini index go from 0 to 1, where 0 means that all the events of a subset have been classified to one class, and 1 that the events of the subset are randomly distributed along all the possible classes. The splitting decision will be made minimizing the value of the Gini index.



## Bibliography

1. Berezhko, E. G. Origin of Galactic Cosmic Rays from Supernova Remnants. *Nuclear Physics B Proceedings Supplements* **256**, 23–35 (Nov. 2014).
2. Gozzini, S. R., Carmona, E, Jankowski, F, Krause, J & and, I. R. The supernova remnant W51C: a plausible source of galactic cosmic rays? *Journal of Physics: Conference Series* **409**, 012116 (Feb. 2013).
3. Thoudam, S. & Hörandel, J. R. Nearby supernova remnants and the cosmic ray spectral hardening at high energies. *Monthly Notices of the Royal Astronomical Society* **421**, 1209–1214. ISSN: 0035-8711 (Mar. 2012).
4. Thoudam, S. *et al.* Cosmic-ray energy spectrum and composition up to the ankle: the case for a second Galactic component. **595**, A33 (Oct. 2016).
5. Bazilevskaya, G. A. Once again about origin of the solar cosmic rays. *Journal of Physics: Conference Series* **798**, 012034 (Jan. 2017).
6. Podgorny, A. I., Podgorny, I. M., Balabin, Y. V., Meshalkina, N. S. & Vashenyuk. The spectrum of solar relativistic cosmic ray measurements and numerical simulation. *Journal of Physics: Conference Series* **798**, 012027 (Jan. 2017).
7. Castellina, A. & Donato, F. in *Planets, Stars and Stellar Systems: Volume 5: Galactic Structure and Stellar Populations* (eds Oswalt, T. D. & Gilmore, G.) 725–788 (Springer Netherlands, Dordrecht, 2013). doi:10.1007/978-94-007-5612-0\_14. <[https://doi.org/10.1007/978-94-007-5612-0\\_14](https://doi.org/10.1007/978-94-007-5612-0_14)>.
8. Alves Batista, R. *et al.* Open Questions in Cosmic-Ray Research at Ultrahigh Energies. *Frontiers in Astronomy and Space Sciences* **6**, 23. ISSN: 2296-987X (2019).
9. Hanlon, W. F. *Updated cosmic ray spectrum 2015*. <<http://www.physics.utah.edu/~whanlon/spectrum.html>>.

10. Hillas, A. M. The Origin of Ultra-High-Energy Cosmic Rays. *Annual Review of Astronomy and Astrophysics* **22**, 425–444 (1984).
11. Perkins, D. H. *Particle Astrophysics* 2nd ed. (Oxford University Press, 2009).
12. Tatischeff, V. & Gabici, S. Particle Acceleration by Supernova Shocks and Spallogenic Nucleosynthesis of Light Elements. *Annual Review of Nuclear and Particle Science* **68**, 377–404 (Oct. 2018).
13. Hillas, A. M. The Origin of Ultrahigh-Energy Cosmic Rays. *Ann. Rev. Astron. Astrophys.* **22**, 425–444 (1984).
14. Petrosian, V. & Bykov, A. M. Particle Acceleration Mechanisms. **134**, 207–227 (Feb. 2008).
15. Melrose, D. B. Acceleration Mechanisms. *arXiv e-prints*, arXiv:0902.1803 (Feb. 2009).
16. Fermi, E. in, 238–252 (Dec. 1972). ISBN: 9780080167244. doi:10.1016/B978-0-08-016724-4.50024-0.
17. Longair, M. S. *High Energy Astrophysics* 3rd ed. (Cambridge University Press, 2011).
18. Lagage, P. O. & Cesarsky, C. J. The maximum energy of cosmic rays accelerated by supernova shocks. **125**, 249–257 (Sept. 1983).
19. Ramana Murthy, P. V. & Wolfendale, A. W. *Gamma-ray Astronomy* **273** (Apr. 1993).
20. Weekes, T. *Very High Energy Gamma-Ray Astronomy* ISBN: 9781420033199. <<https://books.google.com.ua/books?id=wSTOBgAAQBAJ>> (CRC Press, 2003).
21. Maoz, D. *Astrophysics in a nutshell* <<https://cds.cern.ch/record/1142636>> (Princeton Univ. Press, Princeton, NJ, 2007).
22. Oya Vallejo, I. *Observations of Active Galactic Nuclei with the MAGIC Telescope* PhD thesis (UCM, Madrid, Dept. Phys., 2010). <<https://magiccoll.mpp.mpg.de/publications/theses/I0ya.pdf>>.
23. Harwit, M. *Astrophysical Concepts. Fourth edition* <<https://www.springer.com/gp/book/9781475720198>> (Springer Science Business Media, 2006).
24. Ruderman, M. A. & Sutherland, P. G. Theory of pulsars - Polar caps, sparks, and coherent microwave radiation. *Astrophysical Journal* **196**, 51–72 (Feb. 1975).
25. Aharonian, F. A. *Very high energy cosmic gamma radiation : a crucial window on the extreme Universe* doi:10.1142/4657 (2004).
26. Stecker, F. W. The Production of Cosmic Gamma Rays in Interstellar and Intergalactic Cosmic-Ray Collisions. Iv: Gamma-Ray Production from Cosmic Proton-Antiproton Interactions. *SAO Special Report* **261** (Dec. 1967).

27. Domínguez, A. *et al.* Extragalactic background light inferred from AEGIS galaxy-SED-type fractions. *Monthly Notices of the RAS* **410**, 2556–2578 (Feb. 2011).
28. Franceschini, A. & Rodighiero, G. The extragalactic background light revisited and the cosmic photon-photon opacity. *Astronomy and Astrophysics* **603**, A34 (July 2017).
29. Moralejo, A. *et al.* *Measurement of the EBL through a combined likelihood analysis of gamma-ray observations of blazars with the MAGIC telescopes in 35th International Cosmic Ray Conference (ICRC2017)* **301** (Jan. 2017), 604. arXiv: 1709.02238 [astro-ph.HE].
30. Andernach, H. & Zwicky, F. English and Spanish Translation of Zwicky's (1933) The Redshift of Extragalactic Nebulae. *arXiv e-prints*, arXiv:1711.01693 (Nov. 2017).
31. Rubin, V. C., Ford, W. K. Jr. & Thonnard, N. Extended rotation curves of high-luminosity spiral galaxies. IV - Systematic dynamical properties, SA through SC. *Astrophysical Journal* **225**, L107–L111 (Nov. 1978).
32. Planck Collaboration *et al.* Planck 2013 results. XVI. Cosmological parameters. *Astronomy and Astrophysics* **571**, A16 (Nov. 2014).
33. Olive, K. A. TASI Lectures on Dark Matter. *arXiv e-prints*, astro-ph/0301505 (Jan. 2003).
34. Lisanti, M. *Lectures on Dark Matter Physics in New Frontiers in Fields and Strings (TASI 2015)* (Jan. 2017), 399–446. doi:10.1142/9789813149441\_0007. arXiv: 1603.03797 [hep-ph].
35. Kravtsov, A. V., Klypin, A. A., Bullock, J. S. & Primack, J. R. The Cores of Dark Matter-dominated Galaxies: Theory versus Observations. *Astrophysical Journal* **502**, 48–58 (July 1998).
36. Hernquist, L. An analytical model for spherical galaxies and bulges. *Astrophysical Journal* **356**, 359–364 (June 1990).
37. Zhao, H. Analytical models for galactic nuclei. *Monthly Notices of the RAS* **278**, 488–496 (Jan. 1996).
38. Navarro, J. F., Frenk, C. S. & White, S. D. M. The Structure of Cold Dark Matter Halos. *Astrophysical Journal* **462**, 563 (May 1996).
39. Einasto, J. On the Construction of a Composite Model for the Galaxy and on the Determination of the System of Galactic Parameters. *Trudy Astrofizicheskogo Instituta Alma-Ata* **5**, 87–100 (Jan. 1965).
40. Wakely, S. P. & Horan, D. TeVCat: An online catalog for Very High Energy Gamma-Ray Astronomy. *International Cosmic Ray Conference* **3**, 1341–1344 (2008).

41. Aliu, E. *et al.* Observation of Pulsed  $\gamma$ -Rays Above 25 GeV from the Crab Pulsar with MAGIC. *Science* **322**, 1221 (Nov. 2008).
42. Kuiper, L. *et al.* The Crab pulsar in the 0.75-30 MeV range as seen by CGRO COMPTEL. A coherent high-energy picture from soft X-rays up to high-energy gamma-rays. *Astronomy and Astrophysics* **378**, 918–935 (Nov. 2001).
43. McCann, A. Observations of the Crab Pulsar with VERITAS. *arXiv e-prints*, arXiv:1303.0275 (Mar. 2013).
44. Abdo, A. A. *et al.* Fermi Large Area Telescope Observations of the Crab Pulsar And Nebula. **708**, 1254–1267 (Jan. 2010).
45. Hirotani, K. High Energy Emission from Rotation-Powered Pulsars: Outer-gap vs. Slot-gap Models. *arXiv e-prints*, arXiv:0809.1283 (Sept. 2008).
46. Gajdus, M. *The Vela pulsar in very high energy gamma-rays with H.E.S.S. II* PhD thesis (Humboldt-Universität zu Berlin, Mathematisch-Naturwissenschaftliche Fakultät, 2016). doi:<http://dx.doi.org/10.18452/17610>.
47. Chandrasekhar, S. The Maximum Mass of Ideal White Dwarfs. *Astrophysical Journal* **74**, 81 (July 1931).
48. Osterbrock, D. E. & Ferland, G. J. *Astrophysics of gaseous nebulae and active galactic nuclei* (2006).
49. Weiler, K. W. & Sramek, R. A. Supernovae and supernova remnants. *Annual Review of Astron and Astrophys* **26**, 295–341 (Jan. 1988).
50. Becker Tjus, J., Eichmann, B., Kroll, M. & Nierstenhöfer, N. Gamma-ray emitting supernova remnants as the origin of Galactic cosmic rays? *Astroparticle Physics* **81**, 1–11 (Aug. 2016).
51. Cristofari, P., Gabici, S., Terrier, R. & Humensky, T. B. On the search for Galactic supernova remnant PeVatrons with current TeV instruments. **479**, 3415–3421 (Sept. 2018).
52. Gaensler, B. M. & Slane, P. O. The Evolution and Structure of Pulsar Wind Nebulae. *Annual Review of Astron and Astrophys* **44**, 17–47 (Sept. 2006).
53. H. E. S. S. Collaboration *et al.* HESS J1818-154, a new composite supernova remnant discovered in TeV gamma rays and X-rays. **562**, A40 (Feb. 2014).
54. Hewitt, J. W. & Lemoine-Goumard, M. Observations of supernova remnants and pulsar wind nebulae at gamma-ray energies. *Comptes Rendus Physique* **16**, 674–685 (Aug. 2015).
55. Dubus, G., Guillard, N., Petrucci, P.-O. & Martin, P. Sizing up the population of gamma-ray binaries. **608**, A59 (Dec. 2017).
56. Dubus, G. Gamma-ray binaries and related systems. *Astronomy and Astrophysics Reviews* **21**, 64 (Aug. 2013).

57. *Classical Novae* 2nd ed. doi:10.1017/CBO9780511536168 (Cambridge University Press, 2008).
58. Abdo, A. A., Ackermann, M., Ajello, M., Atwood & Fermi LAT Collaboration. Gamma-Ray Emission Concurrent with the Nova in the Symbiotic Binary V407 Cygni. *Science* **329**, 817–821 (Aug. 2010).
59. Ackermann, M. *et al.* Fermi establishes classical novae as a distinct class of gamma-ray sources. *Science* **345**, 554–558 (Aug. 2014).
60. Sitarek, J. & Bednarek, W. GeV-TeV gamma rays and neutrinos from the Nova V407 Cygni. *Physical Review D* **86**, 063011 (Sept. 2012).
61. Albert, J. *et al.* Observation of Gamma Rays from the Galactic Center with the MAGIC Telescope. **638**, L101–L104 (Feb. 2006).
62. H. E. S. S. Collaboration *et al.* The H.E.S.S. Galactic plane survey. **612**, A1 (Apr. 2018).
63. Archer, A. *et al.* TeV Gamma-Ray Observations of the Galactic Center Ridge by VERITAS. **821**, 129 (Apr. 2016).
64. Goldwurm, A. *An Overview of the High-Energy Emission from the Galactic Center in The Galactic Center: a Window to the Nuclear Environment of Disk Galaxies* (eds Morris, M. R., Wang, Q. D. & Yuan, F.) **439** (May 2011), 391. arXiv: 1007.4174 [astro-ph.HE].
65. Goldwurm, A. High energy activity of the super-massive black hole at the Galactic Center. *Comptes Rendus Physique* **8**, 35–44 (Jan. 2007).
66. Su, M., Slatyer, T. R. & Finkbeiner, D. P. Giant Gamma-ray Bubbles from Fermi-LAT: Active Galactic Nucleus Activity or Bipolar Galactic Wind? *Astrophysical Journal* **724**, 1044–1082 (Dec. 2010).
67. Ackermann, M. *et al.* The Spectrum and Morphology of the Fermi Bubbles. *Astrophysical Journal* **793**, 64 (Sept. 2014).
68. Abdo, A. A. *et al.* A population of gamma-ray emitting globular clusters seen with the Fermi Large Area Telescope. *Astronomy and Astrophysics* **524**, A75 (Dec. 2010).
69. H. E. S. S. Collaboration *et al.* Search for very-high-energy  $\gamma$ -ray emission from Galactic globular clusters with H.E.S.S. *Astronomy and Astrophysics* **551**, A26 (Mar. 2013).
70. Freire, P. C. C. *et al.* Fermi Detection of a Luminous -Ray Pulsar in a Globular Cluster. *Science* **334**, 1107–1110. ISSN: 0036-8075 (2011).
71. Wu, J. H. K. *et al.* SEARCH FOR PULSED  $\gamma$ -RAY EMISSION FROM GLOBULAR CLUSTER M28. *The Astrophysical Journal* **765**, L47 (Feb. 2013).
72. Tam, P.-H. T., Hui, C. Y. & Kong, A. K. H. Gamma-ray Emission from Globular Clusters. *Journal of Astronomy and Space Sciences* **33**, 1–11 (Mar. 2016).

73. Urry, C. M. & Padovani, P. Unified Schemes for Radio-Loud Active Galactic Nuclei. *Publications of the Astronomical Society of the Pacific* **107**, 803 (Sept. 1995).
74. Dermer, C. D. & Giebels, B. Active galactic nuclei at gamma-ray energies. *Comptes Rendus Physique* **17**, 594–616 (June 2016).
75. Madejski, G. G. & Sikora, M. Gamma-Ray Observations of Active Galactic Nuclei. **54**, 725–760 (Sept. 2016).
76. Wilson, A. S. & Colbert, E. J. M. The Difference between Radio-loud and Radio-quiet Active Galaxies. **438**, 62 (Jan. 1995).
77. Urry, C. M. & Padovani, P. Unified Schemes for Radio-Loud Active Galactic Nuclei. **107**, 803 (Sept. 1995).
78. Piran, T. The physics of gamma-ray bursts. *Reviews of Modern Physics* **76**, 1143–1210 (Oct. 2004).
79. Kouveliotou, C. *et al.* Identification of two classes of gamma-ray bursts. *Astrophysical Journal* **413**, L101–L104 (Aug. 1993).
80. Piran, T. Gamma-ray bursts and the fireball model. *Physics Reports* **314**, 575–667 (June 1999).
81. Ghirlanda, G., Bernardini, M., Calderone, G. & D’Avanzo, P. Are short Gamma Ray Bursts similar to long ones? *Journal of High Energy Astrophysics* **7**. Swift 10 Years of Discovery, a novel approach to Time Domain Astronomy, 81 –89. ISSN: 2214-4048 (2015).
82. .
83. Ajello, M. *et al.* Fermi-LAT Observations of LIGO/Virgo Event GW170817. **861**, 85 (July 2018).
84. Mirzoyan, R. First time detection of a GRB at sub-TeV energies; MAGIC detects the GRB 190114C. *The Astronomer’s Telegram* **12390** (Jan. 2019).
85. Ohm, S. Starburst galaxies as seen by gamma-ray telescopes. *Comptes Rendus Physique* **17**, 585–593 (June 2016).
86. Acero, F. *et al.* Detection of Gamma Rays from a Starburst Galaxy. *Science* **326**, 1080 (Nov. 2009).
87. VERITAS Collaboration *et al.* A connection between star formation activity and cosmic rays in the starburst galaxy M82. *Nature* **462**, 770–772 (Dec. 2009).
88. Abdo, A. A. *et al.* Detection of Gamma-Ray Emission from the Starburst Galaxies M82 and NGC 253 with the Large Area Telescope on Fermi. *Astrophysical Journal* **709**, L152–L157 (Feb. 2010).
89. Brunetti, G. Gamma rays from galaxy clusters. *AIP Conference Proceedings* **1792**, 020009 (2017).

90. Brunetti, G. & Jones, T. W. Cosmic Rays in Galaxy Clusters and Their Nonthermal Emission. *International Journal of Modern Physics D* **23**, 1430007–98 (Mar. 2014).
91. Ackermann, M. *et al.* GeV Gamma-ray Flux Upper Limits from Clusters of Galaxies. *Astrophysical Journal* **717**, L71–L78 (July 2010).
92. Aleksić, J. *et al.* Constraining cosmic rays and magnetic fields in the Perseus galaxy cluster with TeV observations by the MAGIC telescopes. *Astronomy and Astrophysics* **541**, A99 (May 2012).
93. Xi, S.-Q. *et al.* Detection of gamma-ray emission from the Coma cluster with Fermi Large Area Telescope and tentative evidence for an extended spatial structure. *Physical Review D* **98**, 063006 (Sept. 2018).
94. Czerny, B. *et al.* Astronomical Distance Determination in the Space Age. Secondary Distance Indicators. *Space Science Reviews* **214**, 32 (Feb. 2018).
95. Rezaeikh, S., Javadi, A., Khosroshahi, H. & van Loon, J. T. The star formation history of the Magellanic Clouds derived from long-period variable star counts. *Monthly Notices of the RAS* **445**, 2214–2222 (Dec. 2014).
96. Robitaille, T. P. & Whitney, B. A. The Present-Day Star Formation Rate of the Milky Way Determined from Spitzer-Detected Young Stellar Objects. *Astrophysical Journal* **710**, L11–L15 (Feb. 2010).
97. Sreekumar, P. *et al.* Observations of the Large Magellanic Cloud in High-Energy Gamma Rays. *Astrophysical Journal* **400**, L67 (Dec. 1992).
98. Abdo, A. A. *et al.* Detection of the Small Magellanic Cloud in gamma-rays with Fermi/LAT. *Astronomy and Astrophysics* **523**, A46 (Nov. 2010).
99. Abdo, A. A. *et al.* Observations of the Large Magellanic Cloud with Fermi. *Astronomy and Astrophysics* **512**, A7 (Mar. 2010).
100. Ackermann, M. *et al.* Deep view of the Large Magellanic Cloud with six years of Fermi-LAT observations. *Astronomy and Astrophysics* **586**, A71 (Feb. 2016).
101. Corbet, R. H. D. *et al.* A Luminous Gamma-ray Binary in the Large Magellanic Cloud. *Astrophysical Journal* **829**, 105 (Oct. 2016).
102. H. E. S. S. Collaboration *et al.* The exceptionally powerful TeV  $\gamma$ -ray emitters in the Large Magellanic Cloud. *Science* **347**, 406–412 (Jan. 2015).
103. Komin, N. *et al.* H.E.S.S. observations of the Large Magellanic Cloud. *arXiv e-prints*, arXiv:1201.0639 (Jan. 2012).
104. Ackermann, M. *et al.* Observations of M31 and M33 with the Fermi Large Area Telescope: A Galactic Center Excess in Andromeda? *Astrophysical Journal* **836**, 208 (Feb. 2017).
105. Navarro, J. F. The Structure of Cold Dark Matter Halos. *Symposium - International Astronomical Union* **171**, 255–258 (1996).

106. Cherenkov Telescope Array Consortium *et al.* *Science with the Cherenkov Telescope Array* doi:10.1142/10986 (2019).
107. Abramowski, A. *et al.* Search for a Dark Matter Annihilation Signal from the Galactic Center Halo with H.E.S.S. *Physical Review Letters* **106**, 161301 (Apr. 2011).
108. Aharonian, F. *et al.* HESS Observations of the Galactic Center Region and Their Possible Dark Matter Interpretation. *Physical Review Letters* **97**, 221102 (Dec. 2006).
109. Ackermann, M. *et al.* The Fermi Galactic Center GeV Excess and Implications for Dark Matter. *Astrophysical Journal* **840**, 43 (May 2017).
110. Kuhlen, M, Diemand, J, Madau, P & Zemp, M. The Via Lactea INCITE simulation: galactic dark matter substructure at high resolution. *Journal of Physics: Conference Series* **125**, 012008 (July 2008).
111. Simon, J. D. & Geha, M. The Kinematics of the Ultra-faint Milky Way Satellites: Solving the Missing Satellite Problem. *Astrophysical Journal* **670**, 313–331 (Nov. 2007).
112. Abdo, A. A. *et al.* Observations of Milky Way Dwarf Spheroidal Galaxies with the Fermi-Large Area Telescope Detector and Constraints on Dark Matter Models. *Astrophysical Journal* **712**, 147–158 (Mar. 2010).
113. Abramowski, A. *et al.* Search for dark matter annihilation signatures in H.E.S.S. observations of dwarf spheroidal galaxies. *Physical Review D* **90**, 112012 (Dec. 2014).
114. Ahnen, M. L. *et al.* Indirect dark matter searches in the dwarf satellite galaxy Ursa Major II with the MAGIC telescopes. *Journal of Cosmology and Astroparticle Physics* **2018**, 009 (Mar. 2018).
115. Archambault, S. *et al.* Dark matter constraints from a joint analysis of dwarf Spheroidal galaxy observations with VERITAS. *Physical Review D* **95**, 082001 (Apr. 2017).
116. Oakes, L. *Combined Dark Matter Searches Towards Dwarf Spheroidal Galaxies with Fermi-LAT, HAWC, HESS, MAGIC and VERITAS* in *36th International Cosmic Ray Conference (ICRC2019)* **36** (July 2019), 539. arXiv: 1909.06310 [astro-ph.HE].
117. Cirelli, M., Moulin, E., Panci, P., Serpico, P. D. & Viana, A. Gamma ray constraints on decaying dark matter. *Physical Review D* **86**, 083506 (Oct. 2012).
118. Huang, X., Vertongen, G. & Weniger, C. Probing dark matter decay and annihilation with Fermi LAT observations of nearby galaxy clusters. *Journal of Cosmology and Astroparticle Physics* **2012**, 042 (Jan. 2012).

119. Ackermann, M. *et al.* Constraints on dark matter annihilation in clusters of galaxies with the Fermi large area telescope. *Journal of Cosmology and Astroparticle Physics* **2010**, 025 (May 2010).
120. Abramowski, A. *et al.* Search for Dark Matter Annihilation Signals from the Fornax Galaxy Cluster with H.E.S.S. *Astrophysical Journal* **750**, 123 (May 2012).
121. Acciari, V. A. *et al.* Constraining dark matter lifetime with a deep gamma-ray survey of the Perseus galaxy cluster with MAGIC. *Physics of the Dark Universe* **22**, 38–47 (Dec. 2018).
122. van der Marel, R. P. *The Large Magellanic Cloud: structure and kinematics* in *The Local Group as an Astrophysical Laboratory* (eds Livio, M. & Brown, T. M.) **17** (Jan. 2006), 47–71. arXiv: astro-ph/0404192 [astro-ph].
123. Sofue, Y. Dark Bulge, Exponential Disk, and Massive Halo in the Large Magellanic Cloud. *Publications of the Astronomical Society of Japan* **51**, 445–448. ISSN: 0004-6264 (Aug. 1999).
124. Buckley, M. R. *et al.* Search for gamma-ray emission from dark matter annihilation in the large magellanic cloud with the fermi large area telescope. *Physical Review D* **91**, 102001 (May 2015).
125. *IBIS homepage* <https://www.cosmos.esa.int/web/integral/instruments-ibis>.
126. *INTEGRAL homepage* <https://sci.esa.int/web/integral/home>.
127. Atwood, W. B. *et al.* The Large Area Telescope on the Fermi Gamma-Ray Space Telescope Mission. *Nature* **697**, 1071–1102 (June 2009).
128. Ackermann, M. *et al.* Detection of the Characteristic Pion-Decay Signature in Supernova Remnants. *Science* **339**, 807–811 (Feb. 2013).
129. Ackermann, M. *et al.* Fermi-LAT Observations of the Gamma-Ray Burst GRB 130427A. *Science* **343**, 42–47 (Jan. 2014).
130. Goldstein, A. *et al.* An Ordinary Short Gamma-Ray Burst with Extraordinary Implications: Fermi-GBM Detection of GRB 170817A. *The Astrophysical Journal* **848**, L14 (Oct. 2017).
131. Heitler, W. *Quantum theory of radiation* (1954).
132. Rossi, B. & Greisen, K. Cosmic-Ray Theory. *Rev. Mod. Phys.* **13**, 240–309 (4 Oct. 1941).
133. Vallejo, I. O. *Observation of active galactic [sic] nuclei with the Magic telescope* Tesis de la Universidad Complutense de Madrid, Facultad de Ciencias Físicas, Departamento de Física Atómica, Molecular y Nuclear, leída el 23-06-2010. PhD thesis (Madrid, Oct. 2010). <<https://eprints.ucm.es/11431/>>.

134. Collado, T. H. *Sensitivity studies for the Cherenkov Telescope Array* Tesis inédita de la Universidad Complutense de Madrid, Facultad de Ciencias Físicas, Departamento de Física Atómica, Molecular y Nuclear, leída el 28-09-2015. Madrid, Jan. 2016. <<https://eprints.ucm.es/35143/>>.
135. Gaisser, T. K., Engel, R. & Resconi, E. *Cosmic Rays and Particle Physics* (June 2016).
136. Jelley, J. *Čerenkov radiation, and its applications* <<https://books.google.es/books?id=uzZRAAAAMAAJ>> (Pergamon Press, 1958).
137. Borione, A. *et al.* CASA-MIA: A precision” EAS detector. [Cyg X-3; Her X-1; M1; NGC 1952; PSR 0531+21]. doi:10.1063/1.43832 (June 1993).
138. Di Sciascio, G. & LHAASO Collaboration. The LHAASO experiment: From Gamma-Ray Astronomy to Cosmic Rays. *Nuclear and Particle Physics Proceedings* **279**, 166–173 (Oct. 2016).
139. Huo, X. A. *et al.* *Tibet-AS  $\gamma$  Experiment* in *International Cosmic Ray Conference* **2** (Jan. 1990), 427.
140. Fonseca, V. The HEGRA experiment (High Energy Gamma Ray Array). *Nuclear Physics B - Proceedings Supplements* **28**, 409 –412. ISSN: 0920-5632 (1992).
141. Di Sciascio, G. A.-Y. C. *Latest results from the ARGO-YBJ experiment* in *Journal of Physics Conference Series* **632** (Aug. 2015), 012089. doi:10.1088/1742-6596/632/1/012089. arXiv: 1503.09102 [astro-ph.HE].
142. Mostafá, M. A. The High-Altitude Water Cherenkov Observatory. *Brazilian Journal of Physics* **44**, 571–580 (Oct. 2014).
143. Arqueros, F. *et al.* The Wide Angle Air Cherenkov Detector AIROBICC at La Palma (Aug. 1996).
144. Hillas, A. M. *Cerenkov light images of EAS produced by primary gamma* in *19th International Cosmic Ray Conference (ICRC19), Volume 3* (ed Jones, F. C.) **3** (Aug. 1985).
145. de Naurois, M. Analysis methods for Atmospheric Cerenkov Telescopes. *arXiv e-prints*, astro-ph/0607247 (July 2006).
146. de Naurois, M. & Mazin, D. Ground-based detectors in very-high-energy gamma-ray astronomy. *Comptes Rendus Physique* **16**, 610–627 (Aug. 2015).
147. Kilde, J. *et al.* The Whipple Observatory 10 m gamma-ray telescope, 1997-2006. English (US). *Astroparticle Physics* **28**, 182–195. ISSN: 0927-6505 (Oct. 2007).
148. Cortina, J. *Highlights of the MAGIC telescopes* in *International Cosmic Ray Conference* **11** (Jan. 2011), 147. doi:10.7529/ICRC2011/V12/H12. arXiv: 1110.4747 [astro-ph.HE].
149. Pühlhofer, G. H.E.S.S. highlights. *arXiv e-prints*, arXiv:1801.06074 (Jan. 2018).

150. Furniss, A. *Recent Highlights from the VERITAS Gamma-ray Observatory* in *American Astronomical Society Meeting Abstracts #233* **233** (Jan. 2019), 433.04.
151. *MAGIC homepage* <https://magic.mpp.mpg.de/>.
152. *CTA Performance* <https://www.cta-observatory.org/science/cta-performance/>.
153. *CTA Observatory site* <https://www.cta-observatory.org/>.
154. Acharya, B. *et al.* Introducing the CTA concept. *Astroparticle Physics* **43**. Seeing the High-Energy Universe with the Cherenkov Telescope Array - The Science Explored with the CTA, 3–18. ISSN: 0927-6505 (2013).
155. Bernlöhr, K. *et al.* Monte Carlo design studies for the Cherenkov Telescope Array. *Astroparticle Physics* **43**, 171–188 (Mar. 2013).
156. Hassan, T. *et al.* Monte Carlo performance studies for the site selection of the Cherenkov Telescope Array. *Astroparticle Physics* **93**, 76–85 (July 2017).
157. Maier, G. *et al.* *Performance of the Cherenkov Telescope Array* in *35th International Cosmic Ray Conference (ICRC2017)* **301** (Jan. 2017), 846. arXiv: 1709.01381 [astro-ph.IM].
158. Ambrosi, G. *et al.* The Cherenkov Telescope Array Large Size Telescope. *arXiv e-prints*, arXiv:1307.4565 (July 2013).
159. Mazin, D., Cortina, J. & Teshima, M. *Large size telescope report* in *6th International Symposium on High Energy Gamma-Ray Astronomy* **1792** (Jan. 2017), 080001. doi:10.1063/1.4969022. arXiv: 1610.04403 [astro-ph.IM].
160. Delgado, C. *et al.* Mechanics and cooling system for the camera of the Large Size Telescopes of the Cherenkov Telescope Array (CTA). *arXiv e-prints*, arXiv:1307.4540 (July 2013).
161. Nieto, D. *et al.* Prototype 9.7 m Schwarzschild-Couder telescope for the Cherenkov Telescope Array: status of the optical system. *arXiv e-prints*, arXiv:1709.06324 (Sept. 2017).
162. Glicenstein, J. F. *Status of the Davies Cotton and Schwarzschild-Coude Medium Sized Telescopes for the Cherenkov Telescope Array* in *36th International Cosmic Ray Conference (ICRC2019)* **36** (July 2019), 269. arXiv: 1907.08455 [astro-ph.IM].
163. Garczarczyk, M., Schlenstedt, S., Oakes, L., Schwanke, U. & the MST Team. Status of the Medium-Sized Telescope for the Cherenkov Telescope Array. *arXiv e-prints*, arXiv:1509.01361 (Sept. 2015).

164. Barrio, J. Status of the large size telescopes and medium size telescopes for the Cherenkov Telescope Array observatory. *Nuclear Instruments and Methods in Physics Research Section A: Accelerators, Spectrometers, Detectors and Associated Equipment*. ISSN: 0168-9002. doi:<https://doi.org/10.1016/j.nima.2018.11.047>. <<http://www.sciencedirect.com/science/article/pii/S016890021831622X>> (2018).
165. Pareschi, G. *et al.* The dual-mirror Small Size Telescope for the Cherenkov Telescope Array. *arXiv e-prints*, arXiv:1307.4962 (July 2013).
166. White, R. & Schoorlemmer, H. A Compact High Energy Camera (CHEC) for the Gamma-ray Cherenkov Telescope of the Cherenkov Telescope Array. *arXiv e-prints*, arXiv:1709.05799 (Sept. 2017).
167. Maccarone, M. C. & Astri Project, C. *ASTRI for the Cherenkov Telescope Array in 35th International Cosmic Ray Conference (ICRC2017)* **301** (Jan. 2017), 855. arXiv: 1709.03078 [astro-ph.IM].
168. Funk, S. *et al.* *TARGET: A digitizing and trigger ASIC for the Cherenkov telescope array in 6th International Symposium on High Energy Gamma-Ray Astronomy* **1792** (Jan. 2017), 080012. doi:10.1063/1.4969033. arXiv: 1610.01536 [astro-ph.IM].
169. Heck, D., Knapp, J., Capdevielle, J. N., Schatz, G. & Thouw, T. *CORSIKA: a Monte Carlo code to simulate extensive air showers*. (1998).
170. Klages, H. *et al.* The Kascade experiment. *Nuclear Physics B - Proceedings Supplements* **52**, 92 –102. ISSN: 0920-5632 (1997).
171. Ostapchenko, S. QGSJET-II: towards reliable description of very high energy hadronic interactions. *Nuclear Physics B Proceedings Supplements* **151**, 143–146 (2006).
172. Schmidt, F. & Knapp, J. *CORSIKA Shower Images*
173. Bernlöhr, K. Simulation of imaging atmospheric Cherenkov telescopes with CORSIKA and sim\_telarray. *Astroparticle Physics* **30**, 149–158 (Oct. 2008).
174. *Ctapipe webpage* <https://cta-observatory.github.io/ctapipe/index.html>.
175. Contreras, J. L. *et al.* *Data model issues in the Cherenkov Telescope Array project in 34th International Cosmic Ray Conference (ICRC2015)* **34** (2015), 960. arXiv: 1508.07584 [astro-ph.IM].
176. Knödlseder, J. *et al.* GammaLib and ctools. A software framework for the analysis of astronomical gamma-ray data. **593**, A1 (2016).
177. Iori, M. *et al.* Design of a prototype device to calibrate the Large Size Telescope camera of the Cherenkov Telescope Array. *arXiv e-prints*, arXiv:1508.06752 (Aug. 2015).

178. Palatiello, M., Iori, M., Cassol, F., Cauz, D. & Ferrarotto, F. Performance of the INFN Camera calibration device of the first Large Size Telescope in the Cherenkov Telescope Array. *arXiv e-prints*, arXiv:1909.08475 (Sept. 2019).
179. Mirzoyan, R. *On the Calibration Accuracy of Light Sensors in Atmospheric Cherenkov Fluorescence and Neutrino Experiments in International Cosmic Ray Conference* **7** (Jan. 1997), 265.
180. Parsons, R. D. & Ohm, S. Background Rejection in Atmospheric Cherenkov Telescopes using Recurrent Convolutional Neural Networks. *arXiv e-prints*, arXiv:1910.09435 (Oct. 2019).
181. Shayduk, M. & Consortium, C. *Optimized Next-neighbour Image Cleaning Method for Cherenkov Telescopes* in *International Cosmic Ray Conference* **33** (2013), 3000. arXiv: 1307.4939 [astro-ph.IM].
182. Shayduk, M., Hengstebeck, T., Kalekin, O. R., Pavel, N. A. & Schweizer, T. *A New Image Cleaning Method for the MAGIC Telescope* in (2005).
183. Lessard, R., Cayón, L., Sembroski, G. & Gaidos, J. Wavelet Imaging Cleaning Method for Atmospheric Cherenkov Telescopes. *Astroparticle Physics* **17**. doi:10.1016/S0927-6505(01)00173-6 (Oct. 2001).
184. HEGRA Collaboration: A. Daum. First Results on the Performance of the HEGRA IACT Array. *arXiv e-prints*, astro-ph/9704098 (Apr. 1997).
185. Fomin, V. P. *et al.* New methods of atmospheric Cherenkov imaging for gamma-ray astronomy. I. The false source method. *Astroparticle Physics* **2**, 137–150 (May 1994).
186. Domingo-Santamaría, E. *The DISP analysis method for point-like or extended gamma source searches/studies with the MAGIC Telescope* in (2005).
187. Breiman, L. Random Forests. English. *Machine Learning* **45**, 5–32. ISSN: 0885-6125 (2001).
188. Pedregosa, F. *et al.* Scikit-learn: Machine Learning in Python. *Journal of Machine Learning Research* **12**, 2825–2830 (2011).
189. Li, T. P. & Ma, Y. Q. Analysis methods for results in gamma-ray astronomy. **272**, 317–324 (Sept. 1983).
190. Aharonian, F. *et al.* The Crab Nebula and Pulsar between 500 GeV and 80 TeV: Observations with the HEGRA Stereoscopic Air Cerenkov Telescopes. **614**, 897–913 (Oct. 2004).
191. Sanuki, T. *et al.* Precise Measurement of Cosmic-Ray Proton and Helium Spectra with the BESS Spectrometer. **545**, 1135–1142 (Dec. 2000).
192. Dempster, A. P., Laird, N. M. & Rubin, D. B. Maximum Likelihood from Incomplete Data via the EM Algorithm. *Journal of the Royal Statistical Society. Series B (Methodological)* **39**, 1–38. ISSN: 00359246 (1977).

193. Pietrzyński, G. *et al.* An eclipsing-binary distance to the Large Magellanic Cloud accurate to two per cent. **495**, 76–79 (Mar. 2013).
194. Nikolaev, S. *et al.* Geometry of the Large Magellanic Cloud Disk: Results from MACHO and the Two Micron All Sky Survey. **601**, 260–276 (Jan. 2004).
195. Ridley, J. P. *et al.* Eight new radio pulsars in the Large Magellanic Cloud. **433**, 138–146 (July 2013).
196. Ackermann, M. *et al.* Deep view of the Large Magellanic Cloud with six years of Fermi-LAT observations. **586**, A71 (Feb. 2016).
197. Reid, W. A., Stupar, M., Bozzetto, L. M., Parker, Q. A. & Filipović, M. D. Optical discovery and multiwavelength investigation of supernova remnant MCSNR J0512- 6707 in the Large Magellanic Cloud. **454**, 991–999 (Nov. 2015).
198. Maggi, P., Haberl, F., Sturm, R. & Dewey, D. XMM-Newton observations of SNR 1987A. II. The still increasing X-ray light curve and the properties of Fe K lines. **548**, L3 (Dec. 2012).
199. Maggi, P. *et al.* The population of X-ray supernova remnants in the Large Magellanic Cloud. **585**, A162 (Jan. 2016).
200. H. E. S. S. Collaboration *et al.* The exceptionally powerful TeV  $\gamma$ -ray emitters in the Large Magellanic Cloud. *Science* **347**, 406–412 (Jan. 2015).
201. Gaensler, B. M., Hendrick, S. P., Reynolds, S. P. & Borkowski, K. J. Discovery of a New Pulsar Wind Nebula in the Large Magellanic Cloud. **594**, L111–L114 (Sept. 2003).
202. Campana, R. *et al.* X-ray observations of the Large Magellanic Cloud pulsar PSR B0540-69 and its pulsar wind nebula. **389**, 691–700 (Sept. 2008).
203. Komin, N., Haupt, M. & H. E. S. S. Collaboration. *Discovery of VHE Gamma-Ray Emission from the Binary System LMC P3 in 35th International Cosmic Ray Conference (ICRC2017)* **301** (Jan. 2017), 730. arXiv: 1708.03171 [astro-ph.HE].
204. Cherenkov Telescope Array Consortium *et al.* *Science with the Cherenkov Telescope Array* doi:10.1142/10986 (2019).
205. Socrates, A., Davis, S. W. & Ramirez-Ruiz, E. The Eddington Limit in Cosmic Rays: An Explanation for the Observed Faintness of Starbursting Galaxies. *The Astrophysical Journal* **687**, 202–215 (Nov. 2008).
206. Papadopoulos, P. P. A COSMIC-RAY-DOMINATED INTERSTELLAR MEDIUM IN ULTRA LUMINOUS INFRARED GALAXIES: NEW INITIAL CONDITIONS FOR STAR FORMATION. *The Astrophysical Journal* **720**, 226–232 (Aug. 2010).
207. Harris, J. & Zaritsky, D. The Star Formation History of the Large Magellanic Cloud. **138**, 1243–1260 (Nov. 2009).

208. Siudek, M. *et al.* Infrared composition of the Large Magellanic Cloud. *Earth, Planets and Space* **65**, 13. ISSN: 1880-5981 (Mar. 2013).
209. Porter, T. A., Moskalenko, I. V., Strong, A. W., Orlando, E. & Bouchet, L. Inverse Compton Origin of the Hard X-Ray and Soft Gamma-Ray Emission from the Galactic Ridge. **682**, 400–407 (July 2008).
210. Pollack, J. B. & Fazio, G. G. Production of  $\pi$  Mesons and Gamma Radiation in the Galaxy by Cosmic Rays. *Phys. Rev.* **131**, 2684–2691 (6 Sept. 1963).
211. Abdo, A. A. *et al.* Observations of the Large Magellanic Cloud with Fermi. **512**, A7 (Mar. 2010).
212. Murphy, E. J., Porter, T. A., Moskalenko, I. V., Helou, G. & Strong, A. W. CHARACTERIZING COSMIC-RAY PROPAGATION IN MASSIVE STAR-FORMING REGIONS: THE CASE OF 30 DORADUS AND THE LARGE MAGELLANIC CLOUD. *The Astrophysical Journal* **750**, 126 (Apr. 2012).
213. van der Marel, R. P., Alves, D. R., Hardy, E. & Suntzeff, N. B. New Understanding of Large Magellanic Cloud Structure, Dynamics, and Orbit from Carbon Star Kinematics. **124**, 2639–2663 (Nov. 2002).
214. Sofue, Y. Dark Bulge, Exponential Disk, and Massive Halo in the Large Magellanic Cloud. **51**, 445–448 (Aug. 1999).
215. Sofue, Y. in *Planets, Stars and Stellar Systems Vol. 5, by Oswalt, Terry D.; Gilmore, Gerard, ISBN 978-94-007-5611-3. Springer Science+Business Media Dordrecht, 2013*, p. 985 (eds Oswalt, T. D. & Gilmore, G.) 985 (2013). doi:10.1007/978-94-007-5612-0\_19.
216. Cirelli, M. *et al.* PPPC 4 DM ID: a poor particle physicist cookbook for dark matter indirect detection. **2011**, 051 (Mar. 2011).
217. Pellegrini, E. W. *et al.* THE OPTICAL DEPTH OF H II REGIONS IN THE MAGELLANIC CLOUDS. *The Astrophysical Journal* **755**, 40 (July 2012).
218. De Marchi, G. *et al.* Star Formation in 30 Doradus. **739**, 27 (Sept. 2011).
219. Bergh, S. V. D. Supernova rates: A progress report. *Physics Reports* **204**. doi:10.1016/0370-1573(91)90034-j (6 1991).
220. Berezinsky, V. & Gazizov, A. Z. Diffusion of Cosmic Rays in the Expanding Universe. I. **643**, 8–13 (May 2006).
221. Stephens, I. W. *et al.* Spitzer Observations of Dust Emission from H II Regions in the Large Magellanic Cloud. **784**, 147 (Apr. 2014).
222. Gaensler, B. M. *et al.* The Magnetic Field of the Large Magellanic Cloud Revealed Through Faraday Rotation. *Science* **307**, 1610–1612 (2005).
223. Komin, N. *et al.* H.E.S.S. observations of the Large Magellanic Cloud. *arXiv e-prints*, arXiv:1201.0639 (Jan. 2012).

224. H. E. S. S. Collaboration *et al.* Discovery of gamma-ray emission from the extragalactic pulsar wind nebula N 157B with H.E.S.S. **545**, L2 (Sept. 2012).
225. Marshall, F. E., Gotthelf, E. V., Zhang, W., Middleditch, J. & Wang, Q. D. Discovery of an Ultrafast X-Ray Pulsar in the Supernova Remnant N157B. **499**, L179–L182 (June 1998).
226. Macri, L. M., Stanek, K. Z., Bersier, D., Greenhill, L. J. & Reid, M. J. A New Cepheid Distance to the Maser-Host Galaxy NGC 4258 and Its Implications for the Hubble Constant. **652**, 1133–1149 (Dec. 2006).
227. Wang, Q. D., Gotthelf, E. V., Chu, Y. H. & Dickel, J. R. Detection of an X-Ray Pulsar Wind Nebula and Tail in SNR N157B. **559**, 275–281 (Sept. 2001).
228. Borkowski, K. J., Hendrick, S. P. & Reynolds, S. P. X-Ray-Emitting Ejecta of Supernova Remnant N132D. **671**, L45–L48 (Dec. 2007).
229. Tappe, A., Rho, J. & Reach, W. T. Shock Processing of Interstellar Dust and Polycyclic Aromatic Hydrocarbons in the Supernova Remnant N132D. **653**, 267–279 (Dec. 2006).
230. Bamba, A., Ueno, M., Nakajima, H. & Koyama, K. Thermal and Nonthermal X-Rays from the Large Magellanic Cloud Superbubble 30 Doradus C. *The Astrophysical Journal* **602**, 257–263 (Feb. 2004).
231. Mathewson, D. S. *et al.* Supernova remnants in the Magellanic Clouds. III. **58**, 197–200 (June 1985).
232. Lortet, M. C. & Testor, G. Optical observations of the bubble nebula N 157C (=0536.6-6914) and the tight clusters in the association LH 90 in LMC. **139**, 330–340 (Oct. 1984).
233. Long, K. S., Helfand, D. J. & Grabelsky, D. A. A soft X-ray study of the Large Magellanic Cloud. **248**, 925–944 (Sept. 1981).
234. Seward, F. D. *et al.* DEM L241, A SUPERNOVA REMNANT CONTAINING A HIGH-MASS X-RAY BINARY. *The Astrophysical Journal* **759**, 123 (Oct. 2012).
235. Corbet, R. H. D. *et al.* A LUMINOUS GAMMA-RAY BINARY IN THE LARGE MAGELLANIC CLOUD. *The Astrophysical Journal* **829**, 105 (Sept. 2016).
236. Meurs, E. J. A. & van den Heuvel, E. P. J. The number of evolved early-type close binaries in the galaxy. **226**, 88–107 (Dec. 1989).
237. Hinton, J. A. & Hofmann, W. Teraelectronvolt Astronomy. **47**, 523–565 (Sept. 2009).
238. Mayer, M. *et al.* Predicting the X-ray flux of evolved pulsar wind nebulae based on VHE gamma-ray observations. *arXiv e-prints*, arXiv:1202.1455 (Feb. 2012).

239. H. E. S. S. Collaboration *et al.* The population of TeV pulsar wind nebulae in the H.E.S.S. Galactic Plane Survey. **612**, A2 (Apr. 2018).
240. Knödlseder, J. *et al.* GammaLib and ctools. A software framework for the analysis of astronomical gamma-ray data. **593**, A1 (Aug. 2016).
241. Cowan, G., Cranmer, K., Gross, E. & Vitells, O. Asymptotic formulae for likelihood-based tests of new physics. *European Physical Journal C* **71**, 1554 (Feb. 2011).
242. Wilks, S. S. The Large-Sample Distribution of the Likelihood Ratio for Testing Composite Hypotheses. *Ann. Math. Statist.* **9**, 60–62 (Mar. 1938).
243. Baltz, E. A. Dark Matter Candidates. *arXiv e-prints*, astro-ph/0412170 (Dec. 2004).
244. Bertone, G., Hooper, D. & Silk, J. Particle dark matter: evidence, candidates and constraints. **405**, 279–390 (Jan. 2005).
245. Bergström, L. Dark matter candidates. *New Journal of Physics* **11**, 105006 (Oct. 2009).
246. Kim, S. *et al.* An HiAperture Synthesis Mosaic of the Large Magellanic Cloud. *The Astrophysical Journal* **503**, 674–688 (Aug. 1998).
247. Buckley, M. R. *et al.* Search for gamma-ray emission from dark matter annihilation in the large magellanic cloud with the fermi large area telescope. **91**, 102001 (May 2015).
248. LUKE, K T; ROHLFS. Structure and kinematics of neutral hydrogen gas in the Large Magellanic Cloud. English. *Astronomy and astrophysics (Berlin. Print)*. ISSN: 0004-6361 (1992).
249. Hernquist, L. An Analytical Model for Spherical Galaxies and Bulges. **356**, 359 (June 1990).
250. de Vaucouleurs, G. & de Vaucouleurs, A. An analysis of the composite spectrum of the Large Magellanic Cloud. **63**, 304 (Feb. 1958).
251. Hütten, M., Combet, C. & Maurin, D. CLUMPY v3:  $\gamma$ -ray and  $\nu$  signals from dark matter at all scales. *Computer Physics Communications* **235**, 336–345 (Feb. 2019).
252. Ciafaloni, P. *et al.* Weak corrections are relevant for dark matter indirect detection. **2011**, 019 (Mar. 2011).
253. Sudoh, T., Linden, T. & Beacom, J. F. TeV halos are everywhere: Prospects for new discoveries. **100**, 043016 (Aug. 2019).
254. Abel Barrio, J. *et al.* Analogue Sum ASIC for L1 Trigger Decision in Cherenkov Telescope Cameras. *arXiv e-prints*, arXiv:1410.8526 (Oct. 2014).